Malaysian Journal of Analytical Sciences (MJAS)
Published by Malaysian Analytical Sciences Society

Vol 26 No 1 (2022)

Vol 26 No 2 (2022)

Vol 26 No 3 (2022)

Vol 26 No 4 (2022)

Vol 26 No 5 (2022)

Vol 26 No 6 (2022)

2022

Malaysian Journal of Analytical Sciences Vol 26 No 1 2022

Malaysian Journal of Analytical Sciences (MJAS)
Published by Malaysian Analytical Sciences Society

SYNTHESIS AND MECHANISM STUDY OF NEW BIVALENT β-CARBOLINE DERIVATIVES

(Kajian Sintesis dan Mekanisma Derivatif Bivalen β-karbolin Baharu)

Nurul Tasnim Noor Aaisa[1,2], Karimah Kassim[2], Nur Azzalia Kamaruzaman[3], Mazlin Mohideen[1]*

[1]Faculty of Pharmacy and Health Sciences,
Universiti Kuala Lumpur Royal College of Medicine Perak, 30450 Ipoh, Perak, Malaysia
[2]Institute of Science,
Universiti Teknologi MARA, 40450 Puncak Alam, Selangor, Malaysia
[3]National Poison Centre,
Universiti Sains Malaysia, 11800 Minden, Pulau Pinang, Malaysia

**Corresponding author: mazlin.mohideen@unilkl.edu.my*

Received: 15 September 2021; Accepted: 30 December 2021; Published: 25 February 2022

Abstract

This study reports simple and straightforward methods for synthesizing new bivalent β-carboline compounds using L-tryptophan as a starting material with 1,4-dibromobutane as a dimerization linker. The synthetic route began with coupling L-tryptophan with formaldehyde via Pictet-Spengler condensation to afford tetrahydro-β-carboline, **T1** as the key intermediate. The reaction proceeded with decarboxylation of **T1** using potassium dichromate with acetic acid to afford β-carboline, **T2**. Subsequent alkylation of **T2** using 1,4-dibromobutane as the linker yielded intermediate **T3**, followed by dimerization to furnish the new bivalent β-carboline, **T4**. ^{1}H and ^{13}C NMR confirmed all the synthesized compounds. In addition, this study includes the proposed mechanism for the synthesis of a new bivalent β-carboline compound.

Keywords: synthesis, bivalent β-carboline, L-Tryptophan, Pictet-Spengler condensation, dimerization

Abstrak

Kajian ini melaporkan kaedah mudah dan secara terus untuk mensintesis sebatian baru bivalen β-karbolin menggunakan L-tryptofan sebagai bahan pemulaan dengan 1,4-dibromobutana sebagai penghubung dimerisasi. Laluan sintesis bermula dengan gandingan L-tryptofan dengan formaldehid melalui pemeluwapan Pictet-Spengler untuk mendapatkan tetrahidro-β-karbolin, **T1** sebagai kunci perantaraan. Tindak balas diteruskan dengan pendekarboksilan **T1** menggunakan kalium dikromat dengan asid asetik untuk menghasilkan β-karbolin, **T2**. Seterusnya alkilasi **T2** menggunakan 1,4-dibromobutana sebagai penghubung menghasilkan perantara **T3**, diikuti dengan dimerisasi untuk menghasilkan bivalen β-karbolin baharu, **T4**. Semua sebatian yang disintesis disahkan dengan ^{1}H NMR dan ^{13}C NMR. Sebagai tambahan, kajian ini merangkumi mekanisma yang dicadangkan untuk sintesis sebatian bivalen β-karbolin baharu.

Kata kunci: sintesis, bivalen β-Karbolin, L-Tryptofan, pemeluwapan Pictet-Spengler, dimerisasi

Introduction

β-carbolines are derived from a large group of heterocyclic compounds known as Norharmane (Figure 1), which have a 9H-pyrido[3,4-*b*]indole structural unit [1]. Furthermore, β-carboline can be classified as a synthetic and naturally occurring indole alkaloid with varying degrees of aromaticity that possess a planar tricyclic pyrido[3,4-*b*]indole ring system [2,3,4]. The core skeleton of β-carboline consists of a pyridine ring fused to an indole backbone (Figure 1).

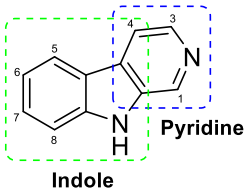

Figure 1. Core skeleton of β-carboline structure

β-carboline is a natural constituent found in plants, human tissues, body fluids, marine life, insects, and mammals [1]. Furthermore, β-carboline is also distributed in fungi and foods with broad pharmacological properties, including sedative, antithrombin, antimalarial, anti-HIV, and anti-inflammatory [5,6]. In addition, previous studies have reported that β-carboline, with its widespread biological properties, is commonly studied for its antitumor activity [7].

β-carboline alkaloid can be isolated from the seeds of a plant named *Peganum harmala,* which belongs to the family of Zygophyllaceae [4,7,8]. Other names for *Peganum harmala* include harmal, African rue, and Syrian rue. It is a perennial herbaceous, glabrous plant that can grow in semi-arid rangeland and sandy soils, especially in the Mediterranean region of North Africa and the Middle East [9]. β-carboline derivatives extracted from this plant are used mainly to treat various diseases, including asthma and jaundice. Despite its toxicity level, *Peganum harmala* has been used to treat a range of human ailments, as the health benefits outweigh the detrimental effects [10].

Interestingly, bivalent β-carboline alkaloids (Figure 2) elicited substantially greater bioactivity than the corresponding monomers. Thus, this suggests that bivalent compounds have better therapeutic potential and thus should be studied in future research [11].

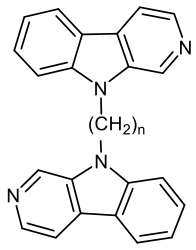

Figure 2. Example of a bivalent β-carboline structure

The bivalent β-carboline structure has two β-carboline monomers linked at positions-1, -2, -3, and -9 by carbon chains, heteroatoms, heterocyclic, amide esters, or amino-groups [11]. In addition, a previous study discovered that bivalent β-carboline elicited anticancer properties via a suitable linker, significantly improving activity by 100- to 500-fold over the corresponding monomers [5,12]. The improvement in anticancer activity might have occurred as the bivalent compound was more favourable to intercalating into DNA [5]. Therefore, bivalent β-carboline was expected to have significantly higher antitumor potency *in vitro* and *in vivo* than the corresponding monomers [12].

There are numerous reports of bivalent β-carboline derivatives. Daoud et al. investigated the anticancer activity of the bivalent β-carboline derivative B-9-3 (**1**) (Figure 3), which demonstrated potent anticancer activity against three cancer cell lines with IC_{50} values ranging from 3.58 μM–10.89 μM [13]. Chen et al. reported the synthesis and anticancer activity of a series of novel N^9-heterobivalent β-carboline (**2**) and (**3**) with strong cytotoxic activities against six cancer cell lines with IC_{50} values lower than 20 μM (Figure 3) [1].

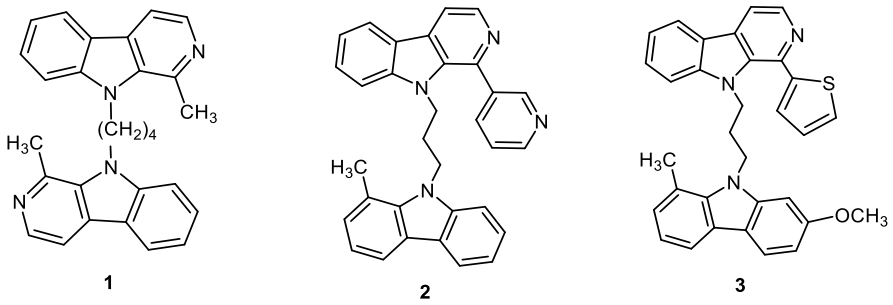

Figure 3. Reported bivalent β-carboline derivatives

Bivalent β-carboline, linked by suitable linkers, could significantly improve DNA-binding affinity as the dimerized compounds can bind to DNA through bis-intercalation mode, causing significant changes in DNA double helix structure [7,14,15]. The structural-activity relationships of the bivalent β-carboline compound indicated a few factors that determined antitumor activity; the common β-carboline moiety was very crucial for antitumor activity, the length of the linker affected antitumor potencies, four to six methylene units were more favourable, and the linker position in positions-1,-2,-3, and -9 were beneficial [14,16]. The problem statement that this study addresses is the importance of developing new anticancer drugs as cancer is currently one of the leading causes of major health problems worldwide. Thus, this study aims to synthesize a new bivalent β-carboline compound using the suitable length of 1,4-dibromobutane in position-9 in the four-step method using commercially available L-tryptophan as a starting material. The bivalent β-carboline was characterized using ^{1}H- and ^{13}C-NMR.

Materials and Methods

This section will describe a sequential decarboxylation and aromatization of tetrahydro-β-carboline-3-carboxylic acid **T1** to furnish β-carboline **T2**. This was followed by the dimerization reaction of the monomer β-carboline to form a new bivalent β-carboline **T4**.

Synthesis of tetrahydro-β-carboline (T1)

Tetrahydro-β-carboline-3-carboxylic acid (**T1**) was prepared through Pictet-Spengler condensation of L-tryptophan (**1**, 2.0 g, 9.8 mmol) with 37% formaldehyde (**2**, 0.98 mL, 32.63 mmol). The reaction started with 3 hours of stirring of L-tryptophan (**1**) and NaOH (0.4 g, 10 mmol) in a specific amount of water (200 mL). Then, 37% formaldehyde (**2**) was added to the solution, and it continued to reflux for 3 hours at room temperature. Upon completion, the reaction mixture was neutralized with glacial acetic acid, and the product was filtered off, washed well with water, and dried overnight.

Synthesis of β-carboline (T2)

Next, we attempted the decarboxylation-aromatization of tetrahydro-β-carboline-3-carboxylic acid (**3**, 1 g, 4.6 mmol) by stirring it in water (100 mL) at 100°C. The reaction continued to stir and heat with $K_2Cr_2O_7$ (9.5 g, 32 mmol) and acetic acid as a base (10 mL). Then, the reaction mixture was cooled by running it under tap water. Upon completion, sodium sulfite was added as a removing oxidizing agent. This was followed by the addition of 2.5 M NaOH drop by drop until it reached pH 7. The solution was extracted with ethyl acetate, and the combined organic layer was collected, washed with water and brine, and dried over anhydrous sodium sulfate. Lastly, the solution was evaporated. Yellowish solid, yield 47%, m.p. 199°C. ^{1}H-NMR (400 MHz, MeOD-d_4): δ 8.77 (s, 1 H), 8.26 (d, J = 5.5 Hz, 1 H), 8.17 (d, J = 7.8 Hz, 1 H), 8.08-8.07 (m, 1 H), 7.55-7.54 (m, 2 H), 7.27-7.23 (m, 1 H); ^{13}C NMR (101 MHz, MeOD-d_4): δ 137.0, 132.7, 129.1, 128.4, 121.4, 120.8, 119.5, 114.8, 111.5.

Synthesis of intermediate bivalent β-carboline (T3)

The intermediate **T3** was prepared by stirring β-carboline (**T2,** 0.5 g, 2.96 mmol) in anhydrous DMF (15 mL) at room temperature for 30 minutes, then 60% NaH dispersed in mineral oil (0.23 g, 5.92 mmol) and

appropriate 1,4-dibromobutane (0.7 mL, 5.92 mmol) was added. The reaction mixture continued to stir at room temperature, and upon completion, the mixture was poured into water, extracted with ethyl acetate, and washed with water and brine. Next, it was dried under anhydrous sodium sulfate, filtered, and evaporated. The final result of the reaction was an oily product. Dark brownish oil product, yield 98%, m.p. 188°C. ^{1}H NMR (400 MHz, $CDCl_3$): δ 8.39 (d, *J* = 5.9 Hz, 1 H), 8.31-8.27 (m, 2 H), 7.85 (d, *J* = 7.3 Hz, 1 H), 7.69 (d, *J* = 8.7 Hz, 2 H), 7.49 (d, *J* = 7.8 Hz, 1 H), 3.50 (d, *J* = 12 Hz, 2 H), 3.43 (d, *J* = 5.9 Hz, 2 H), 2.03-2.00 (m, 4 H); ^{13}C NMR (101 MHz, $CDCl_3$): δ 144.6, 136.2, 132.9, 132.3, 130.8, 123.5, 122.6, 119.6, 117.3, 111.2, 60.3, 44.4, 33.9, 29.7.

Synthesis of bivalent β-carboline (T4)

β-carboline (**T2**, 0.18 g, 1.09 mmol) in anhydrous DMF (6 mL) was added by stirring to a solution of intermediate (**T3**, 0.5 g, 1.64 mmol), 60% NaH dispersed in mineral oil (0.21 g, 5.49 mmol), potassium iodide (0.91 g, 5.49 mmol) in anhydrous DMF (10 mL). Next, intermediate **T3** was further reacted to form bivalent β-carboline **(T4)**. The reaction mixture was stirred at room temperature until the reaction was completed, and then it was poured into ice-cold water. After that, the reaction mixture was extracted with ethyl acetate and washed with water and brine. The combined organic layer was dried over anhydrous sodium sulfate, Na_2SO_4, and filtered. The purification process was conducted using column chromatography (DCM/MeOH 100:1 as the eluent) to furnish bivalent β-carboline **(T4)**. Dark brownish oil product, yield 13%, m.p. >270°C. ^{1}H NMR (400 MHz, $CDCl_3$): δ 8.93 (s, 2 H), 8.45 (d, *J* = 5.5 Hz, 2 H), 8.19 (d, *J* = 8.2 Hz, 2 H), 8.10 (d, *J* = 5.5 Hz, 2 H), 7.70-7.66 (m, 2 H), 7.52 (d, *J* = 8.4 Hz, 2 H), 7.36 (t, *J* = 7.5 Hz, 2 H), 5.06-5.00 (m, 4 H), 4.47 (t, *J* = 7.3 Hz, 4 H); ^{13}C NMR (101 MHz, $CDCl_3$): δ 143.3, 138.1, 137.5, 133.8, 132.0, 129.9, 122.6, 120.7, 118.5, 115.5, 110.1, 43.5.

Results and Discussion

The desired bivalent β-carboline **(T4)** synthesis was performed in a four-step method starting from L-tryptophan **(1)** as outlined in Scheme 1. Firstly, the tetrahydro-β-carboline **(T1)** was prepared from the successful reaction of Pictet-Spengler condensation of L-tryptophan **(1)** with formaldehyde. The reaction was further reacted to form β-carboline **(T2)** with a 47% yield via decarboxylation by using potassium dichromate in the presence of acetic acid. Next, the β-carboline structure was alkylated at position-9 by the action of the strong base, NaH in anhydrous DMF, followed by the addition of 1,4-dibromobutane to successfully afford intermediate **T3** with a 98% yield. The intermediate **T3** was present in an oily product form. Finally, the intermediate **T3** was further reacted with β-carboline **(T2)** with a strong base, NaH in solvent anhydrous DMF, in the presence of potassium iodide. The reaction was carried out at room temperature to successfully afford the targeted compound, bivalent β-carboline **T4** (13%). The bivalent β-carboline **(T4)** underwent a purification process using column chromatography and furnished the oily product. ^{1}H NMR and ^{13}C NMR were utilized to characterize the chemical structures of all synthesized compounds in this study.

The proposed mechanism for the Pictet-Spengler condensation of L-tryptophan forming tetrahydro-β-carboline **T1** was outlined in Scheme 2. Initially, the mechanism started with the production of an iminium ion **3**, followed by the formation of an imine intermediate **5**, Schiff base, which removed H_2O. Next, the imine intermediate **5** underwent 6-endo-trig cyclizations involved in the base's action, forming a new ring, and the final product was tetrahydro β-carboline **(T1)**.

The proposed mechanism of the oxidation-decarboxylation of tetrahydro-β-carboline **(T1),** which produces β-carboline **(T2)**, is outlined in Scheme 3. Based on Scheme 3, the first step of the mechanism involved abstracting protons from tetrahydro-β-carboline **(T1)** by water. Then a new bond was formed: the double bond and functional group -COOH were removed, forming compound **10**. On the other hand, potassium dichromate that has been treated with acetic acid formed a chromic acid known as the common oxidizing agent for the oxidation reaction. Then, the strong nucleophile site of compound **10** attacked the electrophile site of chromic acid-water repeated proton abstraction in compound **11**. Next, the nucleophile site of -OH was abstracted proton from the α-carbon of compound **12**, forming a new bond. This double bond formed a new aromatic pyridine ring which successfully formed β-carboline **(T2)**.

Lastly, the proposed mechanism for the new bivalent of β-carboline **(T4)** is outlined in Scheme 4. The mechanism started with the strong base, NaH, that abstracted protons from β-carboline (T2), producing a strong nucleophile site of compound **13**. Then, the strong nucleophile of N in compound **13** attacked the electrophile of C from the 1,4-dibromobutane, and it removed bromine since it is a good leaving group. Finally, the intermediate of bivalent β-carboline **(T3)** was successfully formed with NaBr. The intermediate bivalent β-carboline **(T3)** further reacted with the monomer β-carboline **(T2)** by the same reaction mechanism as the intermediate bivalent β-carboline **(T3)** to form a symmetrical structure of bivalent β-carboline **(T4)**.

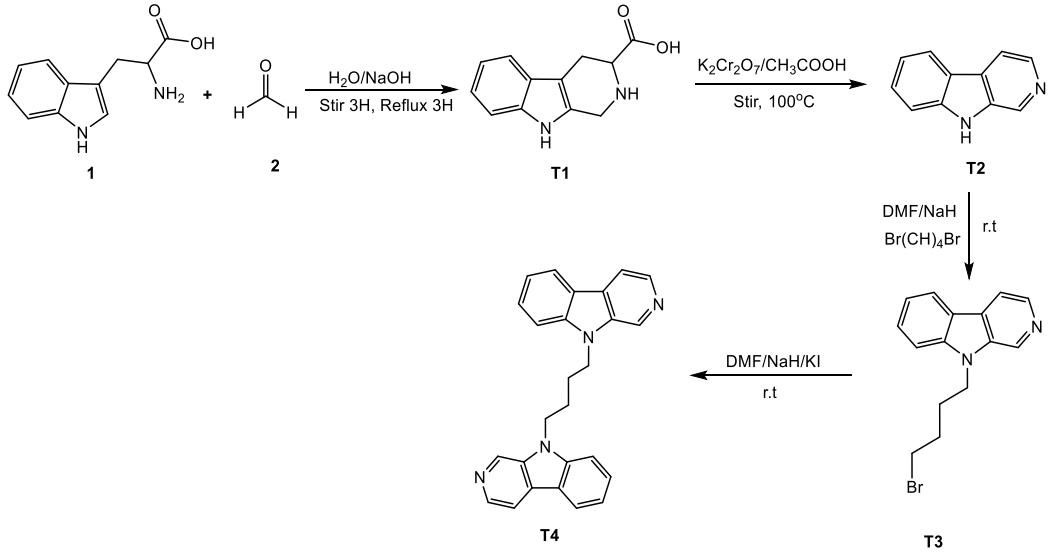

Scheme 1. Overall synthetic route for new bivalent β-carboline compound **T4**

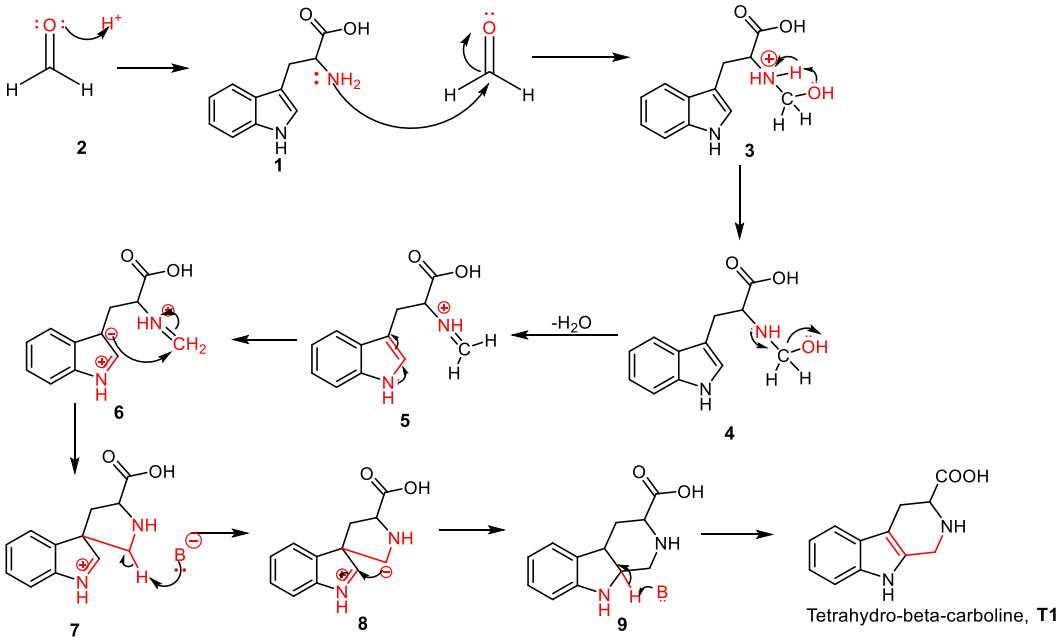

Scheme 2. Proposed mechanism for the Pictet-Spengler condensation of L-tryptophan forming tetrahydro-β-carboline (**T1**)

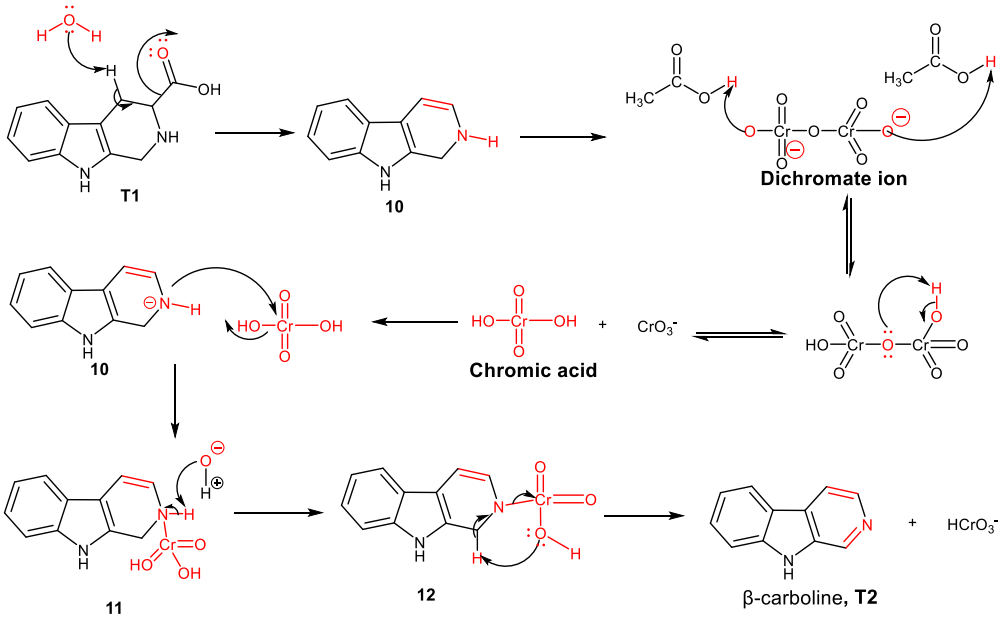

Scheme 3. Proposed mechanism for the oxidation-decarboxylation of tetrahydro-β-carboline (**T1**) forming β-carboline (**T2**)

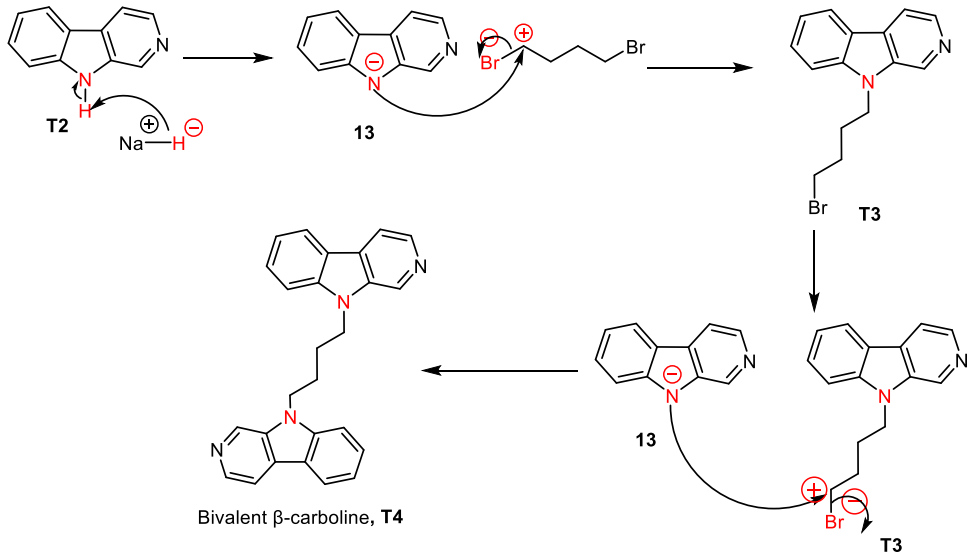

Scheme 4. Proposed mechanism for dimerization of β-carboline (**T4**)

Conclusion

In summary, this study has successfully synthesized a new bivalent β-carboline compound **(T4)** from the starting material L-tryptophan **(1)** with a 13% yield. The synthesis reaction is simple and straightforward, using commercially available, safe, and cheaper chemicals. Moreover, the mechanism for the synthesis route of the new bivalent β-carboline compound **(T4)** has been

proposed in this study for future reference. Future studies will evaluate the *in vitro* cytotoxicity potential of T4 in various cancer cell lines to determine its potential as an anticancer agent.

Acknowledgement

This study was supported by the Ministry of Higher Education Malaysia (MoHE) for the Fundamental Research Grant Scheme (FRGS) (FRGS/1/2019 /ST01/UNIKL/02) as well as the Faculty of Pharmacy and Health Sciences, Universiti Kuala Lumpur Royal College of Medicine Perak (UniKL RCMP) and the Institute of Science, Universiti Teknologi MARA (UiTM) for all of the facilities provided for the lab work. Huge thanks to the National Poison Centre, Universiti Sains Malaysia for their support of this project.

References

1. Chen, X., Guo, L., Ma, Q., Chen, W., Fan, W. and Zhang, J. (2019). Design, synthesis, and biological evaluation of novel n-acylhydrazone bond linked heterobivalent β-carboline as potential anticancer agents. *Molecules,* 24(16): 2950.
2. Ahmad, I., Fakhri, S., Khan, H., Jeandet, P. and Aschner, M. (2020). Targeting cell cycle by β-carboline alkaloids *in vitro*: Novel therapeutic prospects for the treatment of cancer. *Chemico-Biological Interactions*, 330: 109229.
3. Li, S., Yang, B., Zhang, Q., Zhang, J., Wang, J. and Wu, W. (2010). Synthesis and bioactivity of β-carboline derivatives. *Natural Product Communications*, 5(10): 1591-1596.
4. Sharma, S., Yadav, M., Gupta, S. P., Pandav, K. and Kumar, S. (2016). Spectroscopic and structural studies on the interactions of an anticancer β-carboline alkaloid, harmine with GC and AT specific DNA oligonucleotides. *Chemico-Biological Interactions*, 260: 256-262.
5. Du, H., Gu, H., Li, N. and Wang, J. (2016). Synthesis and biological evaluation of bivalent β-carbolines as potential anticancer agents. *Medicinal Chemistry Communications,* 7(4): 636-645.
6. Kumar, S., Singh, A., Kumar, K. and Kumar, V. (2017). Recent insights into synthetic beta-carbolines with anticancer activities. *European Journal of Medicinal Chemistry,* 142: 48-73.
7. Gu, H., Li, N., Dai, J., Xi, Y., Wang, S. and Wang, J. (2018). Synthesis and *in vitro* antitumor activity of novel bivalent beta-carboline-3-carboxylic acid derivatives with DNA as a potential target. *International Journal of Molecule Sciences,* 19(10): 3179.
8. Manasa, K. L., Yadav, S. S. and Nagesh, N. (2020). The β-carboline alkaloids in cancer therapy-recent advancements in this area. *Journal of Pharmacy and Biological Sciences*, 15(3): 1-27.
9. Nenaah, G. (2010). Antibacterial and antifungal activities of (beta)-carboline alkaloids of *Peganum Harmala* (L) seeds and their combinations effects. *Fitoterapia*, 81(7): 779-782.
10. Kuete, V. (2014). Physical, hematological, and histopathological signs of toxicity induced by African medicinal plants. *Toxicological Survey of African Medicinal Plants*, 2014: 635-657.
11. Dai, J., Dan, W., Scheinder, U. and Wang, J. (2018). β-carboline alkaloid monomers and dimers: Occurrence, structural diversity, and biological activities. *European Journal of Medicinal Chemistry,* 157: 622-656.
12. Chen, W., Zhang, G., Guo, L., Fan, W., Ma, Q., Zhang, X., Du, R. and Cao, R. (2016). Synthesis and biological evaluation of novel alkyl diamine linked bivalent β-carbolines as angiogenesis inhibitors. *European Journal of Medicinal Chemistry*, 124: 249-261.
13. Daoud, A., Song, J., Xiao, F. and Shang, J. (2014). B-9-3, a novel beta-carboline derivative exhibits anticancer activity via induction of apoptosis and inhibition of cell migration *in vitro*. *European Journal of Pharmacology,* 724: 219-230.
14. Shi, B., Cao, R., Fan, W., Guo, L., Ma, Q., Chen, X., Guoxian, Z., Qiu, L. and Song, H. (2013). Design, synthesis and *in vitro* and *in vivo* antitumor activities of novel bivalent β-carbolines. *European Journal of Medicinal Chemistry*, 60: 10-22.
15. Sun, R., Liu, R., Zhou, C., Ren, Z., Guo, L., Ma, Q. and Cao, R. (2015). Synthesis and biological evaluation of piperazine group-linked bivalent β-carbolines as potential antitumor agents. *Medicinal Chemistry Communications,* 6(12): 2170-2174.
16. Luo, B. and Song, X. (2021). A comprehensive overview of β-carboline and its derivatives as anticancer agents. *European Journal of Medicinal Chemistry*, 224: 113688.

Malaysian Journal of Analytical Sciences (MJAS)
Published by Malaysian Analytical Sciences Society

INSIGHT MECHANISTIC STUDY OF SAMARIUM OXIDE BASED CATALYST IN METHANATION REACTION

(Kajian Mendalam Mekanistik Pemangkin Berasaskan Samarium Oksida dalam Tindak Balas Metanasi)

Salmiah Jamal Mat Rosid[1]*, Susilawati Toemen[2], Wan Azelee Wan Abu Bakar[2], Ahmad Zamani Ab Halim[3], Sarina Mat Rosid[4]

[1]Unisza Science and Medicine Foundation Centre,
Universiti Sultan Zainal Abidin, Gong Badak Campus, 21300 Kuala Nerus, Terengganu, Malaysia
[2]Department of Chemistry, Faculty of Science,
Universiti Teknologi Malaysia, 81310 UTM Skudai, Johor, Malaysia
[3]Faculty of Industrial Sciences & Technology,
Universiti Malaysia Pahang, 26300 Gambang, Kuantan, Pahang, Malaysia
[4]Advanced Membrane Technology Research Centre (AMTEC),
Universiti Teknologi Malaysia, 81310 UTM Skudai, Johor, Malaysia

**Corresponding author: salmiahjamal@unisza.edu.my*

Received: 8 September 2021; Accepted: 1 January 2022; Published: 25 February 2022

Abstract

An understanding of the mechanism of chemical reactions is needed to optimize the reaction process and improve performance. The adsorption of reactant molecules, formation of reaction intermediates, and finally the distribution of products depend on the composition and surface structure of the catalyst. This research work deployed Fourier transform infrared (FTIR), high performance liquid chromatography (HPLC), and gas chromatography (GC) to identify the mechanism of Sm/Mn/Ru (60:35:5)/Al_2O_3 catalyst. The envisioned methanation reaction initially follows the Langmuir Hinselwood mechanism with the adsorption of CO_2 and H_2 gases on the catalyst surface. From the gaseous product, only methane peak was observed. Meanwhile, from the liquid product, methanol peak is observed at retention time 20 mins which accordance with standard methanol. Therefore, the final products acquired from the methanation reaction of Sm/Mn/Ru (60:35:5)/Al_2O_3 catalyst are CH_4, CH_3OH and H_2O.

Keywords: methanation, hydrogenation, samarium oxide, catalyst, mechanism

Abstrak

Pemahaman kepada mekanisme tindak balas kimia adalah perlu untuk mengoptimumkan proses tindak balas dan meningkatkan prestasi. Penjerapan molekul reaktan, pembentukan perantaraan tindak balas, dan taburan produk pada asasnya bergantung kepada komposisi dan struktur permukaan pemangkin. Kerja penyelidikan ini menggunakan inframerah transformasi Fourier (FTIR), kromatografi cecair prestasi tinggi (HPLC), dan kromatografi gas (GC) untuk mengenal pasti mekanisma mangkin Sm/Mn/Ru (60:35:5)/Al_2O_3. Tindak balas metana yang dipostulatkan adalah mengikut mekanisma Langmuir Hinselwood yang pada mulanya melibatkan penjerapan gas CO_2 dan H_2 pada permukaan mangkin. Daripada produk gas, hanya puncak metana

diperhatikan. Manakala, daripada produk cecair, puncak metanol diperhatikan pada minit ke 20 masa tahanan mengikut larutan piawai metanol. Oleh itu, produk akhir yang diperoleh daripada tindak balas metana mangkin Sm/Mn/Ru (60:35:5)/Al_2O_3 ialah CH_4, CH_3OH dan H_2O.

Kata kunci: metanasi, penghidrogenan, samarium oksida, pemangkin, mekanisma

Introduction

Nowadays, catalytic methanation reaction has been widely explored in order to convert CO_2 gas to CH_4 gas by reducing emission of greenhouse gases using metal oxide. The most conventional metal oxide catalyst used are nickel, cobalt, manganese, copper, iron and lanthanide element. The catalytic ability of metal oxide catalyst deteriorates after several hours of reaction time due to the carbon forming process. The formation of carbon can be avoided by adding a dopant to the metal oxide catalyst [1]. Rosid et al. revealed that dopants and metal-based oxides have varying functions in hydrogenation reactions [2]. The metal-based oxide incites the reaction via combining with CO_2 molecules to form carbonate species on the surface, while the dopant split the H_2 molecules and provides the H atoms required for further hydrogenation of the carbonate to form methane [3].

Carbon dioxide (CO_2) adsorption happens during carbonate species and carrier-related formate formation in H_2 presence [4, 5]. Many studies have proposed varying CO_2 methanation mechanisms. The first proposed mechanism refers to CO_2 reaction in a carrier, while H (ads) species generated in metals yield formate intermediate (COOH) at the interface of metal support. The CO (ads) species generated by formate are hydrogenated to methane [6]. Meanwhile, on second proposed mechanism, CO_2 (ads) and O (ads) dissociated directly on the metal surface. Subsequently, CO (ads) become hydrogenated to CH_4. The dissociation of CO (ads) denotes the rate determining step of the reaction [7].

Other than that, Marc. et al. also pointed out that the methanation process consists of three steps, of which the first step is to adsorb CO_2 on the catalyst chemically [8]. The second step is to separate CO_2 into surface-absorbed CO and O, and the final step is species reaction to separate it from H_2. The particular reaction process is known as Langmuir-Hinselwood mechanism [9]. However, most of the proposed mechanism involved alkaline earth metal dan transition metal which showed the formation of carbonate and formate species during reaction. Therefore, in this study the mechanistic study has been conducted over lanthanide element, which is samarium oxide catalyst in order to identify the mechanism pathway and product formed during the reaction occur. This study was conducted using FTIR, GC and HPLC for identification of product and by-product formed in methanation reaction.

Materials and Methods

Catalyst preparation

The catalyst was prepared by aqueous incipient wetness impregnation method. 5 g of samarium(III) nitrate was firstly weighed in a beaker and dissolved in a small amountof distilled water, then mixed together with a solution of $RuCl_3.xH_2O$ and $Mn(NO_3)_2.4H_2O$ salts according to the desired ratio. The catalyst solutions were stirred continuously for 30 minutes before 7 g of alumina was added to it. After that, the coated alumina was aging at 80 – 90 ^oC for 24 hours followed by calcination at 1000 ^oC for 5 hours using a ramp rate of 10 ^oC/min to remove all the metal counter ions and water present in the catalyst. Lastly, the sample was labelled as Sm/Mn/Ru (60:35:5)/Al_2O_3. All chemicals used in this study were purchased from Sigma Aldrich.

Catalytic screening

A gas mixture consisting of CO_2 and H_2 with a molar ratio of 1: 4 was continuously passed through the catalyst at a flow rate of 50.00 cm^3/min. Prior to starting the catalyst test, the reaction gas was introduced into the microreactor system without passing through the catalyst as a calibration. Then, the reaction gas was passed through a catalyst and the temperature is raised from room temperature (RT) to

400°C using FTIR Nicolet Avatar 370 DTGS spectrophotometer. The percentage of CO_2 conversion calculation is shown in Equation 1.

$$\% \text{ of } CO_2 \text{ conversion} = \frac{\text{Peak Area of } CO_2 \text{ calibration} - \text{Peak Area of } CO_2 \text{ conversion}}{\text{Peak area of } CO_2 \text{ calibration}} \times 100 \quad (1)$$

Mechanistic study

First, the catalyst was ground and placed in a glass tube, while air pre-treatment was executed for 30 minutes at 100 °C for catalyst sample activation. When the sample cooled to ambient temperature, H_2/CO_2 gas was installed into the microreactor system with the temperature increased to 400 °C. The product stream was gathered in a sample cell equipped with a KBr window and scanned through an in-situ Nicolet Avatar FTIR 370 DTGS spectrophotometer. Then, FTIR was used to analyze the catalyst powder to identify adsorbed materials on the catalyst surface. The liquid product of the reaction and methanol standard were analyzed by HPLC (Rezex ROA-Organic Acid), and methanol was detected using a 300 mm × 7.8 mm ID column with a refractive index (RI) detector. Meanwhile, gas products were analyzed by Hewlett Packard 6890 series gas chromatograph with Flame Ionization Detector (FID) and methane production was determined using an Equation 2.

$$\% \text{ Yield of } CH_4 = \frac{[CH_4] \text{ from GC}}{\% \text{ Conversion of } CO_2} \times 100\% \quad (2)$$

Results and Discussion

Marwood et al. and Sharma et al. confirmed the direct decomposition of CO_2 into CO and O [10, 11]. In this study, it seems that the direct decomposition of CO_2 is demonstrated. This proposal is very consistent with the fact that, as described by Solymosi et al. formate was not detected in excessive supports containing low concentrations of OH groups [12]. This was ascribed to hydrogen present in the reaction that hindered CO intermediates formation, thus yielding formate species.

Products analysis

Potential Sm/Mn/Ru (60:35:5)/Al_2O_3 catalyst reveal catalytic routes for methane as main product, methanol and water as a by-product. In this study, it seems that the direct decomposition of CO_2 is demonstrated. The FTIR spectrum of the gaseous product is presented in Figure 1. The spectrum shows that the peak is close to 2351 cm^{-1} due to the CO_2 stretching mode. At the same time, the stretching mode of CH_4 band at the wavenumber of 3014 cm^{-1} and C-H deformation mode at 1310 cm^{-1} [13] can be clearly detected starting at 250 ^oC reaction temperature. From the figure, it can be observed that no methane peak was appeared at room temperature (RT) and 100 ^oC indicating the absence of methane gas produced during the reaction. When the reaction temperature was raised to 400 ^oC, the highest CH_4 gas was formed with around 69% detected by GC-FID. This show that methane formation is advantageous at high reaction temperature [14]. No band of 3300-3600 cm^{-1} of water was observed in the FTIR spectrum because the silica trap system used in the reactor functions as adsorbed water. Interestingly, no CO intermediate was formed as there is no CO peak around 2080 cm^{-1} was detected. This shows that CO_2 gas is directly converted into CH_4 gas without producing CO gas as an intermediate.

As can be observed in Table 1, no methane gas was formed at room temperature (RT) and 100 ^oC of reaction temperature which agreed with the absence of methane peak (~3000 cm^{-1}) in FTIR spectra in Figure 1. However, when increasing reaction temperature to 200 ^oC, about 6% of CH_4 gas was formed from 65.52% of CO_2 conversion. This means that 59.09% of the reacted CO_2 was attained as a by-product. At a reaction temperature of 250 ^oC, the catalyst formed 20% CH_4 gas. Upon raising the reaction temperature to 400 °C (maximum value), the best 69% CH_4 gas was formed

as detected by GC-FID. Although CO_2 conversion is 100%, but the CH_4 gas formed only 69%. This might due to formation of methanol as side product for the catalysts (Refer Figure 2) as confirmed by HPLC analysis which showed the presence of peak at 20 minutes compatible with the retention time of standard methanol. As qualitatively, the presence of methanol was confirmed in the water product. This is because the peak area of 1.708 x 10^6 at 20.038 minutes coincided with the peak of standard methanol (not shown) at 19.122 minutes.

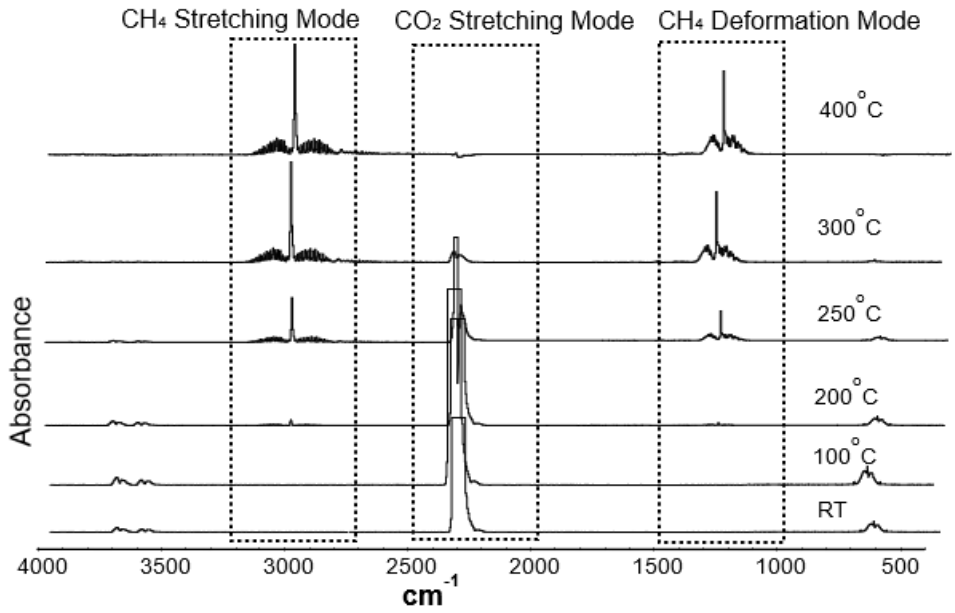

Figure 1. FTIR spectra of gaseous product at various reaction temperatures over calcined Sm/Mn/Ru (60:35:5)/Al_2O_3 catalyst

Table 1. Product analysis via *in-situ* reactions during methanation for Sm/Mn/Ru (60:35:5)/Al_2O_3 catalyst calcined on 1000 °C for 5 hours using GC-FID

Reaction Temperature (°C)	**Converted CO_2 (%)***		**Unreacted CO_2 (%)**
	% Formation of CH_4**	**% Formation of H_2O + with/without CH_3OH*****	
RT	-	0.00	100.00
100	-	0.31	99.69
200	6.43	59.09	34.48
250	20.85	71.67	7.48
300	31.11	65.67	3.22
350	48.91	49.95	1.14
400	68.87	31.13	-

*Converted CO_2 and Unreacted CO_2 was determined from FTIR as in Equation 1
**Formation of CH_4 was calculated from GC-FID as in Equation 2
***The presence of CH_3OH was confirmed with HPLC

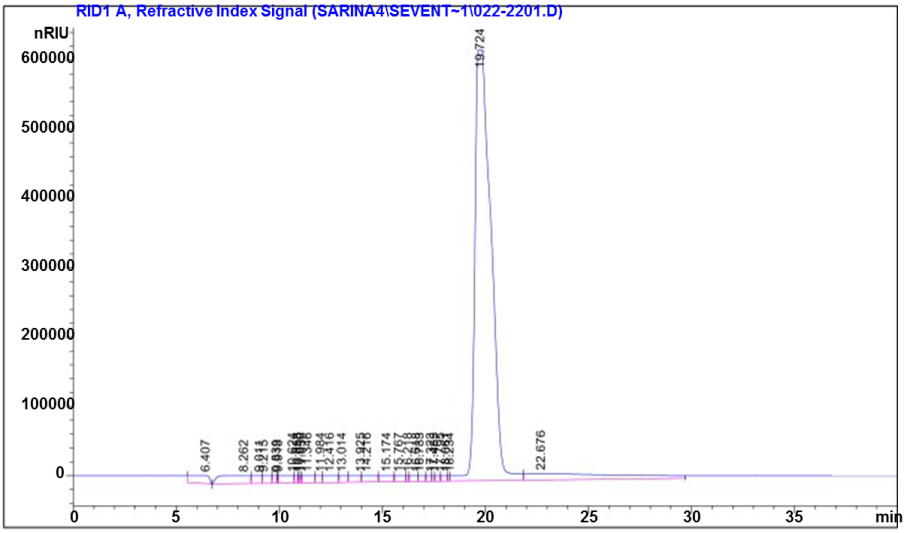

Figure 2. HPLC chromatogram of liquid product over calcined Sm /Mn/Ru (60:35:5)/Al_2O_3 catalyst

Methanation mechanism

The hydrogenation methanation adhered to the Langmuir-Hinshelwood mechanism, which reflected CO_2 and H_2 gases adsorption on the surface of catalyst. All CO_2 adsorption, dissociation, and reaction of the resolved species with H_2 had been established from in-situ FTIR experiments without any carbonate adsorption peak at 1760 and 1570 cm^{-1}. The FTIR spectra for catalyst during reaction is depicted in Figure 3. The spectra exhibited two broad O-H peak around 3443 and 1637 cm^{-1} corresponded to stretching and bending of adsorbed water on Al_2O_3 support [15, 16]. According to Narain et al., a peak band was noted at 1639 cm^{-1} for the similar temperature due to O-H bending derived from H_2O [17]. Initially, CO_2 and H_2 molecules were drawn to the catalyst surface (Step I) and directly coordinated the C atoms to generate inorganic carboxylate as proposed in Figure 4. The peak at 1116 cm^{-1} assigned to the CO species observed during the attachment of CO_2 to the catalyst surface at reaction temperature, 100°C [10]. This suggested the arrangement of C atoms attached to the catalyst surface (Step II). The adsorbed H_2 molecule was dissociated to active H atom species, and this was followed by CO_2 gas dissociation, as reported by Haldor [18] in Step III. The continuous flow of H_2 gas on the catalyst connects with oxygen atoms at the lone pair of electrons with higher electronegativity to form water (step IVa). This was supported with intense peak in the FTIR at reaction temperature, 200°C. A little peak at 1397 cm^{-1} was also observed at 200°C that correspond to the methoxy group (H_3C-O) as suggested in step IVb. Solymosi et al. described the peak around 1397 cm^{-1} on the catalyst surface foremost to the formation of methanol as a by-product [12]. When increased the reaction temperature to 250 – 300°C, the peak at 2892-2926 cm^{-1} was appeared which suggested free carbon from step III react directly with hydrogen to produce methane (step V). The intensity of C-H peak decreased at 350°C indicating that almost all CHx was released as CH_4 gas. At a reaction temperature of 400°C, all peak C-H groups disappeared which resulted higher CH_4 formation at this reaction temperature with 69% as stated in Table 1. This signifying the conversion of all species to CH_4, H_2O, and CH_3OH as the final yields.

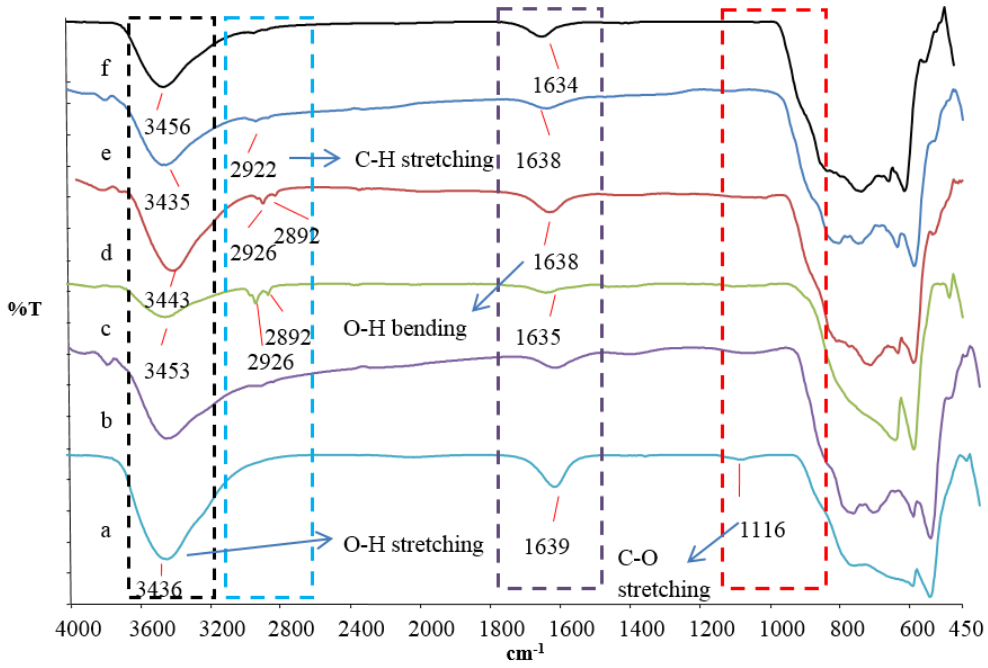

Figure 3. FTIR spectra of Sm/Mn/Ru (60:35:5)/Al_2O_3 catalyst surface at (a) 100ºC, (b) 200ºC, (c) 250ºC, (d) 300ºC, (e) 350ºC, and (f) 400ºC reaction temperature

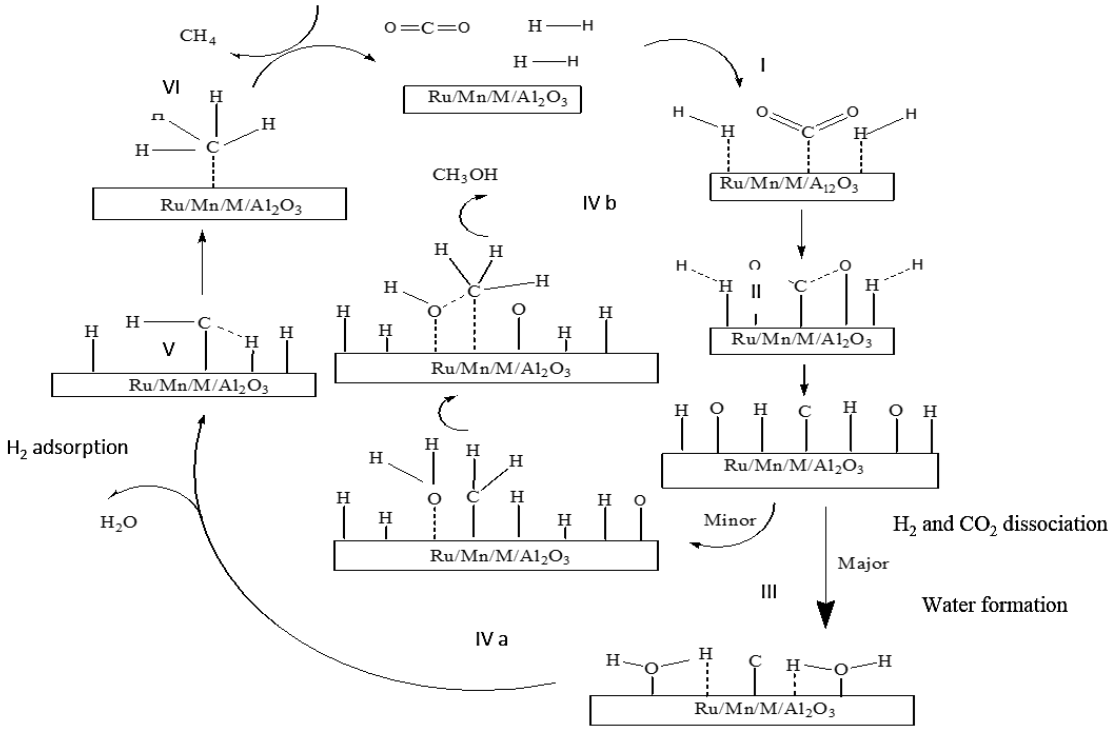

Figure 4. Proposed mechanism of M/Mn/Ru (60:35:5)/Al_2O_3, (M= Sm) calcined for 5 hours at 1000 ºC

Conclusion

This evaluation revealed compliance with the Langmuir Hinselwood mechanism, where CO_2 gas is first adsorbed, and then H_2-reactive gas is adsorbed on the catalyst surface. Based on the mechanistic approach, CH_4 was formed at temperature of 250 ºC and CO_2 peak was gradually decrease when the reaction temperature increased. The CO_2 conversion at 400ºC is 100%, with CH_4 formation of 69%. The others percent conversion was side products which are water and methanol, as detected by HPLC.

Acknowledgement

The authors gratefully acknowledge the Universiti Sultan Zainal Abidin and Universiti Teknologi Malaysia for financial support under GUP grant vote 13H34.

References

1. Asif Iqbal, M. M., Toemen, S., Abu bakar, W. A. W., Razak, F. I. A., Rosid, S. J. M. and Azelee, N. I. W. (2020). Catalytic methanation over nanoparticle heterostructure of Ru/Fe/Ce/γ-Al_2O_3 catalyst: Performance and characterization, *Renewable Energy*, 162: 513-524,
2. Rosid, S. J. M., Toemen, S., Iqbal, M. M. A., Bakar, W. A. W. A., Mokhtar, W. N. A. W. and Aziz, M. M. A. (2019). Overview performance of lanthanide oxide catalysts in methanation reaction for natural gas production. *Environmental Science and Pollution Research,* 26(36): 36124-36140.
3. Hu, D., Gao, J., Ping, Y., Jia, L., Gunawan, P., Zhong, Z., Xu, G., Gu, F. and Su, F. (2012). Enhanced Investigation of CO methanation over Ni/Al_2O_3 catalysts for synthetic natural gas production. *Industrial & Engineering Chemistry Research*, 51: 4875-4886.
4. Panagiotopoulou, P., Kondarides, D. I. and Verykios, X. E. (2008). Selective methanation of CO over supported noble metal catalysts: Effects of the nature of the metallic phase on catalytic performance. *Applied Catalysis A: General,* 344(1-2): 45-54.
5. Erdohelyi, A. (2021). Catalytic reaction of carbon dioxide with methane on supported noble metal catalysts. *Catalysts,* 11: 159.
6. Wang, X., Hong, Y., Shi, H., & Szanyi, J. (2016). Kinetic modeling and transient DRIFTS–MS studies of CO_2 methanation over Ru/Al_2O_3 catalysts. *Journal of Catalysis,* 343:185-195.
7. Fisher I.A. and Bell A.T. (1996). A comparative study of Co and CO_2 hydrogenation over Rh/SiO_2. *Journal of Catalysis,* 162: 54-65.
8. Marc J. Antoine Beuls, Patricio R. (2010). Catalytic production of methane from CO_2 and H_2 at low temperature: Insight on the reaction mechanism. *Catalyst Today*, 157: 462-466.
9. Gabor A. S. and Yimin L. (2010). Major success of theory and experiment-combined studies in surface chemistry and heterogeneous catalysis. *Top Catalyst,* 53: 311-325.
10. Marwood, M., Doepper, R. and Renken, A. (1997). *In-situ* surface and gas phase analysis for kinetic studies under transient conditions: The catalytic hydrogenation of CO_2. *Applied Catalysis A: General*. 151: 223-246.
11. Sharma, S., Hu, Z., Zhang, P., McFarland, E. W. and Metiu, H. (2011). CO_2 methanation on Ru-doped ceria. *Journal of Catalysis,* 278: 297-309.
12. Solymosi, F., Erdehelyi, A. and Bansagi, T. (1981). Methanation of CO_2 on supported rhodium catalyst. *Journal of Catalysis,* 68: 371-382.
13. Zamani, A. H., Shohaimi, N. A. M., Rosid, S. J. M., Abdullah, N. H. and Shukri, N. M. (2019). Enhanced low temperature reaction for the CO_2 methanation over Ru promoted Cu/Mn on alumina support catalyst using double reactor system. *Journal of the Taiwan Institute of Chemical Engineers*, 96: 400-408.
14. Rosid, S. J.M., Abu Bakar, W.A.W., Toemen, S., Yusoff, N. M., Azid, A. and Mokhtar, W. N. A.W. (2019). Investigation of active species in methanation reaction over cerium based loading. *Malaysian Journal of Fundamental and Applied Sciences,* 2018: 319-323.
15. Li, C., Sakata, Y., Arai, T., Domen, K. and Maruya, K. (1989). Carbon monoxide and carbon dioxide adsorption on cerium oxide studied by Fourier- transform infrared spectroscopy. *Journal of Chemical Society: Faraday Transaction*. 85(4): 929-943.
16. Stevens, R. W., Siriwardane, R. V and Logan, J. (2008). *In situ* Fourier transform infrared (FTIR) investigation of CO_2 adsorption onto zeolite materials. *Energy & Fuels*. 22(12): 3070-3079.

17. Narain, K., Yazdani, T., Bhat, M. M. and Yunus M. (2012). Effect on physico-chemical and structural properties of soil emended with distillery effluent and ameliorated by cropping two cereal plant spp. *Environmental Earth Sciences*, 66: 977-984.

18. Haldor Topsøe A/S, (2005). Methanation of CO over nickel mechanism and kinetics at high H_2/Co ratios. *Journal Physical Chemistry B*, 109(6): 2432-2438.

Malaysian Journal of Analytical Sciences (MJAS)
Published by Malaysian Analytical Sciences Society

ENHANCING TRYPSIN RECOVERY USING POLYMER-BASED AFFINITY ULTRAFILTRATION MEMBRANE: EFFECTS OF ELUTION pH AND DISPLACING SALTS

(Meningkatkan Perolehan Tripsin menggunakan Membran Afiniti Ultrafiltrasi berasaskan Polimer: Kesan pH Pengeluatan dan Penggantian Garam)

Norhafiza Ilyana Yatim[1], Sofiah Hamzah[2]*, Maslinda Alias[2], Nora'aini Ali[1,2], Marinah Mohd Ariffin[3], Abdul Wahab Mohammad[4]

[1]Higher Institution Centre of Excellence (HICoE), Institute of Tropical Aquaculture and Fisheries
[2]Faculty of Ocean Engineering Technology and Informatics
[3]Faculty of Science and Marine Environment
Universiti Malaysia Terengganu, 21030 Kuala Nerus, Terengganu, Malaysia
[4]Faculty of Engineering and Built Environment
Universiti Kebangsaan Malaysia, 43600 UKM Bangi, Selangor, Malaysia

**Corresponding author: sofiah@umt.edu.my*

Received: 27 August 2021; Accepted: 11 January 2022; Published: 25 February 2022

Abstract

Downstream processing of trypsin synthesis, which includes purification, is a major issue due to high complexity of the bio-suspension itself and the stress sensitivity of the desired target molecules. Therefore, an affinity membrane was fabricated in this study using polysulfone polymers and modified by chitosan to enhance biofouling resistance. To determine the optimum conditions for maximum trypsin adsorption and desorption during affinity ultrafiltration process, elution buffers and pH were investigated using various types of displacing salts (potassium chloride, KCl; sodium chloride, NaCl; magnesium chloride, $MgCl_2$; calcium chloride, $CaCl_2$) and elution pH (pH 4, 5, 6, 7, 8). The result showed that the buffer using KCl was identified as the best displacing salt as it recovered the highest trypsin of 78.84%, with a purification fold of 1.31. Trypsin recovery increased to 92% and 1.20 purification fold when the experiments were at pH 8. These buffers dissolved the interference chemical bonds comprising trypsin-trypsin inhibitor interactions and restore target trypsin to the permeate stream in an active state for maximum trypsin recovery. The information provided in this study represents a possible future avenue for developing an affinity membrane system.

Keywords: affinity, ultrafiltration, trypsin, elution pH, displacing salt creator

Abstrak

Pemprosesan hiliran sintesis tripsin, yang termasuk penulinan, adalah isu utama kerana kerumitan bio-pengampaian itu sendiri dan kepekaan tekanan molekul sasaran yang dikehendaki. Oleh itu, membran afiniti telah direka dalam kajian ini menggunakan polimer polisulfon dan diubahsuai oleh kitosan untuk meningkatkan rintangan bio-kotoran. Untuk menentukan keadaan optimum untuk penjerapan tripsin maksimum dan penyahjerapan semasa proses ultrafiltrasi perkaitan, penimbal pengeluat dan pH telah

disiasat menggunakan pelbagai jenis garam pengganti (kalium klorida, KCl; natrium klorida, NaCl; magnesium klorida, $MgCl_2$; kalsium klorida, $CaCl_2$) dan pH pengeluatan (pH 4, 5, 6, 7, 8). Hasilnya menunjukkan bahawa penimbal menggunakan KCl dikenal pasti sebagai garam pengganti terbaik kerana ia perolehan tripsin tertinggi sebanyak 78.84%, dengan lipatan penulenan 1.31. Perolehan tripsin meningkat kepada 92% dan 1.20 lipatan penulenan apabila eksperimen berada di pH 8. Penimbal ini telah melarutkan ikatan kimia yang menganggu yang terdiri daripada interaksi perencat tripsin-tripsin dan memulihkan tripsin sasaran ke aliran menelap dalam keadaan aktif untuk perolehan maksimum tripsin. Maklumat yang disediakan dalam kajian ini mewakili jalan masa depan yang mungkin untuk membangunkan sistem membran afiniti.

Kata kunci: afiniti, ultrafiltrasi, tripsin, pH pengeluat, pencipta pengganti garam

Introduction

Affinity ultrafiltration membranes have unfolded a new avenue in membrane technology due to the ability of membranes to bind specifically to target molecules/proteins via a specific interaction. This type of membrane results from a combination of two separation processes, namely affinity adsorption and ultrafiltration. It comprises the use of affinity ligands attached to the crosslinked or activated membrane matrix covalently. Ligands are bound to the target enzyme with different adsorption mechanisms and degrees of specificity, depending on the type of ligand used. This system conducts affinity adsorption and ultrafiltration in stages in ultrafiltration modules or separate systems [1].

The recent literature on the development of affinity chromatographic membranes describes highly diversity for proteins and enzyme purification in particular [2]. In fact, several recent studies have reported the rapid development of affinity membranes for protein recovery which increased gradually due to the need of this protocol to obtain high protein quality [3-6]. To meet the growing market demand for this enzyme, commercial production should focus either on innovating alternative procedures or modifying existing methods with slight improvement [7]. Based on the studies described above, affinity membrane chromatography has great potential to isolate a single protein fraction from protein mixture.

The target enzymes can be dissociated from the enzyme-ligand complex and passed through the affinity membranes by applying a suitable elution buffer on the system at the same operating pressure. Various buffers and conditions can be utilised for these studies; affinity-bound enzyme elution and elution using high-concentration salt solution are widely used [8]. This elution buffer breaks the connections between the target enzyme and ligand, lowers its binding affinity and forces the desired enzyme into the permeate stream.

Trypsin is one of the most well-known proteases and consists of serine endopeptidases [9]. Trypsin has a wide range of applications due to its strong proteolytic function and specificity of action, including its use as a critical intermediary in the manufacture of insulin, cell culture applications, research and production of recombinant proteins for clinical use, debriding agent in the wound care market, and oral treatment for inflammatory edema, hematoma and pain associated with diabetes [10, 11, 12].

In most cases, elution buffers were selected at random, most likely due to convenience or prior experience, although the final aim was to achieve a functional eluate [13]. However, several investigations have shown that elution conditions can substantially impact both the yield and specific activity of eluted products [14, 15]. The selected displacing salts are ensured to be soluble, non-denaturated, stable, transparent, ionic at relevant pH, pH stable, non-hazourdous and available [16].

The main benefit of ultrafiltration techniques over conventional separation methods such as chromatography, electrophoresis and conventional affinity separation is the high product throughput. Furthermore, ultrafiltration technologies are considerably easier to scale up, simple to clean and run, and relatively compact in design [17]. Although the use

of ultrafiltration is widespread, its potential in protein fractionation application has not been fully realised in the biotechnology industry due to lack of knowledge on the separation mechanism concepts and membrane fouling [18]. As a result, this study was conducted to determine the most efficient approach to increase the use of unltrafiltration in the biotechnology industry.

This study provides fundamental knowledge in designing a highly specific affinity ultrafiltration membrane for trypsin purification under proper pressure to selectively eliminate target enzyme-ligand complex as a retentate and simultaneously, other unbound impurities flow through membrane pores. Selectivity of polysulfone as a membrane material was due to its strong and thermally stable characteristics. The integration of chitosan with polysulfone was hypothesized to produce a hydrophilic segment on the membrane surface which can be an ideal method to combine both the advantages of hydrophilic and hydrophobic membranes. The use of ligands to support materials using activator (glutaraldehyde) can enhance the performance of affinity membranes. It is crucial to determine the best conditions for the trypsin recovery protocol; therefore, this study was conducted to identify the effects of displacing salt and pH of the buffer solution in separation process. In conclusion, with the integration of affinity chromatographic and high-performance ultrafiltration concept, it is believed that affinity ultrafiltration membrane will become common in the near future especially for protein and enzyme recovery.

Materials and Methods

Chemicals and raw materials

Membranes were produced using a ternary casting solution including polysulfone (PSf) as the polymer, N-methyl-2-pyrrolidone (NMP) as the solvent (provided by Merck), and water (H_2O) as the non-solvent. In this study, N-Methyl-2-Pyrrolidone (NMP) from MERCK Schuchard OHG, Germany, was used as a solvent for PES. As a coagulation medium, distilled water was employed. Fluka trypsin (Mw = 25 000 g/mol) was used as the target enzyme in this study. Trypsin inhibitor type III (ovomucoid) and trypsin (Mw = 25 000 Dalton) purchased from Sigma Aldrich were used for affinity ligand and adsorption study, respectively. Chitosan particle (Sigma Aldrich) was used for hydrophilic modification of asymmetric PSF membrane. Glutraraldehyde (Sigma Aldrich) was used for membrane activation to develop the affinity membranes. N-α-benzoly-L-arginine p-nitroanilide (BAPNA) was used for enzyme activity. Sodium acetate acetic acid buffer (solution), acetic acid solution, potassium chloride (KCl), sodium chloride (NaCl), calcium chloride ($CaCl_2$), and magnesium chloride ($MgCl_2$) were purchased from Sigma Chemical Co. (St Louis, Missouri) for affinity ultrafiltration experiments. All materials utilised in this study were of analytical grade.

Preparation of affinity membrane

For PSf membrane preparation, the weight of the binary dope was determined at 70 g. Then, 85 (wt.%) NMP was heated at 60 ˚C in a reactor flask for 10 minutes. The solvent was then gently infused with 15 (wt.%) polymer (PSf) until all polymers were dissolved and stirred at 300 to 400 rpm for about 8 hours at a constant temperature of 600 ˚C using a WiseStirTM Digital Overhead Stirrer from DAIHAN Scientific, Co., Ltd. To eliminate trapped air bubbles, the resulting polymer solution was immersed in an ultrasonic bath for about 3 hours. The prepared binary dope was then titrated with water as a non-solvent to produce the ternary dope and the stirrer was set to stir at a moderate speed. The presence of a drop of water that changed the colour of the binary dope solution indicated that the cloud point was achieved, and the volume of water titrated was recorded. The polymer solvent mixture was mixed again until all the components utilised were completely dissolved. Finally, the finished dope solution was put into a Schott bottle.

The affinity membrane (CH/PSf-60) was prepared with simple dry/wet phase inversion technique using an electrically casting machine at shear rate of 200 s^{-1} and then immersed directly into a coagulation bath for 24 hours. For surface modification, a native PSf membrane was immersed into the chitosan solution (0.1 wt.% in acetic acid with pH 5) for 60 minutes to deposit chitosan particles onto the membrane surface and dried in ambient air. The dried membrane was

then neutralized with NaOH solution (0.1 M in 50% of water-ethanol mixture) for 30 minutes to ensure that all chitosan acetate was converted to chitosan. To prevent osmotic cracking and to remove the remaining NaOH, the membrane was rinsed with 50% v ethanol solution for 3 times, and followed by washing with distilled water and stored in distilled water before use.

The membrane support (CH/PSf-60) was cut to an area of 14.6 cm^2 and incubated in an incubation shaker for 150 min in a reacting solution containing different amounts of 25 vol% glutaraldehyde (GTA) aqueous solution in 0.1 M sodium chloride and 0.1 M sodium acetate-acetic acid buffer (pH 7.4). From the reaction, excess glutaraldehyde was removed from the membrane by washing three times with 2 M acetic acid. The trypsin inhibitor was immobilized onto the active membrane for 180 minutes, and the adsorption capacity was measured every 30 minutes. The CH/PSf-60 membrane was referred to as an affinity membrane.

Affinity ultrafiltration experiment

A dead-end cell with a processing volume of 300 mL, and an effective permeation membrane area of 14.6 cm^2 was used for affinity ultrafiltration. This solution was drawn across the membrane using compressed nitrogen at a pressure of 5 bar. A washing step with 0.1 M phosphate buffer was used to eliminate unbound trypsin and contaminants. For the elution step, the bound trypsin was subsequently desorbed from the affinity membrane using 0.01 M Tris-HCl buffer with various displacing salts, namely KCl, NaCl, $CaCl_2$ and $MgCl_2$, and pH (pH 4, 5, 6, 7, 8). When the enzymes were firmly attached to the affinity membrane, it may be beneficial to pause the flow for 15 min after adding the eluent before proceeding with the elution. This phase allows additional time for dissociation to occur, which assists in the recovery of bound trypsin. The total protein content of the eluate was determined using the Bradford assay and trypsin activity.

Determination of total protein and enzyme activity

Protein concentration was calculated using Bradford method with Bovine Serum Albumin (BSA) as the standard. Using a UV-Vis spectrophotometer, absorbance and concentrations were determined by dissolving each 100 µL sample in 5 mL of Bradford reagent. The experiment was repeated with trypsin as the sample. Trypsin activity was assessed with minor changes [19] [12]. As a chromogenic substrate, BAPNA was utilised. Analiquot of the enzyme solution of 200 µL was added to the pre-incubated reaction mixture containing 1000 µL of BAPNA solution (dimethyl sulfoxide) and 200 µL of 0.05 M Tris-HCl. The mixture was incubated at 40°C for 10 min. The enzymatic process was halted by adding 200 µL of 30% (v/v) acetic acid and then centrifuged at 8000x g for 3 min at room temperature. Due to the production of p-nitroaniline, absorbance was used to assess trypsin activity at 410 nm using Equation 1.

$$q = \frac{(C_0 - C)\,V}{A} \quad (1)$$

where q is the amount of trypsin adsorbed onto the membrane ($mg.ml^{-1}$), C_0 and C are the total protein in the initial solution and the aqueous phase after adsorption, respectively ($mg.ml^{-1}$), V is the volume of the aqueous solution (ml), and A is the area of the membranes in the adsorption medium (cm^2).

Results and Discussion

Characteristics of affinity membrane

As seen in Figure 1(a), affinity membrane generally employs two separation concepts, namely affinity adsorption and ultrafiltration. It comprises the use of affinity ligands attached to the crosslinked or activated membrane matrix covalently. Depending on the ligand utilised, the ligands are attached to the target enzyme through different adsorption methods and specificity. Then, for ultrafiltration separation, a buffer media with sufficient pressure selectively excludes the target enzyme-ligand complex as a retentate while allowing other unbound contaminants to flow through the membrane pores. The target enzymes can be separated from the enzyme-ligand combination and processed through an amplification process. By introducing an appropriate elution buffer to the system at the same operating pressure, the target enzymes can be dissociated from the enzyme-ligand complex and passed through the affinity membranes. Figure 1(b) shows the schematic diagram of the developed affinity

membrane consisting of 15% PSf membrane. The PSf membrane underwent surface modification with chitosan to produce membrane hydrophilicity followed by an activation process using glutaraldehyde and immobilised using trypsin inhibitor as ligand.

The separation method of the affinity membrane is based on the affinity characteristics of the desired solute molecules. The selection of suitable membrane is one of the important elements influencing the separation performance of affinity ultrafiltration membrane. Large pore sizes and high porosity membrane matrix are necessary to avoid fouling while also allowing larger pollutants to flow through the membrane during the washing phase. The hydrophilic properties of the CH/PSf membrane enhances its ability to immobilise ligands and transmit trypsin during affinity ultrafiltration. Figure 2 depicts the surface morphology of native PSf 15 and affinity membrane after trypsin inhibitor was effectively adsorbed onto the CH/PSf membrane by glutaraldehyde activation.

Membrane activation with glutaraldehyde results in crosslinking, stabilising the membrane structure during ligand immobilisation [20]. As a result, this affinity membrane has rough and porous surface structure which improves the surface area, minimises mass transfer resistance and facilitates enzyme molecule diffusion. This results in a low diffusional resistance situation in the membrane, which contradicts to the packed bed affinity column, in which significant pressure drops constantly occur [21].

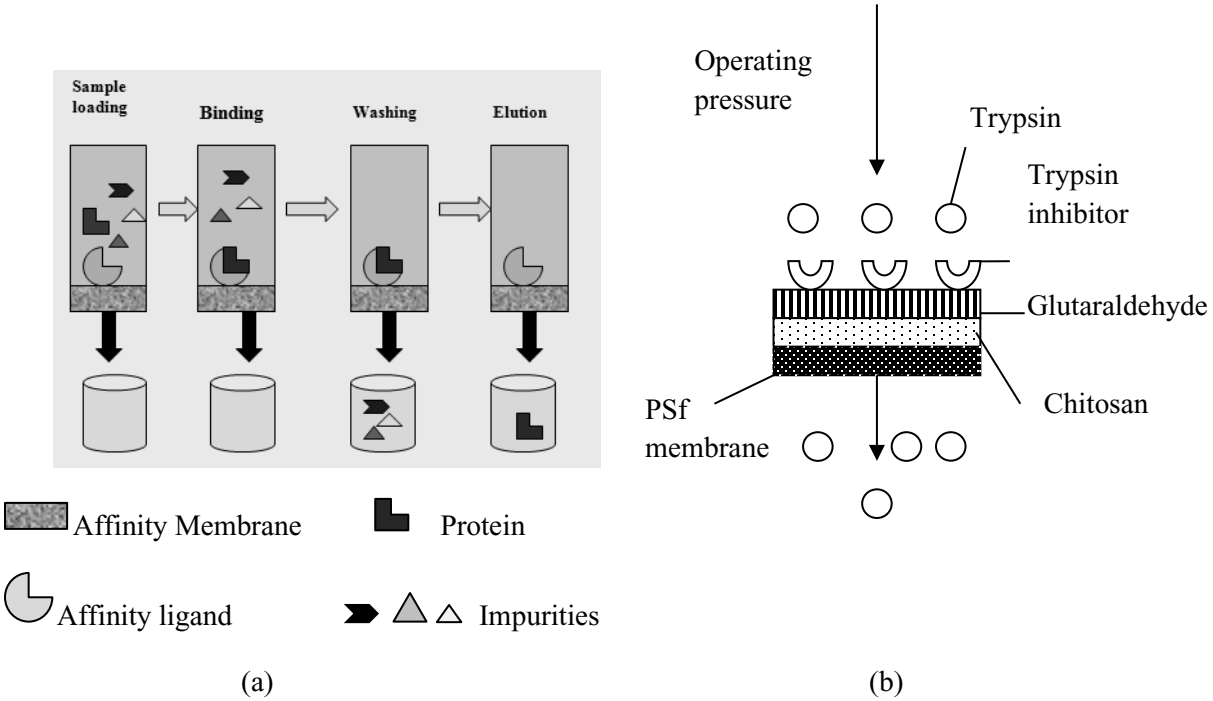

Figure 1. Graphical image of (a) protein purification protocols using affinity chromatographic membrane developed, and (b) synthesis of affinity membrane

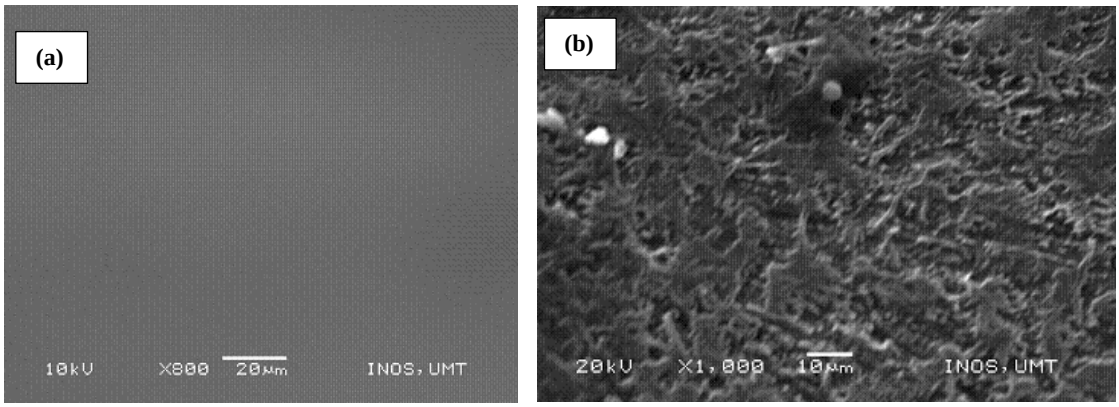

Figure 2. Surface morphology of (a) native membrane (PSf 15), and (b) affinity membrane (CH/PSf-60)

Figure 3 depicts the native membrane (PSf 15) and the affinity membrane by ATR-FTIR. The spectra represented the group of main compounds associated with the native membrane (PSf 15). After incorporating with chitosan, the band stretching was less intense due to the thin layer formation on the PSf 15 membrane. This band revealed the presence of O-H and N-H_2 groups in chitosan in affinity membrane (CH/PSf-60) ranging between 3200 and 3600 cm^{-1} [22,23]. The O–H stretching vibration peak (v=3200 to 3600 cm^{-1}) was reduced by crosslinking CH/PSf with glutaraldehyde (Figure 2 (b)). The wavelength at 2873 cm^{-1} exhibited C-H stretching due to aldehyde as well as duplet adsorption with peaks ascribed to the alkyl chain [24]. The band at 1657 cm^{-1} could be attributed to >C=O stretching (amide I) of the N-acetyl group in chitosan particles and a wavelength of 1722 cm^{-1} may be attributed to the presence of ethylenic chain [7].

The appearance of aldehyde peaks in the affinity membrane spectrum was due to the incomplete reactivity of glutaraldehyde with the chitosan OH groups during crosslinking network formation. As a bifunctional crosslinking, one aldehyde group may form a hemiacetal structure with hydroxyl groups of CH/PSf polymer chain while the other is unreacted associated with a certain conformation. The addition of a small amount of GTA may increase crosslinking chain with the formation of intermolecular covalent bonds between ligands and membrane (CH/PSf-60) via the availability of free amine group in affinity membrane (CH/PSf-60) [25]. Moreover, as a bi-functional reactive agent capable of reacting with the surface –OH groups of membrane and the amines groups of enzyme inhibitor, GTA could efficiently alleviate strong interaction between ligand and matrix apart from its ability to sustain ligand immobilization to be more resistant to pH changes and ionic strength.

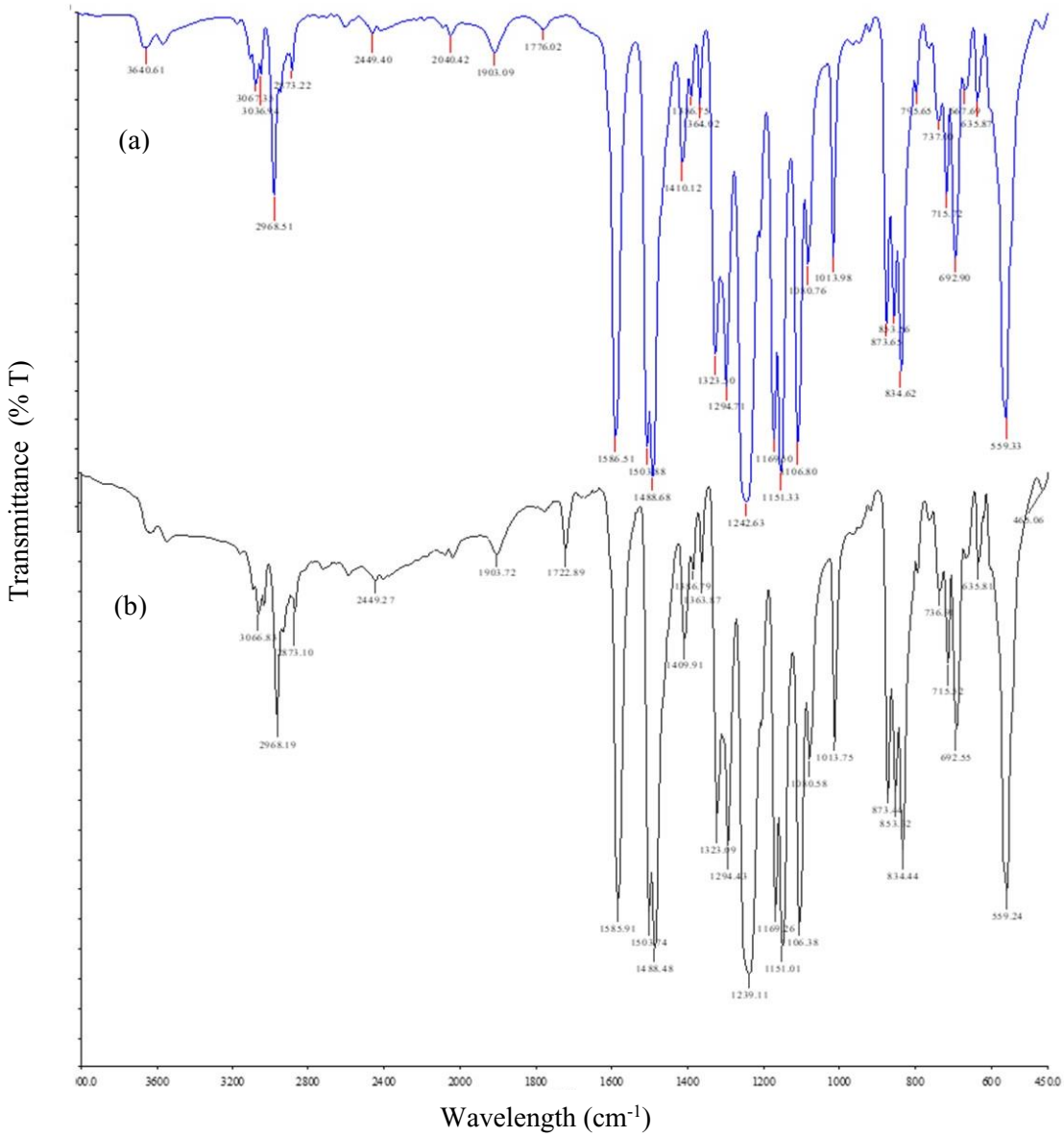

Figure 3. ATR-FTIR spectra of (a) native PSf15 and (b) affinity membrane

Effect of displacing salt in elution buffer

Other impurities and unbound molecules of the desired enzyme were removed using appropriate buffer solution during the washing stage. Although affinity chromatography membrane aims to target enzymes from their affinity ligands, an equally important aspect of this purification technique is the ability to release and recover isolated targets in active form.

A list of buffers and conditions can be applied for this recovery process, or the elution of affinity-bound enzymes using high-concentration salt solution [8] is commonly used. This elution buffer disrupts the interactions between the target enzyme and the ligand to reduce the binding affinity between them and force the desired enzyme in the permeate stream. In most cases, elution buffer options are targeted to obtain a functional eluate [26]. However, a number of studies

have demonstrated that elution conditions can significantly influence both the yield and specific activity of the eluted products [27].

In this study, four displacing salts (KCl, NaCl, $MgCl_2$ and $CaCl_2$) with 0.05 M ionic strength were added to the elution buffer to determine the ionic species that could enhance the dissociation of enzyme-ligand complex and trypsin transmission through affinity membrane. The results presented in Figures 4 and 5 exhibited a series of trypsin recovery in increasing order: $CaCl_2$ < NaCl < $MgCl_2$ < KCl. The main component in the adsorption mechanism is the affinity of positively charged trypsin and negatively charged sites on the membrane surface. The ionic bonding of this enzyme-ligand interaction can be affected by changing the physicochemical environment controlled by the displacing salts.

The pH 7 condition provided a favorable environment for trypsin adsorption with the help of electrostatic interaction that has dominated the adsorption. Trypsin was best adsorbed onto the affinity membrane with low positive charge as the electrostatic interactions between enzyme molecules decreased as the membrane increased. Moreover, in this favourable physicochemical environment, the amine groups of the trypsin molecules can undergo protonation to NH_3^+ [3], and these protonated amino groups on the surface of trypsin enhanced the electrostatic interaction between trypsin and affinity membrane. This observation is in agreement with the previous findings who found that the maximum adsorptive capacity of trypsin occureds around pH 7 [28].

The presence of displacing salts influenced the ionic strength of the elution buffer solution when KCl-HCl was added and then disrupted the electrostatic interaction of enzyme-affinity ligands, thus ionic exchange process occurred. K^+ cation is more electropositive, then the enzyme-ligand complex was dissociated and permeated through the membrane. Therefore, the trypsin recovery by KCl-HCl was highest at 78.8% with 1.31 purification fold. The properties of high chaotropic effect and salting of K^+ may destabilize the bonding between trypsin and trypsin inhibitor, leading to enhanced trypsin transmission [16].

The findings were attributed to different elution strengths of displacing ions during competition with trypsin in the affinity system. The trypsin recovery using the displacing salts such as NaCl-HCl, $MgCl_2$ and $CaCl_2$ were 65.0%, 69.3% and 40.6%, respectively. Compared to Ca^{2+}, Mg^{2+} with higher charge density is a better charge acceptor, thus it is expected to bind more tightly to the protein binding sites [29]. From the experimental observations, the addition of $CaCl_2$ converted the buffer solution to a cloudy solution, resulting in lower total protein readings and trypsin activity. This finding may be explained due to the formation of metal-enzyme complexes interaction. Calcium is a cosmotropic ion that can promote hydrophobic interaction with trypsin and may retain this enzyme on the membrane surface after elution [30]. Moreover, trypsin was assumed to have two binding sites, and the primary site has high affinity for calcium ions. This interaction has considerably stabilized the enzyme against denaturation [31] and was achieved by a conformational shift in the trypsin molecule, resulting in a more compact structure [32]. This change broke the bonding between trypsin and its ligand, and reduced trypsin transmission during the elution process.

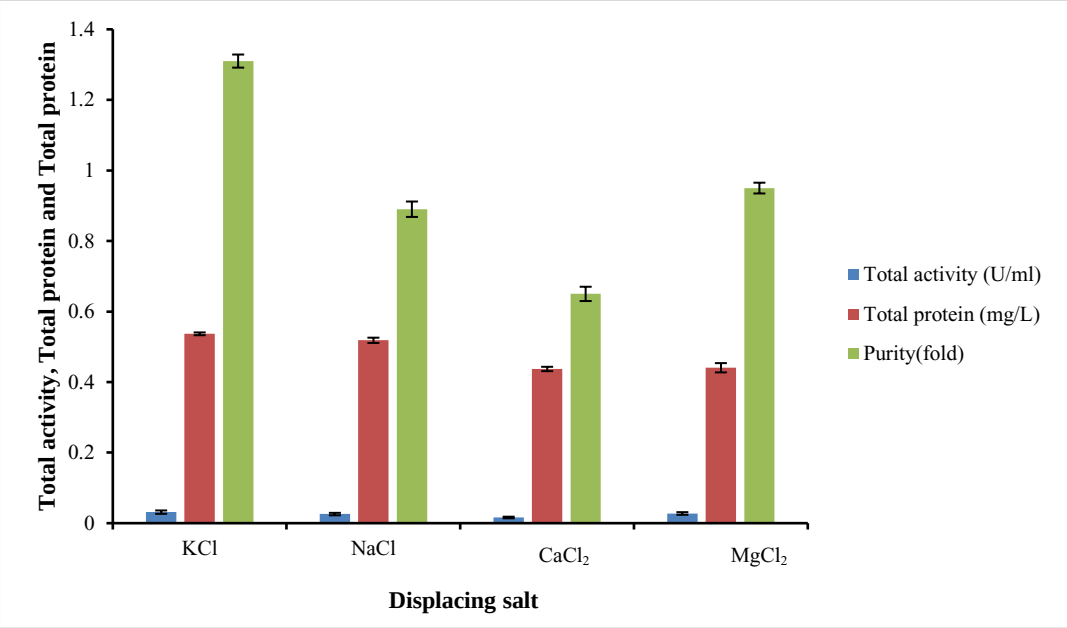

Figure 4. Effect of displacing salts of membrane parameters and data are presented as mean ± standard error (SE), $n = 3$

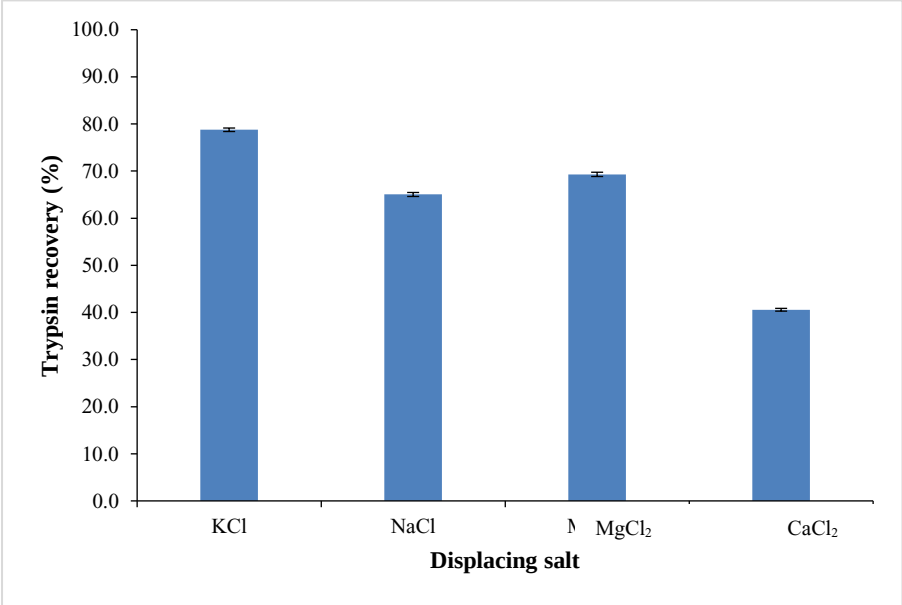

Figure 5. Effect of displacing salts on trypsin recovery activity and data are presented as mean ± standard error (SE), $n = 3$

Effect of elution pH

The adsorption behaviour in this study occurred mostly due to electrostatic interaction, and it is important to consider electrostatic interaction between trypsin molecules as well as between trypsin and membranes. pH can induce alteration in spatial structure of the

trypsin to affect the affinity of trypsin [33]. A small change in the pH of the solution can alter the electrical charge on proteins as well as membrane due to ionization or deionization of various acidic/basic groups on protein and membrane surface, which can cause either repulsive or attractive interactions [34]. The protein activity can be observed in Figures 6 and 7. The ionization of the charged groups on the ligand and/or the bound trypsin alters as the pH changes. This transition may directly influence the binding sites, reduce their affinity, or cause indirect changes in affinity through conformational changes.

Since the optimum adsorption of trypsin occurred at pH7, the trypsin recovery at this condition was 73.6%. This could be due to the fact that the electrostatic attraction of enzyme-ligand was strong and retained on the affinity membrane. Based on the optimum adsorption at pH 7, the pH of the elution buffer should be higher to break down the bonding of the enzyme and its ligand. Using an elution buffer at pH8, trypsin permeated into the membrane and resulted in about 92.0% recovery and 1.2 purification fold. An increase in the pH of elution buffer (pH 8) increased the dissociation of the sulfonic functional group of membranes and created a negative charge of the membrane. Therefore, electrostatic repulsion between enzyme-ligand was disrupted and thus trypsin dissociation occurred. An increase in the surrounding negative charge will cause the trypsin-ligand instability on the affinity membrane, increase the electrostatic repulsion and lead to high protein (trypsin) in eluent [35]. High OH^- anion will trigger enzyme aggregation as the net charge of the enzyme surface becomes zero. Therefore, there is no electrostatic repulsive force between trypsin-ligand [36]. The reduction of enzyme adsorption under alkaline pH could be attributed to the electrostatic repulsion between enzyme-membranes [37] and is responsible for lower adsorption, where thermodynamic entropy difference is the only force inducing the adsorption [38].

At lower pHs (6, 5 and 4), the decrease in protein activity due to trypsin recovery was 66.7%, 55.6%, and 50%, respectively. However, at extreme pH (acidic), the protein will be denatured [39]. Therefore, during the measurement of trypsin activity, the conformational changes of the trypsin molecules (denatured trypsin) at acidic pH affect the proper binding of the enzyme to the substrate, resulting in loss of the activity of the recovered trypsin in the permeate [40].

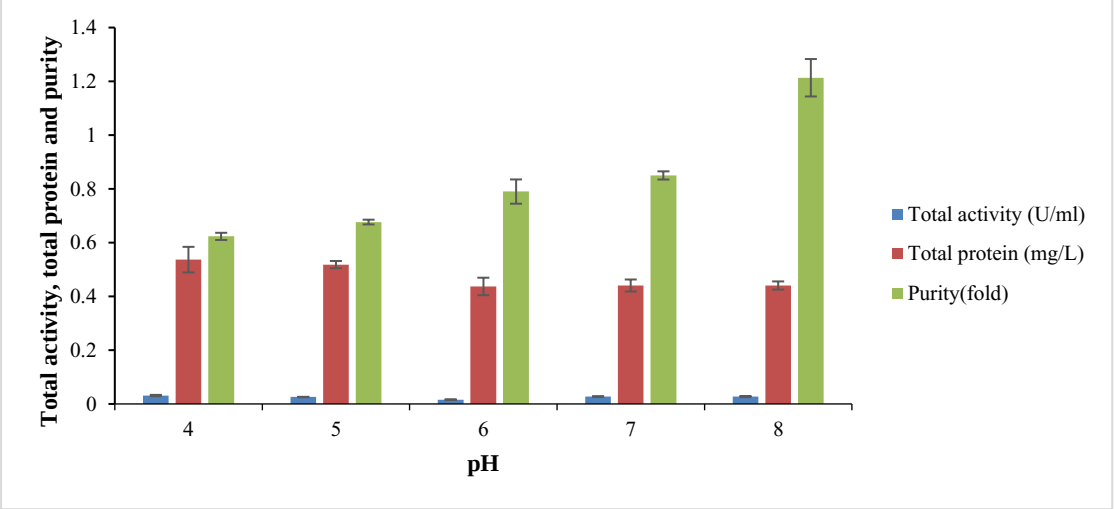

Figure 6. Effect of different pH on total protein, total activity and purity of affinity membranes using KCl buffer and data are presented as mean ± standard error (SE), $n = 3$

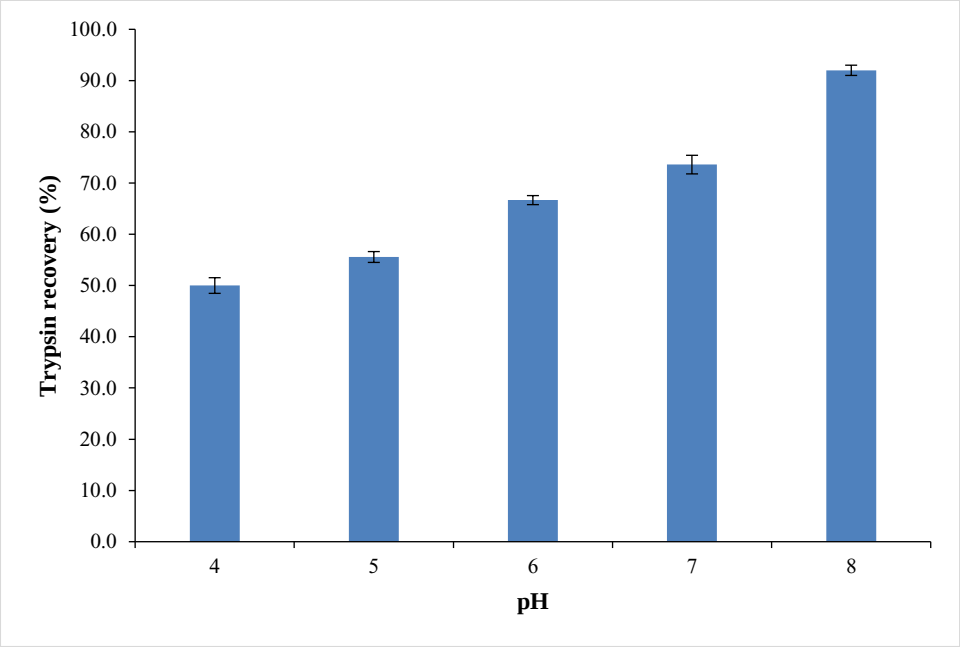

Figure 7. Effect of pH on trypsin recovery of affinity membranes using KCl buffer and data are presented as mean ± standard error (SE), $n = 3$

Conclusion

To conclude, this study suggests that the CH/PSf-60 membrane is the most appropriate membrane for trypsin separation. Furthermore, the modification of membrane with chitosan solution is a potential technique to mitigate fouling and improvemembrane lifespan as an excellent matrix material for developing an affinity membrane for trypsin separation and purification. Although the affinity membrane was well prepared, the physicochemical environment of the enzyme solution was also considered to obtain the greatest adsorption capacity. KCl as the displacing salt in the elution buffer solution was the optimum condition for trypsin recovery (78.8%). The recovery increased to 92% by setting the elution buffer pH at pH8. This study proved that the condition of elution buffer significantly influenced the degree of dissociation between the target enzyme and the affinity ligand, and enhanced the separation and purification performance. Thus, the fundamental chemical properties involved in the adsorption and desorption of proteins should be prioritized to develop affinity membrane protocols. The knowledge proposed in this study could be a good pathway for developing affinity membrane systems in the future.

Acknowledgement

The authors like to acknowledge Universiti Malaysia Terengganu for providing facilities and supporting this research.

References

1. Fane, A. G. and Radovich, J. M. (2020). Membrane systems. *Separation processes in biotechnology*. CRC Press: pp 209-262.
2. Kielkopf, C. L., Bauer, W. and Urbatsch, I. L. (2021). Considerations for membrane protein purification. *Cold Spring Harbor Protocols*, 2021(1): 102285.
3. Bayramoglu, G., Ozalp, V. C., Altintas, B. and Arica, M. Y. (2014). Preparation and characterization of mixed-mode magnetic adsorbent with p-amino-benzamidine ligand: Operated in a magnetically stabilized fluidized bed reactor for purification of trypsin from bovine pancreas. *Process Biochemistry*, 49(3): 520-528.

4. Ghosh, R. (2016). Bioseparations using integrated membrane processes. *Integrated Membrane Systems and Processes*: pp 23-34.
5. Khangembam, B. K. and Chakrabarti, R. (2015). Trypsin from the digestive system of carp *Cirrhinus mrigala*: Purification, characterization and its potential application. *Food Chemistry*, 175: 386-394.
6. Zamani, A. and Benjakul, S. (2016). Trypsin from unicorn leatherjacket (*Aluterus monoceros*) pyloric caeca: Purification and its use for preparation of fish protein hydrolysate with antioxidative activity. *Journal of the Science of Food and Agriculture*, 96(3): 962-969.
7. Sun, J., Yang, L., Jiang, M. and Xu, B. (2017). Stability and activity of immobilized trypsin on carboxymethyl chitosan-functionalized magnetic nanoparticles cross-linked with carbodiimide and glutaraldehyde. *Journal of Chromatography B*, 1054: 57-63.
8. Mondal, K. and Gupta, M. N. 2006. The affinity concept in bioseparation: Evolving paradigms and expanding range of applications. *Biomolecular Engineering*, 23: 59-76.
9. Poonsin, T., Simpson, B. K., Benjakul, S., Visessanguan, W. and Klomklao, S. (2017). Albacore tuna (*Thunnus alalunga*) spleen trypsin partitioning in an aqueous two-phase system and its hydrolytic pattern on Pacific white shrimp (*Litopenaeus vannamei*) shells. *International Journal of Food Properties*, 20(10): 2409-2422.
10. Mukherjee, S., Roy, D. and Bhattacharya, P. (2008). Comparative performance study of polyethersulfone and polysulfone membranes for trypsin isolation from goat pancreas using affinity ultrafiltration. *Separation and Purification Technology*, 60(3): 345-351.
11. Braia, M., Loureiro, D., Tubio, G., Lienqueo, M. E. and Romanini, D. (2017). Interaction between trypsin and alginate: An ITC and DLS approach to the formation of insoluble complexes. *Colloids and Surfaces B: Biointerfaces*, 155: 507-511.
12. Vatić, S., Mirković, N., Milošević, J. R., Jovčić, B. and Polović, N. Đ. (2021). Trypsin activity and freeze-thaw stability in the presence of ions and non-ionic surfactants. *Journal of bioscience and bioengineering*, 131(3): 234-240.
13. Lemma, S. M., Boi, C. and Carbonell, R. G. (2021). Nonwoven Ion-Exchange Membranes with High Protein Binding Capacity for Bioseparations. *Membranes*, 11(3): 181.
14. Soper, A. S. and Aird, S. D. (2007). Elution of tightly bound solutes from concanavalin A Sepharose: Factors affecting the desorption of cottonmouth venom glycoproteins. *Journal of Chromatography A*, 1154(1-2): 308-318.
15. Wang, L., Shen, S., He, X., Yun, J., Yao, K. and Yao, S.-J. (2008). Adsorption and elution behaviors of bovine serum albumin in metal-chelated affinity cryogel beds. *Biochemical Engineering Journal*. 42: 237-242.
16. Malmquist, G. and Lundell, N. 1992. Characterization of the influence of displacing salts on retention in gradient elution ion-exchange chromatography of proteins and peptides. *Journal of Chromatography A*, 627: 107-124.
17. Ghosh, R., Wan, Y. H. and Cui, Z. F. (2003). Parameter scanning ultrafiltration: rapid optimization of protein separation. *Biotechnology Bioengineering*. 81: 673-682.
18. Ghosh, R. and Cui, Z. F. (2000). Protein purification by ultrafiltration with pre-treated membrane. *Journal of Membrane Science*, 167: 47-53.
19. Jellouli, K., Bougatef, A., Daassi, D., Balti, R., Barkia, A. and Nasri, M. (2009). New alkaline trypsin from the intestine of Grey triggerfish (Balistes capriscus) with high activity at low temperature: Purification and characterisation. *Food Chemistry*, 116: 644-650.
20. Guo, W. and Ruckenstein, E. (2002). Crosslinked mercerized cellulose membranes for the affinity chromatography of papain inhibitors. *Journal of Membrane Science*, 197: 53-62.
21. Chen, T. -X., Nie, H. -L., Li, S. -B., Branford-White, C., Su, S. -N. and Zhu, L. -M. (2009). Comparison: Adsorption of papain using immobilized dye ligands on affinity membranes. *Colloids and Surfaces B: Biointerfaces*, 72: 25-31.

22. Boributh, S., Chanachai , A. and Jiraratananon, R. (2009). Modification of PVDF membrane by chitosan solution. *Journal of Membrane Science*, 342: 97–104.
23. Varghese, J. G., Kittur, A. A., Rachipudi, P. S. and Kariduraganavar, M. Y. (2010). Synthesis, characterization and pervaporation performance of chitosan-g-polyaniline membranes for the dehydration of isopropanol. *Journal of Membrane Science*, 364: 111-121.
24. Mansur, H. S., Sadahira, C. M., Souza, A. N. and Mansur, A. A. P. (2008). FTIR spectroscopy characterization of poly (vinyl alcohol) hydrogel with different hydrolysis degree and chemically crosslinked with glutaraldehyde. *Materials Science and Engineering C*, 28: 539-548.
25. Geng, L., Li, N., Xiang, M., Wen, X., Xu, D., Zhao, F. and Li, K. (2003). The covalent immobilization of trypsin at the galleries of layered γ-zirconium phosphate. *Colloids and Surfaces B: Biointerfaces*, 30: 99-109.
26. Firer, M. A. (2001). Efficient elution of functional proteins in affinity chromatography. *Journal of Biochemical and Biophysical Methods*, 49: 433-442.
27. Lee, W. -C., Chen, C. -H. (2001). Predicting the elution behavior of proteins in affinity chromatography on non-porous particles. *Journal of Biochemical and Biophysical Methods*, 49: 63-82.
28. Wu, J., Luan, M. and Zhao, J. (2006). Trypsin immobilization by direct adsorption on metal ion chelated macroporous chitosan-silica gel beads. *International Journal of Biological Macromolecules*, 39: 185-191.
29. Dudev, T. and Lim, C. (2014). Competition among metal ions for protein binding sites: determinants of metal ion selectivity in proteins. *Chemical reviews*, 114(1): 538-556.
30. de Gonzalo, G., and Lavandera, I. (Eds.). (2021). Biocatalysis for Practitioners: Techniques, reactions and applications. John Wiley & Sons.
31. Kishimura, H. and Hayashi, K. (2002). Isolation and characteristics of trypsin from pyloric ceca of the starfish Asterina pectinifera. *Comparative Biochemistry and Physiology Part B. Biochemistry and Molecular Biology*, 132: 485-490.
32. Klomklao, S., Benjakul, S., and Visessanguan, W. (2004) Comparative studies on proteolytic activity of spleen extracts from three tuna species commonly used in Thailand. *Journal of Food Biochemistry*, 28: 355–372.
33. Li, C., Han, Y., Gao, L., Zhang, Y. and Simpson, B. K. (2021). Development of a novel trypsin affinity material using a recombinant buckwheat trypsin inhibitor mutant with enhanced activity. *LWT*, 146, 111382.
34. Aravind, U. K., Mathew, J. and Aravindakumar, C. T. (2007). Transport studies of BSA, lysozyme and ovalbumin through chitosan/polystyrene sulfonate multilayer membrane. *Journal of Membrane Science*, 299: 146-155.
35. Purkait, M. K., Sinha, M. K., Mondal, P. and Singh, R. (2018). Introduction to membranes. *Interface science and technology*, Elsevier, 25: 1-37.
36. Gustafsson, H., Thörn, C. and Holmberg, K. (2011). A comparison of lipase and trypsin encapsulated in mesoporous materials with varying pore sizes and pH conditions. *Colloids and Surfaces B: Biointerfaces*, 87: 464-471.
37. Chen, N., Zou, J., Wang, S., Ye, Y., Huang, Y., Gadda, G. and Yang, J. (2009). Designing protease sensors for real-time imaging of trypsin activation in pancreatic cancer cells. *Biochemistry*, 48: 3519
38. Li, X., Zhang, Y. and Fu, X. 2004. Adsorption of glutamicum onto polysulphone membrane. *Separation and Purification Technology*, 37: 187-198.
39. Zhou, L., Liao, T., Liu, J., Zou, L., Liu, C. and Liu, W. (2019). Unfolding and inhibition of polyphenoloxidase induced by acidic pH and mild thermal treatment. *Food and Bioprocess Technology*, 12(11): 1907-1916.
40. Kim, J. S. and Lee, S. (2019). Immobilization of trypsin from porcine pancreas onto chitosan nonwoven by covalent bonding. *Polymers*, 11: 1462.

Malaysian Journal of Analytical Sciences (MJAS)
Published by Malaysian Analytical Sciences Society

BIOMIMETIC SYNTHESIS OF SILVER NANOPARTICLES USING *Eleusine indica* EXTRACT AND ITS ANTIBACTERIAL PROPERTIES

(Sintesis Biomimetik Nanopartikel Perak Menggunakan Ekstrak *Eleusine indica* dan Ciri Antibakteria)

Ropisah Me[1*], Muhammad Hafiz Istamam[1], Noor Hidayah Pungot[2], Nazlina Ibrahim[3], Alice Shanthi[4]

[1]*Universiti Teknologi MARA, Cawangan Negeri Sembilan, Kampus Kuala Pilah, 72000 Kuala Pilah, Negeri Sembilan, Malaysia.*
[2]*Universiti Teknologi MARA, 40450 Shah Alam, Selangor, Malaysia*
[3]*Universiti Kebangsaan Malaysia, 43600 UKM Bangi, Selangor, Malaysia*
[4]*Universiti Teknologi MARA, Cawangan Negeri Sembilan, Kampus Seremban, 70300 Seremban, Negeri Sembilan, Malaysia.*

**Corresponding author: ropisah@uitm.edu.my*

Received: 14 September 2021; Accepted: 18 December 2021; Published: 25 February 2022

Abstract

The biomimetic method, which relies on natural resources such as plant extracts, bacteria, and fungi, offers an alternative for synthesizing silver nanoparticles (AgNPs). The use of biomimetic method for synthesizing AgNPs have various benefits including cost effectiveness, low toxicity, and suitabiity for biomedical application. This study synthesizes plant mediated nanoparticle using *Eleusine indica* to determine its antibacterial activity. *Eleusine indica* methanol extract is treated with 1 mM of silver nitrate at room temperature (25-27 °C) for 24 hours. The resulting product is characterized using UV-Vis spectroscopy and transmission electron microscope (TEM). UV-Vis absorption spectroscopy displays a strong resonance centered on the surface of AgNPs at approximately 413 nm. Physical appearance of AgNPs as characterized by transmission electron microscopy (TEM) showed formation of AgNPs with average particle size of 20 nm. In the antibacterial activity of the synthesized AgNPs, minimum inhibitory concentration (MIC) and minimum bactericidal concentration (MBC) assays are performed. The plant mediated AgNPs has predicted bacteriocidal activity according to the ratio of MBC to MIC values against selected Gram-positive and Gram-negative bacteria. In this study, plant mediated AgNPs has been successfully synthesized by reduction of silver nitrate with *Eleusine indica* leaves methanol extract.

Keywords: Plant-mediated silver nanoparticles, *Eleusine indica*, UV-Vis analysis, transmission electron microscope, antibacterial activity

Abstrak

Kaedah biomimetik yang bergantung kepada sumber alam seperti ekstrak tumbuhan, bakteria dan kulat, menawarkan alternatif dalam sintesis nanopartikel perak (AgNPs). Penggunaan kaedah biomimetik dalam sintesis AgNPs mempunyai pelbagai kelebihan termasuk keberkesanan kos, ketoksikan yang rendah, dan kesesuaian dalam kegunaan biomedik. Objektif kajian ini adalah untuk mensintesis nanopartikel perak diperantara tumbuhan menggunakan *Eleusine indica* dan menentukan aktiviti antibakteria. Ekstrak metanol *Eleusine indica* telah dirawat dengan 1 mM larutan perak nitrat pada suhu bilik (25 – 27 °C) selama 24 jam. Sampel telah

dicirikan menggunakan spektroskopi UV-Vis dan mikroskopi transmisi elektron (TEM). Spektroskopi penyerapan UV-Vis menunjukkan resonans berpusat yang kuat atas permukaan AgNPs pada kira-kira 413 nm. Rupabentuk fizikal AgNPs yang dicirikan melalui mikroskopi transmisi elektron (TEM) menunjukkan pembentukan AgNP dengan purata saiz partikel 20 nm. Aktiviti antibakteria nanopartikel perak perantaraan-tumbuhan yang disintesis telah diasai melalui penentuan kepekatan perencatan minimum (MIC) dan kepekatan bakterisidal minimum (MBC). Gabungan nanopartikel perak perantaraan-tumbuhan diramal mempunyai aktiviti bacteriosidal berdasarkan nisbah nilai MBC kepada MIC terhadap bakteria Gram positif dan Gram negatif bakteria. Dalam kajian ini, AgNPs perantaraan-tumbuhan telah berjaya disintesis melalui penurunan perak nitrat dengan ekstrak metanol daun *Eleusine indica*.

Kata kunci: nanopartikel perak perantaraan-tumbuhan, *Eleusine indica*, analisa UV-Vis, mikroskopi transmisi elektron, aktiviti antibakteria

Introduction

Nanotechnology is developing - rapidly in the growing field with the applications of science and technology for the purpose of making new nanoscale materials [1]. Communication, electronics, chemistry, physics, robotics, biology, and medicine can benefit from nanotechnology research [2]. Different forms of nanoparticles (NPs) such as copper, zinc, titanium, magnesium, gold, alginate and silver have emerged, but silver NPs have proven to be the most effective since they have strong antimicrobial efficiency against bacteria, viruses and other eukaryotic microorganisms [1]

Conventional methods for synthesizing AgNPs, such as physical and chemical procedures, involved the usage of heavy equipment, substantial amounts of energy consumption, highly toxic and hazardous chemical compounds that can cause biological hazards and therefore, they are not environmentally sustainable and they are unsafe [3]. As a result, biomimetic nanoparticle syntheses or plant-mediated silver nanoparticles are often used because they are simple, cost-effective, environmentally friendly, and they are easily reproduced [4]. AgNPs synthesized in a biomimetic method - useful in a variety of fields, including optoelectronic devices [5], catalytic activities [6], and the food packaging industry [7]. AgNPs is has also be regarded as the agent of wound-healing, antioxidant, antimicrobial, antiviral, and anticancer [8].

Synthesis methods using either plant extract or fruit extract have several advantages over other biological approaches. This includes no requirement in cell culture that can take more time to produce which can scale up the synthesis process [9]. Plant extracts contain a wide range of metabolites that can act as capping and stabilizing agents and thus avoids the need to add these agents from other sources [3]. There are other studies whereby plant-mediated AgNPs have been investigated for the antibacterial properties such as using *Rhazya stricta* [10] and *Azhadirachta indica* [11] to synthesis AgNPs. This study aims to add the possibility of *Eleusine indica* as a plant candidate to synthesize AgNPs. *Eleusine indica* or locally known as sambau has been known to possess antioxidant, antibacterial and antiviral activities among others [12,13]. Thus, it is a good potential for producing AgNPs against bacterial candidates known to be pathogenic. The strategy involves the reduction of silver nitrate and the methanol extract of *Eleusine indica* which can be used as a reductant as well as a stabilizer. The synthesized AgNPs is evaluated for its physical characteristics and antibacterial activity against four pathogenic microorganisms.

In this study, an extract of *Eleusine Indica* is used in the synthesis of plant-mediated AgNPs, and the relation between AgNPs and the extract's metabolites, and evaluate its antibacterial properties The characterization of synthesized AgNPs is analyzed with the use of UV-Vis spectroscopy and transmission electron microscopy (TEM).

Materials and Methods

All the reagents purchased were of laboratory grade and used as received. Silver nitrate ($AgNO_3$) were purchased from R&M Chemicals, US. Methanol was purchased

from Sigma Aldrich, Germany. (3-[4,5-dimethylthiazol-2-yl]-2,5 diphenyl tetrazolium bromide) (MTT), Mueller Hinton agar and nutrient broth was obtained from Universiti Kebangsaan Malaysia. The fresh leaves of *Eleusine indica* were collected in Kuala Pilah, Negeri Sembilan. Authentication of this species was done by Forest Research Institute Malaysia (FRIM) where voucher specimen (FRI-51486) was deposited. Deionized water was used throughout the experiment.

Extractions of *Eleusine indica*

About 250 g of ground dried *Eleusine indica* leaves was soaked in 2500 mL of methanol for 72 hours at room temperature by using maceration technique [14]. The sample was filtered and concentrated by using rotary evaporator. The extract was placed in a fume hood until almost dried to obtain *Eleusine indica* methanol extract and kept in a vial for further analysis.

Biomimetic synthesis and characterization of silver nanoparticles

The biomimetic method was followed by Lee and Jun [15] with some modification. About 10 mL of *Eleusine indica* methanol extract was added drop by drop into 30 mL of 1 mM silver nitrate solution and was allowed to be reacted at room temperature for 24 hours at 25-27 ºC. The appearance of yellowish-brown color of the solution indicates the formation of silver nanoparticles [16]. The formation of plant-mediated AgNPs was analyzed using UV-Vis spectroscopy and TEM.

Characterization of plant-mediated silver nanoparticles

Physicochemical properties of the synthesized plant-mediated silver nanoparticles were characterized using UV-Vis spectra and TEM analysis. The UV-Vis spectra analysis was conducted using a UV 2450 Shimadzu double-beam spectrophotometer, operated at a resolution of 2 nm in the range from 300 to 500 nm. The formation of AgNPs was confirmed by transmission electron microscopy (TEM). TEM analysis of AgNPs was performed using a Philips CM12 instrument operated at an accelerating voltage at 80 kV. The size distribution of the AgNPs was calculated from the TEM images by measuring the diameter in nm of approximately 50 nanoparticles.

Evaluation of antibacterial activity

The antibacterial potential of the synthesized plant-mediated silver nanoparticles was determined using minimum inhibitory concentration (MIC) and Minimum Bactericidal Concentration (MBC) assays [17]. In the assay, four bacteria were tested with two Gram-positive bacteria (*Staphylococcus aureus*, *Bacillus subtilis*) and another two Gram-negative bacteria (*Escherichia coli*, *Enterobacter aerogenes*). MIC assay was performed in triplicate in a 96-well microtiter plate. Serial double dilutions of plant-mediated silver nanoparticles (AgNPs) varying from 100% to 1.562 % in nutrient broth were prepared in the MIC assay. Each dilution (100 µL) was dispensed into the wells and then 100 µL of the bacterial suspension in nutrient broth was incubated at 37ºC for 24 hours. After 24 hours, 10 µL of 0.2 mg/mL (MTT) solution was added into each well and incubated for another 2 hours. The solution color change from pale yellow to red/purple, which indicated biologically active bacteria [18]. MBC is the determination of the lowest concentration without colony growth on the agar plates. This was determined by plating 10 µL from each well that showed no growth on a Mueller Hinton agar plate. Plates was then incubated for further 24 hours at 37°C. Lowest concentration that shows no colony growth was determined as MBC.

Results and Discussion

Extractions of Eleusine indica

Dried ground Eleusine indica leaves was used in this study in order to enhance the surface area and optimize the extraction process (Figure 1). The percentage yield of the crude extract was calculated and presented in Table 1.

Methanol extraction resulted in moderate weight and percentage yield of Eleusine indica. Methanol is a polar solvent that can extract most of the key phytochemical compounds [19]. Compared with aqueous solvent, methanol solvent has less polarity which gives more efficiency in term of extraction because of its capability in degradation of cell wall. Thus, methanol provides excellent capability in extraction of secondary metabolites such as phenolics, glycosides, tannins, flavonoids, saponins, steroids and alkaloids [20, 21].

These secondary metabolites have polyhydroxy group that are suitable in reducing metal ions to nanoparticles [22]. According to Iberahim et al. [23], Eleusine indica methanol extract have several groups of metabolites including phenolics, glycosides, flavonoids and terpenoids. These metabolites substantiate the selection of Eleusine indica in this study to potentially act as reducing and stabilizing agent in the synthesis of AgNPs.

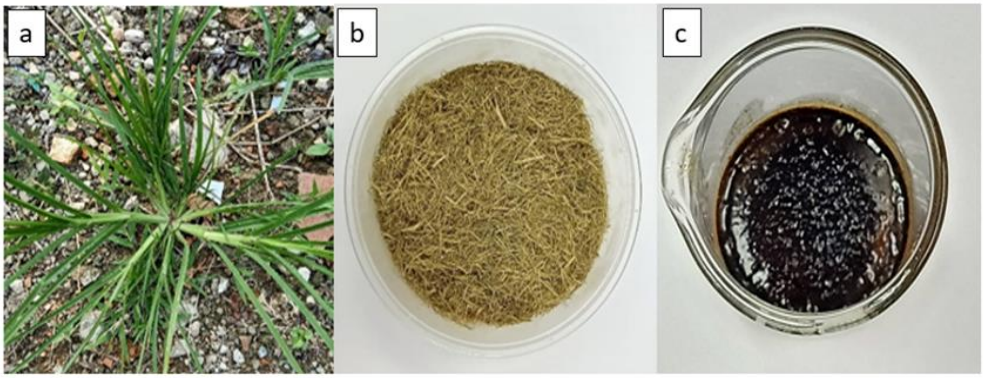

Figure 1. (a) *Eleusine indica* plant, (b) the dried ground leaves, (c) *Eleusine indica* methanol extract

Table 1. Percentage yield of *Eleusine indica* crude extract

Type of Crude Extract	Weight of Sample (g)	Weight of Crude (g)	Percentage of Crude Extract (%)
Methanol	250	13.3	5.32

Biomimetic synthesis and characterization of silver nanoparticles

Formation of silver nanoparticles in this study is monitored by color change. Figure 2 shows the color changes when the Eleusine indica methanol extract was mixed with a 1 mM $AgNO_3$ solution and treated at room temperature for 24 hours. The appearance of a yellowish solution in the reaction vessel indicated the formation of AgNPs due to excitation of surface plasmon resonance in the AgNPs [24,25].

Characterization of silver nanoparticles

Ultraviolet-visible spectroscopy (UV-Vis) and transmission electron microscopy (TEM) were used to characterize the synthesized AgNPs. As illustrated in Figure 3, the surface plasmon resonance of the AgNPs is centered at approximately 413 nm, indicating the presence of AgNPs in the solution. AgNPs are known to exhibit a UV-Visible absorption maximum in the range of 400-500 nm because of surface plasmon resonance [26]. The conduction band and valence band in AgNPs are relatively close to one other, allowing the electrons to travel freely. The collective oscillation of electrons of silver nano particles in resonance with the light wave produces a surface plasmon resonance (SPR) absorption band, which is caused by these free electrons [27]. According to Kerker [28], the absorbance of AgNPs depends mainly upon size and shape. thus, this will affect the absorbance of AgNPs that obtained.

The morphology and size distribution of plant-mediated AgNPs was analyzed using TEM micrograph. The TEM image in Figure 4 (left) shows that the particles are almost spherical. The particles size histograms of the plant-mediated AgNPs (Figure 4-right) suggest that the particles diameter is within the range of 10 nm to 55 nm

with an average size of 20 nm. Silver nanoparticles, in particular, have varying scale sizes depending on the type of plant extracts used [16]. For example, the silver nanoparticles synthesized using Plumbago auriculata leaves has average size between 15 to 30 nm [29]. [30] found that AgNPs synthesized using Datura stramonium leaf extract has average size of 15 to 20 nm. Based on the theory of quantum restraint, a smaller wavelength leads to a higher energy of the wave and a smaller particle size [31].

It has been reported that Eleusine indica extract contains 12 metabolites such as hydroxycinnamic acid, naringenin (flavanones), *2(3,4-dihydroxyphenyl)-7-hydroxy-5-benzenepropanoic acid,* antraquinone, caffeic acid derivative, caffeoyl glucose, hydroxybenzoic acid derivatives methyl 2-[cyclohex-2-en-1-yl(hydroxy)methyl]-3-hydroxy-4-(2-hydroxy ethyl)-3-methyl-5-oxoprolinate (aglycone) from the flavonoid and phenolic groups [12]. Active oxygen found in phenols, flavonoids, and triterpenoic acid can donate electrons into AgNPs to reduce silver precursors [32]. This reduction of silver ions to silver nanoparticles could be possibly due to -OH groups in flavonoids such as quercetin, which can be released during the tautomeric change of flavonoids from the enol to keto type that releases reactive hydrogen atoms that are responsible for the reduction of silver nanoparticles [33]. Figures 5 show the possible mechanism of reduction of silver ions to AgNPs by naringenin (flavonone) molecule.

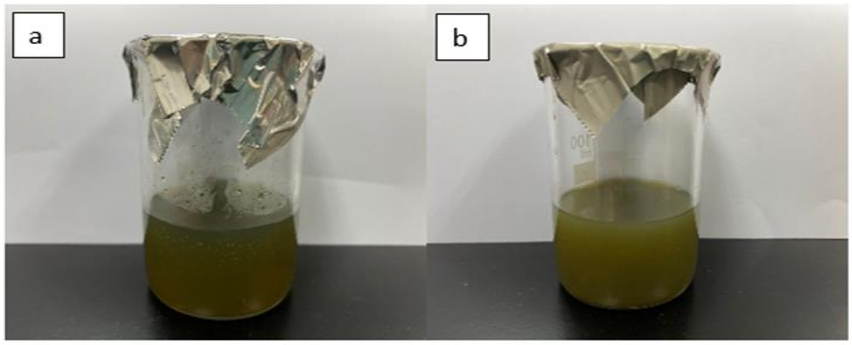

Figure 2. (a) *Eleusine indica* extract, (b) *Eleusine indica* extract mixed with silver nitrate after 24 hours

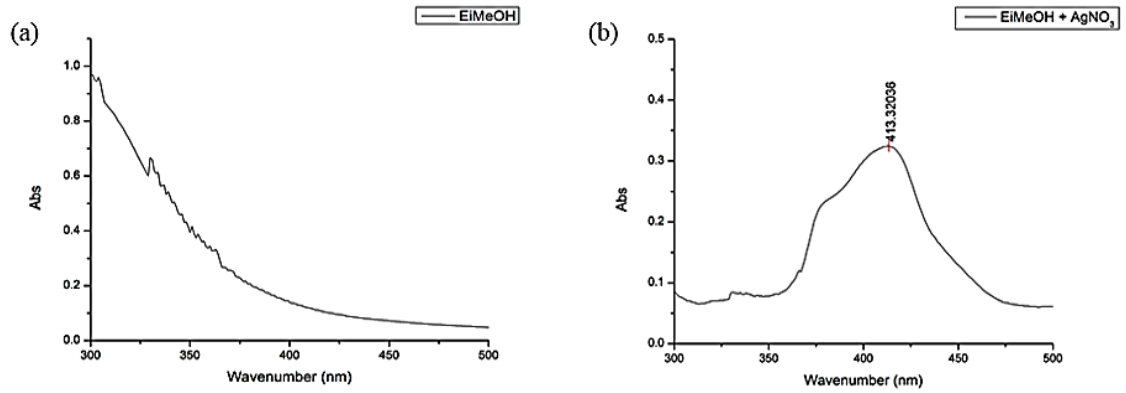

Figure 3. (a) UV-Vis absorption spectrum of Eleusine indica extract (EI-MeOH) and (b) synthesized silver nanoparticles (EI-MeOH-AgNPs)

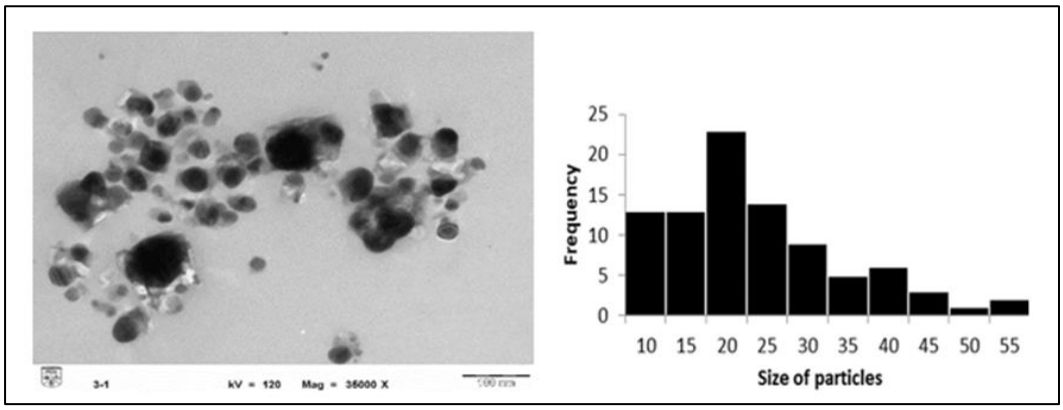

Figure 4. TEM micrograph and particle histogram

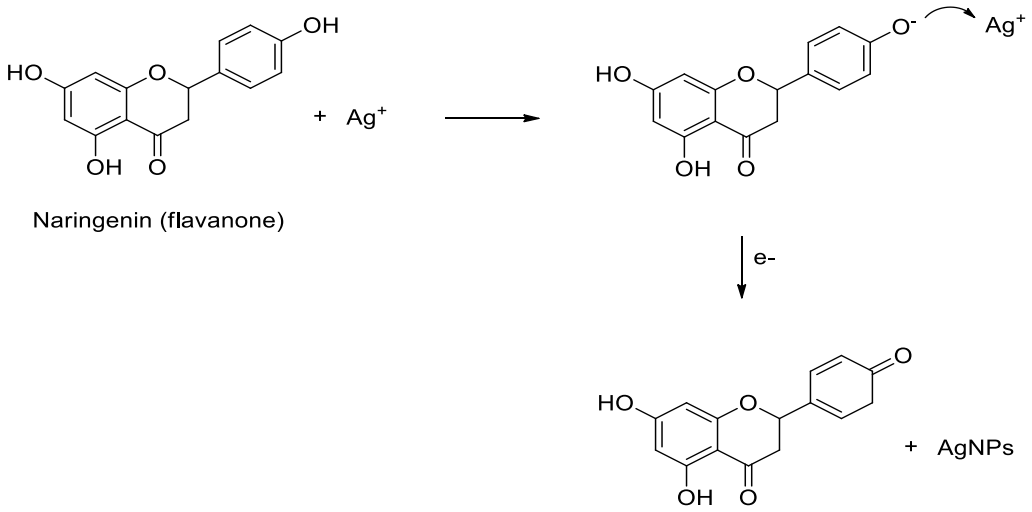

Figure 5. The proposed mechanism for the formation of plant-mediated AgNPs

Antibacterial activity of silver nanoparticles

The efficacy of AgNPs as promising antimicrobial has been experimentally tested against a wide range of medically important planktonic and sessile pathogenic microorganisms including bacteria, viruses, champignons, lichens and yeasts [34, 35]. In this study, the plant-mediated silver nanoparticles were tested against Gram-positive bacteria and Gram-negative bacteria. Table 2 shows the MIC and MBC test of synthesized silver nanoparticles against *Staphylococcus aureus*, *Bacillus subtilis*, *Escherichia coli* and *Enterobacter aerogenes*.

Based on the MIC and MBC values, the synthesized nanoparticle suggest the display of bacteriocidal potentials. The formal definition of a bactericidal agent is the ratio of MBC to MIC is ≤ 4, while a bacteriostatic agent has an MBC to MIC ratio of > 4 (CLSI). AgNPs antibacterial effects may be determined by the characteristics of certain bacterial species and the type of metabolite present in the plant [36] as well as the size

ranges and shapes of the AgNPs [27]. Theoretically, upon interaction with bacteria, nanoparticles bind with bacterial membrane which causes changes to both its physical and chemical nature. Nevertheless, the normal physiological process such as respiration and permeability of cells will be compromised [37]. Besides, the formation of various reactive nitrogen and oxygen species can be induced by nanoparticles that generates oxidative stress on DNA, and other important cell constituents which disrupt the overall functioning of bacterial cells.

Table 2. MIC and MBC test of silver nanoparticles synthesized by *Eleusine indica* against four bacteria

Bacteria	**MIC (µg/mL)**	**MBC (µg/mL)**	**MBC to MIC Ratio**
Staphylococcus aureus	12.5	12.5	1
Bacillus subtilis	1.56	1.56	1
Escherichia coli	6.25	12.5	2
Enterobacter aerogenes	3.13	6.25	2

Conclusion

In conclusion, the biomimetic method was demonstrated as a simple, safe, cost-effective, and ecofriendly preparation of AgNPs using *Eleusine indica* methanol extract. The synthesized plant-mediated AgNPs gave UV-Vis reading at 413 nm and have an average particle size of 20 nm. They showed potential antibacterial activity against Gram-positive and Gram-negative bacteria including *Staphylococcus aureus*, *Bacillus subtilis*, *Escherichia coli* and *Enterobacter aerogenes*. Thus, application of these synthesized AgNPs based on the findings may lead to valuable discoveries in various fields, including medical devices and in the pharmaceutical and biomedical industries. Toxicity studies of these AgNPs using human pathogens may open the door to a new range of antibacterial agents and the possibility to the use of AgNPs as antiviral agents.

Acknowledgement

The authors would like to acknowledge Ministry of Education for the financial support under Fundamental Research Grant Scheme (FRGS/1/ 2019/STG01/UITM/ 02/10) and Universiti Teknologi MARA, Negeri Sembilan Branch, Kuala Pilah Campus, Negeri Sembilan; Faculty of Applied Sciences, Universiti Teknologi MARA, Shah Alam Selangor; Faculty of Science & Technology and CRIM, Universiti Kebangsaan Malaysia, Bangi Selangor for providing the research facilities. Thanks also to Mr Yip Chee Wai for the invaluable guidance in the antibacterial assays. Not to be missed is our profound acknowledgement to Forest Research Institute Malaysia (FRIM), Mrs Syahida Emiza binti Suhaimi and Mr Mohd Aidil bin Nordin for helping in plant identification.

References

1. Logeswari, P., Silambarasan, S. and Abraham, J. (2015). Synthesis of silver nanoparticles using plants extract and analysis of their antimicrobial property. *Journal of Saudi Chemical Society*, 19(3): 311-317.
2. Safari, J. and Zarnegar, Z. (2014). Advanced drug delivery systems: Nanotechnology of health design a review. *Journal of Saudi Chemical Society*, 18(2): 85-99.
3. Rajeshkumar, S. and Bharath, L. V. (2017). Mechanism of plant-mediated synthesis of silver nanoparticles – A review on biomolecules involved, characterisation and antibacterial activity. *Chemico-Biological Interactions*, 273: 219-227.

4. Ahmed, S., Saifullah, Ahmad, M., Swami, B. L. and Ikram, S. (2016). Green synthesis of silver nanoparticles using *Azadirachta indica* aqueous leaf extract. *Journal of Radiation Research and Applied Sciences*, 9(1): 1-7.
5. Poulose, S., Panda, T., Nair, P. P. and Théodore, T. (2014). Biosynthesis of silver nanoparticles. *Journal of Nanoscience and Nanotechnology,* 14(2): 2038-2049.
6. Mosaviniya, M., Kikhavani, T., Tanzifi, M., Tavakkoli Yaraki, M., Tajbakhsh, P. and Lajevardi, A. (2019). Facile green synthesis of silver nanoparticles using *Crocus Haussknechtii Bois* bulb extract: Catalytic activity and antibacterial properties. *Colloids and Interface Science Communications*, 33(8): 100211.
7. Zhao, X., Zhou, L., Riaz Rajoka, M. S., Yan, L., Jiang, C., Shao, D. and Jin, M. (2018). Fungal silver nanoparticles: Synthesis, application and challenges. *Critical Reviews in Biotechnology*, 38(6): 817-835.
8. Larayetan, R., Ojemaye, M. O., Okoh, O. O. and Okoh, A. I. (2019). Silver nanoparticles mediated by *Callistemon citrinus* extracts and their antimalaria, antitrypanosoma and antibacterial efficacy. *Journal of Molecular Liquids*, 273: 615-625.
9. Roy, K., Sarkar, C. K. and Ghosh, C. K. (2015). Plant-mediated synthesis of silver nanoparticles using parsley (*Petroselinum crispum*) leaf extract: spectral analysis of the particles and antibacterial study. *Applied Nanoscience (Switzerland)*, 5(8): 945-951.
10. Shehzad, A., Qureshi, M., Jabeen, S., Ahmad, R., Alabdalall, A. H., Aljafary, M. A. and Al-Suhaimi, E. (2018). Synthesis, characterization and antibacterial activity of silver nanoparticles using *Rhazya stricta*. *PeerJ,* 2018(12): 1-15.
11. Lalitha, A., Subbaiya, R. and Ponmurugan, P. (2013). Green synthesis of silver nanoparticles from leaf extract *Azhadirachta indica* and to study its anti-bacterial and antioxidant property. *International Journal of Current Microbiology and Applied Sciences*, 2(6): 228-235.
12. Abdul, A. B., Al-Zubairi, A. S., Abdelwahab, S. I., Peng, C. Y., Mohan, S. and Elhassan, M. M. (2011). *Eleucine indica* possesses antioxidant, antibacterial and cytotoxic properties. *Evidence-Based Complementary and Alternative Medicine*, 2011: 965370.
13. Iberahim, R., Nor, N. S. M., Yaacob, W. A. and Ibrahim, N. (2018). *Eleusine indica* inhibits early and late phases of herpes simplex virus type 1 replication cycle and reduces progeny infectivity. *Sains Malaysiana*, 47(7): 1431-1438.
14. Devi, M., Devi, S., Sharma, V., Rana, N., Bhatia, R. K. and Bhatt, A. K. (2020). Green synthesis of silver nanoparticles using methanolic fruit extract of *Aegle marmelos* and their antimicrobial potential against human bacterial pathogens. *Journal of Traditional and Complementary Medicine*, 10(2): 158-165.
15. Lee, S. H. and Jun, B. H. (2019). Silver nanoparticles: Synthesis and application for nanomedicine. *International Journal of Molecular Sciences*, 20(4): 1-23.
16. Din, L. B., Mie, R., Samsudin, M. W., Ahmad, A. and Ibrahim, N. (2015). Biomimetic synthesis of silver nanoparticles using the *Lichen ramalina dumeticola* and the antibacterial activity. *Malaysian Journal of Analytical Sciences*, 19(2): 369-376.
17. Wang, W., Li, N., Luo, M., Zu, Y. and Efferth, T. (2012). Antibacterial activity and anticancer activity of *Rosmarinus officinalis L*. essential oil compared to that of its main components. *Molecules*, 17(3): 2704-2713.
18. Zarai, Z., Kadri, A., Ben Chobba, I., Ben Mansour, R., Bekir, A., Mejdoub, H. and Gharsallah, N. (2011). The in-vitro evaluation of antibacterial, antifungal and cytotoxic properties of *Marrubium vulgare L*. essential oil grown in Tunisia. *Lipids in Health and Disease*, 10(1): 161.
19. Ahmad, Aftab, Husain, A., Mujeeb, M., Khan, S. A., Alhadrami, H. A. A., & Bhandari, A. (2015). Quantification of total phenol, flavonoid content and pharmacognostical evaluation including HPTLC fingerprinting for the standardization of *Piper nigrum Linn* fruits. *Asian Pacific Journal of Tropical Biomedicine*, 5(2): 101-107.

20. Truong, D. H., Nguyen, D. H., Ta, N. T. A., Bui, A. V., Do, T. H. and Nguyen, H. C. (2019). Evaluation of the use of different solvents for phytochemical constituents, antioxidants, and in vitro anti-inflammatory activities of *Severinia buxifolia*. *Journal of Food Quality*, 2019: 8178294.
21. Gupta, M., Thakur, S., Sharma, A. and Gupta, S. (2013). Qualitative and quantitative analysis of phytochemicals and pharmacological value of some dye yielding medicinal plants. *Oriental Journal of Chemistry*, 29(2): 475-481.
22. Sahu, N., Soni, D., Chandrashekhar, B., Satpute, D. B., Saravanadevi, S., Sarangi, B. K. and Pandey, R. A. (2016). Synthesis of silver nanoparticles using flavonoids: hesperidin, naringin and diosmin, and their antibacterial effects and cytotoxicity. *International Nano Letters*, 6(3): 173-181.
23. Iberahim, R., Yaacob, W. A. and Ibrahim, N. (2015). Phytochemistry, cytotoxicity and antiviral activity of *Eleusine indica* (sambau). *AIP Conference Proceedings*, 1678: 1–5.
24. Shankar, S. S., Rai, A., Ankamwar, B., Singh, A., Ahmad, A. and Sastry, M. (2004). Biological synthesis of triangular gold nanoprisms. *Nature Materials*, 3(7): 482-488.
25. Kumar R, Ghoshal G, J. A. and G. M. (2017). Rapid green synthesis of silver nanoparticles (AgNPs) using (*Prunus persica*) plants extract: Exploring its antimicrobial and catalytic activities. *Journal of Nanomedicine & Nanotechnology*, 08(04): 2157-7439
26. Ashraf, J. M., Ansari, M. A., Khan, H. M., Alzohairy, M. A. and Choi, I. (2016). Green synthesis of silver nanoparticles and characterization of their inhibitory effects on AGEs formation using biophysical techniques. *Scientific Reports*, 2015(6): 1-10.
27. Zhang, X. F., Liu, Z. G., Shen, W. and Gurunathan, S. (2016). Silver nanoparticles: Synthesis, characterization, properties, applications, and therapeutic approaches. *International Journal of Molecular Sciences*, 17(9): 1534.
28. Kerker, M. (1985). The optics of colloidal silver: something old and something new. *Journal of Colloid and Interface Science*, 105(2): 297-314.
29. Singh, K., Naidoo, Y., Mocktar, C. and Baijnath, H. (2018). Biosynthesis of silver nanoparticles using *Plumbago auriculata* leaf and calyx extracts and evaluation of their antimicrobial activities. *Advances in Natural Sciences: Nanoscience and Nanotechnology*, 9(3): 035004.
30. Gomathi, M., Rajkumar, P. V., Prakasam, A. and Ravichandran, K. (2017). Green synthesis of silver nanoparticles using *Datura stramonium* leaf extract and assessment of their antibacterial activity. *Resource-Efficient Technologies*, 3(3): 280-284.
31. Narchin, F., Larijani, K., Rustaiyan, A., Ebrahimi, S. N. and Tafvizi, F. (2018). Phytochemical synthesis of silver nanoparticles by two techniques using *Saturaja rechengri Jamzad* extract: Identifying and comparing in vitro anti-proliferative activities. *Advanced Pharmaceutical Bulletin*, 8(2): 235-244.
32. Ramesh, A. V., Devi, D. R., Battu, G. R. and Basavaiah, K. (2018). A Facile plant mediated synthesis of silver nanoparticles using an aqueous leaf extract of *Ficus hispida Linn. f.* for catalytic, antioxidant and antibacterial applications. *South African Journal of Chemical Engineering*, 26(7): 25-34.
33. Jain, S. and Mehata, M. S. (2017). Medicinal plant leaf extract and pure flavonoid mediated green synthesis of silver nanoparticles and their enhanced antibacterial property. *Scientific Reports*, 7(1): 1-13.
34. Burdușel, A. C., Gherasim, O., Grumezescu, A. M., Mogoantă, L., Ficai, A. and Andronescu, E. (2018). Biomedical applications of silver nanoparticles: An up-to-date overview. *Nanomaterials*, 8(9): 1-25.
35. Mie, R., Samsudin, M. W., Din, L. B., Ahmad, A., Ibrahim, N. and Adnan, S. N. A. (2013). Synthesis of silver nanoparticles with antibacterial activity using the lichen *Parmotrema praesorediosum*. *International Journal of Nanomedicine*, 9(1): 121-127.
36. Kim, J. S., Kuk, E., Yu, K. N., Kim, J. H., Park, S. J., Lee, H. J. and Cho, M. H. (2007). Antimicrobial effects of silver nanoparticles. *Nanomedicine: Nanotechnology, Biology, and Medicine*, 3(1): 95-101

37. Salomoni, R., Léo, P. and Rodrigues, M. F. A. (2015). Antibacterial activity of silver nanoparticles (agnps) in *staphylococcus aureus* and cytotoxicity effect in mammalian cells. *The Battle Against Microbial Pathogens: Basic Science, Technological Advances and Educational Programs*, 2015: 851-857.

Malaysian Journal of Analytical Sciences (MJAS)
Published by Malaysian Analytical Sciences Society

MEASUREMENT OF SOLVENT PROPERTIES USING KAMLET-TAFT APPROACH FOR APPLICATION IN SYNTHESIS

(Pengukuran Sifat Pelarut Menggunakan Pendekatan Kamlet-Taft untuk Penggunaan dalam Sintesis)

Tariqul Islam[1], A. B. M. Helal Uddin[1], Sahena Ferdosh[2], Md. Zaidul Islam Sarker[1,3]*

[1]Faculty of Pharmacy
[2]Faculty of Science
International Islamic University Malaysia, 25200 Kuantan, Pahang, Malaysia
[3]Program Leader of Food Science Program, Cooperative Research, Education and Extension Services, Northern Marianas College, 501250, Saipan MP 96950, USA

**Corresponding author: mdzaidul.sarker@marianas.edu*

Received: 31 August 2021; Accepted: 11 January 2022; Published: 25 February 2022

Abstract

Solvents are an unavoidable part of pharmaceutical and chemical manufacturing/synthesis, most of them are toxic or hazardous. The study on toxic solvent replacement is ongoing over the world. Researchers are trying to overcome the hazardous issues that can be possible using the mixture of hydrogen bond donor (HBD) and hydrogen bond acceptor (HBA) solvent as a safe/recommended solvent mixture. This study presents the possibility for the replacement/limitation of dipolar aprotic solvent in drug synthesis using solvent-pair mixture where the Kamlet-Taft (KT) parameter works as a tool to alternate the uses of such types of toxic solvents. It has been simplified here among the many methods and equations of the KT approach. The polarity (π*), basicity (β), and acidity (α) of 10 pure solvents and 16 solvent-pair mixtures were measured spectroscopically, utilizing well-suited dyes or indicators. The highest absorption wavenumber value of indicators in the solution was selected and the simplified KT equations were used to determine the solvent properties (π*, β, α). Solvent mixtures were classified as per the solvent selection guideline of GSK2016 and CHEM21. Four pure solvents (tetrahydrofuran, dimethylformamide, dimethylsulfoxide, and acetone) exhibited low KT acidity, high KT basicity, and high KT polarity. Eight aqueous solvent mixtures (water-acetone, water-ethanol, water-isopropyl alcohol, water-dimethylsulfoxide, water-dimethylformamide, water-tetrahydrofuran), and two non-aqueous solvent mixtures (ethanol-dimethylformamide, ethanol-dimethylsulfoxide) showed low KT acidity and high KT basicity. Solvent classification by composite score showed that four solvent mixtures were as recommended and 5 mixtures were near to recommended solvent among 16 solvent mixtures. KT parameter was a simplified approach to determine which mixture can bind with active pharmaceutical ingredients (API) that is indicated by KT solvatochromic properties and solvent classification.

Keywords: Kamlet-Taft parameters, hazardous solvent, solvent-pair mixture, dipolar aprotic solvent, drug synthesis

Abstrak

Pelarut adalah bahagian yang tidak dapat dielakkan dalam pembuatan/sintesis farmaseutikal dan kimia, kebanyakannya beracun atau berbahaya. Kajian mengenai penggantian pelarut toksik sedang dijalankan di seluruh dunia. Penyelidik berusaha mengatasi masalah berbahaya yang mungkin dilakukan dengan menggunakan campuran pelarut penderma ikatan hidrogen (HBD) dan pelarut

ikatan hidrogen (HBA) sebagai campuran pelarut yang selamat/disyorkan. Kajian ini menunjukkan kemungkinan penggantian/pembatasan pelarut aprotik dipolar dalam sintesis ubat dengan campuran pasangan pelarut di mana parameter Kamlet-Taft (KT) berfungsi sebagai alat untuk mengganti penggunaan jenis pelarut toksik tersebut. Ini telah dipermudahkan di sini antara banyak kaedah dan persamaan pendekatan KT. Kekutuban (π*), asas (β), dan keasidan (α) daripada 10 pelarut tulen dan 16 campuran pasangan pelarut telah diukur dengan menggunakan spektroskopi, berdasarkan pewarna atau indikator yang sesuai. Nilai penyerapan gelombang tertinggi dari indikator dalam larutan dipilih dan persamaan KT digunakan untuk menentukan sifat pelarut (π*, β, α). Campuran pelarut dikelaskan mengikut garis panduan pemilihan pelarut GSK 2016 dan CHEM21. Empat pelarut tulen (tetrahidrofuran, dimetilformamida, dimetilsulfoksida, dan aseton) menunjukkan keasidan KT rendah, asas KT tinggi, dan kekutuban KT tinggi. Lapan campuran pelarut berasaskan air (air-aseton, air-etanol, air-isopropil alkohol, air-dimetilsulfoksida, air-dimetilformamida, air-tetrahidrofuran), dan dua campuran pelarut tidak berasaskan air (etanol-dimetilformamida, etanol-dimetilsulfoksida) menunjukkan keasidan KT rendah dan asas KT yang tinggi. Penggolongan terhadap 16 campuran pelarut berdasarkan skor komposit menunjukkan empat campuran pelarut adalah seperti yang disyorkan dan 5 campuran pelarut hampir dengan yang disyorkan. Parameter KT adalah pendekatan yang dipermudah untuk menentukan campuran mana yang dapat mengikat dengan bahan aktif farmaseutikal (API) yang ditunjukkan oleh sifat solvatochromic KT dan klasifikasi pelarut.

Kata kunci: parameter Kamlet-Taft, pelarut berbahaya, campuran pasangan pelarut, pelarut aprotik dipolar, sintesis ubat

Introduction

In 1976, Kamlet and Taft introduced a model to measure the solvatochromic properties, known as Kamlet-Taft parameters [1]. In 1997, Marcus brought some modifications in the measurement of KT parameters [2]. Various equations and indicators were used to calculate the KT parameters (KT acidity, KT basicity, and KT polarity) so that the appropriate result is obtained by averaging [3]. The most used indicators were N, N-dimethyl-4-nitroaniline, 4-nitro anisole, and N,N-dimethyl-3-nitro aniline for π* value; 4-nitroaniline, 4-nitrophenol, 4-aminoacetophenone and (tetramethyl ethylenediamine)(acetylacetonato)copper(II) perchlorate for β value; Cis-bis-(1,10-phenan throline)dicyanoiron(II), 2,6-dichloro-4-(2,4,6-triphenyl-1-pyridinio) phenolate, and 2,6-diphenyl-4-(2, 4, 6-tripheny-1-pyridinio) phenoxide/ phenolate for α value. The indicators were utilized in KT measurement because their UV variations are higher than the UV-Vis cutoff (310 nm) of the cyclic ketone [4]. In analysis, many specific equations are used to calculate the KT parameters that were prepared based on the indicators [2,5], and the concentration of the indicator greatly affects the result [6].

Solvents are categorized into four major types; recommended, problematic, hazardous, and highly hazardous based on health, safety, environment, and global harmonized system (GHS) hazards statements [7]. Most used solvents are hazardous as per the recommendation of the international conference on harmonization (ICH), Pfizer, GSK, and Sanofi [8,9], as shown in Table 1. Recently, KT parameters have been used to investigate the replacement/limitation of hazardous solvents using solvent-pair mixtures in synthetic chemistry. Most of the HBD-HBA solvent mixtures exhibit as solvent of recommended and problematic category [7,10,11], they can be applied in API [4,11] and non-API chemical [5,12,13] synthesis. The maximum use of safe solvents can minimize the health risks and negative impacts on the environment, which can be the most effective way to limit the use of hazardous solvents [14-17]. However, many methods; KT solvatochromic parameters using COSMO-RS [18], KT parameters using solvate ionic liquids [19] were more complex. Taking into consideration the advancement of the KT parameters in synthetic chemistry, the measurement technique has been simplified for determining the solvatochromic parameters. The 16 solvent-pair mixtures and 10 pure solvents were analyzed to determine the probability of application in replacing dipolar aprotic solvents (dimethylformamide, dimethylacetamide, N-methyl-2-pyrrolidone, pyridine etc.).

Table 1. Recommendation from Pfizer, GSK, Sanofi, and ICH regarding the use of the following solvents

Most Used Organic Solvents	**Concern in Use (Comment) [8, 9]**			
	Pfizer	**GSK**	**Sanofi**	**ICH**
Dimethylformamide (DMF)	Undesirable	Major issues	Substitution requested	To be limited
Dimethylacetamide (DMAC)	Undesirable	Major issues	Substitution requested	To be limited
N-methyl-2-pyrrolidone(NMP)	Undesirable	Major issues	Substitution requested	To be limited
Dichloromethane (DCM)	Undesirable	Major issues	Substitution advisable	To be limited
Chloroform	Undesirable	Major issues	No comment	To be limited
1,4-Dioxane	Undesirable	Major issues	Substitution requested	To be limited
Pyridine	Undesirable	No comment	Substitution advisable	To be limited
Diisopropyl ether (IPE)	Undesirable	Major issues	Substitution advisable	Unknown

Materials and Methods

Materials

Analytical reagent (AR) grade methanol (MeOH 99.9%), acetone (Ace 99.8%), tetrahydrofuran (THF 99.8%), dimethyl sulfoxide (DMSO 99.9%), and calcium chloride anhydrous (99.9%) were received from Merck KGaA, Germany. Ethanol (EtOH 99.8%) was purchased from HmbG chemicals, Malaysia. HPLC grade acetonitrile (ACN 99.99%), AR grade dichloromethane (DCM 99.9%) were purchased from QREC (Asia), Malaysia. AR grade dimethylformamide (DMF 99.99%), and isopropyl alcohol (iPrOH 99.99%) were received from Fisher Scientific, UK. Three solvatochromic indicators were purchased: N, N-dimethyl-4-nitroaniline 98% as indicator 1 from Alfa Aesar through Permula chemicals, Malaysia; 4-nitro aniline 99% (Indicator 2) and Reichardt's dye 90% or 2,6-diphenyl-4-(2,4,6-triphenyl-1-pyridinio) phenolate 90% as indicator 3 from Sigma-Aldrich. To avoid humidity contamination or light degradation, the samples and indicators were weighted cautiously. A microbalance (Brand: Mettler Toledo; model: AX-205) was used to prepare the samples by mass with an uncertainty of ±1×10-4 g.

Analytical condition of KT parameters

Organic solvents were dried to free residual water before analysis using calcium chloride anhydrous. Indicator concentration in the solvent was from 0.03 mM to 0.05 mM (for indicator 1 & 2) and 0.1 mM (for indicator 3). The indicator and solvent were mixed properly before analysis to limit a variety of UV absorption to 0.5-1.2. The desired UV spectra of the solution were determined at a resolution of 0.2 nm using a double beam UV-Vis spectrophotometer (Shimadzu, UV-1800). Every UV-Vis spectrum was performed in triplicate. During the UV analysis, the temperature has been controlled at 25±0.1 °C using a temperature controller (Shimadzu, TCC-240A).

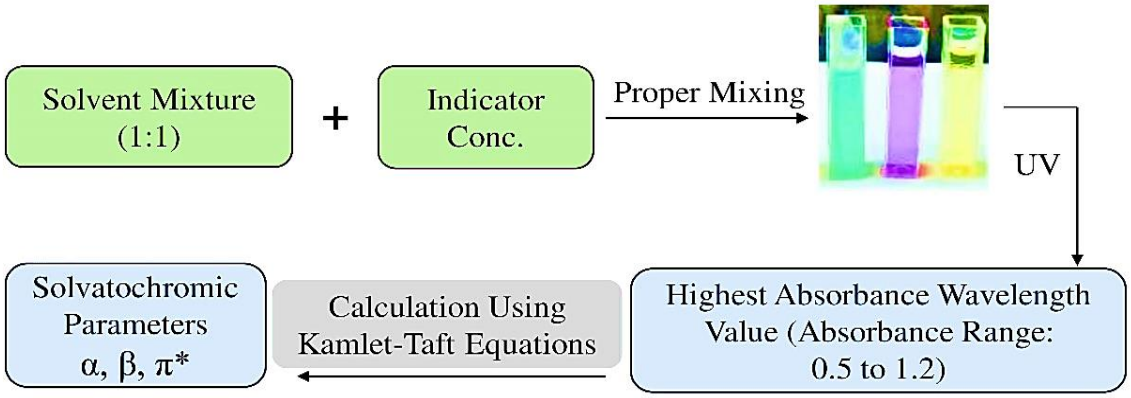

Figure 1. Measurement overview of solvatochromic parameters (π*, β, α) using the KT theory

Measurement equation of KT parameters

Three solvatochromic parameters i.e., KT polarity, KT basicity, and KT acidity were measured according to the original approach of KT theory using three equations (equation S1 to equation S3) [3,4]. The absorption wavenumber (V_{max}) from the highest wavelength value of the analytical sample was converted into KiloKaiser unit (1KK = 1000 cm^{-1}) to calculate the equations (1-3).

Statistical analysis

Experimental results were expressed as mean (n = 3) with uncertainty values and the data was analyzed using ANOVA and Dunnett's t-test in SPSS (version 20). *P values of 0.05 or less were regarded as significant.

Results and Discussion

The values of the measured wavenumbers (Vmax) and the obtained KT parameters have been expressed in Table 2 and Table 3. The absorbance range was established among the samples confined within 0.5 to 1.2. A total of ten pure solvents were analyzed to determine π*, β, and α. At the same time, sixteen mixed (HBD-HBA) solvents were also analyzed, involving eight aqueous and eight non-aqueous solvent pairs. In pure solvents, EtOH, MeOH, H_2O, iPrOH showed a high KT acidity and low KT polarity, whereas, DCM, ACN showed a low KT basicity. On the other hand, Ace, ACN, DMSO, DMF, and THF showed low acidity. In other words, the recommended solvents showed a high KT acidity, low KT basicity, and low KT polarity. In contrast, maximum problematic and hazardous solvents showed low KT acidity, high KT basicity, and high KT polarity except for DCM, iPrOH, and MeOH. Almost similar findings have been reported in the literature [20, 21].

Among the 16 mixed solvents, only four solvent mixtures i.e., H_2O-EtOH, H_2O-iPrOH, H_2O-DMSO, EtOH-DMSO were exhibited as recommended solvents, and the other 12 solvent mixtures were demonstrated as problematic in which 5 solvent mixtures (H_2O-Ace, EtOH-Ace, MeOH-Ace, H_2O-CAN, EtOH-CAN) showed as near to recommended solvent, as shown in Table 4. Eight aqueous (H_2O-MeOH, H_2O-Ace, H_2O-EtOH, H_2O-CAN, H_2O-iPrOH, H_2O-DMSO, H_2O-DMF, H_2O-THF) and two non-aqueous solvent mixtures (EtOH-DMF, EtOH-DMSO) showed a low KT acidity, low KT basicity, and high KT polarity. On the contrary, other non-aqueous solvent mixtures (EtOH-CAN, EtOH-Ace, EtOH-THF, MeOH-Ace, MeOH-DMF, MeOH-THF) showed a high KT acidity, low KT polarity, and low KT basicity, tabulated (Table 3). Similar results were found in the literature and previous work [6,11,12]. The solvent ranking was required for the application of mixed solvents that was prepared based on the GSK2016 and Innovative Medicines Initiative CHEM21 (IMI-CHEM21) solvent selection guideline [22]. The ranking of mixed solvents was ascertained from the minimum value of the GSK health and safety scores of HBA solvent using the equation (S4) [22].

Prat et al. and Byrne et al. stated that the commonly used solvents in drug synthesis and processing are hazardous, such as DMF, DMSO, NMP, DMAC, and pyridine, which are from dipolar aprotic solvents (HBA). IMI-CHEM21, GSK, Pfizer, ICH guidelines suggested that those solvents should be substituted/limited with safe solvents due to their toxic activities [7-9]. American Chemical Society (ACS) and Green Chemistry Institute (GCI) were investigating to replace such solvents in synthetic chemistry [23]. Duereh et al. stated that API has both HBD and HBA sites and dipolar aprotic (HBA) solvents have low KT acidity, high KT basicity, and high KT polarity. HBA solvents could easily create a strong chemical binding with the HBD site of API for these chemical properties [5].

Duereh et al. studied with 52 solvent mixtures and they reported that combinations of HBD-HBA allow the binding with API because solvent mixtures show low KT acidity, high KT basicity, and high KT polarity properties. For that, the solvent mixture can be used for the replacement of dipolar aprotic solvent. Although strong binding with API depends on physicochemical properties of solvent mixture. All mixtures who exhibited low KT acidity and high KT basicity, they are also capable to bind with the HBD site of API, can be selected for drug synthesis [4, 11, 13]. The solvent ranking was prepared to know which mixture is hazardous or problematic and which is recommended before being applied in synthesis. However, pure recommended solvents typically showed high acidity that is not capable to bind with the API. Therefore, when the solvent-pair mixtures show low KT acidity ($\alpha \approx 0$), high KT basicity ($\beta > 0.6$), and high KT polarity ($\pi^* > 0.6$), they offer a strong binding with the API [3, 11].

Indicator 1: Polarity (π^*) = $(28.10 - V_{max1}) / 3.52$ (1)

Indicator 2: Basicity (β) = $(0.984V_{max1} + 3.49 - V_{max2}) / 2.759$ (2)

Indicator 3: Acidity (α) = $(1.318V_{max1} - 47.7 + V_{max3}) / 5.47$ (3)

Composite score = $\sqrt{}$ (Safety score x Health score) (4)

Table 2 The properties of pure solvents from the wavenumber average (V_{max}) using the original approach of KT equations

Solvent	*V_{max}	*Polarity (π^*)	*V_{max}	*Basicity (β)	*V_{max}	*Acidity (α)
	(Mean ± SD)	(Mean)	(Mean ± SD)	(Mean)	(Mean ± SD)	(Mean)
EtOH	25.92 ± 0.06	0.62	25.80 ± 0.03	0.70	25.80 ± 0.02	0.82
MeOH	25.64 ± 0.02	0.70	25.66 ± 0.05	0.64	25.66 ± 0.02	1.00
Ace	25.66 ± 0.04	0.69	25.59 ± 0.03	0.49	25.59 ± 0.02	0.24
CAN	25.41 ± 0.02	0.76	25.39 ± 0.03	0.33	25.39 ± 0.01	0.38
i-PrOH	25.94 ± 0.02	0.61	25.91 ± 0.07	0.56	25.91 ± 0.01	0.60
DMSO	24.55 ± 0.02	1.01	24.57 ± 0.05	0.69	24.57 ± 0.01	0.10
DMF	25.07 ± 0.02	0.86	25.07 ± 0.02	0.71	25.07 ± 0.01	0.09
THF	26.05 ± 0.05	0.58	25.95 ± 0.05	0.48	25.95 ± 0.11	0.00
DCM	25.48 ± 0.03	0.74	25.43 ± 0.04	0.00	25.43 ± 0.06	0.04
H_2O	23.68 ± 0.02	1.26	23.64 ± 0.03	0.16	23.64 ± 0.14	1.27

Key: *P values ($P<0.05$) were regarded as significant. Uncertainty value of $\pi^* = \pm 8\times10^{-3}$, $\beta = \pm 6\times10^{-3}$, and $\alpha = \pm 8\times10^{-3}$

Table 3. The properties of mixed solvents from the wavenumber average (V_{max}) using the original approach of KT equations

HBD-HBA Mixture	*V_{max} (Mean ± SD)	*Polarity (π) (Mean)	*V_{max} (Mean ± SD)	*Basicity (β) (Mean)	*V_{max} (Mean ± SD)	*Acidity (α) (Mean)
Aqueous solvent mixture						
H_2O-MeOH	24.14 ± .02	1.12	24.14 ± 0.05	0.40	24.14 ± 0.03	0.82
H_2O-Ace	24.39 ± 0.03	1.05	24.39 ± 0.03	0.48	24.39 ± 0.01	0.68
H_2O-EtOH	24.31 ± 0.02	1.08	24.31 ± 0.03	0.48	24.31 ± 0.01	0.67
H_2O-CAN	24.51 ± 0.02	1.02	24.51 ± 0.04	0.41	24.51 ± 0.01	0.82
H_2O-iPrOH	24.62 ± 0.02	0.99	24.62 ± 0.03	0.57	24.62 ± 0.01	0.65
H_2O-DMSO	23.88 ± 0.02	1.20	23.88 ± 0.02	0.43		0.58
H_2O-DMF	24.08 ± 0.01	1.14	24.08 ± 0.02	0.48	24.08 ± 0.03	0.62
H_2O-THF	24.98 ± 0.02	0.89	24.98 ± 0.02	0.60	24.98 ± 0.01	0.64
Non-aqueous solvent mixture						
EtOH-CAN	25.46 ± 0.02	0.75	25.46 ± 0.05	0.51	25.46 ± 0.001	0.82
	25.64 ± 0.02	0.70	25.64 ± 0.03	0.59	25.64 ± 0.01	0.76
EtOH-DMF	25.36 ± 0.02	0.78	25.36 ± 0.04	0.65	25.36 ± 0.02	0.67
EtOH-DMSO	25.17 ± 0.02	0.83	25.17 ± 0.04	0.74	25.17 ± 0.01	0.60
EtOH-THF	25.81 ± 0.02	0.65	25.81 ± 0.02	0.64	25.81 ± 0.02	0.70
MeOH-Ace	25.54 ± 0.02	0.73	25.54 ± 0.03	0.56	25.54 ± 0.02	0.88
MeOH-DMF	25.32 ± 0.02	0.79	25.32 ± 0.02	0.63	25.32 ± 0.02	0.81
MeOH-THF	25.71 ± 0.05	0.68	25.71 ± 0.03	0.61	25.71 ± 0.02	0.84

Key: *P values ($P<0.05$) were regarded as significant. Uncertainty value of $\pi^* = \pm 7\times10^{-3}$, $\beta = 8\times10^{-3}$, and $\alpha = \pm 3\times10^{-3}$

Table 4. Ranking of the solvent-pair mixture from the minimum values of GSK health and safety score [22]

Solvent-pair (HBD-HBA)	GSK Scores of HBA Solvent				Composite Score (Rank)
	Safety	Health	Environmental	Waste	
H_2O-EtOH	7.7	8.9	6.7	4.2	8.3
H_2O-iPrOH	6.9	7.7	7.5	4.4	7.3
H_2O-DMSO	6.7	7.9	6.9	4.6	7.3
EtOH-DMSO	6.7	7.9	6.9	4.6	7.3
H_2O-Ace	6	7.7	7.7	3.3	6.8
EtOH-Ace	6	7.7	7.7	3.3	6.8
MeOH-Ace	6	7.7	7.7	3.3	6.8
H_2O-ACN	7.7	5.9	8.9	2.8	6.7
EtOH-ACN	7.7	5.9	8.9	2.8	6.7
H_2O-MeOH	7.1	4.9	8.4	4.0	5.9

Table 4 (cont'd). Ranking of the solvent-pair mixture from the minimum values of GSK health and safety score [22]

Solvent-pair (HBD-HBA)	GSK Scores of HBA Solvent				Composite Score (Rank)
	Safety	Health	Environmental	Waste	
H_2O-THF	4.9	5.9	5.2	3.5	5.4
EtOH-THF	4.9	5.9	5.2	3.5	5.4
MeOH-THF	4.9	5.9	5.2	3.5	5.4
H_2O-DMF	9	2.4	6.3	4.6	4.6
EtOH-DMF	9	2.4	6.3	4.6	4.6
MeOH-DMF	9	2.4	6.3	4.6	4.6

Keys: Recommended solvent-pairs (green highlight) = score 7-10, problematic solvent-pairs (yellow highlight) = score 4-7, hazardous solvent-pairs (red highlight) = score 0-4 are score ranges adopted from IMI-CHEM21 [7]

Conclusion

The Kamlet-Taft analytical approach was simple and efficient to measure the KT acidity, basicity, and polarity of solvents or solvent mixtures. However, the proper mixing and temperature control of the solvent and indicator was the prerequisite to get the correct result in KT analysis. The ranking of HBD-HBA combinations facilitated to find out a suitable solvent mixture to substitute hazardous solvents in drug synthesis. The highest yield was found when the solvent creates a strong interaction with the HBD site of API. It is possible if the solvent mixture carries low KT acidity and high KT basicity. The maximum use of this methodology could bring a revolutionary change in synthetic chemistry.

Acknowledgement

The authors are thankful to the Fundamental Research Grant Scheme of the Ministry of Education, Malaysia (GRANT NO: FRGS19-002-0610) and International Islamic University Malaysia for their support.

References

1. Kamlet, M. J., and Taft, R. W. (1976). The solvatochromic comparison method. I. The beta-scale of solvent hydrogen-bond acceptor (HBA) basicity. *Journal of the American chemical Society*, 98(2): 377-383.
2. Labban, A. S. and Marcus, Y. (1997). Solvatochromic parameters of ethanolamines. *Journal of the Chemical Society, Faraday Transactions*, 93(1): 77-79.
3. Islam, T., Sarker, M. Z. I., Uddin, A. H., Yunus, K. B., Prasad, R., Mia, M. A. R. and Ferdosh, S. (2020). Kamlet Taft parameters: A tool to alternate the usage of hazardous solvent in pharmaceutical and chemical manufacturing/synthesis-A gateway towards green technology. *Analytical Chemistry Letters*, 10 (5): 550-561.
4. Duereh, A., Guo, H., Honma, T., Hiraga, Y., Sato, Y., Lee Smith Jr, R. and Inomata, H. (2018). Solvent polarity of cyclic ketone (cyclopentanone, cyclohexanone): Alcohol (methanol, ethanol) renewable mixed-solvent systems for applications in pharmaceutical and chemical processing. *Industrial & Engineering Chemistry Research*, 57(22): 7331-7344.
5. Duereh, A., Sato, Y., Smith Jr, R. L., and Inomata, H. (2016). Analysis of the cybotactic region of two renewable lactone–water mixed-solvent systems that exhibit synergistic Kamlet–Taft basicity. *The Journal of Physical Chemistry B*, 120(19): 4467-4481.
6. Marcus, Y. (1994). The use of chemical probes for the characterization of solvent mixtures. Part 2. Aqueous mixtures. *Journal of the Chemical Society, Perkin Transactions 2*(8): 1751-1758.

7. Prat, D., Wells, A., Hayler, J., Sneddon, H., McElroy, C. R., Abou-Shehada, S. and Dunn, P. J. (2015). CHEM21 selection guide of classical-and less classical-solvents. *Green Chemistry*, 18(1): 288-296.
8. European Medicines Agency (2019), ICH guideline Q3C (R6) on impurities: guideline for residual solvents, step 5. https://www.ema.europa.eu/en/ich-q3c-r6-residual-solvents [Access online 08 October 2021].
9. Byrne, F. P., Jin, S., Paggiola, G., Petchey, T. H., Clark, J. H., Farmer, T. J., Hunt, A. J., McElroy, C. R. and Sherwood, J. (2016). Tools and techniques for solvent selection: green solvent selection guides. *Sustainable Chemical Processes*, 4(1): 1-24.
10. Prat, D., Hayler, J. and Wells, A. (2014). A survey of solvent selection guides. *Green Chemistry*, 16(10): 4546-4551.
11. Duereh, A., Sato, Y., Smith Jr, R. L. and Inomata, H. (2017). Methodology for replacing dipolar aprotic solvents used in API processing with safe hydrogen-bond donor and acceptor solvent-pair mixtures. *Organic Process Research & Development*, 21(1): 114-124.
12. Duereh, A., Sato, Y., Smith Jr, R. L. and Inomata, H. (2015). Spectroscopic analysis of binary mixed-solvent-polyimide precursor systems with the preferential solvation model for determining solute-centric Kamlet–Taft solvatochromic parameters. *The Journal of Physical Chemistry B*, 119(46): 14738-14749.
13. Duereh, A., Sato, Y., Smith Jr, R. L. and Inomata, H. (2015). Replacement of hazardous chemicals used in engineering plastics with safe and renewable hydrogen-bond donor and acceptor solvent-pair mixtures. *ACS Sustainable Chemistry & Engineering*, 3(8): 1881-1889.
14. Capello, C., Fischer, U. and Hungerbühler, K. (2007). What is a green solvent? A comprehensive framework for the environmental assessment of solvents. *Green Chemistry*, 9(9): 927-934.
15. Clark, J. H., and Tavener, S. J. (2007). Alternative solvents: shades of green. *Organic Process Research & Development*, 11(1): 149-155.
16. Jessop, P. G. (2011). Searching for green solvents. *Green Chemistry*, 13(6): 1391-1398.
17. Ashcroft, C. P., Dunn, P. J., Hayler, J. D. and Wells, A. S. (2015). Survey of solvent usage in papers published in organic process research & development 1997–2012. *Organic Process Research & Development*, 19(7): 740-747.
18. Sherwood, J., Granelli, J., McElroy, C. R. and Clark, J. H. (2019). A method of calculating the Kamlet–Abboud–Taft solvatochromic parameters using COSMO-RS. *Molecules*, 24(12): 2209.
19. Dolan, D. A., Sherman, D. A., Atkin, R., and Warr, G. G. (2016). Kamlet–taft solvation parameters of solvate ionic liquids. *ChemPhysChem*, 17(19): 3096-3101.
20. Marcus, Y. (1998). The properties of solvents. John Wiley & Sons, England: pp. 256
21. Marcus, Y. (1993). The properties of organic liquids that are relevant to their use as solvating solvents. *Chemical Society Reviews*, 22(6): 409-416.
22. Alder, C. M., Hayler, J. D., Henderson, R. K., Redman, A. M., Shukla, L., Shuster, L. E. and Sneddon, H. F. (2016). Updating and further expanding GSK's solvent sustainability guide. *Green Chemistry*, 18 (13): 3879-3890.
23. Hellsten, S., Qu, H. and Louhi-Kultanen, M. (2011). Screening of binary solvent mixtures and solvate formation of indomethacin. *Chemical Engineering & Technology*, 34(10): 1667-1674.

Malaysian Journal of Analytical Sciences (MJAS)
Published by Malaysian Analytical Sciences Society

SYNTHESIS, CHARACTERIZATION, AND IN-SILICO STUDIES OF CINNAMIC ACID DERIVATIVES TOWARDS DENGUE VIRUS

(Sintesis, Pencirian dan Kajian In-Siliko Sebatian Terbitan Asid Sinamik Terhadap Virus Denggi)

Anis Najwa Mohd Wahid[1], Nadia Mohamed Yusoff[1], Asnuzilawati Asari[1,2]*, Siti Nor Khadijah Addis[1], Hanis Mohd Yusoff[1,2], Habsah Mohamad[3], Fauziah Abdullah[4]

[1]*Faculty of Science and Marine Environment*
[2]*Advanced Nano Materials (ANoMa) Research Group, Faculty of Science and Marine Environment*
[3]*Institute of Marine Biotechnology*
Universiti Malaysia Terengganu, 21030 Kuala Nerus, Terengganu, Malaysia
[4]*Phytochemistry Programme, Natural Products Division,*
Forest Research Institute of Malaysia, 52109 Kepong, Selangor, Malaysia

**Corresponding author: asnu@umt.edu.my*

Received: 7 August 2021; Accepted: 18 December 2021; Published: 25 February 2022

Abstract

The dengue virus (DENV) has posed a serious global threat to human health for the past few decades. However, there are still no clinically approved antiviral drug available for the treatment of DENV. Cinnamic acid and its derivatives have attracted great attention due to their broad range of pharmacological properties. The present study aimed to synthesize and investigate the affinity of cinnamic acid derivatives against DENV. Six cinnamic acid derivatives (AC1-AC6) were synthesized by the reaction of substituted cinnamoyl chloride with the corresponding alcohol and amine. The structures of the compounds were confirmed by using ^{1}H and ^{13}C Nuclear Magnetic Resonance (NMR) and mass spectrometry. The synthesized compounds were then simulated for molecular docking to investigate their binding affinity to the protein target of DENV-2 NS2B/NS3 protease. The in-silico study reveals that the compound AC5 has the highest binding affinity and fit into the allosteric pocket of DENV-2 NS2B/NS3 serine protease with van der Waals interaction, C-H bonding and a few pi interactions such as π-cation, π-lone pair, π-π T-shaped as well as π-alkyl interaction.

Keywords: cinnamic acid, synthesis, anti-dengue virus, docking

Abstrak

Virus denggi (DENV) memberikan ancaman sejagat yang serius dalam kesihatan manusia sejak beberapa dekad yang lalu. Walau bagaimanapun, masih belum ada ubat anti-virus yang diluluskan secara klinikal bagi rawatan DENV. Asid sinamik dan terbitannya telah menarik banyak perhatian oleh kerana sifat farmakologi yang mempunyai julat yang luas. Kajian ini bertujuan untuk mensintesis dan menyiasat afiniti terbitan asid sinamik terhadap DENV. Enam terbitan asid sinamik (**AC1-AC6**) telah disintesis dengan tindakbalas penukargantian sinnamoil klorida dengan alkohol dan amina. Struktur sebatian telah disahkan dengan menggunakan ^{1}H dan ^{13}C Resonans Magnet Nukleus (NMR) dan spektrometer jisim. Sebatian yang telah disintesis kemudian disimulasikan dengan mengedok molekul untuk mengkaji sifat afiniti dengan protein sasaran iaitu protease DENV-2

NS2B / NS3. Kajian in-siliko mendedahkan bahawa sebatian **AC5** mempunyai afiniti pengikatan tertinggi dan dapat memasuki poket alosterik DENV-2 NS2B / NS3 protease serin dengan interaksi van der Waals, ikatan C-H dan beberapa interaksi pi seperti π-cation, π -lone pair, π-π berbentuk T dan juga interaksi π-alkil.

Kata kunci: asid sinamik, sintesis, anti-virus denggi, mengedok

Introduction

Dengue virus (DENV), the most significant virus in the *Flaviviridae* family with the highest morbidity and mortality rates, has been a serious global threat in the past few decades. The latest statistics from the World Health Organization (WHO) has shown an increasing trend of DENV infection throughout Malaysia with 127,407 reported cases in 2019. Despite this alarming issue, there is currently no effective vaccine nor antiviral treatment available for dengue patients. Prevention against DENV infection largely depends on controlling the mosquito vectors as well as on the use of the natural remedies. This underscores an urgent need to discover and develop a novel antiviral agent that is safe and effective in controlling dengue infection.

Cinnamic acid has gained a lot of interest due to its simple structure with great potential of pharmacological properties. It is a group of aromatic carboxylic acids, appearing naturally in the plant kingdom. Cinnamic acids occur in all green plants as well as the reproductive organs of flowering plants [1]. Cinnamic acids with varied substitution on the aryl ring, and their esters have been identified in natural bee products including honey and propolis [2]. It is also readily available from coffee beans, tea, cocoa, apples, tomatoes, and cereals [3]. It is a safe and extensive source of material due to its natural and low toxicity properties.

Cinnamic acid and its related molecules have a variety of biological activities, such as anticancer, antimalarial, antimicrobial and antioxidant [4,5]. Recently, cinnamic acid was reported to be an effective antiviral drug against Zika virus (ZIKV) [6]. It was found that cinnamic acid possessed anti-ZIKV properties against the post-entry stage of the ZIKV replication cycle, and inhibited RNA-dependent RNA polymerase (RdRp) activity. Additionally, cinnamic acid was also reported to have an excellent activity against *Tobacco mosaic virus* (TMV) in which most target compounds in this research exhibited good anti-plant virus activities [7]. One of the cinnamic acid derivatives also significantly inhibits hepatitis C virus (HCV) replication via the induction of oxidative stress [8].

Despite their rich medicinal tradition and remarkable biological activities, cinnamic acid derivatives and their potentials remained underutilized for several decades. Currently, the antiviral activity of cinnamic acid related molecules against dengue virus infection has never been experimentally addressed despite of its well-known therapeutic potential. In this study, six cinnamic acid derivatives have been synthesized and simulated for molecular docking to investigate their binding interactions to the protein target of DENV-2 NS2B/NS3 protease. Overall, this study demonstrated that cinnamic acid would be an excellent potential candidate for the development of antiviral drugs against DENV.

Materials and Methods

Chemicals and instrumentations

Ferulic acid, cinnamoyl chloride, anthranilic acid, 3-aminobenzotrifluoride, 2,6-dimethylaniline, 4-bromo benzyl alcohol, thymol, eugenol, anhydrous dichloromethane (DCM), triethylamine, hydrochloric acid (HCl), sodium bicarbonate ($NaHCO_3$), magnesium sulphate (Mg_2SO_4), hexane, ethyl acetate and acetone were purchased from standard commercial suppliers such as Sigma-Aldrich, Merck, Acrós Organics, Fisher Scientific, HmbG® Chemicals and R & M Chemical. All chemicals and solvents used in this study were of reagent grade (AR) and were used without further purification. Column chromatography was performed using silica gel 60 (230-400 mesh, Merck). Analytical thin-layer chromatography (TLC) was done on precoated silica gel 60 (F254, Merck) plates and visualized under UV 254 nm without treatment.

^{1}H and ^{13}C nuclear magnetic resonance (NMR) spectra were determined by Bruker Avance II 400 spectrometer in deuterated dimethyl sulfoxide (DMSO-d_6). The chemical shifts were reported in a ppm scale. The synthesized compounds were dissolved in dichloromethane (DCM) and analysed using Perkin Elmer GC-MS (Clarus 500 Chromatography/Mass Spectrometry).

Chemistry

The synthetic route of the synthesized compounds is described in Scheme 1.

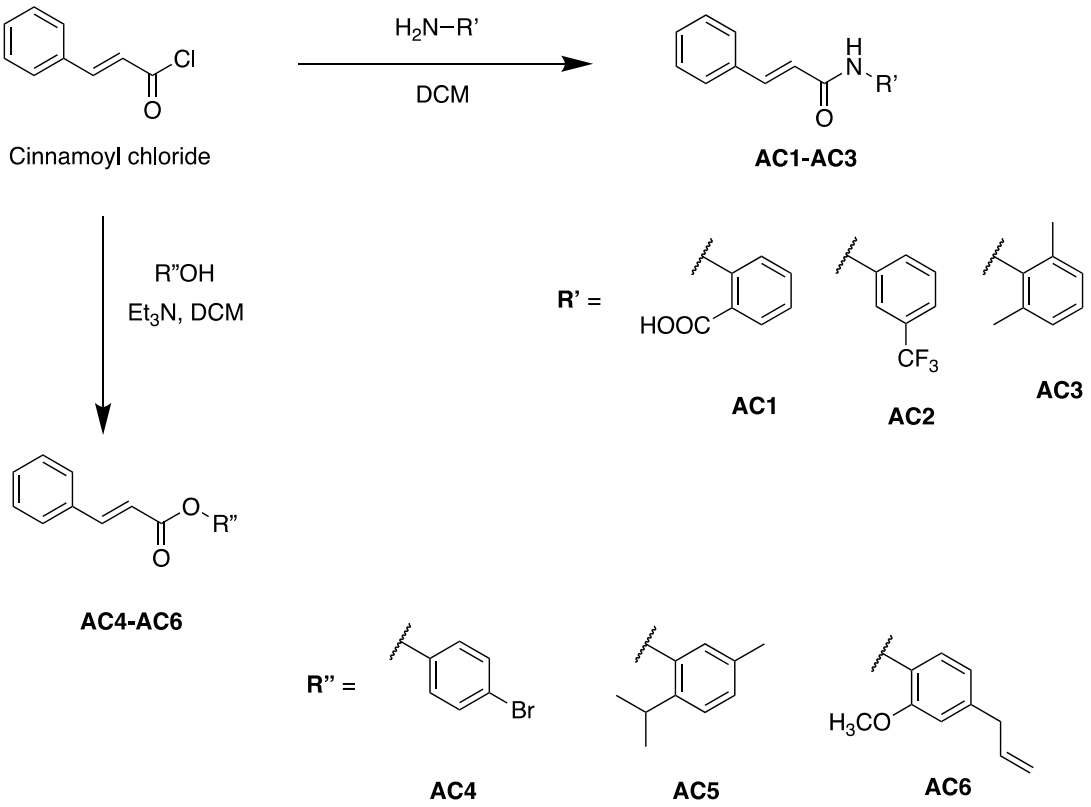

Scheme 1. The synthetic work of cinnamic acid amide and ester derivatives

Synthesis of cinnamoyl amide derivatives (AC1-AC3)

Cinnamoyl chloride (0.40 g, 2.4 mmol) in anhydrous DCM (5 mL) was added dropwise at 0 ℃ to a stirred solution of 3.6 mmol of amine (anthranilic acid, 3-aminobenzotrifluoride and 2,6-dimethylaniline) in anhydrous DCM (10 mL). The mixture was stirred at 0℃ for 30 min and then at RT for 3 hours. After completion of the reaction, 10 mL of DCM was added. The solution was washed 3 times with 1 N HCl and 2 times with 1 N $NaHCO_3$. The separated organic layer was dried over Mg_2SO_4 and the solvent was evaporated completely to obtain a residue. The residue was purified by silica gel column chromatography to afford the desired products of **AC1-AC3** by using a solvent system of hexane and ethyl acetate.

2-cinnamamidobenzoic acid (AC1)

Colorless powder (0.34 g, 53 %), **AC1** was prepared from the reaction of cinnamoyl chloride (0.40 g, 2.4 mmol) with anthranilic acid (0.49 g, 3.6 mmol) in the same manner as described in Scheme 1, ^{1}H NMR (400MHz, DMSO-d_6): δ_H ppm, 11.38 (1H, s, NH) , 8.61 (1H, d, J = 7Hz, H-ar), 8.02 (1H, d, J = 6Hz, H-

ar), 7.74 (1H, t, *J* = 7Hz, H-ar), 7.66 (1H, d, *J* = 7Hz, CH), 7.62 (1H, t, *J* = 9Hz, H-ar), 7.44 (4H, m, H-ar), 7.19 (1H, t, *J* = 14Hz, H-ar), 6.89 (1H,d, *J* = 15Hz, CH); ^{13}C NMR (100MHz, DMSO-d_6): δ_C ppm, 117.5, 120.9, 123.4, 128.6, 129.4, 130.5, 131.6, 134.4, 134.8, 141.26 (CH-aromatic), 141.7 & 122.9 (C=C), 169.9 (C=O). HRESIMS (positive mode) m/z calculated for $[C_{16}H_{13}NO_3]^+$: 267, $[M+H]^+$; found: 268.2639.

N-(3-(trifluoromethyl)phenyl)cinnamamide (AC2)

Colorless powder (0.42 g, 61 %), **AC2** was prepared from the reaction of cinnamoyl chloride (0.40 g, 2.4 mmol) with 3-aminobenzotrifluoride (0.58 g, 3.6 mmol) in the same manner as described in Scheme 1, ^{1}H NMR (400MHz, DMSO-d_6): δ_H ppm, 10.57 (1H, s, NH) , 8.22 (1H, s, H-ar), 7.87 (1H, d, *J* = 8Hz, H-ar), 7.66 (2H, m, H-ar), 7.62 (1H, d, *J* = 4Hz, CH), 7.58 (1H, t, *J* = 8Hz, H-ar), 7.45 (4H, m, H-ar), 6.82 (1H, d, *J* = 16Hz, CH); ^{13}C NMR (100MHz, DMSO-d6): δ_C ppm, 115.7, 120.1, 123.2, 125.9, 128.3, 129.8, 1130.1, 130.5, 134.9, 140.4 (CH-aromatic), 141.4 & 122.1 (C=C), 164.5 (C=O). HRESIMS (positive mode) m/z calculated for $[C_{16}H_{12}NOF_3]^+$: 291, $[M+H]^+$; found: 292.0951.

N-(2,6-dimethylphenyl)cinnamamide (AC3)

Colorless powder (0.28 g, 46 %), **AC3** was prepared from the reaction of cinnamoyl chloride (0.40 g, 2.4 mmol) with 2,6-dimethylaniline (0.44 g, 3.6 mmol) in the same manner as described in Scheme 1, ^{1}H NMR (400MHz, DMSO-d_6): δ_H ppm, 9.52 (1H, s, NH) , 7.64 (2H, d, *J* = 7.0 Hz, H-aromatic), 7.57 (1H, d, *J* = 16.0 Hz, CH), 7.45 (3H, m, H-aromatic), 7.09 (3H, s, H-aromatic), 6.89 (1H, d, *J* = 16.0 Hz, CH), 2.00 (6H, s, CH_3); ^{13}C NMR (100MHz, DMSO-d_6): δ_C ppm, 18.6 (CH_3), 126.9, 128.1, 129.4, 130.1, 135.2, 135.5 (CH-aromatic), 163.9 (C=O), 140.1 & 122.2 (C=C). HRESIMS (positive mode) m/z calculated for $[C_{17}H_{17}NO]^+$: 251, $[M+H]^+$; found: 252.1391.

Synthesis of cinnamoyl ester derivatives (AC4-AC6)

Triethylamine (3 eq) was added into a stirred solution of 1 eq of alcohol (4-bromobenzyl alcohol, thymol, and eugenol) in anhydrous DCM (20 ml). The mixture was magnetically stirred for 0.5h at 0-5°C. Then, cinnamoyl chloride (1 eq) was slowly added to the mixture within a 15 min period. The reaction mixture was continued stirring for 0.5h at 0-5°C before being slowly removed to room temperature. Then, the stirring continued for another 24 h. The completion of the reaction was monitored by TLC. The solvent was evaporated by using a rotary evaporator and the compound was purified via column chromatography. Hexane/ethyl acetate was used as the eluent to afford the title ester products of **AC4**-**AC6**.

4-bromophenyl cinnamate (AC4)

Colorless powder (0.32 g, 43 %), **AC4** was prepared from the reaction of cinnamoyl chloride (0.40 g, 2.4 mmol) with 4-bromobenzyl alcohol (0.44 g, 2.4 mmol) in the same manner as described in Scheme 1, ^{1}H NMR (400MHz, DMSO-d_6): δ_H ppm, 7.69 (2H, m, H-aromatic) , 7.61 (1H, d, *J* = 16.0 Hz, H-aromatic), 7.52 (1H, d, *J* = 8.4 Hz, H-aromatic), 7.42 (3H, m, H-aromatic), 7.28 (1H, d, *J* = 8.4 Hz, CH), 6.55 (1H, d, *J* = 16.0 Hz, CH), 4.46 (1H, s, H-aromatic), 2.51 (1H, s, H-aromatic); ^{13}C NMR (100MHz, DMSO-d_6): δ_C ppm, 128.6, 129.0, 129.3, 130.7, 131.3, 134.7 (CH-aromatic). 142.4 &119.6 (C=C), 144.4 (C-O), 168.0 (C=O). HRESIMS (positive mode) m/z calculated for $[C_{15}H_{11}O_2Br]^+$: 303, $[M+H]^+$; found: 304.3010.

2-isopropyl-5-methylphenyl cinnamate (AC5)

Colorless powder (0.24 g, 35 %), **AC5** was prepared from the reaction of cinnamoyl chloride (0.40 g, 2.4 mmol) with thymol (0.36 g, 2.4 mmol) in the same manner as described in Scheme 1, ^{1}H NMR (400MHz, DMSO-d_6): δ_H ppm, 9.11 (1H, s, H-aromatic) , 7.92 (1H, d, *J* = 16.0 Hz, CH), 7.83 (3H, m, H-aromatic), 7.27-7.05 (2H, d, *J* = 8 Hz, H-aromatic), 6.97-6.61 (2H, m, H-aromatic), 6.56 (1H, d, *J* = 7.6 Hz, CH), 3.42 (3H, s, CH_3), 1.17 (6H, m, CH_3); ^{13}C NMR (100MHz, DMSO-d_6): δ_C ppm, 27.1-21.1 (CH_3), 123.2, 126.0, 126.8, 127.4, 129.1, 129.4, 135.7, 136.6, 137.2 (CH-aromatic), 146.8 & 116.0 (C=C), 148.1 (C-O), 165.6 (C=O). HRESIMS (positive mode) m/z calculated for $[C_{19}H_{20}O_2]^+$: 280, $[M+H]^+$; found: 281.1537.

4-allyl-2-methoxyphenyl cinnamate (AC6)

Colorless powder (0.33 g, 43 %), **AC6** was prepared from the reaction of cinnamoyl chloride (0.40 g, 2.4

mmol) with eugenol (0.39 g, 2.4 mmol) in the same manner as described in Scheme 1, ^{1}H NMR (400MHz, DMSO-d_6): δ_H ppm, 8.72 (1H, s, H-aromatic) , 7.54 (2H, m, H-aromatic), 7.48 (1H, d, J = 4.0 Hz, CH), 7.35 (3H, m, H-aromatic), 6.71 (2H, m, H-aromatic), 6.56 (1H, d, J = 4.0 Hz, CH), 3.74 (3H, s, CH_3) 3.25 (2H, d, J = 8.0 Hz, CH_2); ^{13}C NMR (100MHz, DMSO-d_6): δ_C ppm, 23.4 (CH_3), 115.9, 116.0, 123.3, 126.2, 148.3, 149.5 (CH-aromatic), 144.9 & 116.0 (C=C), 148.3 (C-O), 168.4 (C=O). HRESIMS (positive mode) m/z calculated for $[C_{18}H_{18}O_3]^+$: 282, $[M+H]^+$; found: 282.0887. Structures of synthesized cinnamic acid derivatives are shown in Figure 1.

Computational study

The synthesized derivatives (**AC1**-**AC6**) were simulated for molecular docking to investigate their binding affinity to the protein target of DENV type 2 (DENV-2) NS2B/NS3 protease, with Ser135, His51 and Asp75 as their catalytic triad amino acid residues. The virtual screening was carried out on the homology model of the DENV non-structural protein, NS2B/NS3pro developed by Wichapong et al. [16]. The DENV-2 NS2B/NS3pro model was built based on the DENV-2 complex cofactor-protease using the crystal structure of NS2B/NS3pro West Nile Virus (WNV) as the template. The protein structure was prepared as a macromolecule prior to docking using AutoDock version 1.5.6 package (www.autodock.scrips.edu). Briefly, the protein preparation was done by removing the native ligand, tetrapeptide inhibitor (Bz-Nle-Lys-Ar-H) and water molecules, the addition of polar hydrogen and Kollmann charges.

The 3D structures of all cinnamic acid derivatives were constructed and energetically optimized using ChemDraw Professional 16.0. The minimized structures were saved in sdf format before converted into pdb format using OpenBabel-3.1.1 software. The validation of the docking protocol was done by re-docking the inhibitor tetrapeptide (Bz-Nle-Lys-Ar-H) with the RMSD value not greater than 2.0 Å. The ligands were prepared by merging non-polar hydrogen and assigned a Gasteiger charge. The center of the grid box was employed around the protease active site at 23.038, 43.372, -0.316 in x, y, and z coordinates, respectively, with a box size of 60 × 60 × 60 dimensions and grid spacing 0.375 Å. The docking of ligands was run with the Lamarckian Genetics Algorithm (GA) search program applied to generate 100 runs. The binding modes of compounds were analyzed using Discovery Studio Client 2020 (www.accelrys.com). The identification of hit compound was identified based on the conformations with the ones of lowest free binding energy and of the most populated cluster.

Preparation of enzyme and ligand for docking

The structure of available DENV2, which is a complex of NS2B-NS3 protease (PDB code: 2FOM), is devoid of any ligand. Thus, to get an insight into the binding cavity we used coordinates of co-crystallized ligand from West Nile virus (PDB code: 2FP7) belonging to the same family as that of DENV and that shares the structural similarity of the catalytic triad. It is available in complex with the inhibitor tetrapeptide Bz-Nle-Lys-Arg-Arg-H. The structure of DENV2 complexed with the inhibitor tetrapeptide Bz-Nle- Lys-Arg-Arg-H was constructed by homology modelling method.

Results and Discussion

Chemistry

Six cinnamic acid derivatives (Figure 1) were successfully synthesized in moderate yield (35-61%) by modification of established methods [9]. The synthesis of the target compounds was straightforward, and the general synthetic pathway is illustrated in Scheme 1. Cinnamoyl chloride was reacted with various amines; anthranilic acid, 3-aminobenzotrifluoride and 2,6-dimethylaniline to produce the titled compounds of cinnamic acid amides (**AC1**, **AC2** and **AC3)**. For the synthesis of cinnamic acid ester derivatives, different alcohols; 4-bromobenzyl alcohol, thymol and eugenol were reacted with cinnamoyl chloride in DCM to afford the title compounds **AC4**, **AC5** and **AC6**. To optimize the reaction conditions, the polarity of the solvent medium from polar to non-polar was adjusted using DMSO, ethanol and tetrahydrofuran (THF) in the reaction of substituted cinnamoyl chloride with the corresponding alcohol and amine.

^{1}H and ^{13}C nuclear magnetic resonance (NMR) analysis confirmed the identity of all synthesized cinnamic acid derivatives. The presence of NH resonance peaks as observed in all three ^{1}H NMR spectra of **AC1**-**AC3** prove that the cinnamoyl amide derivatives were successfully synthesized. NH resonance which appears as singlet is found to be at the most downfield region (δ_H 11.38-9.52 ppm) for **AC1** to **AC3**. There is also a high-intensity singlet resonance in the upfield region at δ_H 2.17 ppm representing two methyl moieties presented in the **AC3** compound. For cinnamoyl ester derivatives, in the range of δ_H 7.41-7.70 ppm, multiple peaks can be observed in **AC4** indicating the presence of aromatic groups. Meanwhile, for **AC6** the peaks are in the range of δ_H 6.55-6.70 ppm. There are other high-intensity singlet resonances at δ_H 1.13-2.29 ppm and at δ_H 3.73 ppm respectively, representing methyl moieties presented in both compounds **AC5** and **AC6**. The alkene groups for all three compounds of **AC4**-**AC6** can be observed in the peak range of δ_H 6.51-6.57 ppm.

The resonance of the C=O group was clearly observed for all synthesized compounds at δ 169.9-163.8 ppm. The alkene group is also presented in all compounds which are in the range of δ 146.8-116.0 ppm. For the aromatic ring, the resonance carbon was found at the range between δ 129.8-123.3 ppm. Furthermore, the resonance for CH_3 moieties can also be observed for the compounds of **AC3**, **AC5** and **AC6** which are in the region δ 27.1-18.7 ppm.

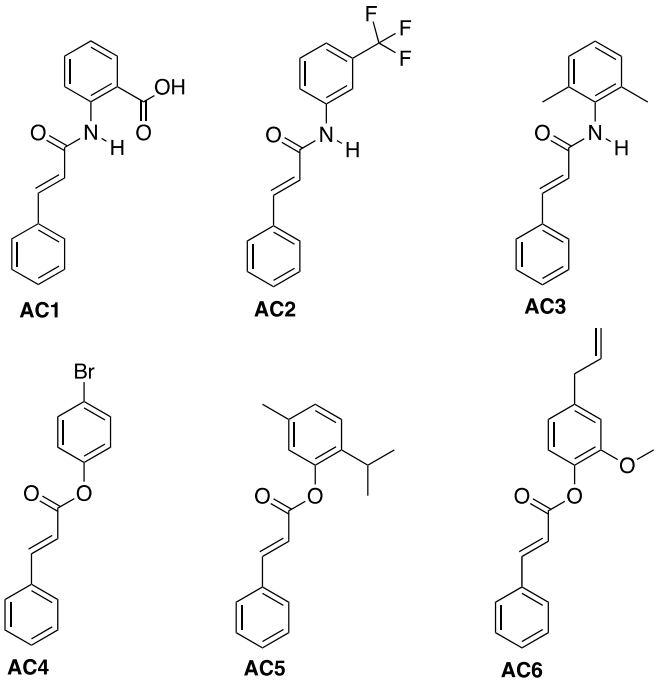

Figure 1. Structure of synthesized cinnamic acid derivatives

Molecular docking

The in-silico studies were conducted to investigate the binding interactions of the synthesized compounds **AC1**-**AC6** towards DENV-2 NS2B/NS3 protease and search for the best orientation of ligand-protease complex with the lowest free energy of binding (FEB). This step serves as a good tool to predict and match the desired binding site, understanding possible conformation of the compounds and further clarifies the binding interactions in the binding pocket [10].

DENV is a single-stranded RNA genome that encodes a single open reading frame (5-C-prM-E-NS1-NS2A-NS2B-NS3-NS4A-NS4B-NS5-3) with three structural and seven non-structural proteins [11]. The N-terminal of NS3 is a trypsin-like serine protease, which when combined with its co-factor can cleave the viral polyprotein [12]. Disruption of NS2B-NS3 protease inhibits viral replication [13]. This poses NS2B-NS3 protease of DENV-2 as a promising target for antiviral drug design [14].

The three catalytic triad amino acid residues were located in NS3 serine proteases namely His51, Asp75 and Ser135. The NS2B protease acted as an NS3 serine protease co-factor for an optimal catalytic activity [15]. The homology protein crystal structure generated by Wichapong et al., (2010) was used due to the lack of DENV-2 NS2B/NS3 serine protease inhibitor-bound 3D structures. Moreover, some of the protease database structures were found to have missing amino acid residues [16].

The Lamarckian genetic algorithm was employed in AutoDock version 1.5.6 to determine the binding modes and compounds conformation towards DENV-2 NS2B/NS3 protease homology protein crystal structure. In the preparation for docking simulation, only protease was retained as a part of the macromolecule file, while the Bz-Nle-Lys-Arg-Arg-H was extracted and saved as a positive control ligand. The ligand was extracted and re-docked into the binding site to evaluate the success of the docking method in reproducing the experimentally known complex.

The covalent map parameter was used during positive control docking simulation to constrain the molecular geometry of the peptide inhibitor. After that, all the synthesized compounds were docked with Wichapong et al., [16] homology crystal structure using the same parameter. The re-docked was carried out successfully with the root mean square deviation (RMSD) value of 1.23 Å. Henever et al. stated that the programs that able to poses the RMSD value in the range of 1.5-2 Å, depending on the ligand size, are considered to have performed successfully [17].

The synthesized compounds, **AC1**-**AC6** fit into the allosteric pocket of NS2B/NS3 serine protease. The free energy of binding (FEB) obtained was tabulated in Table 1. Figure 2 shows the overlay docked conformation of the cinnamic acid derivatives between the Wichapong et al. [16] homology model and Bz-Nle-Lys-Arg-Arg-H referenced ligand. The image was generated using Discovery Studio Visualizer 4.5.

The detailed ligand-binding site interaction in 2D structural views of all the compounds are shown in Figure 3 below. Compound **AC5** shows the lowest free energy of binding (-6.53 kcal mol^{-1}) indicating the highest binding affinity towards NS2B/NS3 protease of DENV-2 compared to the other five compounds [18]. Figure 3 also shows the poses and non-covalent interactions involved between the ligands and the protease-binding site. This compound showed a few van der Waals interaction, one C-H bonding interaction, one π-cation interaction, one π-lone pair interaction, one π-π T-shaped interaction, and two π-alkyl interactions with the amino acid residue in the DENV-2 NS2B/NS3 protease.

The presence of the aromatic group in the synthesized cinnamic acid derivatives enhances the possibilities of van der Waals interaction. Hence, we can see this interaction in all the synthesized compounds of **AC1**-**AC6**. Individually, van der Waals interaction was also observed in compound **AC5**, involving Ser135 (one of the catalytic triads) and other residues namely Asp129, Ser131, Gly151 and Thr134. Pi interactions such as π-π T-shaped interaction and π-lone pair interaction were also observed between the ester moiety of the synthesized compound with Tyr161 and Phe130, respectively. Meanwhile, another aromatic ring at cinnamic moiety of compound **AC5** appeared to have a π-cation interaction with the His51 (from the catalytic triad) and π-alkyl interactions with Val52. The π-cation interaction with the His51 suggested that the DENV-2 NS2B/NS3 replication was affected as His51 is one of the catalytic triads of NS2B required for replication activities [19].

Table 1. The free energy of binding (FEB) of compounds **AC1-AC6**

Compound	**FEB (kcal mol^{-1})**
Positive Control (peptide inhibitor)	-6.58
AC1	-6.11
AC2	-6.36
AC3	-6.45
AC4	-6.33
AC5	-6.53
AC6	-6.50

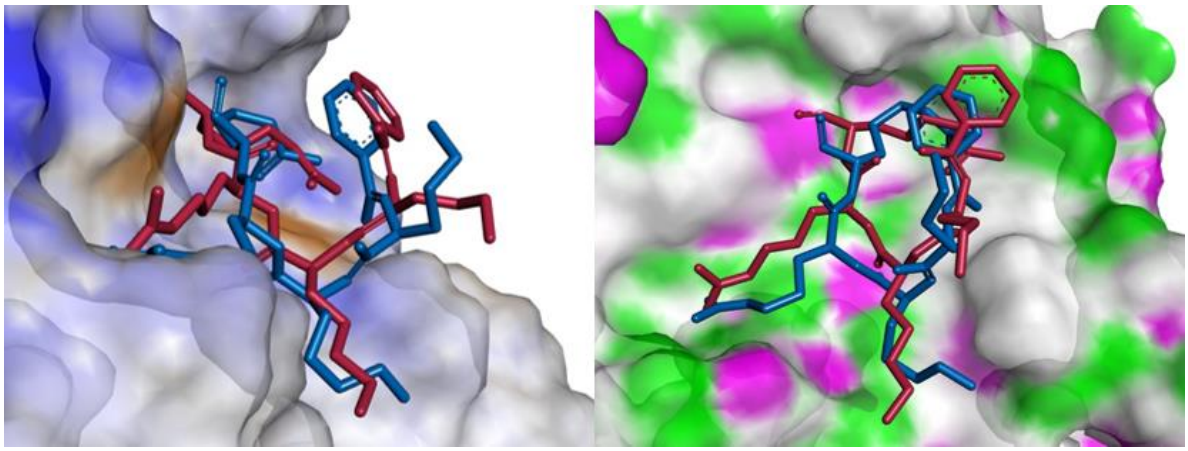

Figure 2. The overlay docked conformation of the cinnamic acid between the Wichapong et al. [16] homology model and Bz-Nle-Lys-Arg-Arg-H referenced ligand (red: original ligand conformation, blue: docked ligand conformation).

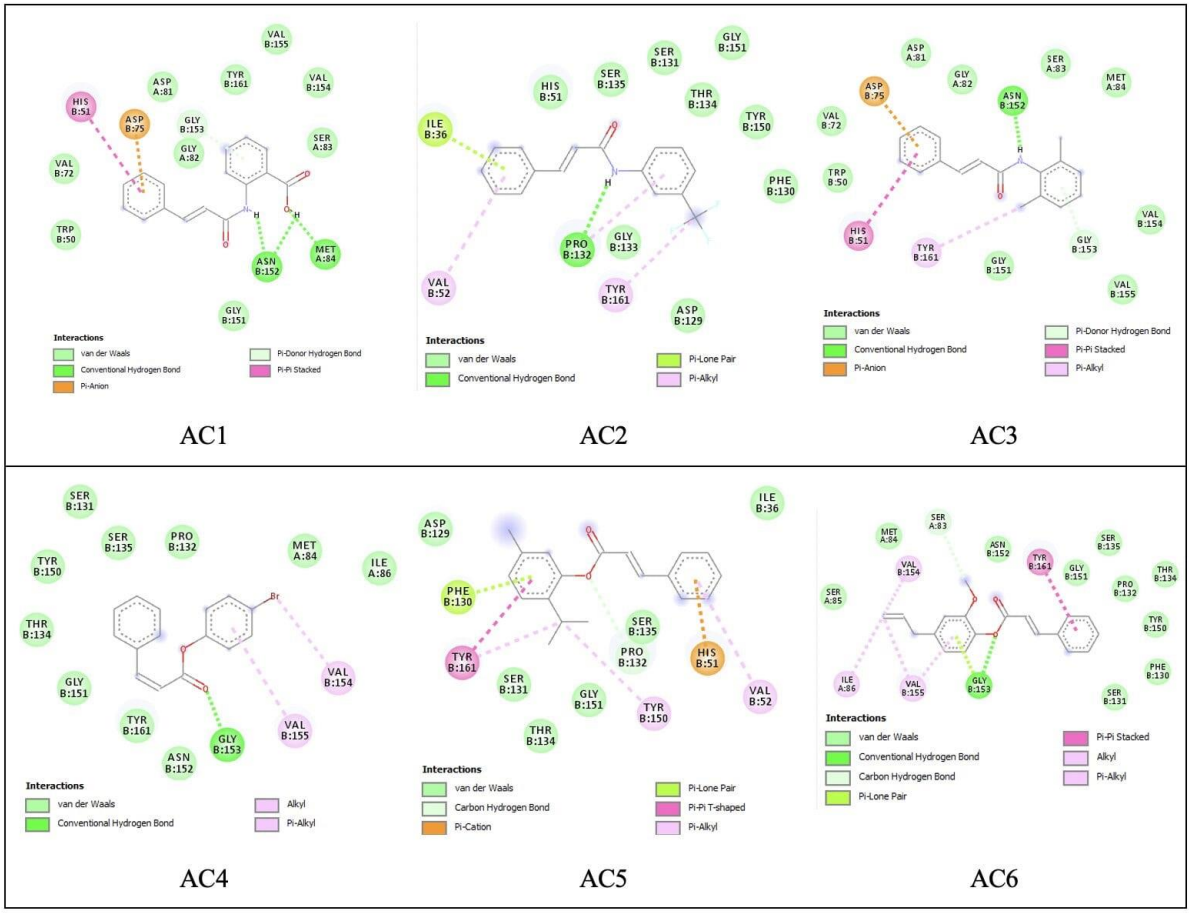

Figure 3. The 2D structural views of ligand-binding site interactions for synthesized compounds AC1-AC5

Conclusion

The present work has demonstrated that six cinnamic acid derivatives were successfully synthesized by the reaction of cinnamoyl chloride with various amines and alcohols. All synthesized compounds were characterized by ^{1}H and ^{13}C-NMR, and mass spectrometry. The significant molecular interaction between the synthesized compounds and DENV2 NS2B/NS3 protease were revealed by molecular studies indicating their potential activity as a protease inhibitor. The compound **AC5** is predicted to have a higher DENV-2 NS2B/NS3 protease inhibitor as it has the highest binding affinity, with a significant van der Waals force and pi interactions between the synthesized compound and the amino acid residues. Further verification studies such as *in-vitro*, toxicity analysis, and *in-vivo* analysis are required for identifying the possibilities of the cinnamic acid derivatives to be a lead molecule for anti-dengue drug development.

Acknowledgement

The authors would like to acknowledge the financial support from Ministry of Higher Education, Malaysia for Fundamental Research Grant Scheme FRGS 59580 (FRGS/1/2019/STG01/UMT/02/4). A sincere thanks to the Faculty of Science and Marine Environment, Universiti Malaysia Terengganu (UMT) for providing the space and facilities. We also would like to thank the Institute of Marine Biotechnology, Universiti Malaysia Terengganu for NMR services and analysis.

References

1. Martin-Tanguy, J., Cabanne, F., Perdrizet, E. and Martin, C. (1978). The distribution of hydroxycinnamic acid amides in flowering plants. *Phytochemistry*, 17(11): 1927-1928.
2. Mohammadzadeh, S., Shariatpanahi, M., Hamedi, M., Ahmadkhaniha, R., Samadi, N. and Ostad, S. N. (2007). Chemical composition, oral toxicity and antimicrobial activity of Iranian propolis. *Food Chemistry*, 103(4): 1097-1103.
3. Clifford, M. N. (1999). Chlorogenic acids and other cinnamates – nature, occurrence and dietary burden. *Journal of the Science of Food and Agriculture*, 79(3): 362-372.
4. De, P., Baltas, M. and Bedos-Belval, F. (2011). Cinnamic acid derivatives as anticancer agents-a review. *Current Medicinal Chemistry*, 18(11): 1672-1703.
5. Sova, M. (2012). Antioxidant and antimicrobial activities of cinnamic acid derivatives. *Mini-Reviews in Medicinal Chemistry*, 12(8): 749-767.
6. Amano, R., Yamashita, A., Kasai, H., Hori, T., Miyasato, S., Saito, S., Yokoe, H., Takahashi, K., Tanaka, T., Otoguro, T., Maekawa, S., Enomoto, N., Tsubuki, M. and Moriishi, K. (2017). Cinnamic acid derivatives inhibit hepatitis C virus replication via the induction of oxidative stress. *Antiviral Research*, 145: 123-130.
7. Chen, Y., Li, Z., Pan, P., Lao, Z., Xu, J., Li, Z., Zhan, S., Liu, X., Wu, Y., Wang, W. and Li, G. (2021). Cinnamic acid inhibits Zika virus by inhibiting RdRp activity. *Antiviral Research*, 192(11): 105117.
8. Wang, Y., He, F., Wu, S., Luo, Y., Wu, R., Hu, D. and Song, B. (2020). Design, synthesis, anti-TMV activity, and preliminary mechanism of cinnamic acid derivatives containing dithioacetal moiety. *Pesticide Biochemistry and Physiology*, 164(1): 115-121.
9. Abdul Rahim, N. H. C., Asari, A., Ismail, N. and Osman, H. (2017). Synthesis and antibacterial study of eugenol derivatives. *Asian Journal of Chemistry*, 29(1): 22-26.
10. Grinter, S. Z. and Zou, X. (2014). Challenges, applications, and recent advances of protein-ligand docking in structure-based drug design. *Molecules*, 19(7): 10150-10176.
11. Leung, D., Schroder, K., White, H., Fang, N. X., Stoermer, M. J., Abbenante, G., Martin, J. L., Young, P. R. and Fairlie, D. P. (2001). Activity of recombinant Dengue 2 Virus NS3 protease in the presence of a truncated NS2B co-factor, small peptide substrates, and inhibitors. *Journal of Biological Chemistry*, 276(49): 45762-45771.
12. Chiu, M. W., Shih, H. M., Yang, T. H. and Yang, Y. L. (2007). The type 2 dengue virus envelope protein interacts with small ubiquitin-like modifier-1 (SUMO-1) conjugating enzyme 9 (Ubc9). *Journal of Biomedical Science*, 14(3): 429-444.
13. Chen, W. N., Loscha, K. V., Nitsche, C., Graham, B. and Otting, G. (2014). The dengue virus NS2B-NS3 protease retains the closed conformation in the complex with BPTI. *FEBS Letters*, 588(14): 2206-2211.
14. Tomlinson, S., Malmstrom, R. and Watowich, S. (2012). New approaches to structure-based discovery of dengue protease inhibitors. *Infectious Disorders - Drug Targets*, 9(3): 327-343.
15. Preugschat, F., Yao, C. W. and Strauss, J. H. (1990). In vitro processing of dengue virus type 2 nonstructural proteins NS2A, NS2B, and NS3. *Journal of Virology*, 64(9): 4364-4374.
16. Wichapong, K., Pianwanit, S., Sippl, W. and Kokpol, S. (2010). Homology modeling and molecular dynamics simulations of Dengue virus NS2B/NS3 protease: Insight into molecular interaction. *Journal of Molecular Recognition*, *23*(3): 283-300.
17. Hevener, K., Zhao, W., Ball, D., Babaoglu, K., Qi, J., White, S. and Lee, R. (2009). Validation of molecular docking programs for virtual screening against dihydropteroate synthase. *Journal of Chemical Information and Modeling,* 49(2): 444-460.
18. Datar, P. A and Jadhav, S. R. (2015). Design and synthesis of pyrazole-3-one derivatives as hypoglycaemic agents. *International Journal of Medicinal Chemistry*, 2015: 1-10.

19. Noble, C. G., Seh, C. C., Chao, A. T. and Shi, P. Y. (2012). Ligand-bound structures of the dengue virus protease reveal the active conformation. *Journal of Virology*, 86(1): 438-446.

Malaysian Journal of Analytical Sciences (MJAS)
Published by Malaysian Analytical Sciences Society

EFFECT OF DEEP EUTECTIC SOLVENT ON TENSILE PROPERTIES AND BIODEGRADATION OF PECTIN WITH EGGSHELL BIOPLASTIC

(Kesan Pelarut Eutektik kepada Sifat Tensil dan Biodegradasi Bioplastik Pektin dengan Cangkang Telur)

Non Daina Masdar, Rizana Yusof *, Nur Amni Ramzani

Faculty of Applied Sciences,
Universiti Teknologi MARA, Perlis Branch, Arau Campus, 02600 Arau, Perlis, Malaysia

**Corresponding author: rizana@uitm.edu.my*

Received: 12 September 2021; Accepted: 21 December 2021; Published: 25 February 2022

Abstract

Pectin has excellent potential as a main source of bioplastic due to its biodegradability. However, the neat pectin-based film has poor chemo-physical properties and low mechanical performance. In this study, the pectin-based film is successfully modified by adding eggshell and deep eutectic solvent (DES), comprising choline chloride and malonic acid, as a filler and plasticiser to enhance the performance of bioplastic. Five pectin-based bioplastics were prepared: pectin/eggshell (without DES) and pectin/eggshell with each 1%, 2%, 3%, and 4% of DES. The bioplastics were characterised by the Fourier-transform infrared (FTIR) spectroscopy and inverted camera analysis. The presence of filler and the effect of different DES concentrations were studied based on mechanical properties, biodegradability, and water uptake. The results showed that the addition of different percentages of DES had decreased the tensile strength and increased the flexibility of the bioplastic. Biodegradability testing using compost soil demonstrated an increased degradation rate when a high concentration of DES (4%) was added. The DES of choline chloride and malonic acid shows high potential as a plasticiser in pectin/eggshell bioplastic.

Keywords: pectin, plasticiser, deep eutectic solvent, eggshell filler, bioplastic

Abstrak

Pektin berpotensi sebagai sumber utama bioplastik kerana sifat biodegradasinya. Walau bagaimanapun, bioplastik yang hanya berasaskan pektin sahaja mempunyai sifat kimia-fizikal yang lemah dan prestasi mekanikal yang rendah. Dalam kajian ini, filem bioplastik berdasarkan pektin telah berjaya diubah suai dengan menambahkan cangkang telur dan pelarut eutektik (DES), yang mengandungi kolin klorida dan asid malonik, sebagai pengisi dan pemplastik yang bertujuan untuk meningkatkan prestasi bioplastik. Lima bioplastik berasaskan pektin disediakan: pektin/cangkang telur (tanpa DES) dan pektin/cangkang telur dengan masing-masing 1%, 2%, 3%, dan 4% DES. Bioplastik yand dihasilkan dicirikan secara fizik menggunakan spektroskopi Fourier-penukaran inframerah (FTIR) dan analisis kamera terbalik. Kehadiran pengisi dan kesan kepekatan DES yang berbeza dikaji berdasarkan sifat mekanik, kebolehbiodegradasian, dan pengambilan air. Hasilnya menunjukkan bahawa penambahan peratus DES yang berbeza telah menurunkan kekuatan dan meningkatkan fleksibiliti bioplastik. Ujian biodegradasi menggunakan tanah kompos menunjukkan peningkatan kadar degradasi apabila peratus DES yang tinggi (4%) digunakan. DES bagi kolin klorida dan asid malonik menunjukkan potensi yang tinggi sebagai pemplastik di dalam bioplastik pektin/cangkang telur.

Kata kunci: pektin, pemplastik, pelarut eutektik, pengisi cangkang telur, bioplastik

Introduction

Petrochemical plastic materials are important in our daily lives. However, the vast amounts of plastic waste materials generated contribute to worldwide environmental concerns [1]. About 34 million tons of plastic trash is produced each year, with 93% ending in landfills and the seas. Furthermore, the disposal of non-biodegradable plastic leads to significant global warming, ozone depletion, eco-toxicity, eutrophication, and long-lasting decomposition [2]. Improper management of plastic causes a severe effect on the ecosystem. Thus, biodegradable plastic is the best alternative to reduce plastic waste, save the environment and sustain green global issues. The use of natural sources, such as cellulose, pectin, starch, chitosan, and alginate as food packaging materials has slowly replaced petrochemical plastics [3, 4, 5]. Pectin is a polysaccharide found abundantly in fruits like apple, orange, lemon, mango, grapes, and peach [1, 6]. It is very compatible as a biodegradable and edible biopolymer for food packaging. However, due to its poor chemo-physical properties and low mechanical performance, the pectin biofilm must be improvised by adding a plasticiser and organic filler accordingly to meet the food packaging requirements [1]. Like most polysaccharides, pectin is glassy at room temperature, causing defects such as cracking or curling in a film due to its shrinking, followed by water evaporation or rapid drying [7]. Gennadios et al. [8] asserted that these films are often fragile and rigid due to extensive interactions between the polymer molecules. Therefore, a filler is commonly used to improve the rigidity and strength of the biofilm [9, 10]. A natural bio filler such as eggshell has grown popular since they are environmentally friendly, renewable, cheap, and abundantly available [11, 12].

However, a biofilm made of pectin with eggshells is mostly brittle. A plasticiser is a useful compound in minimising film brittleness by reducing intermolecular forces among polymer chains, increasing their mobility, and improving mechanical properties [13] by holding the polymer bonds together [14]. Deep eutectic solvent (DES) is a new category of plasticiser that has been competently tested for polysaccharide biofilms in various methods [15, 16, 17, 18]. The two most common plasticisers in the polymer industry are *o*-hydroxyphenyl (HBP) and di-2-ethylhexyl phthalate (DEHP), known for their ability to disrupt the endocrine system, with carcinogenic and mutagenic properties [19]. Phthalate is not bonded to plastic; therefore, it will easily leak out into the human body, causing major health effects [20]. According to Mekonnen et al. [21], an ideal plasticiser significantly reduces the glass transition temperature (T_g), biodegradable, non-volatile, non-toxic, and have minimal leaching or migration properties. DES, comprising two self-associating components, met the requirements as a plasticiser in bioplastic [22, 23]. The ability of DES to swell inside biopolymers has enabled bioplastic plasticisation [19], as well as improved thermal stability and decreased the glass transition temperature (T_g) of bioplastics [24]. Previously, Shafie et al. [17] have successfully used DES as a plasticiser in pectin extracted from *Momordica charantia* or known as *peria*. According to their findings, DES caused different degrees of plasticisation via hydrogen bonds and ionic bonds with the polymer chains, which improved thermal stability, tensile properties, percentage of moisture absorption, and water vapour transmission rate of bioplastic. However, the strength of biofilm is reduced without fillers. Hence, this study investigates the compatibility of pectin/DES with eggshells as a natural filler. The pectin/eggshell bioplastic was developed with different concentrations of DES (choline chloride: malonic acid) to analyse bioplastic performance based on tensile strength, biodegradability, and water uptake.

Materials and Methods

Material and reagents

The commercial pectin from citrus was purchased from Sigma Aldrich, Malaysia. The choline chloride (ChCl), malonic acid, and sodium hypochlorite were purchased from Acros, Belgium, with 99% purity. All chemicals used are of analytical grade. The DES was prepared as

suggested by Abbot et al. [15], with a 1:1 ratio of ChCl and malonic acid. The mixture was magnetically stirred at 80 °C until the colourless liquid was formed and maintained as a liquid after 24 hours at room temperature. The eggshell powdered filler was prepared according to Kasmuri et al. [14]. The eggshells were crushed using a mortar and pestle and placed in a beaker. Sodium hypochlorite was added until all the eggshells were soaked and stirred using a glass rod until heat and bubble were released. The beaker was covered using aluminium foil and left for 24 hours before filtering and washing using distilled water. The dried eggshell sample was then dried in the oven and left to cool at room temperature. The eggshell sample was then ground into powder to obtain the size of 58 μm.

Preparation of pectin-based bioplastic

The pectin-based bioplastic was prepared according to Cataldo et al. [25] and Almeida et al. [26]. A volume of 3% (w/v) aqueous pectin was stirred at 70 °C until completely dissolved. About 1% to 4% wt of DES was added to the pectin solution and stirred to homogenise and form film-forming solutions. Approximately 3% wt of eggshell filler was added until completely dissolved. The well-dispersed aqueous dispersions were poured into Petri dishes and dried in the oven at 50 °C for 24 hours. The control was prepared without DES, i.e., 3% of aqueous pectin with 3% wt of eggshell as the filler.

Characterisation of DES

The thickness of the bioplastic was measured using a Digimatic thickness gauge (Model 547-301, Mitutoyo). At least five measurements were performed at different positions for each bioplastic, and the average thickness was calculated. The mechanical properties, including tensile strength, Young's modulus, and elongation at break, were determined using the Instron Universal Testing Instrument (Instron 3365, Instron, USA) equipped with a 1 kN load cell. The sample was cut into a rectangular shape with the size of 7 cm × 1 cm. The initial grip separation was 50 mm, with a crosshead speed of 5 mm min^{-1}. At least five replicates were performed for each film formulation. The soil burial test was conducted according to the ASTM D6003-96 standard method to determine the ability of bioplastics to degrade in compost soil. The initial mass of each bioplastic was weighed and recorded. The bioplastic was buried in compost soil, and the mass was recorded daily until fully degraded. The W_o (g) is the average of the initial bioplastic weight before being buried in soil samples, and the W_t (g) is the average weight of bioplastic at the time of measurement.

The following equation was used to calculate the weight loss of the sample:

$$\text{Weight Loss}(\%) = \frac{W_o - W_t}{W_o} \times 100 \quad (1)$$

The synthetic seawater was prepared by dissolving 35 g of sodium chloride in a total mass of 1000 g distilled water in a beaker. The bioplastic with the size of 1.5 cm × 2 cm was weighed before being immersed in the synthetic seawater. The samples were dried and reweighed at three days intervals. The percentage weight loss of the bioplastic was calculated using the following formula, where M_0 is the average initial mass of the sample, and M_1 is the average residual mass of the bioplastic after the test.

$$\text{Weight Loss } (\%) = \frac{M_0 - M_1}{M_0} \times 100 \quad (2)$$

The water uptake method was conducted according to Zárate-Ramírez et al. [27]. A 1.5 cm × 2 cm sample was cut, dried in the oven at 50 °C for 24 hours, and weighed as W_o. The sample was then immersed in distilled water for 10 seconds at room temperature and reweighed as W_t. The experiment was conducted in triplicate. Water uptake was calculated using the following equation:

$$\text{Water Uptake } (\%) = \frac{W_t - W_o}{W_o} \times 100 \quad (3)$$

Results and Discussion

FTIR analysis was carried out to analyse the functional group present in pure pectin, eggshell, and pectin/eggshell (P-E) composites (Figure 1). The O-H stretching, C=O stretching, and C-O stretching at 3440 cm^{-1}, 1746 cm^{-1}, and 1018 cm^{-1} characterise the structure of pectin.

According to Bichara et al. [28], the main peaks observed at 3436 cm^{-1}, 1743-1640 cm^{-1}, and 1103-1146 cm^{-1} represented the O-H, C=O, and C-O glycosidic bonds in pectin. Meanwhile, the pure eggshell showed peaks at 712, 876, and 1425 cm^{-1}, as similarly reported by Li et al. [29], who characterised calcite by an in-plane bending, out-of-plane bending, and asymmetric CO_3^{2-} stretching at the peaks of 713, 875, and 1424 cm^{-1}. Similar findings were also reported by Siriprom et al. [30] and Pradhan et al. [31]. The combination of pectin with eggshell in the composite film shows all peaks in individual pectin and eggshell. However, a C-O peak from CO_3^{2-} at 1424 cm^{-1} disappeared in the composite as the formation of new bonding is expected between the calcite of eggshell with the glycosidic bond of pectin. The pectin/eggshell composite is enhanced with the addition of DES as a plasticiser. Figure 1(b) shows the FTIR analysis on the increasing concentration of DES from 1% to 4% on the pectin/eggshell composite. As observed, the intensity peaks at 3350 cm^{-1} and 1000 cm^{-1} are slightly decreased when the concentration of DES increases. The IR spectra of all films are dominated by vibration, related to the presence of the pectin compound. A similar result was also reported by Gouveia et al. [32], indicating the interaction between pectin and the additives.

The images of bioplastic sample surfaces were analysed using an Olympus CKX53 inverted microscope (Figure 2). The bubbles trapped in the pectin/eggshell biofilm surfaces are due to the agitation process and the addition of the eggshell powder with pectin solution during sample preparation. The number of bubbles is reduced with the addition of a high percentage of DES, as shown in Figures 2(b) to 2(e). In general, it is also observed that the solubility of eggshell powder increases with the concentration of DES, especially at 3% to 4% of DES (Figure 2(d) and 2(e)). Kong et al. [33] stated that the addition of plasticiser might modify polymer chain intermolecular forces and reduce viscosity in the system. Thus, the DES enhances the dispersion of the added eggshells within the polymer matrices, which is expected to affect the mechanical performance of the bioplastics.

The thickness of the biofilms is an important characteristic that determines its purpose and function. A thin biofilm can lead to fragility and easily be torn, while a very thick biofilm has less flexibility. Table 1 shows the thickness of the pectin/eggshell biofilms. According to ASTM D885, the standard maximum thickness for plastic is 1 mm. Meanwhile, the pectin/eggshell bioplastic is the thinnest bioplastic with 0.0985 ± 0.01 mm. The thickness of bioplastic increases as the plasticiser is added from 1% to 4%, i.e., 0.0991 ± 0.01mm to 0.2687 ± 0.06 mm. The film tends to be thicker as the amount of DES increases. The result is congruent with Esposito et al. [34], which showed that the pectin film thickness increased as polyamines were added as a new cationic plasticiser for pectin-based edible (PEC) films. In this work, the thickness of the PEC films is doubled in the absence of glycerol.

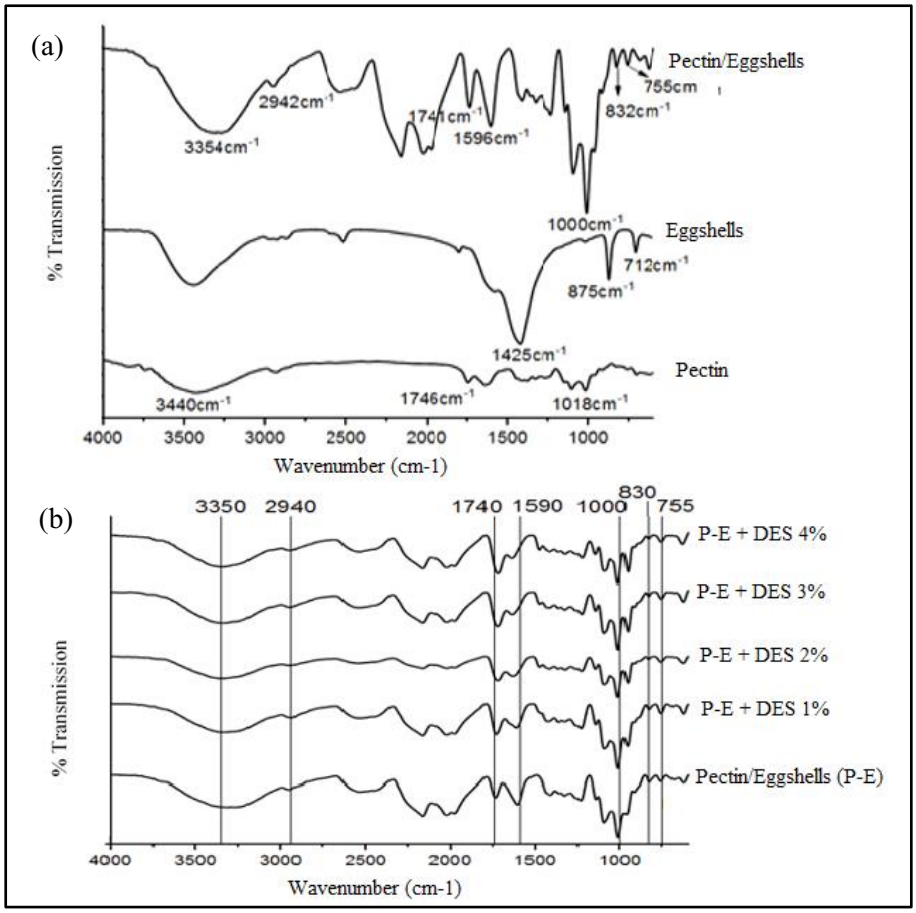

Figure 1. FTIR spectrum for (a) Pectin/Eggshell composite, pure eggshell, and pure pectin (b) Pectin/Eggshell composite with different DES concentrations

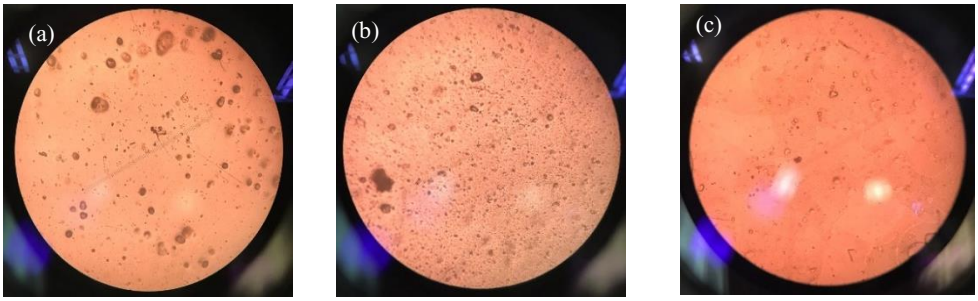

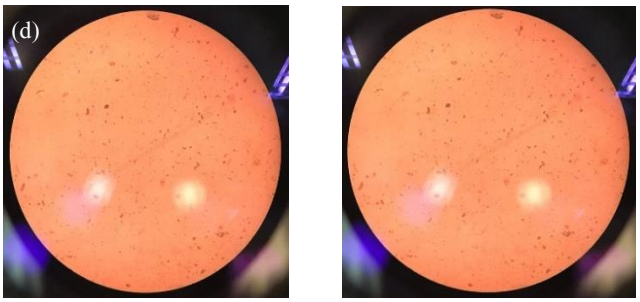

Figure 2. Bioplastic surface images in 4× magnification of (a) Pectin/Eggshell; (b) Pectin/Eggshell in DES 1%; (c) Pectin/Eggshell DES 2%; (d) Pectin/Eggshell DES 3%; and (e) Pectin/Eggshell DES 4%

Table 1. Thickness of pectin-based bioplastic

Sample Bioplastic	Thickness (mm)
Pectin/Eggshell (P-E)	0.0985 ± 0.01
P-E + DES 1%	0.0991 ± 0.01
P-E + DES 2%	0.1448 ± 0.02
P-E + DES 3%	0.2146 ± 0.02
P-E + DES 4%	0.2687 ± 0.06

The mechanical properties of the prepared bioplastic in 1% to 4% DES concentration were determined via tensile testing analysis. Figures 3(a-c) show the trend of tensile stress, strain, and modulus of the bioplastic at different DES concentrations. The results indicated that the pectin/eggshell bioplastic is the most rigid with high tensile stress at 33.30 MPa. As a filler, eggshells fill the space in the pectin polymer and increase the stiffness of bioplastic. The tensile strain of pectin/eggshell bioplastic is observed at 1.87%, with the modulus reaching 2754.00 MPa. A study by Kong et al. [33] stated that the addition of eggshell powder to polylactic acid (PLA) yielded a more rigid plastic than PLA only. The PLA/eggshell had superior tensile stress with 200% strain at break and a high modulus. Hence, a similar effect is observed in this study, where the addition of eggshells resulted in substantial improvement in the tensile strength and modulus of the pectin/eggshell bioplastic.

The DES was later added to pectin/eggshell as a plasticiser. The tensile stress and modulus are reduced from 33.30 to 16.47 MPa and 2754.00 to 774.00 MPa, with the addition of 1% DES to the pectin/eggshell. However, the addition of 1% DES caused the tensile strain to increase from 1.87% to 14.32%. The continual addition of DES from 1% to 3% has decreased the tensile stress from 16.47 to 2.18 MPa. A similar effect was observed on the modulus, which is reduced from 774.00 to 14.00 MPa with 1% to 3% DES. The opposite happened to tensile strain, which increased from 14.32% to 31.95% DES. The addition of plasticiser creates substantial intermolecular interaction between the polymer chains, preventing them from gathering close to each other, restricting the molecular chains to compact and cohesive strength in the sample. Thus, it can be concluded that DES has reduced the tensile stress of pectin/eggshell by subsequently weakening the hydrogen bonds between the pectin chains. Eggshells that caused the films to break after a certain force is applied. Muscat et al. [35], who previously used starch to make a film, stated that plasticisers diminish the strong intramolecular attraction between the starch chains. A similar

observation by Sanyang et al. [36] found that the tensile strength decreases with an increasing percentage of mixture glycerol/sorbitol/glycerol-sorbitol as the plasticiser increased from 15% to 45% on sugar palm starch films. However, the tensile strain value remains at the same range with 4% DES, which is 2.26 MPa. Similar results are observed for tensile strain and tensile modulus, i.e., constant at the addition of 4% DES. The addition of plasticiser did not significantly change the properties of bioplastic after 3%, indicating that at 3%, the liquid has swelled and filled up the free volume within polymer chains to prevent intermolecular interaction. Hence, the study only conducted only up to 4% of DES.

The biodegradability test was carried out to determine the weight loss of the pectin/eggshell after ten days in soil. The biodegradation process mainly depends on the moisture content and the presence of microorganisms in the ground. Figure 4 indicates the biodegradability behaviour in the weight loss of the bioplastic at a different DES percentage. All bioplastics show a continuous weight loss increase, with the bioplastic with 4% DES fully degraded (100%) on the third day and bioplastic with 1%, 2%, and 3% DES fully degraded on the fifth day. The pectin/eggshell composite without DES showed the highest percentage loss on the first day, but only 93% degraded on the fifth day and remained around 97% on the tenth day of the test. The higher percentage of DES concentration in bioplastic, led to a higher weight loss of the bioplastic. The bioplastic at 4% DES degrades faster than lower DES concentration. Kasmuri et al. [14] stated that the presence of the eggshell filler reduced the biodegradability rate since 95% of the eggshell is made up of calcium carbonate compounds, which mostly remained in the soil after the bioplastic had degraded. However, as proven by the tests, DES enhanced the biodegradability properties of bioplastic.

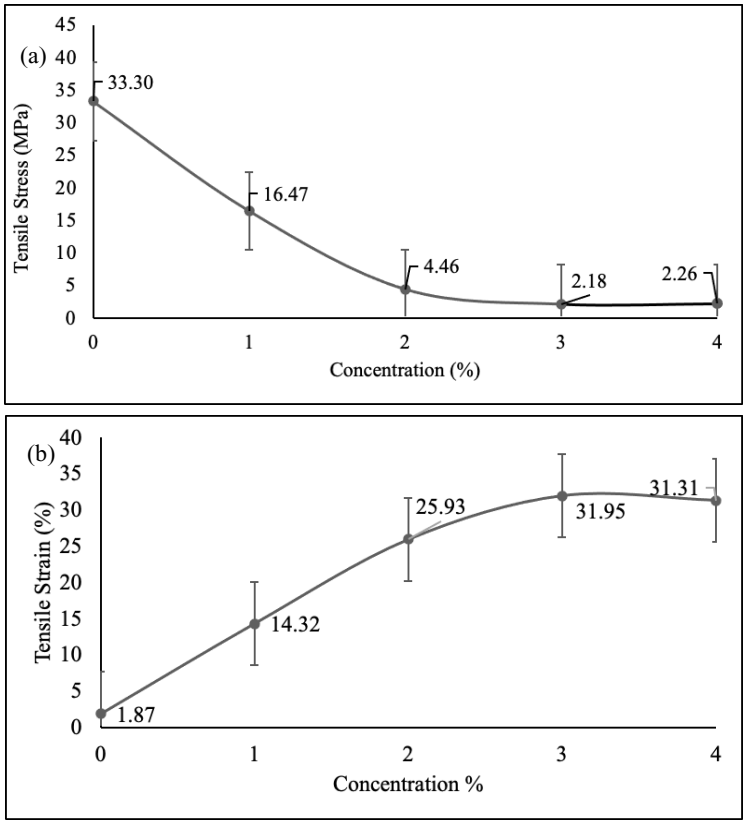

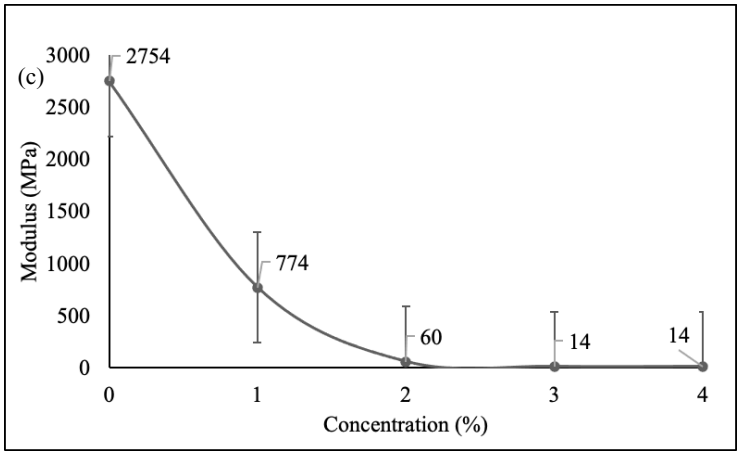

Figure 3. The properties of bioplastic in (a) tensile stress; (b) tensile strain and (c) modulus

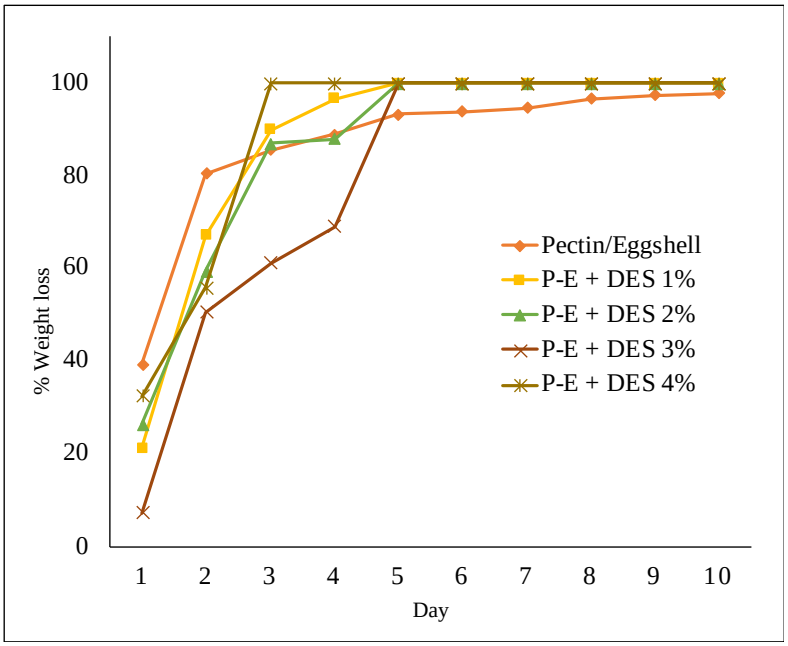

Figure 4. The percentage of weight loss of bioplastic in 10 days of biodegradability test in soil

Another biodegradability test was conducted in synthetic seawater. All bioplastics immediately swelled and curved when immersed in seawater. After one day in seawater, the pectin/eggshell bioplastic was fully degraded, but not the pectin/eggshell/DES bioplastics. Figure 5 shows the degradation of bioplastics in seawater. The result is contrary to the biodegradability test conducted in soil. In seawater, the bioplastic with a high DES concentration takes longer to degrade than those without DES. The inclusion of electrolytes from NaCl in synthetic seawater influenced bioplastic breakdown. According to Trindade et al. [37], ionic liquid shows the effect of salting out in salt solution. The same effect might be seen in the biofilm

containing DES. The added salt (NaCl) might compete with the ions in DES, causing the migration of NaCl molecules from the DES ions, decreasing the hydration and solubility of bioplastic-containing DES.

The analysis of water uptake was performed to measure the ability of bioplastic to absorb water with the addition of different concentrations (%) of DES. Figure 6 shows that the highest percentage of water uptake is at 1% concentration of DES, with 85% of water uptake. According to Suppakul et al. [38], the presence of hydroxyl group in plasticiser is strongly interacted with water molecules by forming hydrogen bonds. DES (choline chloride: malonic acid) consists of O-H bonds that interact directly with water, increasing the volume of the water uptake. However, when the percentage concentration of DES is more than 1%, the water absorption is reduced since the holding ability is weakened.

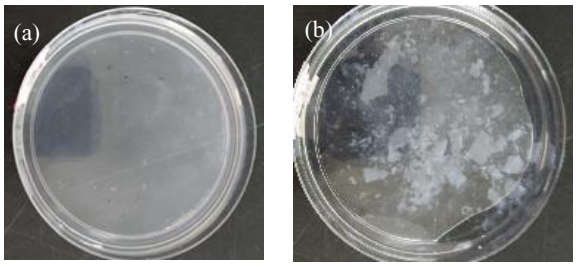

Figure 5. The images of (a) complete degradation of pectin/eggshell bioplastic and (b) incompleted degradation of pectin/eggshell/DES bioplastic in seawater

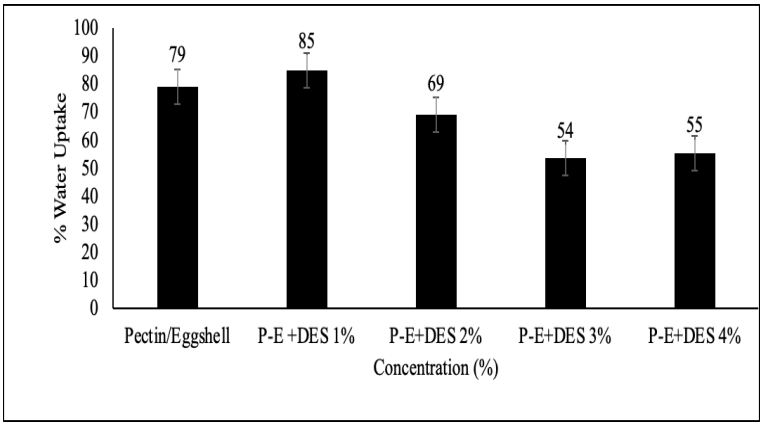

Figure 6. Percentage water uptake of bioplastics test in different concentration (%) of DES

Conclusion

The pectin/eggshell bioplastics with different concentrations of DES were successfully prepared. The eggshell and choline chloride: malonic acid are compatible with pectin, and no crystallisation occurred during the formation of biofilm. DES allowed the bioplastic to become more flexible by disrupting the polymer chains, causing an increase in elongation and a decrease in tensile strength of pectin/eggshell/DES. The higher concentration of DES leads to more flexibility and higher biodegradation in soil but with lower water uptake. These results indicated that

Choline chloride:malonic acid could be used as a potential plasticiser for pectin/eggshell bioplastic.

Acknowledgement

The authors are grateful for the financial support of the Fundamental Research Grant Scheme (FRGS) provided by the Ministry of Education, Malaysia, FRGS 5/3 (113/2019) and facilities in Universiti Teknologi MARA, Perlis Branch.

References

1. Šešlija, S., Nesic, A., Ruzic, J., Krusic, M. K., Velickovic, S., Avolio, R., Santagata, G. and Malinconico, M. (2018). Edible blend films of pectin and poly (ethylene glycol): Preparation and physico-chemical evaluation. *Food Hydrocolloids,* 77: 494-501.
2. Anastas, P. T. and Kirchhoff, M.M (2002). Origins, current status, and future challenges of green chemistry. *Accounts of Chemical Research*, 35(9): 686-694.
3. Fabra, M. J., Lopez-Rubio, A. and Lagaron, J. M. (2014). Biopolymers for food packaging application. *Smart Polymers and Their Application*, 15: 476-509.
4. Cavallaro, G., Lazzara, G. and Milioto, S. (2011). Dispersions of nanoclays of different shapes into aqueous and solid biopolymeric matrices. *Langmuir,* 27(3): 1158-1167.
5. Biddeci, G., Cavallaro, G., Blasi, F. D, Lazzara, G. Massaro, M. Milioto, S., Parisi, F., Riela, S. and Spinelli, G. (2016). Halloysite nanotubes loaded with peppermint essential oil as filler for functional biopolymer film. *Carbohydrate Polymers*, 152: 548-557.
6. Munarin, F., Tanzi, M.C. and Petrini, P. (2012). Advances in biomedical applications of pectin gels. *International Journal of Biological Macromolecules*, 51(4): 681-689.
7. Obara, S. and McGinity, W. (1995). Influence of processing variables on the properties of free films prepared from aqueous polymeric dispersions by a spray technique. *International Journal of Pharmaceutics,* 126 (1-2): 1-10.
8. Gennadios, A., Hanna, M. A. and Kurth, L. B. (1997). Application of edible coatings on meats, poultry and seafoods: a review. *LWT-Food Science and Technology,* 30(4): 337-350.
9. Pilla, S. (2011). Handbook of Bioplastic and *Biocomposites Engineering Applications.* ISBN 978 0-470-62607-8, Publisher John Wiley & Sons.
10. Abolibda, T. Z. (2015). Physical and chemical investigations of starch based bio-plastics. PhD Diss., University of Leicester.
11. Kang, D. J., Pal, K., Park, S. J., Bang, D. S., & Kim, J. K. (2010). Effect of eggshell and silk fibroin on styrene–ethylene/butylene–styrene as bio-filler. *Materials & Design,* 31(4): 2216-2219.
12. Toro, P. Quijada, R., Arias, J. L. and Yazdani-Pedram, M. (2007). Mechanical and morphological studies of poly (propylene)-filled eggshell composites. *Macromolecular Materials and Engineering,* 292(9): 1027-1034.
13. Vieira, M. G. (2011). Natural-based plasticizers and biopolymer films: A review. *European Polymer Journal,* 47(3): 254-263.
14. Kasmuri, N. and Abu Zait, M. S. (2018). Enhancement of bio-plastic using eggshells and chitosan on potato starch based. *International Journal of Engineering & Technology,* 7:110-115.
15. Abbott, A. P., Ballantyne, A. D., Conde, J. P., Ryder, K. S. and Wise, W. R. (2012). Salt modified starch: sustainable, recyclable plastics. *Green Chemistry,* 14(5): 1302-1307.
16. Galvis-Sánchez, A. C., Sousa, A. M. M, Goncalves, M. P. and Souza, H. K. S. (2016). Thermo-compression molding of chitosan with a deep eutectic mixture for biofilms development. *Green Chemistry* 18(6): 1571-1580.
17. Leroy, E., Decaen, P., Coativy, G., Pontoire, B., Reguerre, A. and Lourdin, D. (2012). Deep eutectic solvents as functional additives for starch based plastics. *Green Chemistry,* 14(11): 3063-3066.
18. Zdanowicz, M. and Johansson, C. (2016). Mechanical and barrier properties of starch-based films plasticized with two-or three component deep eutectic solvents. *Carbohydrate Polymers* 151: 103-112.

19. Shafie, M. H., Samsudin, D., Yusof, R. and Gan, C.Y. (2018). Characterization of bio-based plastic made from a mixture of Momordica charantia bioactive polysaccharide and choline chloride/glycerol based deep eutectic solvent. *International Journal of Biological Macromolecules*, 118: 1183-1192.
20. Malarvannan G, Onghena, M., Verstraete, S., Puffelen, E.V., Jacobs, A., Vanhorebeek, I., Verbruggen, C. A. T., Joosten, K. F. M., Berghe, G. V. D., Jorens, P. G. and Covaci, A. (2018). Phthalate and alternative plasticisers in indwelling medical devices in pediatric intensive care units. *Journal of Hazardous Materials,* 363: 64-72.
21. Mekonnen, T., Mussone, P., Khalil, H. and Bressler, D. (2013). Progress in bio-based plastics and plasticizing modifications. *Journal of Materials Chemistry A*, 1(43): 13379-13398.
22. Tome, L. I., Baiao, V., Silva, W. D. and Brett, M. A. (2018). Deep eutectic solvents for the production and application of new materials. *Applied Materials Today,* 10: 30-50.
23. Zhang, Q., Vigier, K. D. O., Royer, S. and Jerome, F. (2012). Deep eutectic solvents: Syntheses, properties and applications. *Chemical Society Reviews,* 41(21): 7108-7146.
24. Shamsuri, A. A. and Daik, R. (2012). Plasticizing eutectic-based ionic liquid on physicochemical. *BioResources*, 7(4): 4760-4775.
25. Cataldo, V. A., Cavallaro, G., Lazzara, G., Milioto, S. and Parisi, F. (2017). Coffee grounds as filler for pectin: Green composites with competitive performances dependent on the UV irradiation. *Carbohydrate Polymers*, 170: 198-205.
26. Almeida, C. M.R., Magalhaes, J.M.C.S., Souza, H.K.S. and Concalves, M.P. (2018). The role of choline chloride-based deep eutectic solvent and curcumin on chitosan films properties. *Food Hydrocolloids,* 81: 456-466.
27. Zárate-Ramírez, L. S., Bengoechea, C., Partal, P. and Guerrero, A. (2014). Thermo-mechanical and hydrophilic properties of polysaccharide/gluten-based bioplastics. *Carbohydrate polymers,* 112: 24-31.
28. Bichara, L. C, Alvarez, P. E., Bimbi, M. V. F, Vaca, H., Gervasi, C. and Brandan, S. A. (2016). Structural and spectroscopic study of a pectin isolated from citrus peel by using FTIR and FT-Raman spectra and DFT calculations. *Infrared Physics & Technology,* 76: 315-327.
29. Li, Y., Xin, S., Bian, Y., Xu, K., Han, C. and Dong, L. (2016). The physical properties of poly (l-lactide) and functionalized eggshell powder composites. *International Journal of Biological Macromolecules,* 85: 63-73.
30. Siriprom, W., Sangwaranatee, N., Hidayat, R., Kongsriprapan, S., Teanchai K. and Chamchoi, N. (2018). The physicochemical characteristic of biodegradable methylcellulose film reinforced with chicken eggshells. *Materials Today: Proceedings,* 5(7): 14836-14839.
31. Pradhan, A. K. and Sahoo, P. K. (2017). Synthesis and study of thermal, mechanical and biodegradation properties of chitosan-g-PMMA with chicken egg shell (nano-CaO) as a novel bio-filler. *Materials Science and Engineering: C,* 80: 149-155.
32. Gouveia, T. I. A. Biernacki, K., Castro, M. C. R., Goncalves, M. P. and Souza, H. K. S. (2019). A new approach to develop biodegradable films based on thermoplastic pectin. *Food Hydrocolloids,* 97:105175.
33. Kong, J., Li, Y., Bai, Y., Li, Z., Cao, Z., Yu, Y., Han, C. and Dong, L. (2018). High-performance biodegradable polylactide composites fabricated using a novel plasticiser and functionalized eggshell powder. *International Journal of Biological Macromolecules,* 112: 46-53.
34. Esposito, M., Pierro, P. D, Gonzales, C.R., Mariniello, L., Giosafatto, C. V. L and Porta, R. (2016). Polyamines as new cationic plasticisers for pectin-based edible films. *Carbohydrate polymers*, 153: 222-228.
35. Muscat, D. Adhikari, B., Adhikari, R. and Chaudhary, D. S. (2012). Comparative study of film forming behaviour of low and high amylose starches using glycerol and xylitol as plasticisers. *Journal of Food Engineering*, 109(2): 189-201.

36. Sanyang, M. L., Sapuan, S.M., Jawaid, M., Ishak, M.R. and Sahari, J. (2016). Effect of plasticiser type and concentration on physical properties of biodegradable films based on sugar palm (arenga pinnata) starch for food packaging. *Journal of Food Science and Technology*, 53: 326-336.
37. Trindade, J. R., Visak, Z. P., Blesic, M., Marrucho, I. M., Coutinho. J. A. P., Lopes, J. N. C. and Rebelo, L. P. N. (2007). Salting-out effects in aqueous ionic liquid solutions: Cloud-point temperature shifts. *The Journal of Physical Chemistry B*, 111(18): 4737-4741.
38. Suppakul, P., Chalernsook, B., Ratisuthawat, B., Prapasitthi, S. and Munchukangwan, N. (2013). Empirical modeling of moisture sorption characteristics and mechanical and barrier properties of cassava flour film and their relation to plasticizing–antiplasticizing effects. *LWT-Food Science and Technology,* 50(1): 290-297.

Malaysian Journal of Analytical Sciences (MJAS)
Published by Malaysian Analytical Sciences Society

SUPRAMOLECULAR ASSEMBLIES OF 1,2-DISUBSTITUTED CYCLOHEXANE AMIDE LIGANDS AND THEIR COORDINATION POLYMER: SYNTHESIS, CHARACTERISATION, AND CRYSTAL STRUCTURE

(Himpunan Supramolekul Ligan Amida Sikloheksana 1,2-Tertukar Ganti dan Polimer Koordinatannya: Sintesis, Pencirian, dan Struktur Hablur)

Nur Shuhaila Haryani Haris[1], Nafisah Mansor[1], Maisara Abdul Kadir[1,2]*

[1]*Faculty of Science and Marine Environment,*
[2]*Advanced Nano Materials Research Group, Faculty of Science and Marine Environment,*
Universiti Malaysia Terengganu, 21030 Kuala Nerus, Terengganu, Malaysia

**Corresponding author: maisara@umt.edu.my*

Received: 13 September 2021; Accepted: 18 December 2021; Published: 25 February 2022

Abstract

Supramolecular interactions such as hydrogen bonding, π-π stacking, Van der Waals interactions, and metal-ligand are important in stabilising the structure of molecules. In order to determine the presence of supramolecular interactions in two novel compounds, 1,2-disubstituted cyclohexane amide ligands, namely 1,2-bis[*N,N'*-6-(3-pyridylmethylamido)pyridyl-2-carboxyamido]cyclohexane (L1) and 1,2-bis[*N,N'*-6-(4-pyridylmethylamido)pyridyl-2-carboxyamido]cyclohexane (L2) were successfully synthesised and fully characterised by FTIR, ^{1}H and ^{13}C NMR and mass spectrometry, while the molecular formula was determined by elemental analysis. X-ray crystallography revealed that the folded conformations of both ligands were stabilised by intramolecular N-H···O=C and N-H···N hydrogen bonds at the pre-organised amide moieties. The crystal's structure was stabilised by weak face-to-face π-stacking interaction or centroid-centroid π-stacking interaction involving the two pendant pyridine rings. In the crystal structure of one-dimensional coordination polymer, there are two intermolecular hydrogen bonding interactions (N-H···O=C, d = 2.094 Å, D = 2.946 Å and d = 2.090 Å, D = 2.938 Å, N-H···O angle = 161.52°) formed between the pre-organised NH amide donors of a molecule of L1 in one coordination polymer and the amide carbonyl group of a molecule of L1 in an adjacent polymer that leads to the formation of 2-D hydrogen-bonded sheets extend in the *ac* diagonal.

Keywords: supramolecular, coordination polymer, cyclohexane, hydrogen bonding, racemic

Abstrak

Interaksi supramolekul seperti ikatan hidrogen, susunan π-π, interaksi Van der Waals dan logam-ligan adalah penting dalam menstabilkan struktur molekul. Dalam usaha mengenalpasti kehadiran interaksi supramolekul dalam dua sebatian baharu, ligan amida sikloheksana 1,2-tertukar ganti, iaitu 1,2-bis[*N,N'*-6-(3-piridilmetilamido)piridil-2-karboksiamido]sikloheksana (L1) dan 1,2-bis[*N,N'*-6-(4-piridilmetilamido)piridil-2-karboksiamido]sikloheksana (L2) telah disintesis dan dicirikan sepenuhnya dengan FTIR, ^{1}H dan ^{13}C NMR serta spektrometri jisim, manakala formula molekul ditentukan melalui analisis unsur. Kristalografi

sinar-X menunjukkan bahawa konformasi bagi kedua-dua ligan distabilkan oleh ikatan hidrogen intramolekul N-H···O=C dan N-H···N pada kawasan amida separa tersusun. Struktur hablur juga distabilkan oleh interaksi lemah susunan muka ke muka atau titik pusat ke titik pusat di antara gelang aromatik piridina. Dalam struktur hablur polimer koordinatan satu dimensi, terdapat dua ikatan hidrogen intermolekul (N-H···O=C, d = 2.094 Å, D = 2.946 Å dan d = 2.090 Å, D = 2.938 Å, N-H···O sudut = 161.52°) yang terbentuk di antara NH amida dari molekul L1 dalam polimer koordinatan dan karbonil amida dari molekul L1 dalam polimer bersebelahannya dan menghasilkan lapisan 2-D ikatan hidrogen yang bersambung ke diagonal *ac*.

Kata kunci: supramolekul, polimer koordinatan, sikloheksana, ikatan hidrogen, rasemik

Introduction

Supramolecular chemistry is often defined as 'the chemistry beyond the molecule' [1]. This term was introduced by Jean-Marie Lehn who won the Nobel Prize in Chemistry in 1987 together with Donald J. Cram and Charles J. Pedersen. They received the prize for their contributions to the synthesis of shape-selective and ion-selective receptors, in particular, the development of selective 'host-guest' complexes. In broader terms, supramolecular chemistry is defined as the self-assembly of small molecular subunits into large aggregates *via* weak intermolecular forces or reversible covalent bonding. The interactions commonly involved in the self-assembly process are hydrogen bonds, π-π interactions (stacking of aromatic rings), Van der Waals forces, cation-interactions, and metal-ligand (M-L) interactions [2]. The order of strength for the intermolecular interactions from very weak to very strong is broadly as follows: hydrophobic/hydrophilic interactions, Van der Waals forces, H-bonding interactions, electrostatic forces and metal coordination [3].

In general, the intermolecular interactions are individually weak, but by using multiple weak intermolecular forces within the assemblies, robust structures can be generated. Besides, the dynamic nature of noncovalent interactions endows supramolecular polymeric systems with many fascinating properties and functions, such as reversibility, adaptability, self-healing, and stimuli-responsiveness [4]. Hydrogen bonding interactions are commonly employed in supramolecular chemistry [5]. Hydrogen bonding occurs between a proton donor attached to an electronegative atom such as O, N, S, F or C (D-H) and an acceptor (A). The donor is partially positive hydrogen while the acceptor is a partially negative atom with unshared valence electrons or polarisable π electrons. The strength of hydrogen bonds is typically around 20 kJmol^{-1}, but can even be as strong as 163 kJmol^{-1} as has been reported for the F···HF interaction [6,7]. Weak interactions involving π-systems such as π-stacking interactions (π···π) are observed in many supramolecular systems [8]. Other weak interactions involving π-systems are C-H···π, cation···π and anion···π interactions. The C-H···π interaction is classified as weak H-bonding and have similar properties to the weak hydrogen bonds. Cation···π interactions occur between metallic or organic cations and π-bonded systems of the molecule.

Open chain molecules such as amide, thiourea, and urea are of interest because intermolecular amide-amide hydrogen bonding can promote the fabrication of well-defined assemblies of supramolecular chemistry [9]. Furthermore, amide ligands with the presence of pyridyl as one of the outstanding N or O-donor organic linkers have been effectively selected because they can connect metal centres through their pyridyl groups or the amide groups [10]. Thus, in this research, two novel amide compounds containing 1,2-disubstituted cyclohexane spacer were prepared (Figure 1). Compounds 1,2-bis[*N,N'*-6-(3-pyridylmethyl amido)pyridyl-2-carboxyamido]cyclohexane (L1) and 1,2-bis[*N,N'*-6-(4-pyridylmethylamido)pyridyl-2-carboxyamido]cyclohexane (L2) were synthesised from a racemic mixture of *trans*-1,2-diamino cyclohexane in two steps. The incorporation of a cyclohexyl spacer was anticipated to limit the relative arrangements of the two 2,6-pyridine dicarboxamide moieties as compared to common approaches of using aliphatic alkyl chains spacer [11].

The advantages of the pyridyl-amide ligands are the amide groups with both N-H hydrogen donor and C=O hydrogen acceptor can enhance the formation of hydrogen bonds and supramolecular structures. The isomerism and flexibility of ligands play important roles in permitting guest molecules such as anions to interact with the host molecules by using weak hydrogen bonding. The presence of aromatic rings from 1,2-disubstituted cyclohexane amide moieties and pyridine pendant groups is important to achieve well-defined frameworks with higher stability contributed by the supramolecular interactions of π-π stackings. In a work by Yusof et al. [12] the conformation of cyclohexane derived compound was stabilised by intramolecular hydrogen bonds and intermolecular N-H···O and C-H···O hydrogen bonds, which led to centrosymmetric dimers arrangement [12].

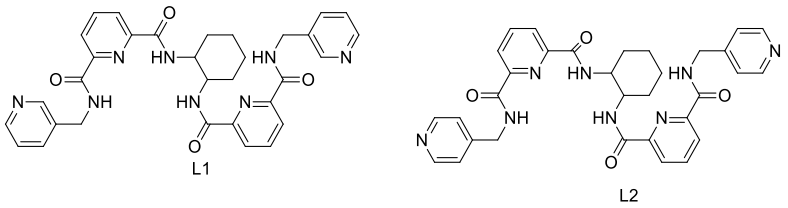

Figure 1. The structure of 1,2-bis[*N,N'*-6-(3-pyridylmethylamido)pyridyl-2-carboxyamido]cyclohexane (L1) and 1,2-bis[*N,N'*-6-(4-pyridylmethylamido)pyridyl-2-carboxyamido]cyclohexane (L2)

Materials and Methods

Synthesis of 1,2-bis[*N,N'*-6-(3-pyridylmethyl amido)pyridyl-2-carboxyamido]cyclohexane (L1)

1,2-bis[6-methoxycarbonyl)pyridyl-2-carboxyamido] cyclohexane (0.50 g, 1.1 mmol) and 3-aminomethylpyridine (0.22 mL, 2.3 mmol) were suspended in toluene (20 mL). The reaction mixture was heated at reflux for 72 hours, during which time a white solid precipitated. After cooling to room temperature, the solvent was removed in vacuo, the residue re-dissolved in dichloromethane (40 mL), washed with saturated aqueous sodium bicarbonate solution (2 × 100 mL), and the chlorinated extract was dried over magnesium sulphate. The solvent was removed in vacuum to give a sticky off-white solid. The solid was washed with diethyl ether, dried, and recrystallised from ethanol to give L1 as a white solid (0.55 g, 82%). Mp 250-252 °C. Anal. found: C, 64.19; H, 5.52; N 18.70. ($C_{32}H_{32}N_8O_4$) requires C, 64.84; H, 5.45; N 18.90%. ^{1}H (300 MHz; $CDCl_3$; Me_4Si) δ = 1.32 (2H, m, CH_2), 1.65 (1H, m, CH_2), 2.17 (1H, m, CH_2), 3.87 (1H, s, CH), 4.15 (2H, d, J = 11.43 Hz, CH_2), 7.23 (1H, m, pyH5), 7.82 (2H, m, pyH3, pyH4', pyH4), 8.28 (2H, m, pyH5'), 8.54 (2H, d, J = 4.81 Hz, pyH6'), 8.65 (2H, m, NH, pyH2') and 9.07 (1H, d, J = 8.38 Hz, NH). ^{13}C (75.1 MHz; $CDCl_3$; Me_4Si) δ = 23.1, 28.3, 45.1, 54.6, 123.9, 125.7, 125.9, 134.8, 136.7, 139.2, 148.1, 149.5, 149.9, 150.8, 161.1, 162.4. m/z (ES-MS) 592.2 (MH^+, 100), 593.6 (MH^+, 50%), 614.5 (MNa^+, 65%), 1204.2 ($M.H_2O+H)^+$, 30%). Selected IR bands (KBr disk, cm^{-1}): 3368 (m), 3267 (m), 2916 (s) 1627 (m), 1650 (s), 1527 (s), 1424 (m), 1306 (s). Crystals were obtained by slow evaporation of a methanol solution of L1 and copper nitrate.

Synthesis of 1,2-bis[*N,N'*-6-(4-pyridylmethyl amido)pyridyl-2-carboxyamido]cyclohexane hydrate L2·H_2O (L2)

1,2-bis[6-methoxycarbonyl)pyridyl-2-carboxyamido]cyclohexane (0.52 g, 1.2 mmol) and 4-aminomethylpyridine (0.24 mL, 2.4 mmol) were dissolved in hot toluene (20 mL) and heated at reflux for 72 hours. During the course of the reaction, a yellow solid precipitated. The solvent was removed in vacuum to give a yellow solid. The solid was re-dissolved in dichloromethane (40 mL), washed with saturated sodium bicarbonate solution (2 × 100 mL), and the chlorinated layer was dried over magnesium sulphate. The solvent was removed in vacuum to give a yellow oil which was triturated with hot ethyl acetate (5 mL) to give a brown solid. This solid was purified by column chromatography, eluting with 1:9 methanol–CH_2Cl_2 to give L2·H_2O as a brown solid (0.24 g, 33%). Mp 220 – 225 °C. Anal. found: C,

64.67; H, 5.89; N, 18.90. ($C_{32}H_{34}N_8O_5$) requires C, 64.84; H 5.45; N, 18.91%. ^{1}H (300 MHz; $CDCl_3$; Me_4Si) δ = 1.43 (2H, m, CH_2), 1.93 (2H, d, *J* = 6.73 Hz, CH_2), 2.14 (2H, d, *J* = 13.29 Hz, CH_2), 3.77 (1H, s, CH), 4.72 (2H, m, CH_2), 7.25 (2H, m, pyH3', pyH5'), 7.74 (2H, m, pyH3, pyH5), 8.32 (1H, m, pyH4), 8.54 (2H, d, *J* =5.70 Hz, pyH2', pyH6'), 9.15 (1H, d, *J* = 6.25 Hz, NH) and 9.75 (1H, t, *J* = 6.40 Hz, NH). ^{13}C (75.1 MHz; $CDCl_3$; Me_4Si) δ = 22.5, 28.9, 45.6, 54.0, 124.3, 125.6, 125.9, 139.8, 147.3, 148.9, 149.2, 149.9, 160.5, 161.8. *m/z* ES-MS) 592.3 (MH^+, 100%), 593.1 (MH^+, 75%). Selected IR bands (KBR disk, cm^{-1}): 3282 (m), 2923 (s), 1652 (s), 1671 (s), 1529 (s), 1444 (m), 672 (s). Crystals were obtained by slow evaporation of a methanol solution of L2 and copper perchlorate.

Synthesis of $\{[CdBr_2(L1)_4]\cdot 4H_2O\}_n$

$CdBr_2$ (0.0026 g, 0.010 mmol) was dissolved in water (5 mL), heated for 5 minutes, before being added dropwise to a solution of L1 (0.0120 g, 0.020 mmol) dissolved in methanol (15 mL). The resulting slightly cloudy solution was heated for 45 minutes to re-dissolve the precipitate and was left to evaporate at room temperature. The solution afforded $\{[CdBr_2(L1)_4]\cdot 4H_2O\}_n$ as colourless crystals in low yields (0.009 g, 24%). Mp 230-235ºC.

Results and Discussion

Compounds 1,2-bis[*N,N'*-6-(3-pyridylmethyl amido)pyridyl-2-carboxyamido]cyclohexane (L1) and 1,2-bis[*N,N'*-6-(4-pyridylmethylamido)pyridyl-2-carboxyamido]cyclohexane (L2) were synthesised from a racemic mixture of *trans*-1,2-diaminocyclohexane in two steps (Scheme 1). To synthesise the ligand, firstly, pyridine-2,6-dicarboxylic acid monomethyl ester (i) was reacted with thionyl chloride to produce 6-(methoxycarbonyl)pyridine-2-carboxylic acyl chloride (ii). Then, compound (ii) was reacted with 1,2-diaminocyclohexane (iii) with a 2:1 mol ratio to provide 1,2-bis[6-methoxy carbonyl)pyridyl-2-carboxyamido]cyclohexane (iv). At the second step, precursor (iv) and 3-aminomethylpyridine were suspended in toluene and heated at reflux for approximately 72 hours to give 1,2-bis[*N,N'*-6-(3-pyridylmethylamido)pyridyl-2-carboxy amido]cyclohexane (L1) (Scheme 1). The crude product of L1 was obtained as an off-white solid after being isolated after re-dissolved in hot ethanol. The insoluble solids were removed by filtration, and the filtrate was left to evaporate to afford L1 as a colourless powder in an 82% yield.

Ligand L2 was prepared with a similar procedure, but the 3-aminomethylpyridine was replaced with 4-aminomethylpyridine. The coordination chemistry of these ligands was investigated with a range of late transition metals, including cadmium(II), copper(II), cobalt(II), silver(I), and zinc(II). The focus of this synthesis was to produce coordination polymers that display anion coordinating pockets (Figure 2). Compounds L1 and $L2\cdot H_2O$ were found to preferentially crystallise from solutions containing metal salts. It showed that the ligands were insoluble in the metal salts solution and caused limitations to obtain metal complexes. Rectangular block-shaped colourless crystals of both compounds were obtained from several different reactions and were suitable for X-ray crystallography.

The FTIR spectra for the three compounds showed distinctive peaks for *ν*(N-H), *ν*(O-H), *ν*(C=N), *ν*(C=O), *ν*(Cd-N), and *ν*(N-O). As for compound L1, the *ν*(N-H) stretching displayed a broad peak due to the water molecule and the weak hydrogen bond interactions interrupted the chemical changes. The low frequency (N-H) stretching appeared at 3267 cm^{-1} showing that the steric effect occurred with the presence of methyl located near the amino group [13]. Meanwhile, the *ν*(N-H) bending was interpreted at 1527 cm^{-1} because of the hydrogen bond donor. The strong frequency band at 2916 cm^{-1} referred to *ν*(C-H) aromatics vibration respective to the formation of sp^3 hybridisation. The carbonyl *ν*(C=O) band shifted to the low frequency at 1650 cm^{-1} suggested the involvement of hydrogen bonds formed between the amide moieties and pendant pyridyl group [14]. In the IR spectrum, the high frequency above 3000 cm^{-1} regions is a signature area for recognition phenyl C-H stretching vibrations. The region below 2000 cm^{-1} showed very sharp and strong peaks [15]. The spectrum of L2 showed a close resemblance of the absorbance pattern

compared with L1. Compound L2 observed the appearance of amide stretching, ν_{str}(N-H) at 3282 cm^{-1}. A significant stretching vibration of ν_{str}(C-H) aromatics band attributed at 2923 cm^{-1}. Nevertheless, the wavenumbers captured in both compounds for *ν*(C=O) amide revealed a significant difference. Compound L2 recorded the appearance of the carbonyl stretching at wavenumbers 1647 cm^{-1}. The compounds showed bands at 1529 cm^{-1} which was ascribed to the N-H bending.

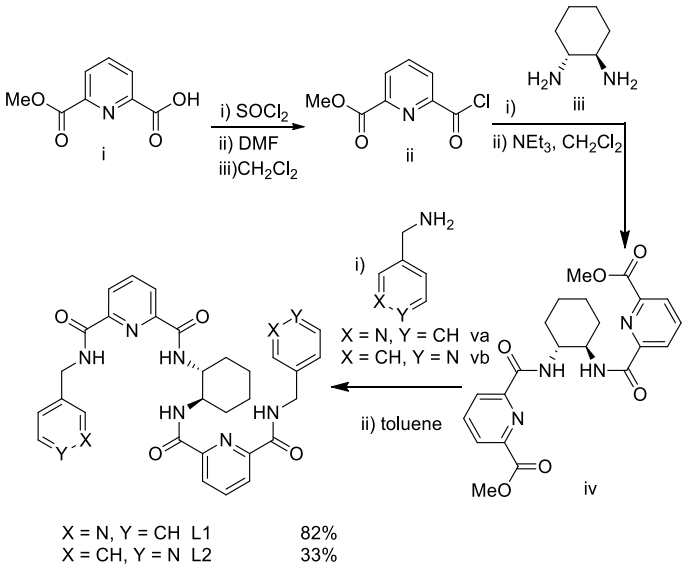

Scheme 1. The synthesis of L1 and L2

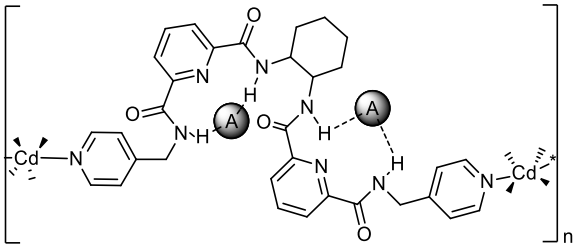

Figure 2. Coordination polymers that display anion coordinating pockets, where A in the circle represents anion

The ^{1}H NMR spectra of L1 were recorded in deuterated chloroform (Table 1). A signal that appears as a triplet at 9.09 ppm corresponding to the N-H protons of the pyridine core amide [16,17]. The signals for the cyclohexyl amide and the pendant pyridyl H2' are overlapped to give a broad singlet at 8.65 ppm. Another two signals (H6' at 8.54 and H5'at 8.28 ppm) were assigned to the pendant pyridine protons H6' and H5', while the multiplet near 7.82 ppm corresponded to the overlap between one triplet and doublets from the pyridine carboxamide H4 proton and the H4' of the pendant pyridine ring. The nearby doublet was assigned as the H3 and H5 hydrogen atoms from the pyridine core. The multiplets at 4.15 ppm arise from the CH_2 protons from the methylene linker adjacent to the pyridine rings. The cyclohexane protons are doublets that appear upfield at 3.87, 2.17, 1.65 and 1.32 ppm. The ESI-MS obtained on a methanol solution of

L1 revealed peaks for the parent ion $[L1+H]^+$ at m/z 591.2. Meanwhile, a peak at m/z 1204.2 corresponded to the hydrated dimeric species, $[(L1)_2 \cdot H_2O+H]^+$, while a hydrated trimeric species $[(L1)_3 \cdot H_2O+H]^+$ was observed at m/z 1793.2 in low relative abundance. There is also a peak observed for a sodium-containing ion, $[L1+Na]^+$, at m/z 614.5 (25%).

Based on the conditions employed for the synthesis of L1, the reaction of 6-(methoxycarbonyl)pyridine-2-carboxylic acyl chloride with a greater than two-fold excess of 4-aminomethylpyridine gave L2. Similar to the synthesis of L1, the reaction was heated at reflux for approximately 72 hours, and the formation of the product was monitored by TLC and NMR spectroscopy. Compound L2 was isolated by flash column chromatography techniques using the mixture of dichloromethane-methanol (9:1) as the eluting solvent system. Unfortunately, L2 was isolated in a much lower yield (33%) compared to L1. This is a consequence of the reduced nucleophilicity of the amine nitrogen compared to the 3-substituted precursor, as reported by Ikawa et al., 2011 [18]. Elemental analysis of the product obtained supports the isolation of the hydrate, $L2 \cdot H_2O$. In the ^1H NMR spectrum of $L2 \cdot H_2O$, the amide protons were observed downfield compared to L1, with a doublet at 9.75 ppm and a doublet at 9.15 ppm. The remaining signals between 7.25-8.54 ppm corresponded to the protons from the pyridine ring and the pyridine core. The methylene linker had a resonance at 4.72 ppm, while the cyclohexane protons showed signals at 3.77, 2.14, 1.93, and 1.43 ppm. The mass spectrometry indicated the presence of a dominant molecular ion corresponding to $[L2+H]^+$ at m/z 592.3 (100%).

Table 1. ^1H NMR data for L1 and L2

Proton signals	**L1**	**Proton signals**	**L2**
2H, m, CH_2	1.32		1.43
1H, m, CH_2	1.65	2H, d, CH_2	1.93
1H, m, CH_2	2.17	2H, d, CH_2	2.14
1H, s, CH	3.87		3.77
2H, d, CH_2	4.15	2H, m, CH_2	4.72
1H, m, pyH5	7.23	2H, m, pyH3', pyH5'	7.25
2H, m, pyH3, pyH4', pyH4	7.82	2H, m, pyH3, pyH5	7.74
2H, m, pyH5'	8.28	1H, m, pyH4	8.32
2H, d, pyH6'	8.54	2H, d, pyH2', pyH6'	8.54
2H, m, NH, pyH2'	8.65	1H, d, NH	9.15
1H, d, NH	9.07	1H, t, NH	9.75

X-ray crystallography

Crystal structure of L1

The particular crystals of L1 studied here were readily obtained from a methanol solution of copper nitrate and L1, consistent with the poor solubility of these compounds. Compound L1 crystallises in the triclinic space group *P*-1 with one molecule of L1 in the asymmetric unit. The structure reveals that this compound retained the two pre-organised amide hydrogen bond donor regions in the anticipated conformation (Figure 3), but as observed in molecule L1, these were arranged to form two separate pockets rather than one larger pocket. This arrangement is attributed to the planar arrangement of the substituents on the cyclohexane ring at the 1 and 2 positions.

In the conformation of L1 observed in the crystal structure, it appears there were intramolecular N-

H···O=C and N-H···N hydrogen bonds that stabilised the folded conformation. Figure 3 shows these hydrogen bonds have the following distances, N15-H15···O14 (*d* = 2.201 Å, *D* = 2.953 Å), N49-H49···O14 (*d* = 2.333 Å, *D* = 3.157 Å), N49-H49···N41 (*d* =2.308 Å, *D* = 2.697 Å), and N15-H15···N41 (*d* = 2.251 Å, *D* = 2.663 Å). The N-H···N angles are 106.78° and 108.41°, respectively.

Figure 4 shows that several intermolecular interactions were responsible for the formation of a dimeric arrangement of L1 in the solid state. The dimer was stabilised by four N-H···O=C hydrogen bonds between each molecule of L1 (N12-H12···O17, *d* = 2.158 Å, *D* = 3.000 Å; and N29-H29···O17 *d*= 2.111 Å; *D* = 2.951 Å).

The structure was further stabilised by π-π stacking interactions between the pyridine rings [19]. In the dimer, the pendant pyridyl group and the central pyridine core interact in an edge-to-face interaction, in which the C-H···π(centroid) distance is 2.912 Å. Adjacent dimers were then further involved in the π-stacking interactions involving one 2,6-pyridine dicarboxamide core of each molecule of L1 (Figure 5). The two pyridine cores formed a weak face-to-face π-stacking interaction (centroid-centroid distance 4.20 Å; angle 47.46°; centroid offset 1.32 Å). This ultimately resulted in a 1-D chain-like arrangement of the dimers.

Crystals of L2 were obtained from a methanol solution of copper perchlorate and compound L2. Like compound L1, compound L2 also crystallised in the triclinic space group *P*-1 but with two molecules of compound L2 in the asymmetric unit. The two molecules of L2 have similar conformations, with the major distinction between the two molecules being differences in bond lengths and angles. As observed in compound L1, intramolecular hydrogen bonding (*d* = 2.249-2.445 Å; N-H···N angles = 107.7 and 105.60°) pre-organised the NH functionalities of the compound to provide two anion pockets (Figure 6).

Like L1, one of these pockets was occupied by carbonyl oxygen of the other 2,6-pyridine dicarboxamide moiety (N-H···O, *d* = 2.380 Å ; *D* = 3.234 Å). Once again, intermolecular hydrogen bonding between the carbonyl oxygen (N-H···O) (*d* = 2.107 Å and *D* = 2.135 Å) and the pre-organised amide led to the formation of a dimer in the solid-state (Figure 7). Both molecules in the asymmetric unit demonstrated the same hydrogen bonding motifs with slightly different hydrogen bond distances (Table 2). One of the dimers had N-H···O hydrogen bond lengths of *d* = 2.109 - 2.137 Å, while the second dimer had hydrogen bond lengths of 2.106-2.153 Å. As observed in compound L1, the structures were also stabilised by intermolecular π-π stacking interactions. In the crystal packing, compound L2 was stabilised a centroid-centroid π-stacking interaction involving the two pendant pyridine rings (centroid-centroid distance 3.731 Å). The presence of excessive hydrogen-bonds networks in the compounds explains the huge range in the melting points for both compounds L1 and L2.

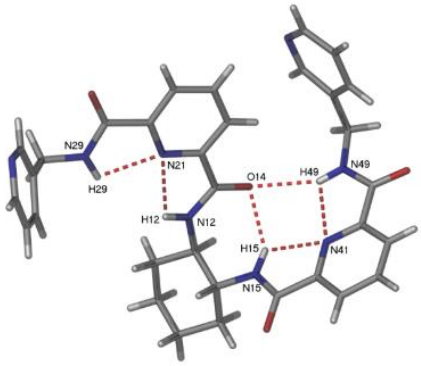

Figure 3. The asymmetric unit of compound L1, showing the presence of intramolecular N-H···O=C and N-H···N hydrogen bonds

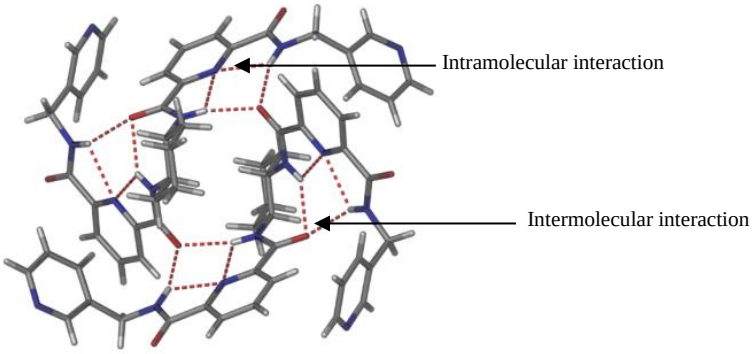

Figure 4. A perspective view of a dimer of L1 showing the weak intramolecular and intermolecular hydrogen bonds responsible for the conformation of L1 and the formation of the dimeric aggregate

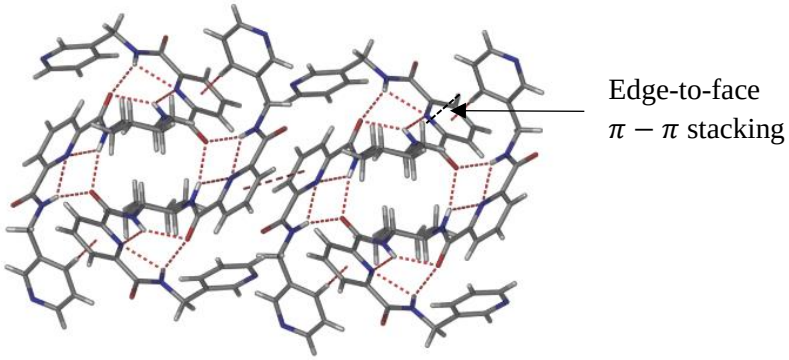

Figure 5. A perspective view of the π-π stacking interactions observed between the two pyridine cores of molecules of L1 that are involved in forming dimers

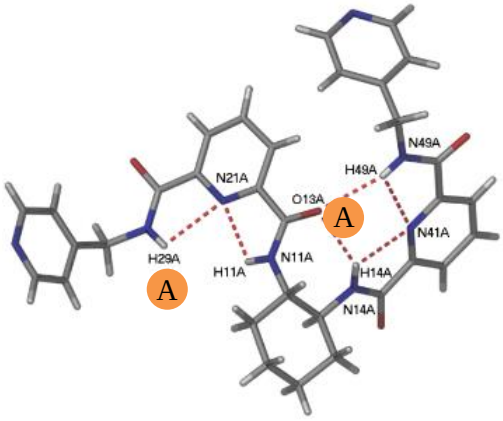

Figure 6. A perspective view of one of the molecules of L2 in the asymmetric unit, showing the pre-organizing intramolecular hydrogen bonding interactions that provided two potential anion pockets marked by A.

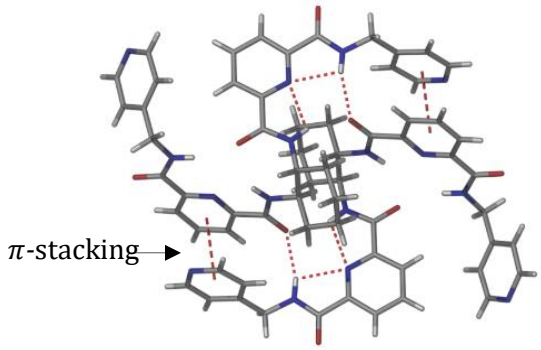

Figure 7. A perspective view of one of the dimers of compound L2, showing the intramolecular and intermolecular interactions, including the π-stacking interactions

Table 2. The asymmetric unit of hydrogen bond distances for L1 and L2

L1	
N15-H15···O14	*d* = 2.201 Å, *D* = 2.953 Å
N49-H49···O14	*d* = 2.333 Å, *D* = 3.157 Å
N49-H49···N41	*d* =2.308 Å, *D* = 2.697 Å
N15-H15···N41	*d* = 2.251 Å, *D* = 2.663 Å
L2	
N-H···O	*d* = 2.380 Å ; *D* = 3.234
N-H···O	*d* = 2.107 Å ; *D* = 2.135 Å
N-H···O	*d* = 2.109 - 2.137 Å
N15-H15···O14	*d* = 2.249 -2.445 Å

Crystal structure of CP-L1

Crystals of $\{[CdBr_2(L1)_2]\cdot 4H_2O\}_n$ were obtained from a methanol-water solution of L1 and cadmium bromide upon slow evaporation in 24% yield. Complex $\{[CdBr_2(L1)_2]\cdot 4H_2O\}_n$ was crystallised in the triclinic space group *P*-1 with one ligand L1, one cadmium atom (on a centre of inversion), two water molecules, and one bromide in the asymmetric unit (Figure 8). The cadmium atom adopts an octahedral coordination environment, with two bromide atoms in the axial positions and the equatorial positions occupied by four pyridyl donors from four separate molecules of L1. The Cd-N bond length is 2.453(4) Å and the Cd-Br bond length is 2.6805(5) Å, which is typically observed [20]. The Cd-Br bond distance was approximately 0.08-0.1 Å longer than the Cd-Br distance in compound 4.27, while the Cd-Cd distance in this compound is 16.765 Å.

The extended structure of compound CP-L1 is shown in Figure 9. Within the ligand, the pendant 4-pyridyl rings twisted backwards and forward relative to the 1,2-cyclohexane core with an -N-CH_2-CH_2-N- torsion angle of 56.3(2)° (Figure 9). This enabled the ligand to coordinate with two different cadmium centres which are also linked by a second molecule of L1.

Each cadmium is coordinated by four molecules of the ligand to generate a necklace-type 1-D coordination polymer. This coordination polymer was also

constructed from a dinuclear metallo-macrocylic repeating unit (Figure 9). Two types of ligand derived hydrogen bonding interactions are responsible for the internal conformation of the coordination polymers and the packing of adjacent 1-D coordination polymers in the solid-state. In the inter-polymer packing there are two intermolecular hydrogen bonding interactions in (N-H···O=C, d = 2.094 Å, D = 2.946 Å and d = 2.090 Å, D = 2.938 Å, N-H···O angle = 161.52°) formed between the pre-organized NH amide donors of a molecule of L1 in one coordination polymer and the amide carbonyl group of a molecule of L1 in an adjacent polymer (Figure 10(a)). The intermolecular hydrogen bonding led to the formation of 2-D hydrogen bonded sheets of the 1-D coordination polymers that extended in the *ac* diagonal (Figure 10(b)). Internally, each ligand within the coordination polymer adopts a conformation whereby the amide C=O forms a moderately strong N-H···O=C intramolecular hydrogen bonding interaction (d = 1.862 Å, D= 2.911 Å). This blocked one of the anion binding pockets of the ligand (Figure 10 (a)). In the 2-D crystal packing, the 1-D coordination polymers in each 2-D layer form C-H···π stacking interactions with 1-D coordination polymers in adjacent layers. These interactions occur between the pendant pyridyl rings of molecules of L1 in the adjacent layers (C-H-centroid distance 2.73 Å; angle 95.30°, centroid offset 1.39 Å Figure 10 (c). Weak intramolecular hydrogen bonding interactions of CP-L1 is shown in Table 3 while crystal data for CP-L1 is shown in Table 4.

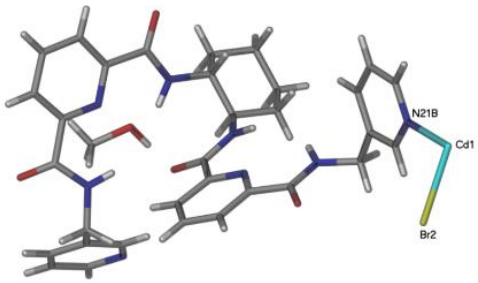

Figure 8. A perspective view of the asymmetric unit of compound CP-L1

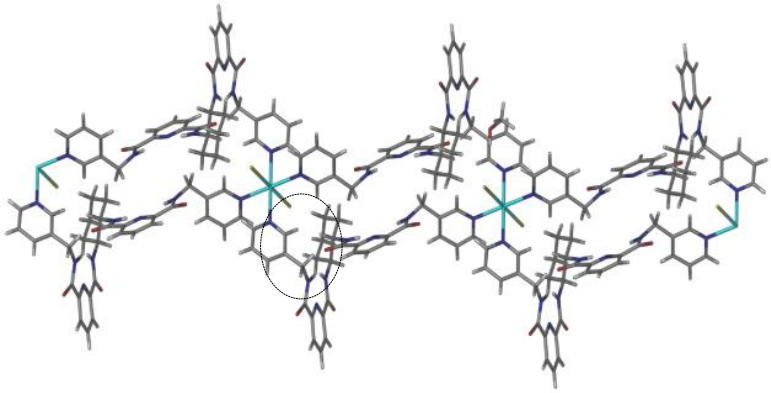

Figure 9. A perspective view of the extended structure of complex CP-L1

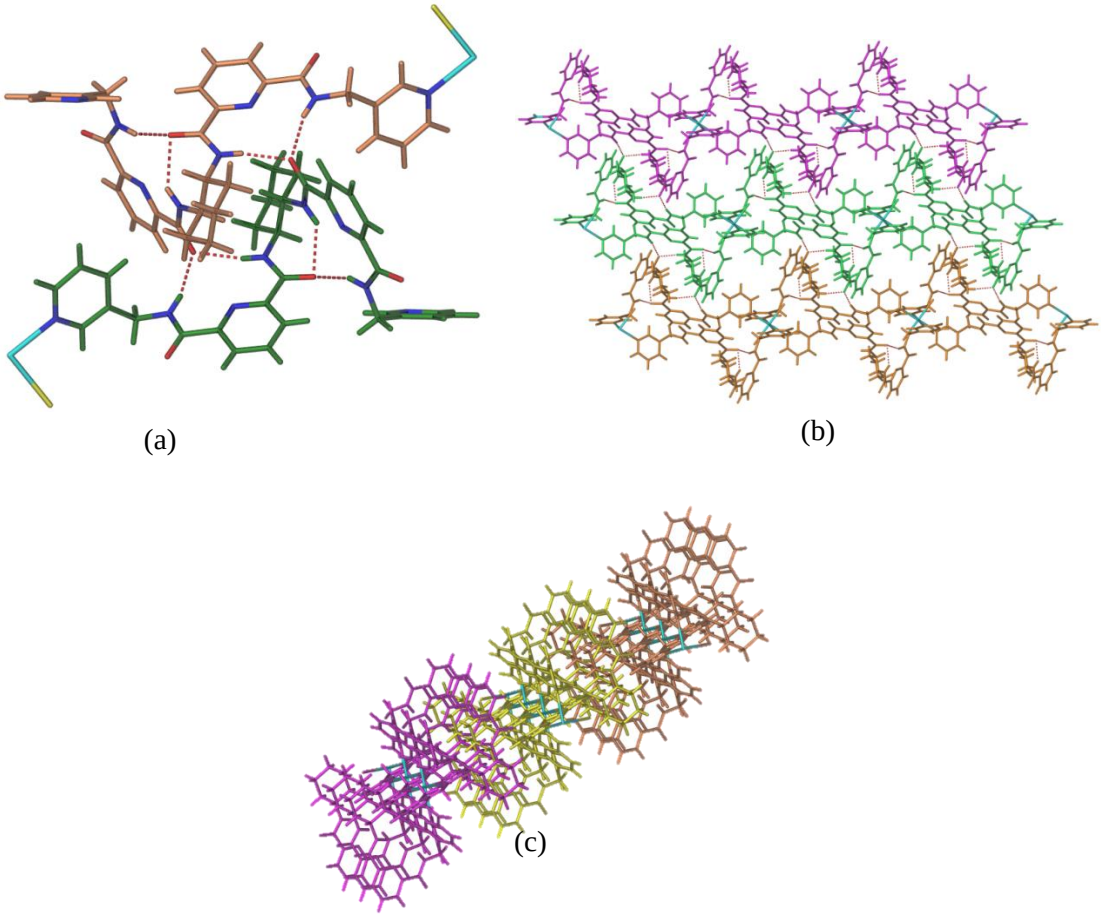

Figure 10. (a) A perspective view of intra- and the intermolecular hydrogen bonding in CP-L1 (b) The packing of 1-D coordination polymers into 2-D hydrogen bonded sheets (c) A perspective view of the crystal packing

Table 3. Weak hydrogen bonding of CP-L1

CP-L1	
N15-H15···O14	*d* = 2.201 Å, *D* = 2.953 Å
N49-H49···O14	*d* = 2.333 Å, *D* = 3.157 Å
N49-H49···N41	*d* =2.308 Å, *D* = 2.697 Å
N15-H15···N41	*d* = 2.251 Å, *D* = 2.663 Å
N-H···O	*d* = 2.380 Å ; *D* = 3.234
N-H···O	*d* = 2.107 Å ; *D* = 2.135 Å
N-H···O	*d* = 2.109 - 2.137 Å
N15-H15···O14	*d* = 2.249 - 2.445 Å

Table 4. Crystal data for L1, L2 and the CP-L1

Compound	**L1**	**L2**	**CP-L1**
Empirical formula	$C_{32}H_{32}N_8O_4$	$C_{32}H_{32}N_8O_4$	$C_{33}H_{36}BrCd_{0.50}N_8O_5$
Formula weight	592.66	592.66	760.81
Crystal system	Triclinic	Triclinic	Triclinic
Space group	*P*-1	*P*-1	*P*-1
a (Å)	9.0155(10)	13.0319(15)	9.4207(5)
b (Å)	12.1413(9)	15.1859(13)	11.4609(7)
c (Å)	13.7390(16)	16.7954(16)	16.1643(9)
α (º)	81.057(8)	111.971(8)	103.151(5)
β (º)	81.067(9)	103.352(9)	103.088(5)
γ (º)	78.114(8)	101.168(8)	97.360(5)
Volume ($Å^3$)	1441.9(3)	2965.8(5)	1625.38(16)
Z	2	4	2
Density (calculated) (Mg/m^3)	1.365	1.327	1.555
Absorption coefficient (mm^{-1})	0.094	0.091	1.638
F(000)	624	1248	778
Crystal size (mm^3)	0.30x0.13x0.09	0.35x0.08x0.04	0.20x0.08x0.04
Theta range for data (º)	2.91 – 29.86	2.47 – 28.24	2.57 – 29.94
Reflections collected	27261	34643	8454
Observed reflections [I>2s(I)]	7549	12267	5156
Data/restraints/parameters	7549/0/397	12267/0/793	8454/0/432
Goodness-of-fit on F^2	0.819	1.044	1.33
R_1 [I>2s(I)]	0.0604	0.0336	0.0485
wR_2 (all data)	0.2629	0.2629	0.1369
Largest diff. peak and hole ($e.Å^{-3}$)	0.194 and -0.213	1.369 and -0.775	1.049 and -0.727

Conclusion

In conclusion, two new 1,2-disubstituted cyclohexane amide ligands and one-dimensional coordination polymer were successfully prepared. L1 and L2 still maintained the pre-organisation of the 2,6-pyridine dicarboxamide in the solid states. X-ray crystallography also revealed that these three compounds crystallised in a triclinic crystal system with space group *P*-1. Several supramolecular interactions such as intramolecular and intermolecular hydrogen bonding interactions, π-π stacking interactions, C-H···π stacking interactions, and metal to ligand interactions were observed in the crystal structure in order to form a stable molecular architecture.

Acknowledgement

The authors thank the Ministry of Education of Malaysia and the Universiti Malaysia Terengganu for financial support through FRGS (vot. number 59579, FRGS/1/2019/STG01/UMT/02/3). The University of Adelaide is also acknowledged for the access to a single-crystal X-ray diffractometer for crystal-structure determination.

References

1. Lehn, J. M. (1988). Supramolecular chemistry-scope and perspectives molecules, supermolecules, and molecular devices (nobel lecture). *Angewandte Chemie International Edition in English*, 27(1): 89-112.

2. Lu, R., Zhang, X., Cheng, X., Zhang, Y., Zan, X. and Zhang, L. (2020). Medical applications based on supramolecular self-assembled materials from tannic acid. *Frontiers in Chemistry*, 8: 1-25.
3. Shuturminska, K., O'Malley, C., Collis, D. W. P., Conde, J. and Azevedo H.S. (2018). Displaying biofunctionality on materials through template self-assembly. *Self-Assembling Biomaterials*, 341-370.
4. Qin, B., Yin, Z., Tang, X., Zhang, S., Wu, Y., Xu, J. F. and Zhang, X. (2020). Supramolecular polymer chemistry: From structural control to functional assembly. *Progress in Polymer Science*, 100: 101167.
5. Deng, J. H., Luo, J., Mao, Y. L., Lai, S., Gong, Y. N., Zhong, D. C. and Lu, T. B. (2020). π-π Stacking interactions: Non-negligible forces for stabilizing porous supramolecular frameworks. *Science Advances*, 6(2): eaax9976.
6. Frey, P. A. (2004). Low barrier hydrogen bonds. *Encyclopedia of Biological Chemistry*, 2004: 594-598.
7. Wendler, K., Thar, J., Zahn, S. and Kirchner, B. (2010). Estimating the hydrogen bond energy. *The Journal of Physical Chemistry A*, 114: 9529-9536.
8. Castiñeiras, A., Fernández-Hermida, N., García-Santos, I., Gómez-Rodríguez, L., Gil, D. M. and Frontera, A. (2021). Supramolecular, spectroscopic and computational analysis of weak interactions in some thiosemicarbazones derived from 5-acetylbarbituric acid. *Journal of Molecular Structure*, 5: 131031.
9. Ghule, N. V., La, D. D., Bhosale, R. S., Kobaisi, M. A., Raynor, A. M., Bhosale, S. V. and Bhosale, S. V. (2016). Effect of amide hydrogen bonding interaction on supramolecular self-assembly of naphthalene diimideamphiphiles with aggregation induced emission. *ChemistryOpen*, 5(2): 157-163.
10. Rong, X., Lin, H., Liu, D., Wang, X., Liu, G. and Wang X. (2016). Solvothermal synthesis, structures and properties of two new octamolybdate-based compounds with tetrazole- and pyridyl-containing asymmetric amide ligands. *Inorganic Chemistry Communications*, 71: 9-14.
11. Haris, N. S. H., Mansor, N., Yusof, M. S. M., Sumby, C. J. and Kadir, M.A. (2021). Investigating the potential of flexible and pre-organized tetraamide ligands to encapsulate anions in one-dimensional coordination polymers: synthesis, spectroscopic studies and crystal structures. *Crystals*, 11: 77.
12. Yusof, M. S. M., Ayob, N. A. C., Kadir, M. A. and Yamin, B. M. (2008). 1, 2-bis [*N'*-(2, 2-dimethylpropionyl) thioureido] cyclohexane. *Acta Crystallographica Section E: Structure Reports Online*, 64(5): o937.
13. Shanmugharaj, A. M., Rhee, K. Y. and Ryu, S.H. (2006). Influence of dispersing medium on grafting of aminopropyltriethoxysilane in swelling clay materials. *Journal of Colloid and Interface Science*, 298(2): 854 -859.
14. Oprea, S., Potolinca, V. O. and Varganici, C. D. (2016). Synthesis and properties of polyurethane urea with pyridine-2,6-dicarboxamide moieties in their structure. *The Royal Society of Chemistry*, 6(108): 106904–106913.
15. Yalcin, S. P., Ceylan, U., Sarioglu, A. O. and Sonmez, M. (2015). Sythesis, structural, spectral (FT-IR, ^{1}H and ^{13}C NMR and UV-Vis), NBO and first order hyperpolarizability analysis of *N*-(4-nitrophenyl)-2, 2-dibenzoylacetamide by density functional theory. *Journal of Molecular Structure*, 1098: 400-407.
16. Basak, A., Ghosh, S. C., Das, A. K. and Bertolasi, V. (2005). A novel azetidinyl γ-lactam based peptide with a preference for β-turn conformation. *Organic and Biomolecular Chemistry*, 3: 4050-4052
17. Kushwaha, N., Saini, R. K. and Kushwaha, S. K. S. (2011). Synthesis of some amide derivatives and their biological activity. *International Journal of ChemTech Research*, 3(1): 203-209.
18. Ikawa, T., Nishiyama, T., Shigeta, T., Mohri, S., Morita, S., Takayanagi, S-I., Terauchi, Y., Morikawa, Y., Takagi, A., Ishikawa, Y., Fujii, S., Kita, Y. and Akai, S. (2011). *Ortho*-selective nucleophilic addition of primary aminesto silylbenzynes: synthesis of 2-silylanilines. *Angewandte Chemie*, 123: 5792-5795.

19. Hadadzadeh, H., Rezvani, A. R., Abdolmaleki, M. K., Ghasemi, K., Esfandiari, H. and Daryanavard, M. (2009). Pyridine-2,6-dicarboxylic acid (dipic): crystal structure from co-crystal to a mixed ligand nickel(II) complex. *Journal of Chemical Crystallography*, 40(1): 48-57.

20. Kadir, M. A., Yusof, M. S. M., Sumby, C. J (2018). Conjoint experimental and theoretical evaluation of zinc (II) coordination polymer as potential anion receptors for nitrate and chromate. *ASM Journal of Science*, 1: 136-146.

Malaysian Journal of Analytical Sciences (MJAS)
Published by Malaysian Analytical Sciences Society

SPECTROSCOPIC FINGERPRINTING COMBINED WITH CHEMOMETRICS FOR PESTICIDE RESIDUE SCREENING ON ORGANIC PRODUCE: A CASE STUDY OF CHILI

(Gabungan Cap Jari Spektroskopi dengan Kemometrik untuk Saringan Sisa Racun Perosak pada Hasil Organik: Kajian Kes ke atas Cili)

Intan Amirah Restu[1], Nur Fatin Zahra Mohamad Zhahir[1], Shum Mun-Hoe[1], Yong Chin Hong[1], Ng Jing Sheng[1], Syahidah Akmal Muhammad[1,2]*

[1]Environmental Technology Division, School of Industrial Technology, Universiti Sains Malaysia, 11800 USM, Penang, Malaysia
[2]Analytical Biochemistry Research Centre (ABrC), Inkubator Inovasi Universiti (I²U), Kampus SAINS@USM, Universiti Sains Malaysia, Lebuh Bukit Jambul, 11900 Bayan Lepas, Pulau Pinang

**Corresponding author: syahidah.muhammad@usm.my*

Received: 15 September 2021; Accepted: 30 December 2021; Published: 25 February 2022

Abstract

Pesticide detection for organic produce authentication requires laboratory work involving sample testing, which is generally arduous and time-consuming. In this study, a simple and reliable technique to produce an instant result for the pesticide screening of organic chili was developed, using attenuated total reflection-Fourier transform infrared (ATR-FTIR) spectroscopy. The resultant spectra observed in the region between 600-1800 cm^{-1} were further analyzed using principal component analysis (PCA) and orthogonal partial least square-discriminant analysis (OPLS-DA). Accordingly, the outcomes underline the potential for distinguishing chili samples sprayed with pesticides, such as cypermethrin, fenobucarb, and malathion, versus their organic counterparts. Furthermore, the models constructed by OPLS-DA were capable of classifying chili samples, yielding high-classification rates ranging between 91.67-100%. Thus, ATR-FTIR combined with chemometrics may be utilized as a potentially reliable screening tool for 'front-line' organic produce screening, where only flagged samples need to undergo further confirmation testing.

Keywords: chili, organic produce, pesticide screening, ATR-FTIR spectroscopy, principal component analysis

Abstrak

Pengesanan racun perosak untuk tujuan pengesahan hasil organik memerlukan kerja makmal yang melibatkan ujian sampel, yang biasanya sukar dan memakan banyak masa. Dalam kajian ini, satu teknik yang mudah dan berkesan dijalankan dengan menggunakan kaedah spektroskopi inframerah transformasi Fourier-pantulan keseluruhan dikecilkan (ATR-FTIR) bagi tujuan saringan racun perosak untuk sayuran cili organik. Spektrum yang dihasilkan dalam lingkungan antara 600-1800 cm^{-1} dianalisis dengan lebih lanjut dengan analisis komponen prinsipal (PCA) dan analisis ortagonal kuasa dua terkecil separa-diskriminan (OPLS-DA). Hasil kajian menunjukkan potensi yang baik dalam membezakan sampel cili yang disembur dengan racun perosak seperti cypermethrin, fenobucarb, dan malathion daripada sampel organik. Model yang dibina oleh OPLS-DA dapat

mengklasifikasikan sampel cili dengan kadar klasifikasi yang tinggi dalam lingkungan antara 91.67-100%. Oleh itu, penggabungan spektroskopi ATR-FTIR bersama aplikasi kimometrik dapat digunakan sebagai alat saringan yang berpotensi tinggi untuk pengesahan hasil organik, di mana hanya sampel yang dikenal pasti sahaja perlu menjalani ujian pengesahan dengan lebih lanjut.

Kata kunci: cili, hasil organik, saringan racun perosak, spektroskopi ATR-FTIR, analisis komponen prinsipal

Introduction

The demand for organic fruits and vegetables is growing in domestic and global markets alike, following consumers perceiving them as a healthier, safer, and more environmentally friendly option than non-organic types. Subsequently, there people have become increasingly apprehensive about the safety of the food that they consume on a daily basis. Accordingly, pesticide-free production is one of the most important factors influencing consumer preference for organic food options. Contrary to popular belief, however, some pesticides are permitted in organic farming as long as they have natural substances, such as hydrogen peroxide, lime sulfur, and copper sulfate, as ingredients [1]. Besides this, certain fairly low-risk synthetic pesticides are allowed in limited circumstances to manage pests and weeds, whereby their use markedly differs from the approach employed in non-organic farming.

It should be noted that organic fruits and vegetables may contain residues of synthetic pesticides, due to drift from neighboring non-organic farms or to irrigation contamination, originating at streams and groundwater polluted by synthetic fertilizers and pesticide runoff. According to the U.S. National Organic Program, the U.S. Environmental Protection Agency defines a level of tolerance in which organic claims are allowed for products containing synthetic pesticide residues as no more than 5% of said specified tolerance level [1]. In general, major manufactured pesticides are classified based on their chemical composition; examples include carbamates and dithiocarbamates, organophosphorus, and pyrethroids [2]. Malathion, an organophosphate insecticide, is especially prevalent as one of the oldest and widely-used active ingredients for pest control in fruits and vegetables [3]. Cypermethrin belongs to the class of pyrethroid insecticides, which are more effective and less toxic compared to organophosphates. Fenobucarb is a carbamate insecticide extensively implemented in controlling plant hopper, thrips, aphids, and whiteflies.

The increased utilization of pesticides has been associated with various health and environmental effects. Hence, maximum residue limits (MRLs) are defined by respective countries to monitor the level of pesticide chemical residues allowable in their food crops. The MRL represents the highest level of pesticide residue legally permitted in food crops [4]. In particular, the Malaysia Food Regulation 1985 in the 16th Schedule (Regulation 41) provides the MRLs for selected pesticides, as shown in Table 1. Standard techniques used for pesticide detection in fruits and vegetables, such as gas chromatography and high-performance liquid chromatography (HPLC), are often time-consuming and laborious. These methods necessitate sample destruction, lengthy test duration, controlled test conditions and expert lab skills, rendering them unsuitable for on-site analysis [5].

Therefore, a robust and quick technique capable of providing immediate results during organic produce screening for pesticides is currently necessary in the commercial world, particularly for the fast-moving consumer goods (FMCG) industry. As an alternative technique, attenuated total reflection-Fourier transform infrared (ATR-FTIR) spectroscopy represents an attractive option for pesticide detection in organic produce authentication, due to its non-destructive capability and portability, as well as its reliability in producing accurate results in a matter of minutes when combined with chemometrics [6]. Previous studies have shown that ATR-FTIR could be used to confirm the presence of organophosphate insecticides in vegetables [7]. Furthermore, data from several works also demonstrate the potential of ATR-FTIR, combined

with chemometrics, to solve adulteration and authentication issues for various food products, such as green tea, rice, and fruits [8, 9, 10].

Principal component analysis (PCA) is the most widely-used statistical procedure for interpreting large spectral data. As an unsupervised technique, it provides an overview of any patterns and groupings observable in studied samples, via a graphical representation in the form of 2D or 3D scatter plots [10]. However, it is not always possible to obtain differentiating features and adequate information directly from PCA models. On the other hand, supervised techniques such as orthogonal partial least squares-discriminant analysis (OPLS-DA) are often utilized to build classification models for further exploration of the data generated [11]. The combination of PCA and OPLS-DA may offer remarkable information for the classification and discrimination of the considered samples.

Chili (*Capsicum annuum L. var Kulai*) is one of the most widely cultivated and consumed vegetables in Malaysia [12]. The chili plant is highly susceptible to many diseases caused by insects, such as mites and thrips, resulting in the routine use of chemical insecticides to combat the problem. Therefore, this study aims to develop a screening method for the detection of pesticide presence in chili samples by using ATR-FTIR combined with chemometrics (PCA and OPLS-DA). The developed procedure can, thus, be utilized as a 'front-line' detection tool by food regulators prior to advanced laboratory testing, reserved only for flagged samples, resulting in cost and time-saving opportunities.

Table 1. The maximum residue limit for selected pesticides used in chili plant

Pesticide	Molecular Formula	Classification	Maximum Residue Limit (mg/kg)
Malathion	$C_{10}H_{19}O_6PS_2$	Organophosphate (OP)	2
Cypermethrin	$C_{22}H_{19}Cl_2NO_3$	Synthetic Pyrethroid (SP)	2
Fenobucarb	$C_{12}H_{17}NO_2$	Carbamate	0.5

Materials and Methods

Sample preparation

Three types of pesticides that were selected contained different concentrations and were in liquid form. The commercial pesticides, namely Wesco Malathion 57 (malathion, 57% w/w), Wesco Cyperin 550 (cypermethrin, 5.5% w/w), and Hoppergone (Fenobucarb, 50% w/w), were purchased from Volcano Agribusiness Sdn. Bhd. These pesticides were selected as they are frequently quantified in fruit and vegetable samples, and can be easily obtained from pesticide distributors [13]. The pesticides were diluted using distilled water, according to commercial formulations under Pesticides Act 1974, to replicate actual field conditions (Table 2). The prepared solutions were kept at room temperature and used within one week.

A total of 120 samples of organic chili (*Capsicum annuum L. var Kulai*) were purchased directly from a local certified farmer in Pulau Pinang. The farmer was aware of the aim of this study; hence the chance of including any fraudulent or inauthentic organic products in the dataset is minimized. The chili samples were left unwashed and randomly divided into four groups. In the first group, the chili samples were not treated and marked as group O (Organic). In the second, third and fourth groups, the chili samples were evenly sprayed with different pesticide solutions and marked as group M (Malathion), C (Cypermethrin), and F (Fenobucarb), respectively. All samples were left to dry for 2 hours so that the pesticide solution was evenly distributed over the surface of the chili prior to analysis.

Infrared spectroscopy measurements

The chili samples were scanned using a Perkin-Elmer Spectrum ATR-FTIR spectrophotometer. The equipment was connected to computer software

(Spectrum for Windows, Perkin-Elmer), and mid-infrared spectra were recorded in the wavenumber range of 4000-600 cm^{-1}, with a spectral resolution of 4 cm^{-1} at 16 scans. To simulate the on-site pesticide screening analysis, the whole chili was placed on the sample stage for direct measurement with no sample preparation. As a reference, the background spectrum of air was collected. Prior to each analysis, the ATR crystal surface was thoroughly cleaned with ethanol and wiped with clean tissue paper. The spectra for each of the three pesticide samples (cypermethrin, fenobucarb, and malathion) were also measured in ATR mode. Spectrum acquisition of each sample was repeated in triplicate under the same conditions, and an average spectrum was obtained.

Data pre-processing and chemometrics

Experimental data were subjected to chemometrics using SIMCA software (version 14.1, Umetrics, Sweden), wherein both unsupervised PCA and supervised OPLS-DA were performed for sample classification. The usual spectral region for mid-IR (4000-600 cm^{-1}) was observed and taken into account for the analysis; however, the fingerprint region between 1800-600 cm^{-1} was scrutinized further, due to this being the primary region where biomolecules absorb IR radiation [14]. Spectral pre-processing, such as first derivative transformation with third-degree polynomial, and standard normal variate (SNV) was applied to the IR data matrices to increase the predictive ability and accentuate any subtle features [15]. All variables were scaled and normalized using UV-scaling (unit variance) and log-10, respectively. The assessment of PCA's ability to detect and discriminate organic from pesticide-contaminated chili samples was made based on score plots observations, in which the principal component (PC) score plots were constructed using the first two resultant principal components. The OPLS-DA models were presented with several components based on the predictive performance from the internal sevenfold cross-validation by default, as suggested by the SIMCA software.

Table 2. Pesticide preparation according to commercial formulations

Pesticide	Amount Taken (mL)	Total Volume (solvent, mL)
Wesco Cyperin 550 (cypermethrin 5.5% w/w)	5	1000
Hoppergone (fenobucarb 50% w/w)	1.5	1000
Wesco Malathion 57 (malathion 57% w/w)	1.5	1000

Results and Discussion

ATR-FTIR spectral analysis of organic chili

The mid-FTIR spectrum of organic chili in the range of 4000-600 cm^{-1} is shown in Figure 1. As expected, the spectrum showed absorption bands corresponding to the vibrations of functional groups belonging to carotenoids, phenolic compounds and ascorbic acid, which corresponded to previously reported studies [16, 17]. A strong absorption band was observed at 3342.05 cm^{-1}, corresponding to characteristic stretching vibrations of O-H from amino acids. The small sharp cluster of peaks at 2900-2800 cm^{-1} was assigned to the C-H stretching band of methyl and methylene groups from the carboxylic acid structure. The medium-intensity peak at 1635 cm^{-1} corresponded to the C=O stretching, indicating the characteristic amide I band, while a low-intensity band at 1454 cm^{-1} was observed for the characteristic bending vibrations of C-H. The presence of polyphenols could be identified by the intense bands in the region of 1260-1180 cm^{-1}, caused by the stretching vibration of C-C-O and low-intensity C-H bending [16]. The functional groups associated with the absorption peaks identified from the spectra of the organic chili samples are summarized in Table 3.

ATR-FTIR spectral analysis of pesticides

The IR spectra of the three pesticides were also recorded to identify functional groups with unique absorption bands. As depicted in Figure 2, the green spectrum represents cypermethrin, the blue spectrum represents fenobucarb, and the red spectrum represents malathion. Each peak was contributed by a particular functional group present in the compound. In general, the pesticides revealed similar spectral patterns with a minimal shift of absorption band positions and intensity across the samples.

The C-H stretching in the two benzene rings of cypermethrin contributed to the stronger peaks within the wavenumber range of 3080–2820 cm^{-1}; thus, distinguishing this from the other two pesticides. The other, stronger peak which was more obvious for cypermethrin is the peak at 806 cm^{-1}, which is contributed by the C-Cl functional group, present in cypermethrin but not in fenobucarb or malathion. The peaks contributing to the fenobucarb cluster were mainly the N-H stretching at 3346 cm^{-1}, C=O stretching at 1718 cm^{-1}, C-O-C stretching at 1216 cm^{-1}, and C-N stretching at 1183 cm^{-1}. Malathion has a strong peak at 1013 cm^{-1}, mainly due to the presence of two P-O-C stretches. The P-O-C stretching was only observed in malathion as compared to cypermethrin and fenobucarb. Another prominent strong peak present only in malathion was observed at 654 cm^{-1}, mainly due to S=P-S-C stretching.

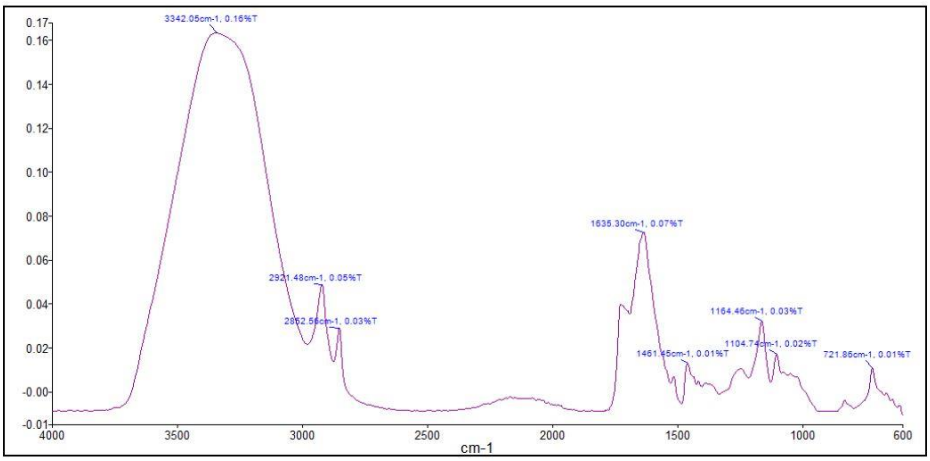

Figure 1. The FTIR spectrum of chili at wavenumber 4000-600 cm^{-1}

Table 3. The functional groups associated with absorption peaks identified in organic chili

Absorption Peak (cm^{-1})	**Possible Functional Group**
3342.05	O-H stretching from amino acids
2921.48 and 2852.56	C-H stretching (from CH_3 and CH_2 groups)
1635.3	C=O stretching of amide I band
1461.45	C-H bending
1164.46	C-C-O stretching
1104.74	C-H bending

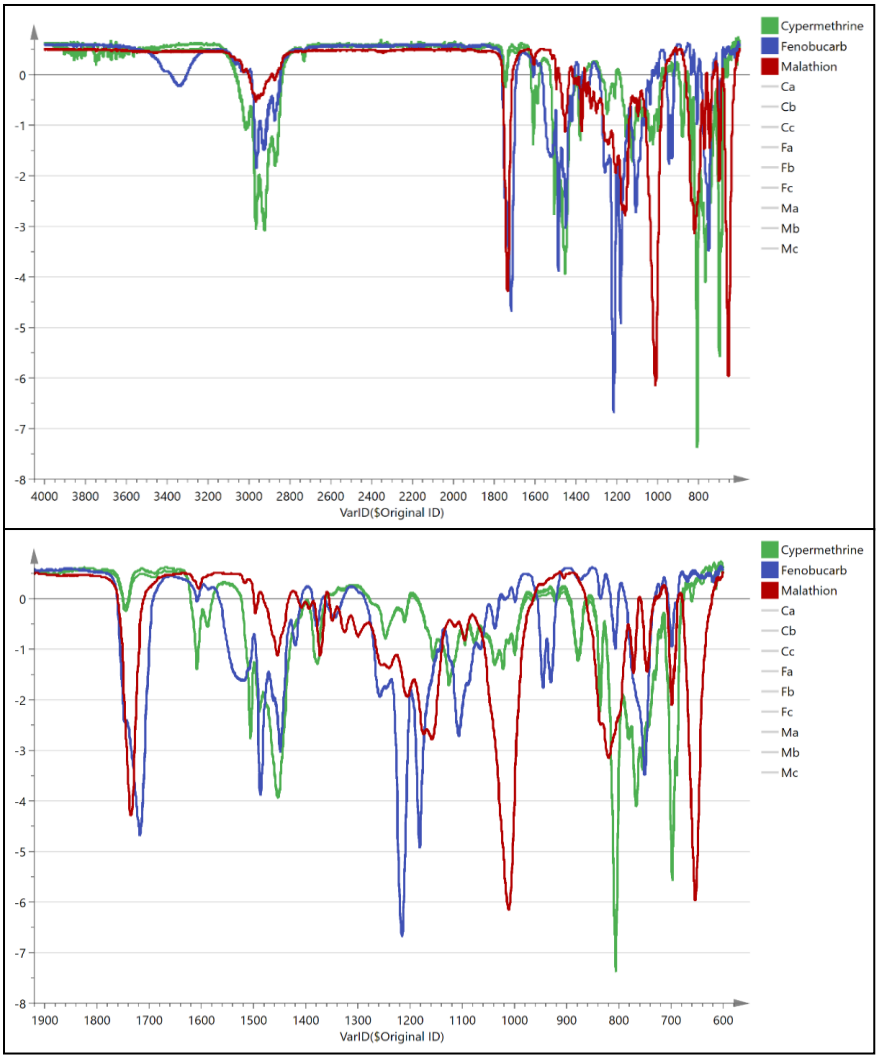

Figure 2. Full range FTIR spectra at wavenumber 4000–600 cm^{-1} (top) and the FTIR spectra enlarged at wavenumber 1900-600 cm^{-1} (bottom) for the three pesticides

Principal component analysis

Prior to analysis, the IR spectra of the chili samples were pre-processed to minimize data variation and overcome the dominating effect of strong peak absorbance over weaker absorbance intensity [18]. Selecting a proper spectral range may be beneficial in reducing the computational burden of the software in terms of variables. Hence, the spectral region 1800–600 cm^{-1} was selected for further analysis, due to the high positive correlations between changes in the composition and spectral response observed, which may be due to biomolecules' absorption of IR radiation occurring primarily in this region [14, 17].

As an unsupervised method, PCA was adopted for the initial exploratory data analysis, whereby the score plot reflected separation among the samples. PCA was applied to the dataset of 120 chili samples to detect outliers, as well as to predict possible patterns and trends of clustering. For a visual illustration and understanding, different classes of organic and pesticide samples were mapped and labeled with representative symbols. Figure 3(a) shows the score scatter plot for PCA overview using the first two principal components, PC1 (as in t1) and PC2 (as in t2). Most samples fell within Hotelling's T2 ellipse at

95% confidence intervals, with a few outliers. The combination of PC1 and PC2 explained 43.6% of the variation in the dataset. However, the organic and pesticide-contaminated samples could not be distinctly classified into two clusters, as some samples overlapped with each other. The presence of outliers may indicate experimental error due to sample preparation. Direct measurement of the samples without additional preparation may cause possible background noise, leading to inconsistencies.

PCA was performed further by plotting the individual score plots of each pesticide and organic sample, to allow better qualitative discrimination between sample groups. Results showed that a distinct separation into two clusters was observed in each of the scatter plots, meaning that PCA adequately captured relevant information within the dataset. As illustrated in Figure 3(b), the organic samples were well-segregated from cypermethrin-containing samples, with clearly defined clusters along PC2. When both PC1 and PC2 were combined, they contributed about 56.7% of the total variance, with some samples overlapping with each other. As for the outcome of PCA on organic samples and fenobucarb-containing samples (Figure 3(c), the result shows that the samples were well-distinguished, also mostly based on PC2. When both PC1 and PC2 were combined, these accounted for 57.5% of the total variance. Likewise, as shown in Figure 3(d), partially overlapping samples were observed in the score plot of organic and pesticide malathion-sprayed samples, with a total variance of 56.7%. This may be due to a low concentration of spiked malathion, making it difficult to differentiate between the IR spectra of both organic and pesticide-containing samples.

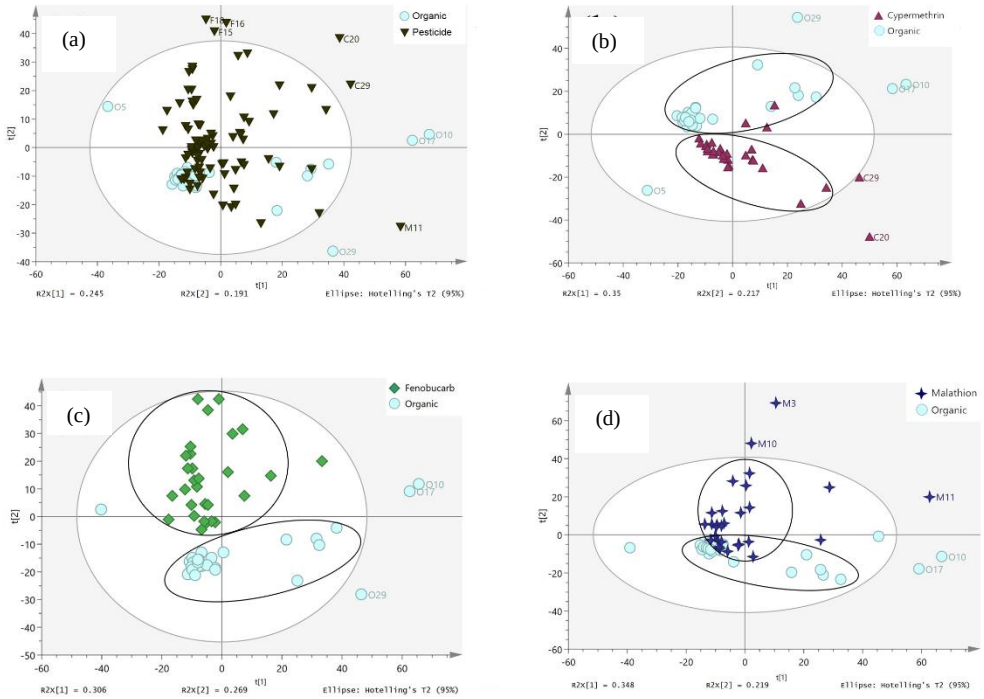

Figure 3. PCA score scatter plot based on PC1 and PC2 (a) organic and pesticide-contaminated samples, (b) organic and cypermethrin-contaminated samples, (c) organic and fenobucarb-contaminated samples, and (d) organic and malathion-contaminated samples

PCA was also performed on the IR spectra of neat cypermethrin, fenobucarb and malathion samples, to investigate the main variance among the three pesticides used in this study (Figure 4). The first two principal components explained 90.6% of data variation and showed observable clustering of the samples, according to the main active compound for the three pesticides.

Predictive models

As PCA had successfully distinguished the dataset into the observable cluster, a supervised OPLS-DA method was later performed using each dataset separately: organic with cypermethrin, organic with fenobucarb, and organic with malathion. The original dataset was divided into a training set and testing set, using an 80:20 ratio. Initially, 80% of the samples from the original dataset (24 samples from each class) were randomly selected as a training dataset, to build the predictive models aimed at differentiating organic and pesticide-contaminated chili samples. Classification rates were obtained from the internal sevenfold cross-validation by default in the SIMCA software. The remaining 20% of the samples (6 samples from each class) were set aside as an external validation test set, to evaluate the robustness of the predictive models. The overall efficiency of the models was assessed by observing the numbers of correctly and incorrectly assigned members of different classes for training and test datasets.

The score scatter plots displayed the samples by specific color-coded classes are shown in Figure 5. The four classes in the training set were organic chili (denoted as Organic Training Set), and organic chili that had been sprayed with pesticides: cypermethrin (denoted as Cypermethrine Training Set), fenobucarb (denoted as Fenobucarb Training Set), and malathion (denoted as Malathion Training Set). The scatter plots in OPLS-DA showed better separation between classes compared to PCA. As depicted in Figure 5, the samples in each cluster were more tightly grouped in OPLS-DA than in PCA.

The predictive model for organic and cypermethrin has a fitness of data (R^2) of 64.6%. The predictive ability (Q^2) was above moderate at 79.6%, with a total sum of variation ($R^2(Y)$) of 84.2%. The model for organic and fenobucarb has an R^2 of 62%, high predictive ability (Q^2) of 80.3%, and $R^2(Y)$ of 85.8%. For organic and malathion-contaminated samples, the predictive model has an R^2 of 78.1%, moderate Q^2 of 70.6%, and $R^2(Y)$ of 88.9%. The cross-validated analysis of variation (CV-ANOVA) for cypermethrin, fenobucarb, and malathion models reported *P*-values of 1.10×10^{-12}, 5.70×10^{-13}, and 3.15×10^{-7}, respectively. The results showed that the discrimination between organic and pesticide-contaminated chili samples was significant ($p < 0.05$).

The classification of the samples has been accurately performed (100% accuracy) for organic and cypermethrin models (Table 4), as well as organic and fenobucarb models (Table 5). In the case of organic and malathion models (Table 6), a single sample was misclassified into the organic class (91.67% accuracy), while all six organic chili samples fell accurately into their right cluster (100% accuracy). These results demonstrate the reliability of the models as a primary screening tool to detect the presence of pesticides in organic produce. It may help food regulators to ascertain whether the fruits or vegetables require further testing using more sophisticated instrumentation.

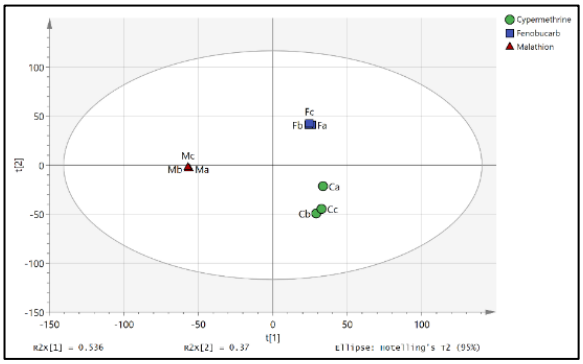

Figure 4. PCA score scatter plot according to the main active compound for the three pesticides

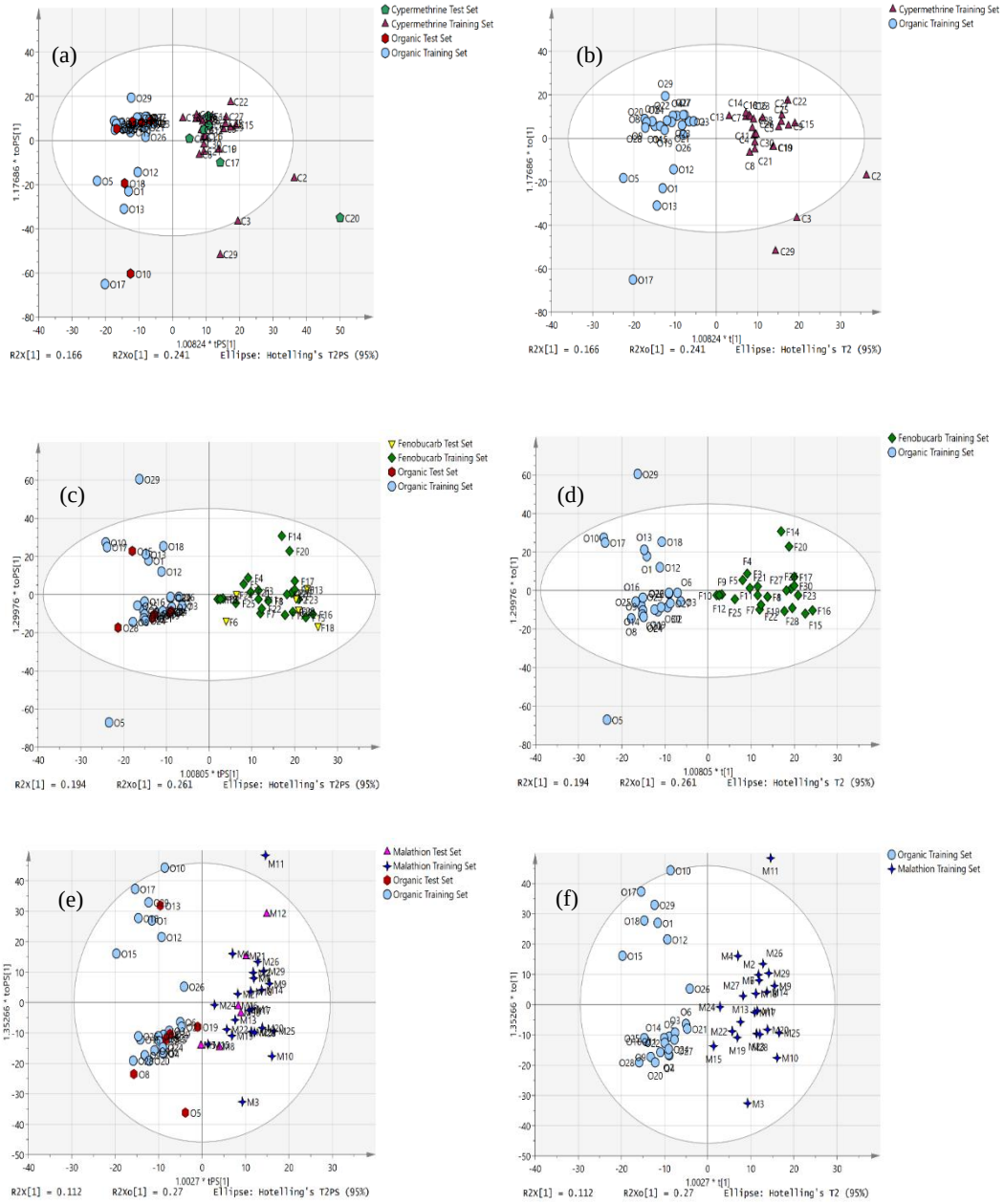

Figure 5. OPLS-DA scatter plots by the class of organic and pesticide-contaminated samples (a) training set for organic and cypermethrin, (b) predicted plot for organic and cypermethrin, (c) training set for organic and fenobucarb, (d) predicted plot for organic and fenobucarb, (e) training set for organic and malathion and (f) predicted plot for organic and malathion

Table 4. Misclassification table for organic and cypermethrin samples

	Members	Correct (%)	Organic Training Set	Cypermethrine Training Set
Organic Training Set	24	100	24	0
Cypermethrine Training Set	24	100	0	24
Test Set	12	100	6	6
Total	60	100	30	30

Table 5. Misclassification table for organic and fenobucarb samples

	Members	Correct (%)	Organic Training Set	Fenobucarb Training Set
Organic Training Set	24	100	24	0
Fenobucarb Training Set	24	100	0	24
Test Set	12	100	6	6
Total	60	100	30	30

Table 6. Misclassification table for organic and malathion samples

	Members	Correct (%)	Organic Training Set	Malathion Training Set
Organic Training Set	24	100	24	0
Malathion Training Set	24	100	0	24
Test Set	12	91.67	7	5
Total	60	100	31	29

Conclusion

The combination of ATR-FTIR and chemometrics can be utilized for preliminary screening of pesticides in organic produce, yielding benefits such as high speed, non-invasiveness, and simplicity of sample preparation. In general, distinguishing each pesticide was possible according to its functional groups, as analyzed by ATR-FTIR. Cypermethrin, for example, revealed stronger peaks contributed by C-H (from benzene rings) and C-Cl functional groups, whereas fenobucarb was identifiable by N-H stretching, C-O-C stretching, and C-N stretching. Malathion had strong peaks contributed by two P-O-C stretches and S=P-S-C stretching. The results also showed clear discrimination and classification between organic and pesticide-contaminated chili samples through PCA, and can be considered as a successful attempt, despite a few outliers observed in the process. With the use of OPLS-DA, it is possible to classify samples according to organic and pesticide-contaminated classes and predict

the residues of unknown pesticides. This study serves as an approach for pesticide screening of organic produce, thereby suggesting further investigation, based on the detection limit of pesticide residues for various fruit and vegetables, in ensuring more robust classification models.

Acknowledgment

The authors greatly acknowledge the funding provided by Universiti Sains Malaysia Bridging Grant (Khas) with Project Code: USM 304/PTEKIND/6316224, which has enabled this work to be conducted.

References

1. Winter, C. K. (2012). Pesticide residues in imported, organic, and "suspect" fruits and vegetables. *Journal of Agricultural and Food Chemistry*, 60(18): 4425-4429.
2. Akashe, M. M., Pawade, U. V. and Nikam, A. V. (2018). Classification of pesticides: A review. *International Journal of Research in Ayurveda and Pharmacy*, 9(4): 144-150.
3. Chatterjee, S., Das, S. K., Chakravarty, R., Chakrabarti, A., Ghosh, S. and Guha, A. K. (2010). Interaction of malathion, an organophosphorus pesticide with *Rhizopus oryzae* biomass. *Journal of Hazardous Materials*, 174(1–3): 47-53.
4. Munawar, A. and Hameed, S. W. (2013). Quantification of pesticide residues in vegetables by different chromatographic techniques. *Journal of Chromatography and Separation Techniques*, 4(8): 8-11.
5. Sadi, B. B., Vonderheide, A. P. and Caruso, J. A. (2004). Analysis of phosphorus herbicides by ion-pairing reversed-phase liquid chromatography coupled to inductively coupled plasma mass spectrometry with octapole reaction cell. *Journal of Chromatography A*, 1050(1): 95-101.
6. Ellis, D. I., Brewster, V. L., Dunn, W. B., Allwood, J. W., Golovanov, A. P. and Goodacre, R. (2012). Fingerprinting food: Current technologies for the detection of food adulteration and contamination. *Chemical Society Reviews*, 41(17): 5706-5727.
7. Xiao, G., Dong, D., Liao, T., Li, Y., Zheng, L., Zhang, D. and Zhao, C. (2015). Detection of pesticide (chlorpyrifos) residues on fruit peels through spectra of volatiles by FTIR. *Food Analytical Methods*, 8(5): 1341-1346.
8. Cheajesadagul, P., Arnaudguilhem, C., Shiowatana, J., Siripinyanond, A. and Szpunar, J. (2013). Discrimination of geographical origin of rice based on multi-element fingerprinting by high resolution inductively coupled plasma mass spectrometry. *Food Chemistry*, 141(4): 3504-3509.
9. Liu, Z., Yuan, Y., Zhang, Y., Shi, Y., Hu, G., Zhu, J. and Rogers, K. M. (2019). Geographical traceability of Chinese green tea using stable isotope and multi-element chemometrics. *Rapid Communications in Mass Spectrometry*, 33(8): 778-788.
10. Sârbu, C., Nacu-Briciu, R. D., Kot-Wasik, A., Gorinstein, S., Wasik, A. and Namieśnik, J. (2012). Classification and fingerprinting of kiwi and pomelo fruits by multivariate analysis of chromatographic and spectroscopic data. *Food Chemistry*, 130(4): 994-1002.
11. Cubero-Leon, E., De Rudder, O. and Maquet, A. (2018). Metabolomics for organic food authentication: Results from a long-term field study in carrots. *Food Chemistry*, 239(555): 760-770.
12. Lob, S., Aris, M. N. M., Sidique, S. N. M., Ibrahim, N. F. and Jin, X. (2017). Growth development and natural infection incidence of tobacco mosaic virus (TMV) on silicon-treated chilli (*Capsicum annuum* L.) cultivated in commercial soil. *Malaysian Applied Biology*, 46(3): 221-226.
13. Zaidon, S. Z., Hamsan, H. and Bin, H. Y. (2016). A review on pesticides occurrence in fruits and vegetables in Malaysia and their potential health risk among adults. *Indian Journal of Environmental Protection*, 36(10): 826-832.
14. Skolik, P., McAinsh, M. R. and Martin, F. L. (2019). ATR-FTIR spectroscopy non-destructively detects damage-induced sour rot infection in whole tomato fruit. *Planta*, 249(3): 925-939.

15. Devos, O., Downey, G. and Duponchel, L. (2014). Simultaneous data pre-processing and SVM classification model selection based on a parallel genetic algorithm applied to spectroscopic data of olive oils. *Food Chemistry*, 148: 124–130.
16. Ciulu-Costinescu, F., Neamţu, J., Popescu, M., Chirigiu, L., Simionescu, A., Bubulică, M. V. and Belu, I. (2015). Preliminary analysis of *Capsicum annuum* L. extracts. *Current Health Sciences Journal*, 41(4): 311-316.
17. Domínguez-Martínez, I., Meza-Márquez, O. G., Osorio-Revilla, G., Proal-Nájera, J. and Gallardo-Velázquez, T. (2014). Determination of capsaicin, ascorbic acid, total phenolic compounds and antioxidant activity of *Capsicum annuum* L. var. serrano by mid infrared spectroscopy (Mid-FTIR) and chemometric analysis. *Journal of the Korean Society for Applied Biological Chemistry*, 57(1): 133-142.
18. Ismail, D., Rahimi, A., Wan Ishak, W. R., Mahat, N. A. and Mat Desa, W. N. S. (2021). Classification model for detection and discrimination of inedible plastic adulterated palm cooking oil using ATR-FTIR spectroscopy combined with principal component analysis. *Malaysian Journal of Analytical Sciences*, 25(3): 388-398.

Malaysian Journal of Analytical Sciences (MJAS)
Published by Malaysian Analytical Sciences Society

ELICITATION OF INDUCED POLYKETIDE COMPOUNDS FROM A CO-CULTURE BETWEEN *Streptomyces* sp. STRAIN SUK10 AND *Fusarium* sp. AND THEIR ANTIBACTERIAL ACTIVITIES

(Elisitasi Sebatian Poliketida Teraruh daripada Satu Kultur-bersama di antara *Streptomyces* sp. Strain SUK10 dan *Fusarium* sp. dan Aktiviti Antibakteria)

Muhammad Asyraf Zawawi[1], Nurul Izzati Rosdi[1], Noor Wini Mazlan[1,2]*, Mariam Taib[1], Kamariah Bakar[2], Noraziah Mohamad Zin[3], Siti Nordahliawate M. Sidique[4], Saif Aldeen Mohammad Fayiz Jaber[5], RuAngelie Edrada-Ebel[5]

[1]Faculty of Science and Marine Environment
[2]Institute of Marine Biotechnology
Universiti Malaysia Terengganu, 21030 Kuala Nerus, Terengganu, Malaysia
[3]Center for Diagnostic, Therapeutic and Investigative Studies, Faculty of Health Sciences,
Universiti Kebangsaan Malaysia, Jalan Raja Muda Abd Aziz, 50300 Kuala Lumpur, Malaysia
[4]Faculty of Fisheries and Food Science,
Universiti Malaysia Terengganu, 21030 Kuala Nerus, Terengganu, Malaysia
[5]Strathclyde Institute of Pharmacy and Biomedical Sciences,
University of Strathclyde, The John Arbuthnott Building, 161 Cathedral Street, Glasgow G4 0RE, Scotland

**Corresponding author: noorwini@umt.edu.my*

Received: 3 November 2021; Accepted: 30 December 2021; Published: 25 February 2022

Abstract

Endophytes including bacteria and fungi produce an array of biologically active secondary metabolites. Different approaches have been applied in order to increase the probability production of new metabolites including mimicking the environment, media and the microbes. However, the use of single culture usually re-produces known compounds with known bioactivities. Therefore, co-culturing between *Streptomyces* sp. strain SUK10 and *Fusarium* sp. in the same media at different growth stages leads to direct interaction which may trigger the expression of "silent" biosynthetic pathway to produce novel secondary metabolites. In this study, we elicited the production of the unknown secondary metabolites from co-culture extracts by using high resolution liquid chromatography-mass spectrometry, while data was processed by utilizing the quantitative expression analysis software MZmine 2.40.1 and SIMCA P+ 15.0 coupled with macro analysis and supported with DNP database for dereplication studies. The results showed that only the extract from co-culture of F7S15 showed enhances antibacterial activity on the Gram-positive bacteria with minimum inhibition concentration (MIC) values of 5 mg/mL and 10 mg/mL against *Micrococcus* sp. and *Staphylococcus aureus*, respectively, compared with their independent and other co-culture extracts were non-active. However, all extracts were non-active on the Gram-negative bacteria. Our preliminary results showed that the potential of co-culture method leading the production of novel metabolites which could be explored for future antibacterial agents.

Keywords: co-culture, metabolomics, liquid chromatography-mass spectrometry, multivariate analysis, dereplication

Abstrak

Endofit termasuk bakteria dan fungus menghasilkan satu tatasusunan metabolit sekunder yang mempunyai keaktifan biologi. Pelbagai pendekatan telah digunakan bagi tujuan meningkatkan kebarangkalian penghasilan metabolit baru termasuk mengajuk persekitaran, media dan mikrob. Walaubagaimanapun, penggunaan kultur tunggal selalumya menghasilkan semula sebatian dengan bioaktiviti yang telah diketahui. Oleh itu, satu pengkulturan bersama di antara *Streptomyces* sp. strain SUK10 dan *Fusarium* sp. di dalam media yang sama di peringkat pertumbuhan yang berbeza, memacu kepada interaksi yang mungkin pencetus kepada ungkapan laluan biosintetik senyap untuk menghasilkan metabolit sekunder baru. Dalam kajian ini, kami telah memperolehi penghasilan metabolit sekunder yang belum diketahui daripada ekstrak kultur bersama dengan menggunakan kromatografi cecair-spektrometri jisim resolusi tinggi, sementara itu data telah dianalisis menggunakan perisian analisis ungkapan kuantitatif MZmine 2.40.1 dan SIMCA P+ 15.0 beserta analisis makro dan disokong oleh pengkalan data DNP bagi kajian dereplikasi. Keputusan telah menunjukkan bahawa hanya ekstrak daripada kultur bersama F7S15 telah menunjukkan peningkatan aktiviti antibakteria ke atas bakteria Gram-positif dengan nilai minimum kepekatan perencatan (MIC) 5 mg/mL dan 10 mg/mL melawan *Micrococcus* sp. dan *Staphylococcus aureus*, masing-masing, berbanding ekstrak kutur bebas dan kultur bersama yang lain adalah tidak aktif. Walaubagaimanapun, semua ekstrak tidak aktif ke atas bakteria Gram-negatif. Keputusan awal kajian kami telah menunjukkan potensi kaedah kultur bersama memacu penghasilan metabolit baru yang boleh diterokai bagi agen antibakteria masa hadapan.

Kata kunci: kultur bersama, metabolomik, kromatografi cecair-spektrometri jisim, analisis multivariat, dereplikasi

Introduction

Natural products have been rich sources of therapeutic agents as they inspire the advancement of synthetic methodologies to allow the possibility of making analogues of original lead compounds with improved pharmaceutical properties. For example, the secondary metabolites obtained from endophytic microbes are found to have antimicrobial, antiviral, anticancer, antioxidants, antidiabetic and immunosuppressant properties. The endophytic fungi and bacteria are known to produce these types of natural products that are potent for antibiotics [1]. They live inside the living plant tissues for at least a part of their life without causing any apparent disease symptoms in the host. Various bioactive metabolites are produced by endophytes that are proven to have potential to be anticancer, antioxidant, antifungal, antibacterial, antiviral and anti-insecticidal [2]. The induction of secondary metabolites is triggered by the interaction between the microorganisms, simulating the microbial competition for nutrition and space. Besides, the cultivation of the microbes is sustainable and reproducible in laboratory conditions. A well-known drugs-producer *Streptomyces* sp. belonging to actinobacteria varies in structures and has a great potential to be developed as therapeutic drugs for human use [3]. *Streptomyces* sp. is an aerobic, Gram-positive mycelial bacteria that disperse sporse as a method of reproduction and can develop branching vegetative hyphae in which the mycelium helps in scavenging nutrients from the surroundings [4]. *Streptomyces* sp. is able to synthesise potent secondary metabolites for medical applications such as antibiotics, herbicidal, antiparasitic, antitumor, antifungal and enzyme inhibiting agents as well as having the ability to inhibit various human pathogens including gancidin W [5], divergolides A-D [6], polycyclic anthraquinones [7], cyclic dipeptide [8-10] and xiamycin [11]. Meanwhile, a pathogenic fungus *Fusarium* sp. produces metabolites including naphthoquinones [12, 13], pyrones [14-16] and indole-acetic acids [17], naphthalenone derivatives [18] and aminobenzamide [19].

However, the discovery of new potential bioactive metabolites from independent cultures is challenging due to re-isolation of the known compounds with the same reported bioactivity. The re-occurrence of the known metabolites from an independent culture either of *Streptomyces* sp. SUK10 or *Fusarium* sp. may lead to similar bioactivities. Therefore, a co-culture method is introduced to challenge different strains instead of

individual strains. A co-culture is a process of culturing of two or more different microorganisms that mimic the complex microbial habitat in nature where they co-exist, leading to competition among them due to limited source and antagonism. Microbial community is a complex and dynamically changing consortium in which metabolic interactions between microbial species take place. The interaction between microbial communities often involves exchange of molecules for nutritional purposes that may benefit one or both species, which is known as symbiosis [20]. The co-cultures of different microbes in comparison to mono-cultures are increasingly being used in microbial natural product research as the interaction of two different microbes can increase the availability of existing natural products or may induce the expression of silent biosynthetic pathways resulting in new metabolites that are useful in the medical field [21].

A co-cultivation between *Streptomyces* sp. SUK10 and *Fusarium* sp. at different growth stages was carried out. Present study, the metabolomics approach was used to predict and identify potential novel bioactive components from the crude extracts, leading to the rapid and high-throughput assessment of metabolites. Metabolite profiling of the active metabolites in crude extracts of natural sources was supported by dereplication in which the novel compounds from the active groups were differentiated from known compounds that have been studied previously [22]. The dereplication method is a process for screening the known metabolites from the crude extracts before further scale-up or isolation work is undertaken, in order to avoid repetitive work.

High-resolution electrospray ionisation-liquid chromatography-mass spectrometry (HRESI-LCMS) data from both positive and negative ionisation modes were subjected to multivariate statistical analysis including unsupervised principal component analysis (PCA) and orthogonal partial least squares-discriminant analysis (OPLS-DA) to establish the optimal position of the discriminating plane, which would best separate classes. The high-resolution mass spectral data generated predicted molecular formulas used for dereplication of the secondary metabolites found in the crude extracts. Later in the final step of the metabolomics approach, the selected unique biomarkers were interpreted to putatively identify the novel metabolite using databases like Dictionary of Natural Products (DNP). The ultimate aim of this study was to fast track the identification of the metabolites from the co-culture extracts, which can lead to the decision-making of the optimum parameter for up-scaling of targeted metabolites responsible for biological activities. In future, the targeted metabolites will be isolated and absolute elucidation and identification of the molecule structures will be achieved using one and two dimensional-nuclear magnetic resonance (NMR) and high-resolution mass spectrometry (MS).

Materials and Methods

Preparation of microbial samples

A stock culture of *Streptomyces* sp. strain SUK10 was obtained from the Novel Antibiotics Laboratory, Programme of Biomedical Sciences, Faculty of Health Sciences, Universiti Kebangsaan Malaysia (UKM), Kuala Lumpur, while *Fusarium* sp. was obtained from the culture collection of Fungus Laboratory, Central Laboratory, Universiti Malaysia Terengganu (UMT). *Streptomyces* sp. SUK10 was originally isolated from the barks of *Shorea ovalis* [5] and *Fusarium* sp. was isolated from the roots of *Avicennia lanata* collected from Setiu Wetlands, Terengganu [13]. A 5 mm x 5 mm diameter plug containing *Fusarium* sp. mycelium was cut from the edge of the colony and placed in the middle of a new malt agar plate to establish a fresh and pure colony. The plates were incubated at 27 ± 2 °C (Vindon Scientific Ltd., UK) for 7-15 days. Meanwhile, *Streptomyces* sp. SUK10 was streaked onto fresh ISP2 agar plates and incubated at room temperature for 7-15 days.

Independent cultures

The International Streptomyces Project (ISP) medium was prepared by adding 10.0 g of malt extract, 4.0 g of D-(+)-glucose monohydrate, 4.0 g of yeast extract and 1 L of distilled water, vigorously shaken until completely mixed and dissolved. The pH was adjusted ranging at 7.2-7.4 using 10% NaOH or 36.5% HCl, and autoclaved at 121 ℃ for 15 minutes. The independent

cultures of *Streptomyces* sp. strain SUK10 and *Fusarium* sp. were achieved in which each active growing strain on the agar plate was cut into small cubes and transferred separately into seven 500 mL Erlenmeyer flasks containing 100 mL of ISP medium. The cultures were incubated in an orbital shaker and shaken at 150 rpm and 28 °C for 7 and 15 days (seven replicates). The metabolites were extracted twice with equal volumes of ethyl acetate, homogenised and filtered. The organic layer was discarded into a 500 mL round bottom flask using liquid-liquid extraction technique to obtain an organic solvent that was then concentrated under vacuum using a rotary evaporator (Büchi, Switzerland) to afford crude extracts ± 10.0 mg. The crude extracts were kept at 4 °C prior to analysis.

Co-cultivation between *Streptomyces* sp. strain SUK10 and *Fusarium* sp.

The co-cultivation between *Streptomyces* sp. strain SUK10 and *Fusarium* sp. was achieved including sets FS7, FS15, F7S15, and S7F15. The co-cultivation of sets FS7 and FS15 were obtained by mixing the agar cubes containing active growing *Streptomyces* sp. strain SUK10 and *Fusarium* sp. at initial incubation in the ISP broth. The incubation of co-cultivation of set FS7 was continued until day 7, while the co-cultivation of set FS15 was incubated until day 15. The co-cultivation of set F7S15 was obtained in which the agar plugs containing *Streptomyces* sp. strain SUK10 were introduced into the *Fusarium* sp. culture after 7 days of incubation, and the incubation was continued until day 15. The co-cultivation of set S7F15 was obtained in which the agar plugs containing *Fusarium* sp. mycelia were introduced into the *Streptomyces* sp. strain SUK10 culture after 7 days of incubation, and the incubation was also continued until day 15. A 100 mL of ISP broth was used for each culture and the incubation was done in an orbital shaker at 150 rpm and 28 °C (seven replicates). The metabolites were extracted twice with equal volumes of ethyl acetate, homogenised, and filtered. The organic layer was discarded into a 500 mL round bottom flask using liquid-liquid extraction technique to obtain an organic solvent that was then concentrated under vacuum using a rotary evaporator (Büchi, Switzerland) to afford crude extracts ± 15.0 mg. The crude extracts were kept at 4 °C prior to analysis.

Dereplication using HRESI-LCMS

The dereplication strategy on the crude extracts was performed using HRESI-LCMS and processed with the MZmine software 2.40.1, an in-house macro coupled with the Dictionary of Natural Products (DNP) 2015 and SIMCA P+ 15.0 (Umetrics AB, Umeå, Sweden). The procedure and programme for HRESI-LCMS was set up as described here [23]. 1 mg/mL of each extract was dissolved in methanol and analysed on an Accela HPLC (Thermo Scientific, UK) coupled with a UV detector at 280 and 360 nm and an Exactive-Orbitrap high-resolution mass spectrometer (Thermo Scientific, UK). A methanol blank was also analysed. The mass spectral data was processed using the procedure by MacIntyre et al. [23] which was established in the Natural Products Metabolomics Group Laboratory at Strathclyde Institute of Pharmacy and Biomedical Sciences (SIPBS) as described here [13, 23]. The LC-MS chromatograms and spectra were viewed using Thermo Xcalibur 2.1 or MZmine 2.40.1.

Antibacterial activity using agar disk-diffusion

An antibacterial activity of the extracts from independent and co-cultures was conducted using the agar disk-diffusion method as described here [24]. Each extract was diluted with 2-fold dilutions in dimethyl sulfoxide (DMSO) with concentration values of 0.156 mg/mL, 0.313 mg/mL, 0.625 mg/mL, 1.25 mg/mL, 2.50 mg/mL, 5.00 mg/mL and 10 mg/mL. The inhibition zone diameter (IZD) was measured to the nearest millimetres. Minimum inhibitory concentration (MIC) was taken as the lowest concentration of the extracts that shows the inhibition zone. MIC values of the extracts against the Gram-positive and Gram-negative bacteria were determined by averaging the results of three independent assays. Six strains of Gram-positive bacteria namely *Staphylococcus aureus*, *Bacillus cereus* and *Micrococcus* sp. and Gram-negative bacteria - *Vibrio cholera*, *Salmonella* sp. and *Escherichia coli* from glycerol stock were obtained from the Microbiology Laboratory, Institute of Marine Biotechnology, UMT.

Statistical analysis

All data were presented as mean ± SD and statistically analysed with One-Way ANOVA in the comparison between selected fractions using statistical analyses software PRISM ver. 5. Data were significantly different at $p < 0.05$.

Results and Discussion

Dereplication study on crude extracts

Each extract was screened on antibacterial activity at different concentrations: 10 mg/mL to 0 mg/mL. The inhibition zone diameter (IZD) was measured to the nearest millimetres. The results showed that the minimum inhibition concentration (MIC) values of the extracts against the Gram-positive and Gram-negative bacteria were determined by averaging the results of three independent assays (Table 1). The co-culture extract F7S15 revealed marginal antibacterial activity on *Micrococcus* sp. and *S. aureus* with MIC values of 5 mg/mL and 10 mg/mL, respectively, as compared to the non-active independent and other co-culture extracts. Meanwhile, the antibacterial activity on the Gram-negative bacteria showed that all extracts were non-active in this screening test, thereby supporting further investigation of the biologically-active compounds from the co-cultivation extracts.

Total ion chromatogram for the extract of co-cultivation between *Streptomyces* sp. strain SUK10 and *Fusarium* sp. F7S15 (Figure 1) showed the distribution of known and unknown compounds present in the extract (Table 2). The dereplication studies revealed that the co-culture extract F7S15 possessed certain types of compounds including macrocylic aromatic compounds such as macrolide- oligomycin A and cyclic peptolides-icosalide A1 and A3, which have also been previously isolated from different *Streptomyces* and fungi species, respectively (Table 2). The values and predicted formulas of unknown compounds are also shown (highlighted rows). The extracts of co-cultivation between *Streptomyces* sp. strain SUK10 and *Fusarium* sp. as well as the independent cultures were preliminarily screened on antibacterial activity and subjected to HRESI-LCMS prior to multivariate analysis. A dereplication study was performed to obtain the metabolomic profile of each extract.

The relationship between the occurrence of the metabolites in the independent and co-cultivation extracts and their bioactivity on antibacterial activity were evaluated through multivariate analysis. The PCA scores plot showed strong separation of the extracts (Figure 2a). There was clear separation between the co-culture extract of F7S15 from other extracts. The PCA loadings plot (Figure 2b) predicted the metabolites in the extracts. Meanwhile, a supervised multivariate OPLS-DA score plot analysis (Figure 2c) exhibited a distinctive separation between the active extract F7S15, while other extracts were the non-active group. These predicted antibacterial active compounds by MVA were indicated with their MZmine IDs as listed in Table 2. Peak IDs used in this table corresponded to those designated for the chromatogram as shown in Figure 1.

Table 1. Antibacterial activity for independent and co-culture extracts (calculated as mean value percentage viability) at different concentrations ranging at 10 mg/mL to 0 mg/mL. Highlighted rows showed enhanced antibacterial activity

Extracts	**Concentration of Crude Extract (mg/mL)**						
	***Micrococcus* sp.**						
	0.156	0.313	0.625	1.25	2.50	5.00	10.00
	Diameter of inhibition (mm)						
F7	n.d	n.d	n.d	n.d	n.d	n.d	n.d
F15	n.d	n.d	n.d	n.d	n.d	n.d	n.d
S7	n.d	n.d	n.d	n.d	n.d	n.d	n.d
S15	n.d	n.d	n.d	n.d	n.d	n.d	
FS7	n.d	n.d	n.d	n.d	n.d	n.d	n.d
FS15	n.d	n.d	n.d	n.d	n.d	n.d	n.d
F7S15	n.d	n.d	n.d	n.d	n.d	7.5 ± 0.6	8.7 ± 0.5
S7F15	n.d	n.d	n.d	n.d	n.d	n.d	8.0 ± 0
Oxytetracycline (30 µg)	35.7 ± 0.2						
	Staphylococcus aureus						
F7	n.d	n.d	n.d	n.d	n.d	n.d	n.d
F15	n.d	n.d	n.d	n.d	n.d	n.d	n.d
S7	n.d	n.d	n.d	n.d	n.d	n.d	n.d
S15	n.d	n.d	n.d	n.d	n.d	n.d	n.d
FS7	n.d	n.d	n.d	n.d	n.d	n.d	n.d
FS15	n.d	n.d	n.d	n.d	n.d	n.d	n.d
F7S15	n.d	n.d	n.d	n.d	n.d	n.d	n.d
S7F15	n.d	n.d	n.d	n.d	n.d	n.d	8.0 ± 0
Oxytetracycline (30 µg)	26.0 ± 1.4						

*Legend: extracts F7 = mono-culture *Fusarium* sp. incubation day 7; F15 = mono-culture *Fusarium* sp. incubation day 15; S7 = mono-culture *Streptomyces* sp. SUK10 incubation day 7; S15 = mono-culture *Streptomyces* sp. SUK10 incubation day 15; F7S15 = co-cultivation between *Fusarium* sp. and *Streptomyces* sp. SUK10 in which *Streptomyces* sp. SUK10 was added into *Fusarium* sp. culture after 7 days incubation and the incubation was continued until day 15; S7F15 = co-cultivation between *Fusarium* sp. and *Streptomyces* sp. SUK10 in which *Fusarium* sp. was added into *Streptomyces* sp. SUK10 culture after 7 days incubation and the incubation was continued until day 15; n.d: not detected; n=3.

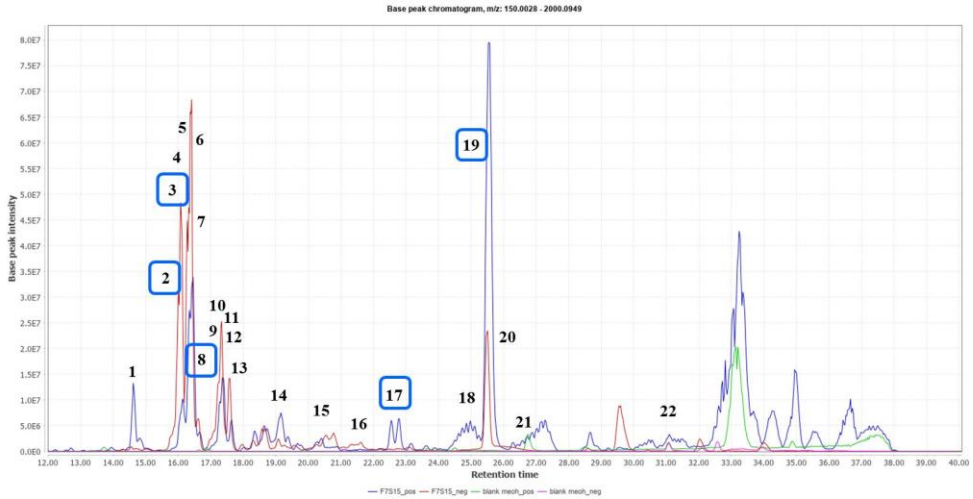

Figure 1. Total ion chromatogram for the extract of co-cultivation between *Streptomyces* sp. strain SUK10 and *Fusarium* sp. F7S15 (blue and red represent positive and negative ionization modes of F7S1 extract, respectively; green and pink represent positive and negative ionization modes of blank methanol, respectively). Dereplication of numbered peaks is shown on Table 1. Boxed in blue are the metabolites putatively identified using DNP database.

Table 2. List of compounds indicated on the total ion chromatogram for the extract of co-cultivation between *Streptomyces* sp. strain SUK10 and *Fusarium* sp. F7S15 that were putatively identified using DNP database. Peak IDs used in this table correspond to those designated for the chromatogram shown on Figure 1. Highlighted rows represent the unknown compounds as indicated with their MZmine IDs.

Peak ID	ESI Modes/ MZmine ID	Rt (min)	MS (*m/z*)	Molecular Weight	Chemical Formula	Chemical Name	Tolerance (ppm)	Sources	Peak Area
1	P_22521	14.58	274.2015	273.1943	$C_{14}H_{27}NO_4$	No hits			1.27E+08
2	N_2411	16.03	795.5293	796.5361	$C_{41}H_{80}O_{12}S$	bovine seminolipid	-1.1324	bovine spermatozoa	6.10E+08
3	P_21220	16.04	779.5308	778.5235	$C_{44}H_{74}O_{11}$	narasin D	0.5015	*Strep. aureofaciens*	2.75E+08
4	N_2409	16.19	633.4391	634.4464	$C_{30}H_{64}N_6O_4P_2$	No hits			3.81E+08
	N_2441	16.33	777.5188	778.5258	$CH_5NO_{15}P_4S_{12}$	No hits			8.40E+08
6	P_21679	16.35	801.5129	800.5056	$C_{10}N_3O_6PS_{16}$	No hits			3.80E+08
7	N_2435	16.36	759.5081	760.5154	$C_6HN_5O_3P_6S_{12}$	No hits			3.00E+08
8	P_21649	16.45	761.5204	760.5135	$C_{44}H_{72}O_{10}$	oligomycin A; 26-Demethyl, 12-deoxy	1.2529	*S. aureofaciens*	8.62E+08
9	N_2422	17.26	659.4550	660.4622	$C_{40}H_{70}OP_2S$	No hits			1.89E+08
10	P_21450	17.28	793.5469	792.5396	$C_2H_{18}NO_3P_{15}S_7$	No hits			4.10E+08
11	P_22522	17.32	833.5393	832.5320	$C_5H_9N_3O_8P_{14}S_5$	No hits			3.36E+08
12	N_2495	17.33	809.5449	810.5525	$C_2H_2N_3O_{19}P_9S_5$	No hits			2.12E+08
13	N_2496	17.58	777.5192	778.5264	$C_{38}H_{72}N_{10}O_3P_2$	No hits			1.69E+08

Table 2 (cont'd). List of compounds indicated on the total ion chromatogram for the extract of co-cultivation between *Streptomyces* sp. strain SUK10 and *Fusarium* sp. F7S15 that were putatively identified using DNP database. Peak IDs used in this table correspond to those designated for the chromatogram shown on Figure 1. Highlighted rows represent the unknown compounds as indicated with their MZmine IDs.

Peak ID	ESI Modes/ MZmine ID	Rt (min)	MS (*m/z*)	Molecular Weight	Chemical Formula	Chemical Name	Tolerance (ppm)	Sources	Peak Area
14	P_22523	19.10	783.5023	782.4957	$C_2H_4N_5O_5P_3S_{16}$	No hits			1.90E+08
15	N_2511	20.79	1556.0436	1557.0510	$C_{46}H_{88}N_9O_2P_9S_{15}$	No hits			1.11E+08
16	N_2549	21.62	1589.0730	1590.0803	$C_{41}H_{74}N_{14}O_{20}P_4S_{12}$	No hits			4.41E+07
17	P_22525	22.74	685.4392	684.4319	$C_{34}H_{60}N_4O_{10}$	icosalide A3	1.3669	fungus OSI 74159	9.07E+07
18	N_2408	25.38	711.4578	712.4649	$C_{38}H_{56}N_{12}O_2$	No hits			4.31E+08
19	P_21186	25.48	713.4698	712.4622	$C_{36}H_{64}N_4O_{10}$	icosalide A1	-0.1214	*Aureobasidium* sp. fungus OSI 59166	1.27E+09
20	N_2410	25.46	681.4474	682.4547	$C_{34}H_{63}N_6O_6P$	No hits			2.87E+08
21	P_21721	26.85	471.4048	470.3975	$C_{23}H_{51}N_8P$	No hits			8.99E+08
22	P_23269	31.03	523.3828	522.3755	$C_{27}H_{54}O_9$	1-Heptacosene-4,6,8,10,12,14,16, 18,24-nonol	-2.3912		4.07E+05

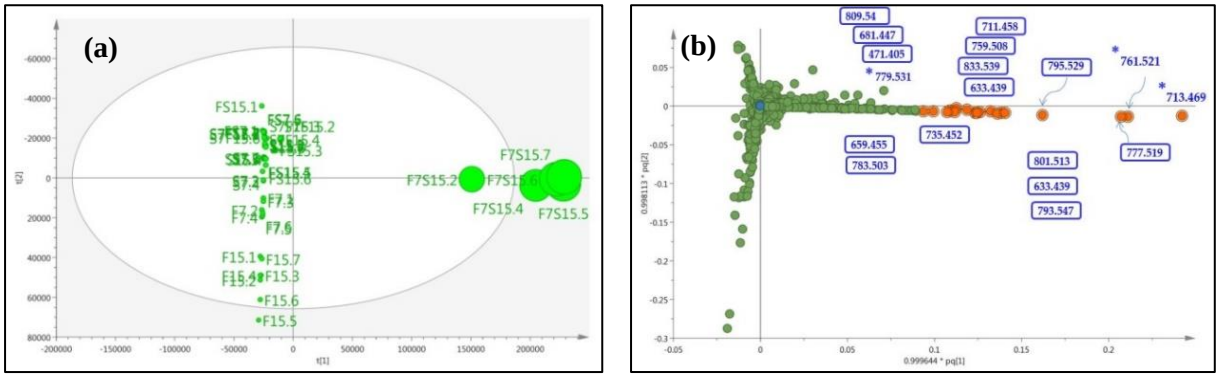

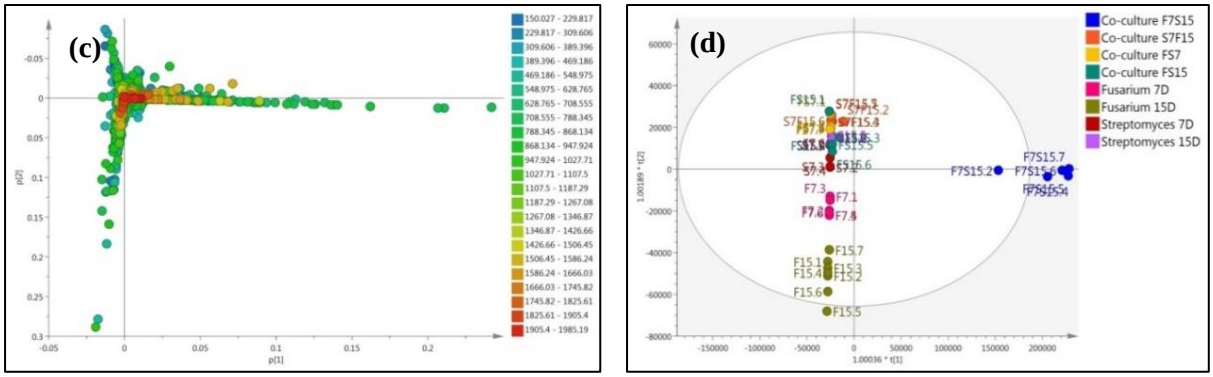

Figure 2. (a) Unsupervised PCA scores plot of mono- and co-cultivation extracts showed distinctive separation between the datasets. (b) PCA loadings plot showed the discriminating metabolites within the extracts. (c) OPLS-DA scores scatter plot of the extracts (R^2(Y) = 1.00; Q^2 =0.998); Q^2(Y intercept). (d) Supervised OPLS-DA loadings plot showed the discriminating metabolites of the active co-culture extract F7S15 within the extracts. Asterisk specifies the identified metabolites from where the respective active extract F7S15. Legend: set F7.1-F7.7 = mono-culture *Fusarium* sp. incubation day 7; set F15.1-F15.7 = mono-culture *Fusarium* sp. incubation day 15; set S7.1-S7.7 = mono-culture *Streptomyce*s sp. SUK10 incubation day 7; S15.1-S15.7 = mono-culture *Streptomyces* sp. SUK10 incubation day 15; set F7S15.1-F7S15.7 = co-cultivation between *Fusarium* sp. and *Streptomyces* sp. SUK10 in which *Streptomyces* sp. SUK10 was added into *Fusarium* sp. culture after 7 days incubation and the incubation was continued until day 15; set S7F15.1-S7F15.7 = co-cultivation between *Fusarium* sp. and *Streptomyces* sp. SUK10 in which *Fusarium* sp. was added into *Streptomyces* sp. SUK10 culture after 7 days incubation and the incubation was continued until day 15, n=7.

The OPLS-DA loadings plot (Figure 2d) exhibited the discriminating metabolites in the active group F7S15 in which the ion peaks at *m/z* $[M+H]^+$ 713.469, 761.521, and 801.513 as well as *m/z* $[M-H]^-$ 777.519, 795.529, and 633.439 were outliers, indicating the presence of unique chemical profiles in the F7S15 extract. From the DNP database, it was putatively determined that the F7S15 extract contained polyketide and aromatic compounds [25-28] that perhaps contributed towards the antibacterial activity of F7S15. Some of the ion peaks in the F7S15 extract have been dereplicated as presented in Table 1. Characteristic metabolite for co-culture F7S15 extract observed at *m/z* $[M+H]^+$ 713.469 were putatively identified as icosalide A1, which has been identified from an *Aureobasidium* sp. fungus OSI 59166 [26, 29]. The ion peaks at *m/z* $[M+H]^+$ 761.521 and 779.531 were putatively identified as oligomycin A; 26-demethyl, 12-deoxy, and narasin D, respectively. Both compounds were isolated from *Streptomyces aureofaciens* [30, 31]. The *m/z* $[M-H]^-$ 795.529 was putatively identified as bovine seminolipid, which has been isolated from bovine spermatozoa [32]. Meanwhile, the ion peaks at *m/z* $[M+H]^+$ 801.513 and *m/z* $[M-H]^-$ 777.519 and 633.439 were the unidentified metabolites that were only produced in the active co-culture extract F7S15. The relative occurrence of the targeted putatively identified and unknown metabolites in the bioactive extract F7S15 is shown in Figure 3. Based on the predicted chemical formula of the unknown compounds, they may consist of at least one nitrogen atom that contributes to the presence of macrocyclic polyketide-membered rings. Isolation of polyketide compounds from *Streptomyces* sp. under normal condition is widely known [5, 33-35], and perhaps the discovery of most antibiotics in the market are from this species. However, the world is facing a multidrug resistant against bacteria. Thus, dual cultivation of different strains used in our preliminary study may enlighten the opportunity to discover more potential new drug candidates that could be further

explored. The optimization works in this study showed that the co-cultivation of F7S15 produced promising metabolites with enhanced antibacterial activity, which can be further scaled up to obtain larger volume extracts for isolation and identification of target metabolites that were absent in their parent culture. Our future study will focus on the identification of molecule structures of the unknown metabolites by using tandem mass spectrometry (MS/MS) analysis and one/two-dimensional nuclear magnetic resonance (1D/2D NMR) spectroscopy.

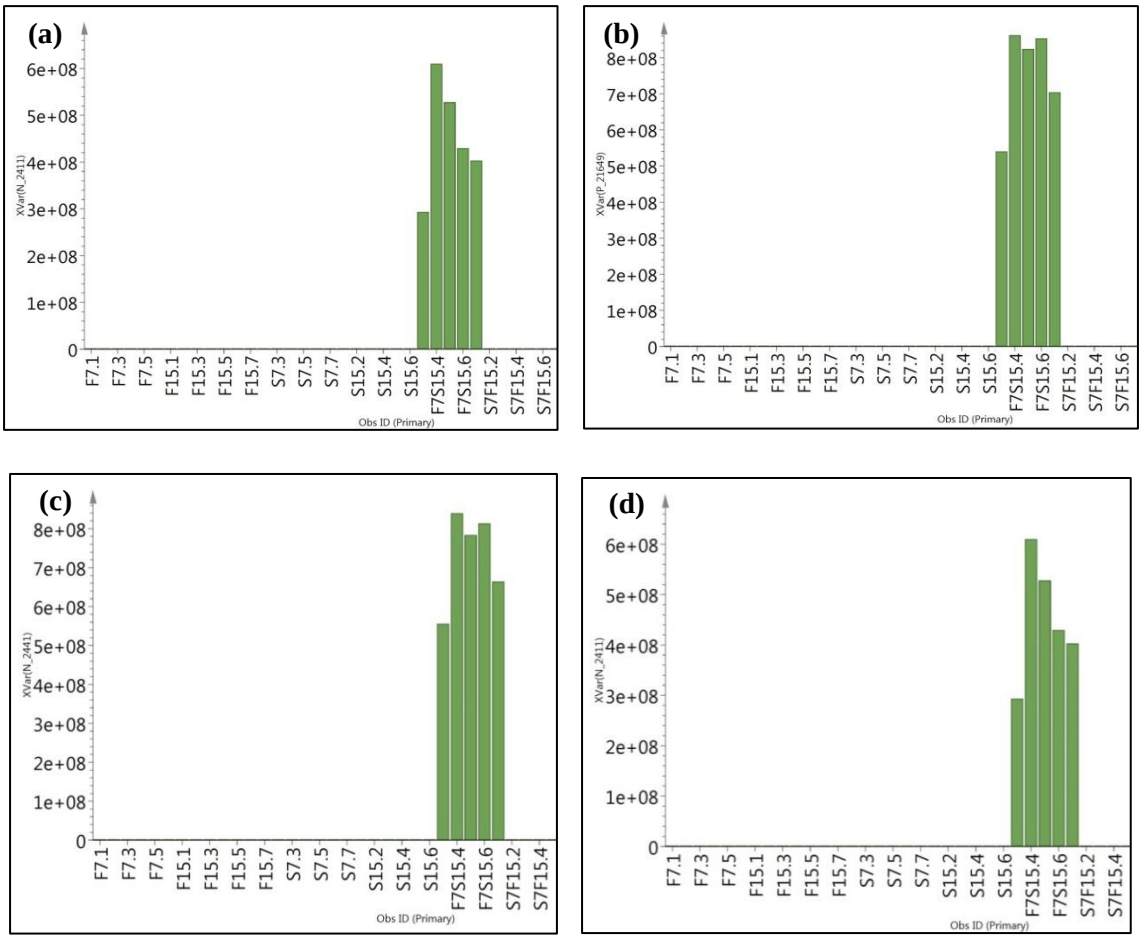

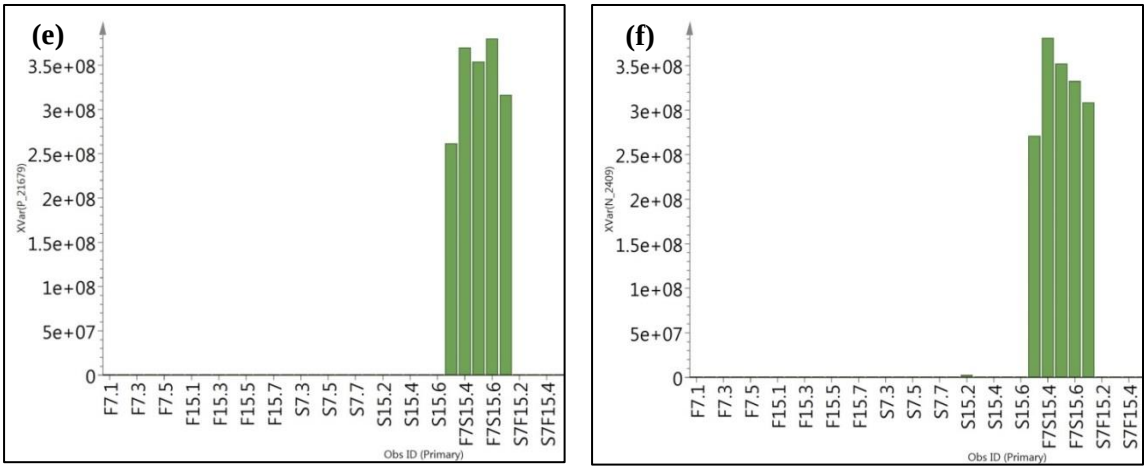

Figure 3. Relative abundance of target metabolites (a-f) which only present in the active co-culture extract of F7S15. Asterisk specifies the identified metabolites from where the respective active extract F7S15. (a) P_21186: *m/z* = 713.469, RT = 25.48 min; (b) P_21649: *m/z* = 761.521, RT = 16.45 min; (c) N_2496: *m/z* = 777.519, RT = 17.58 min; (d) N_2411: *m/z* = 795.529, RT = 16.03 min; (E) P_21679: *m/z* = 801.513, RT = 16.35 min; (F) N_2409: *m/z* = 633.439, RT = 16.19 min

Conclusion

The main aims in this study were to establish an optimum parameter to target and pinpoint the bioactive secondary metabolites directly from the extracts that were absent in the independent culture and subsequently imply the same parameter in the scale-up of the co-cultivation. By means of high-resolution liquid chromatography-mass spectrometry, the extracts obtained from mono- and co-cultivation were preliminarily screened for bioactive molecules and analyzed by multivariate analysis such as PCA and OPLS-DA. Dereplication study was used to screen the known metabolites and predict the novelty metabolites from the extracts which were not detected in single cultures, to avoid repetitive work on the same compounds with known bioactivity. Our future study will focus on the scale-up and isolation works of the targeted active metabolites from co-culture extract F7S15. In addition, identification of the molecule structures will be achieved using 1D and 2D-nuclear magnetic resonance (NMR) and high-resolution mass spectrometry (MS).

Acknowledgement

We wish to thank the Ministry of Higher Education Malaysia for the grant awarded to Noor Wini Mazlan FRGS/1/2018/STG05/UMT/03/2. The research described in this study has been done in IMB and Central Laboratory, UMT. The authors would like to thank Siti Aisha Mohd Radzi for assisting in the sample preparation.

References

1. Christina, A., Christapher, V. and Bhore, S. J. (2013). Endophytic bacteria as a source of novel antibiotics: an overview. *Pharmacognosy Reviews,* 7(13): 11.
2. Sarasan, M., Puthumana, J., Job, N., Han, J., Lee, J. S. and Philip, R. (2017). Marine algicolous endophytic fungi-a promising drug resource of the era. *Journal of Microbiology and Biotechnology*, 27(6): 1039-1052.
3. Berdy, J. (2005). Bioactive microbial metabolites. *The Journal of Antibiotics*, 58(1): 1-26.
4. Chater K. F., Losick, R. and Shapiro, L. (1984). Microbial development. *Cold Spring Habor Laboratory, Cold Spring Habor, New York*: pp. 89-116.
5. Zin, N. M., Baba, M. S., Zainal-Abidin, A. H., Latip, J., Mazlan, N. W. and Edrada-Ebel, R. (2017). Gancidin W, a potential low-toxicity antimalarial agent isolated from an endophytic Streptomyces SUK10. *Drug Design, Development and Therapy*, 11: 351.

6. Gao, H., Li, G. and Lou, H. X. (2018). Structural diversity and biological activities of novel secondary metabolites from endophytes. *Molecules*, 23(3): 646.
7. Liang, Y., Xie, X., Chen, L., Yan, S., Ye, X., Anjum, K., Huang, H. Lian, X. and Zhang, Z. (2016). Bioactive polycyclic quinones from marine Streptomyces sp. 182SMLY. *Marine Drugs,* 14(1): 10.
8. Cheng, C., Othman, E. M., Stopper, H., Edrada-Ebel, R., Hentschel, U. and Abdelmohsen, U. R. (2017). Isolation of petrocidin A, a new cytotoxic cyclic dipeptide from the marine sponge-derived bacterium Streptomyces sp. SBT348. *Marine Drugs,* 15(12): 383.
9. Gondry, M., Lautru, S., Fusai, G., Meunier, G., Ménez, A. and Genet, R. (2001). Cyclic dipeptide oxidase from *Streptomyces noursei*: Isolation, purification and partial characterization of a novel, amino acyl α, β-dehydrogenase. *European Journal of Biochemistry*, 268(6): 1712-1721.
10. Saadouli, I., Zendah El Euch, I., Trabelsi, E., Mosbah, A., Redissi, A., Ferjani, R. and Ouzari, H. I. (2020). Isolation, characterization and chemical synthesis of large spectrum antimicrobial cyclic dipeptide (l-leu-l-pro) from *Streptomyces misionensis* V16R3Y1 bacteria extracts. A novel ^{1}H NMR metabolomic approach. *Antibiotics*, 9(5): 270.
11. Ding, L., Münch, J., Goerls, H., Maier, A., Fiebig, H. H., Lin, W. H. and Hertweck, C. (2010). Xiamycin, a pentacyclic indolosesquiterpene with selective anti-HIV activity from a bacterial mangrove endophyte. *Bioorganic & Medicinal Chemistry Letters*, 20(22): 6685-6687.
12. Khan, N., Afroz, F., Begum, M. N., Rony, S. R., Sharmin, S., Moni, F. and Sohrab, M. H. (2018). Endophytic *Fusarium solani*: A rich source of cytotoxic and antimicrobial napthaquinone and aza-anthraquinone derivatives. *Toxicology Reports*, 5: 970-976.
13. Mazlan, N. W., Tate, R., Yusoff, Y. M., Clements, C. and Edrada-Ebel, R. (2020). Metabolomics-guided isolation of anti-trypanosomal compounds from endophytic fungi of the mangrove plant A*vicennia lanata*. *Current Medicinal Chemistry*, 27(11): 1815-1835.
14. Zhen, X., Mao, M. J., Wang, R. Z., Chang, S. S., Xiao, T. M., Wu, Y. X., Yu, Y., Song, Y. L., Chen, M. H. and Si, S. Y. (2021). Fusapyrone A, a γ-pyrone derived from a desert *Fusarium* sp. *Journal of Asian Natural Products Research*, 23(5): 504-511.
15. Choi, H. G., Song, J. H., Park, M., Kim, S., Kim, C. E., Kang, K. S. and Shim, S. H. (2020). Neuroprotective γ-pyrones from Fusarium Solani JS-0169: Cell-based identification of active compounds and an informatics approach to predict the mechanism of action. *Biomolecules*, 10(1): 91.
16. Gao, H., Li, G., Peng, X. P. and Lou, H. X. (2020). Fupyrones A and B, two new α-pyrones from an endophytic fungus, *Fusarium* sp. F20. *Natural Product Research*, 34(3): 335-340.
17. Luo, K., Rocheleau, H., Qi, P. F., Zheng, Y. L., Zhao, H. Y. and Ouellet, T. (2016). Indole-3-acetic acid in Fusarium graminearum: Identification of biosynthetic pathways and characterization of physiological effects. *Fungal Biology*, 120(9): 1135-1145.
18. Xiao, W. J., Chen, H. Q., Wang, H., Cai, C. H., Mei, W. L. and Dai, H. F. (2018). New secondary metabolites from the endophytic fungus Fusarium sp. HP-2 isolated from "Qi-Nan" agarwood. *Fitoterapia*, 130: 180-183.
19. Ibrahim, S. R., Mohamed, G. A., Al Haidari, R. A., Zayed, M. F., El-Kholy, A. A., Elkhayat, E. S. and Ross, S. A. (2018). Fusarithioamide B, a new benzamide derivative from the endophytic fungus *Fusarium chlamydosporium* with potent cytotoxic and antimicrobial activities. *Bioorganic & Medicinal Chemistry*, 26(3): 786-790.
20. Rodrigues Reis, C. E., Ogero D'Otaviano, L., Rajendran, A. and Hu, B. (2018). Co-culture of filamentous feed-grade fungi and microalgae as an alternative to increase feeding value of ethanol coproducts. *Fermentation*, 4(4): 86.
21. Kamdem, R. S., Wang, H., Wafo, P., Ebrahim, W., Özkaya, F. C., Makhloufi, G. and Proksch, P. (2018). Induction of new metabolites from the endophytic fungus *Bionectria* sp. through bacterial co-culture. *Fitoterapia*, 124: 132-136.

22. Harvey A. L., Edrada-Ebel, R. and Quinn, R. J. (2015). The re-emergence of natural products for drug discovery in the genomics era. *Nature Reviews Drug Discovery*, 14(2): 111-129.
23. Macintyre, L., Zhang, T., Viegelmann, C., Martinez, I. J., Cheng, C., Dowdells, C. and Edrada-Ebel, R. (2014). Metabolomic tools for secondary metabolite discovery from marine microbial symbionts. *Marine Drugs*, 12(6): 3416-3448.
24. Assaw, S., Mohd Amir, M. I. H., Khaw, T. T., Bakar, K., Mohd Radzi, S. A. and Mazlan, N. W. (2020). Antibacterial and antioxidant activity of naphthofuranquinones from the twigs of tropical mangrove Avicennia officinalis. *Natural Product Research*, 34(16): 2403-2406.
25. Chan, W. Y., Hickey, E. E., Khazandi, M., Page, S. W., Trott, D. J. and Hill, P. B. (2020). *In vitro* antimicrobial activity of narasin and monensin in combination with adjuvants against pathogens associated with canine otitis externa. *Veterinary Dermatology*, 31(2): 138-e26.
26. Boros, C., Smith, C. J., Vasina, Y., Che, Y., Dix, A. B., Darveaux, B. and Pearce, C. (2006). Isolation and identification of the icosalides--cyclic peptolides with selective antibiotic and cytotoxic activities. *Journal of Antibiotics*, 59(8): 486-494.
27. Dose, B., Niehs, S. P., Scherlach, K., Flórez, L. V., Kaltenpoth, M. and Hertweck, C. (2018). Unexpected bacterial origin of the antibiotic icosalide: two-tailed depsipeptide assembly in multifarious *Burkholderia* symbionts. *ACS Chemical Biology*, 13(9): 2414-2420.
28. Lysenkova, L. N., Saveljev, O. Y., Omelchuk, O. A., Zatonsky, G. V., Korolev, A. M., Grammatikova, N. E. and Shchekotikhin, A. E. (2020). Synthesis, antimicrobial and antiproliferative properties of epi-oligomycin A, the (33 S)-diastereomer of oligomycin A. *Natural Product Research*, 34(21): 3073-3081.
29. Jenner, M., Jian, X., Dashti, Y., Masschelein, J., Hobson, C., Roberts, D. M. and Challis, G. L. (2019). An unusual *Burkholderia gladioli* double chain-initiating nonribosomal peptide synthetase assembles 'fungal'icosalide antibiotics. *Chemical science*, 10(21): 5489-5494.
30. Khebizi, N., Boudjella, H., Bijani, C., Bouras, N., Klenk, H. P., Pont, F. and Sabaou, N. (2018). Oligomycins A and E, major bioactive secondary metabolites produced by *Streptomyces* sp. strain HG29 isolated from a Saharan soil. *Journal de Mycologie Medicale*, 28(1): 150-160.
31. Anadón, A. and Martínez-Larrañaga, M. R. (2014). Veterinary drugs residues: coccidiostats: 63-75.
32. Alvarez, J. G., Storey, B. T., Hemling, M. L., & Grob, R. L. (1990). High-resolution proton nuclear magnetic resonance characterization of seminolipid from bovine spermatozoa. *Journal of Lipid Research*, 31(6): 1073-1081.
33. Bekiesch, P., Oberhofer, M., Sykora, C., Urban, E. and Zotchev, S. B. (2019). Piperazic acid containing peptides produced by an endophytic *Streptomyces* sp. isolated from the medicinal plant *Atropa belladonna*. *Natural Product Research*, 35(7): 1090-1096.
34. Cho, E., Kwon, O. S., Chung, B., Lee, J., Sun, J., Shin, J. and Oh, K. B. (2020). Antibacterial activity of chromomycins from a marine-derived *Streptomyces microflavus*. *Marine Drugs*, 18(10): 522.
35. Qureshi, K. A., Bholay, A. D., Rai, P. K., Mohammed, H. A., Khan, R. A., Azam, F. and Prajapati, D. K. (2021). Isolation, characterization, anti-MRSA evaluation, and in-silico multi-target anti-microbial validations of actinomycin X2 and actinomycin D produced by novel S*treptomyces smyrnaeus* UKAQ_23. *Scientific Reports*, 11(1): 1-21.

Malaysian Journal of Analytical Sciences (MJAS)
Published by Malaysian Analytical Sciences Society

THE CONJUGATION AND CHARACTERISATION OF THERMORESONSIVE POLY (*N*-ISOPROPYLACRYLAMIDE) WITH TERNATIN BIOMOLECULE

(Konjugasi dan Pencirian Poli (*N*-Isopropilakrilamida) dengan Biomolekul Ternatin)

Adrina Zulkifli, Farahiyah Najah Ab Samad, Nukman Ameen Rosli, Nurul Aina Jamaluddin, Nor Nadiah Mohamad Yusof, Noor Faizah Che Harun*

Green Chemistry and Sustainable Engineering Technology, Polymer Technology Section, Universiti Kuala Lumpur (UniKL) MICET, Lot 1988, Kawasan Perindustrian Bandar Vendor, Taboh Naning, 78000 Alor Gajah, Melaka, Malaysia

**Corresponding author: noorfaizah@unikl.edu.my*

Received: 15 September 2021; Accepted: 4 January 2022; Published: 25 February 2022

Abstract

Poly (*N*-isopropylacrylamide) (PNIPAAm) is a well-known thermoresponsive polymer that shows a reversible coil-to-globule transition at the lower critical solution temperature (LCST) (32°C) in aqueous solution. Chemically modified PNIPAAm with hydrophilic/hydrophobic compound will tune its LCST. Below the LCST, PNIPAAm and its conjugate behave as an extended coil form in an aqueous solution, whereas it shrinks into a globule form above the LCST. In this study, a direct conjugate of PNIPAAm with a ternatin biomolecule and their physicochemical characterizations were investigated. Ternatin biomolecule is an anti-adipogenic cyclic peptide that has a potential as a new treatment approach for obesity and metabolic disorders. Poly (*N*-isopropylacrylamide)-chain transfer agent (PNIPAAm-CTA) was synthesized through reversible addition fragmentation chain transfer (RAFT) polymerization using 2-(Dodecylthiocarbonothioyltho)-2-methylpropanoic acid (DDMAT) as chain transfer reagent. One end-group of PNIPAAm-CTA was subsequently modified with maleimide to form PNIPAAm-Maleimide through aminolysis reaction. Thereafter, a carboxylic end-group of PNIPAAm-Maleimide was directly conjugated with a hydroxyl group of ternatin biomolecule (PNIPAAm-Ternatin) through esterification method. The chemical structure, molecular weight (Mw) and molecular weight distribution (Mw/Mn) of PNIPAAm were determined through the proton nuclear magnetic resonance (^{1}H-NMR), Fourier transform infrared (FTIR) and size exclusion chromatography (SEC) measurements. Moreover, the LCST of PNIPAAm and its conjugate were determined through light scattering intensity analysis. The results indicated that upon heating the solutions of PNIPAAm and its conjugates in 10 mM HEPES solution pH 7.4 at 25°C-40 °C, PNIPAAm-CTA, PNIPAAm-Maleimide and PNIPAAm-Ternatin solutions started to increase their light intensities at 32 °C, 34 °C and 35 °C, respectively. In conclusion, chemical structure modification of PNIPAAm could tune their LCST.

Keywords: poly (*n*-isopropylacrylamide), raft polymerization, ternatin biomolecule, conjugation, lower critical solution temperature

Abstrak

Poli (*N*-isopropilakrilamida) (PNIPAAm) adalah polimer termoresponsif terkenal yang menunjukkan peralihan gegelung-ke-globule yang boleh berbalik pada suhu larutan kritikal rendah (LCST) (32°C) dalam larutan akueus. PNIPAAm yang diubahsuai

secara kimia dengan sebatian hidrofilik/hidrofobik akan mengubahkan LCSTnya. Pada suhu di bawah LCST, PNIPAAm dan konjugatnya berbentuk gegelung di dalam larutan akueus, manakala ia akan mengecut menjadi bentuk globul pada suhu di atas LCST Dalam kajian ini, konjugasi secara langsung PNIPAAm dengan biomolekul ternatin dan sifat fizikokimianya dikaji. Biomolekul ternatin adalah peptida siklik anti-adipogenik. Ia berpotensi sebagai rawatan baharu untuk obesiti dan gangguan metabolik. Poli (*N*-isopropilakrilamida)-agen pemindahan rantai (PNIPAAm-CTA) disintesis melalui polimerisasi radikal hidup menggunakan asid 2-(dodekilthiokarbonothioiltho)-2-metilpropanoik(DDMAT) sebagai reagen pemindahan rantai. Selepas itu, satu kumpulan akhir pada PNIPAAm-CTA diubahsuai dengan maleimida untuk membentuk PNIPAAm-Maleimida melalui tindak balas aminolisis. Kemudian, kumpulan akhir karboksilik PNIPAAm-Maleimida dihubungkan secara langsung dengan kumpulan hidroksil pada biomolekul ternatin (PNIPAAm-Ternatin) melalui kaedah esterifikasi. Struktur kimia, berat molekul (Mw) dan taburan berat molekul (Mw/ Mn) bagi PNIPAAm dikaji melalui analisis proton resonans magnetik nuklear (^{1}H-NMR), spektroskopi inframerah Fourier transformasi (FTIR) dan kromatografi ekslusi saiz (SEC). Seterusnya, sifat LCST bagi PNIPAAm dan konjugatnya dikaji melalui analisis intensiti penyerakan cahaya. Hasilnya, setelah larutan PNIPAAm dan konjugat dalam larutan HEPES 10 mM pH 7.4 dipanaskan pada suhu 25-40 °C, intensiti cahaya bagi PNIPAAm-CTA, PNIPAAm-Maleimida dan PNIPAAm-Ternatin mula meningkat pada 32 °C, 34 °C dan 35 °C. Kesimpulannya, pengubahsuaian struktur kimia PNIPAAm dapat mengubah sifat LCST polimer.

Kata kunci: poli (*n*-isopropilakrilamida), pempolimeran raft, biomolekul ternatin, konjugasi, suhu larutan kritikal rendah

Introduction

Over the years, a great deal of effort has been devoted to the development of stimuli-responsive smart polymers that can provide a variety of applications for cosmetic, agriculture, biomedical and biotechnology [1-4]. Smart polymers are polymeric materials, in which the structure, function, and stability drastically change by slight changes in external stimuli. These stimuli could be temperature, pH, light, redox and/or photo [5-9]. In the case, whereby the external stimulus is the temperature change, the polymers are often referred as thermoresponsive polymers. Poly(*N*-isopropylacrylamide (PNIPAAm) is one of the well-known thermoresponsive polymer. PNIPAAm displays a lower critical solution temperature (LCST) of 33 °C [10-12]. PNIPAAm remains in coil conformation in water below LCST, meanwhile, it collapses into globule conformation above LCST [13, 14]. The LCST of PNIPAAm chain could be tuned by several approaches, such as modification of end-group with hydrophilic or hydrophobic compound, adding comonomers and/or changing its tacticity [15-17]. The introduction of hydrophilic compound into PNIPAAm chain leads to an increase of LCST, meanwhile, PNIPAAm incorporated with hydrophobic compound tends to decrease LCST. Moreover, a reported study demonstrated that PNIPAAm conjugated with a small interfering of ribonucleic acid (RNA) (siRNA) biomolecule using click chemistry tools tuned the LCST of PNIPAAm conjugates [18].

In the present study, a facile synthetic route for the conjugation of PNIPAAm with ternatin biomolecule was prepared to investigate the thermoresponsive behaviour. Ternatin biomolecule is a natural compound that is extracted from a plant, known as butterfly pea, or its scientific name *Clitoria ternatea* [19]. Ternatin is an anti-adipogenic cyclic peptide containing one or more *N*-methyl (or *N*-alkyl) amino acids [20, 21]. Furthermore, this study hypothesised that the modification of PNIPAAm chain with hydrophilic compound end-group and ternatin biomolecule would tune the thermoresponsive behaviour of PNIPAAm. Concisely, this study prepared PNIPAAm and its conjugate through controlled living radical polymerisation and esterification techniques (Figure 1). It is expected that the prepared facile synthetic route for the conjugation of thermoresponsive polymer with biomolecule and the resulted thermoresponsive behaviour in this study would be useful for further related field studies.

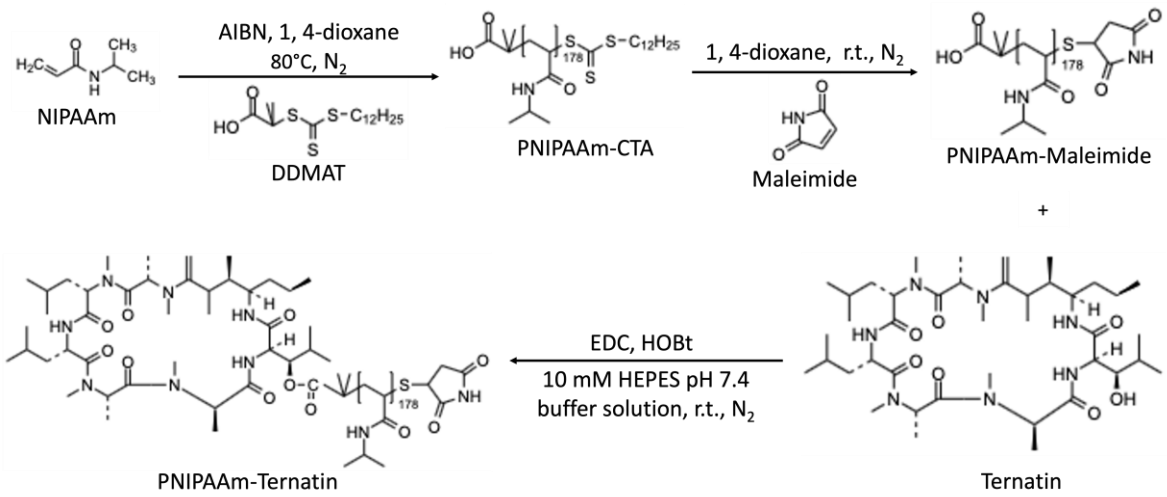

Figure 1. Synthetic route of PNIPAAm-Ternatin conjugation

Materials and Methods

Materials

N-Isopropylacrylamide (NIPAAm), 2-(Dodecylthiocarbonothioyltho)-2-methylpropanoic acid (DDMAT), 2,2'-Azobis(2-methylpropionitrile) (AIBN), 1,4-dioxane, diethyl ether, ethanolamine, maleimide, tributylphosphine (TBP), HEPES solution, N-ethyl-N'-(3-dimethylaminopropyl) carbodiimide (EDC), 1-Hydroxybenzotriazole (HOBt), tetrahydrofuran (THF) and acetonitrile were purchased from Sigma-Aldrich, Malaysia. NIPAAm was purified by recrystallisation from n-hexane and dried in a vacuum. AIBN purification was performed by recrystallisation from cold methanol. Prior to the usage, 1,4-dioxane was purified using reflux condenser. Ternatin was purchased from Cayman Chemical (Ann Arbor, Michigan, USA). Deuterated methanol (MeOD) was purchased from Merck and it was used without further purification.

Synthesis of PNIPAAm–CTA

PNIPAAm-CTA was synthesised by dissolving NIPAAm (3.0 g, 30.0 mmol), DDMAT (110 mg, 0.3 mmol), AIBN (2.5 mg, 0.015 mmol) in 1,4-dioxane (10 mL) ([NIPAAm]: [DDMAT]: [AIBN] = 100: 1: 0.05, respectively). The solution was stirred at room temperature until a homogeneous mixture was formed. Next, the nitrogen gas was purged into the reaction for 15 minutes. The mixture was stirred and heated in an 80 °C oil bath for 12 hours. After 12 hours, the reaction solution was precipitated into cold diethyl ether to remove the unreacted monomer. The produced polymer was filtered using vacuum pump and dried in a desiccator for a day. Finally, the polymer was collected, weighted and stored in the refrigerator.

Synthesis of PNIPAAm–maleimide

PNIPAAm–Maleimide was synthesised by dissolving PNIPAAm-CTA (1.5 g, 0.27 mmol), ethanolamine (1.6 g, 27.20 mmol) and maleimide (0.26 g, 2.72 mmol) into the 1,4-dioxane (5 mL). The solution was stirred at room temperature until a homogeneous mixture was formed. Next, the nitrogen gas was purged into the reaction for five minutes. After five minutes, TBP (0.10 mL, 0.54 mmol) was added to the mixture ([PNIPAAm–CTA]: [maleimide]: [TBP]: [ethanolamine] = 1: 10: 2: 100, respectively). The mixture was stirred at room temperature for six hours. After six hours, the reaction solution was precipitated into cold diethyl ether to remove the unreacted monomer. The produced polymer was filtered using a vacuum pump and dried in a desiccator for a day. The polymer was collected, weighted and stored in the refrigerator.

Synthesis of PNIPAAm–ternatin

PNIPAAm–Maleimide solution was prepared by dissolving PNIPAAm-Maleimide (33.33 mg, 0.02 mmol) into 4 mL of 10 mM HEPES pH 7.4 buffer solution. The mixture was stirred for 20 hours at room temperature. After 20 hours, EDC (3 mg, 0.02 mmol) and HOBt (1 mg, 0.01 mmol) were added to the mixture and stirred continuously for three hours at room temperature to activate the carboxylate group. Next, the nitrogen gas was purged into the reaction for 15 minutes and 0.5 mL of 10 ppm ternatin was slowly added to the mixture. After 15 minutes, the mixture was stirred for 20 hours at room temperature. Thereafter, 4 mL of 10 mM HEPES pH 7.4 buffer solution was added to the mixture and cooled at room temperature. After two days, it was purified by centrifugation using ultra centrifugal filter (MWCO 3kDa, Millipore) to remove the unreacted molecules. Finally, the produced PNIPAAm-Ternatin was collected and stored in the refrigerator.

Molecular weight and molecular weight distribution

The polymer molecular weight and molecular weight distribution (Mw/Mn) was measured by using Waters® ACQUITY® Advanced Polymer Chromatography™ (APC) with THF, which was used as an eluent at a flow rate of 1.0 mL/min at 40°C using the standard polystyrene. The ACQUITY UPLC Refractive Index Detector ACQUITY APC Column were used.

Chemical structure characterisations

Fourier transform infrared (FTIR) spectra of the PNIPAAm-CTA and PNIPAAm-Maleimide were recorded with FTIR Nicolet 510 spectrometer in the 4,000 cm^{-1} – 400 cm^{-1} range. The samples were prepared by grinding the polymer with KBr pellets and compressing the mixture to form disks. For PNIPAAm-Ternatin, FTIR spectra was recorded with Shimadzu FTIR-8300 instrument in the 4,000 cm^{-1} - 600 cm^{-1} range. The polymer chemical structure and the conjugated polymers were also characterised using ^1H NMR spectra. It was conducted on a Bruker Spectrospin 400 MHz UltraShield Spectrometer. Chloroform-d ($CDCl_3$) and methanol-d (MeOD) were used as solvents.

Reversed-phase high-performance liquid chromatography analysis

Reversed-phase high-performance liquid chromatography (RP-HPLC) analysis was used to separate, identify and quantify each component in the produced polymer conjugated with ternatin. For polymer-peptide conjugate, the HPLC gradients consisted of eluent A with 0.1% formic acid in water and eluent B with 0.1% formic acid in acetonitrile. The flow rate was maintained at 0.5 mL/min, detected at 200 nm and the column temperature was at room temperature.

Light scattering intensity analysis

Light scattering intensity analysis was performed to determine the LCST of polymer by using Zetasizer Nano (Malvern Instrument Ltd.) at a detection angle of 173°. The sample solutions were prepared by dissolving the polymer, ternatin and its polymer conjugates in 10 mM HEPES solution (pH 7.4) (sample solution concentration at 0.5 mg mL^{-1}). It was measured at various temperatures from 25°C to 40°C. The results were presented as mean value of count rate in kilo counts per second (kcps) and the standard deviation was obtained from three times repetitions.

Results and Discussion

Chemical structure characterisation of PNIPAAm-CTA and PNIPAAm-Maleimide

The synthesised PNIPAAm-CTA possessed molecular weight, Mw at 20140 g/mol and had a narrow molecular weight distribution (Mw/Mn) of 1.26. The obtained molecular weight of PNIPAAm-CTA was purely theoretical. Furthermore, a quite narrow molecular weight distribution suggested that a successful controlled polymerization of PNIPAAm.

The chemical structure of PNIPAAm-CTA and PNIPAAm-Maleimide were characterised by ^1H NMR and FTIR analysis. The ^1H NMR spectrum of PNIPAAm-CTA in Figure 2 showed the presence of signal characteristic of PNIPAAm at δ = 3.9 ppm for CH connected to the NH, 1.15 ppm for CH_3, 1.61 ppm ($-CH_2-$) and 2.13 ppm (-CH-) [22, 23]. The formation of PNIPAAm-CTA was proven by the existence of trithiocarbonate functionality at the PNIPAAm-CTA

end-group, which was demonstrated in the ^{1}H NMR spectrum through the peak at 0.88 ppm (CH_3–$(CH_2)_{10}$–CH_2–S–) [24]. Furthermore, the ^{1}H NMR spectrum of PNIPAAm-Maleimide (Figure 3) confirmed the existence of maleimide at the peak of 8.55 ppm which belong to the -NH group in maleimide [25]. The disappearance of the peak at 0.88 ppm for trithiocarbonate group in the spectrum suggested the successful conversion into PNIPAAm-Maleimide through aminolysis reaction [26].

PNIPAAm-CTA and PNIPAAm-Maleimide chemical structures were further confirmed through FTIR analysis. In Figure 4, the FTIR spectrum for PNIPAAm-CTA showed that the formation was proven by the C=S stretching band of the chain at 1,065 cm^{-1} [27]. The C=S group was belong to the trithiocarbonate end in PNIPAAm-CTA. The FTIR spectra for PNIPAAm-CTA also represented the N-H stretch at 3,414 cm^{-1}, carbonyl group (C=O) at 1,554 cm^{-1} and 1,643 cm^{-1}, and C–N stretching at 1,462 cm^{-1} [28]. The FTIR spectrum for PNIPAAm–Maleimide showed that the aminolysis reaction was succeeded because the C=S stretching band (1,050 cm^{-1} – 1,080 cm^{-1}) of the trithiocarbonate end was no longer being observed after the aminolysis reaction [29]. Furthermore, there was a peak at 1,743 cm^{-1} for maleimide C=O stretching. For symmetric C-N-C stretch, the peak was situated at 1,457 cm^{-1}, which affirmed the existence of maleimide [30]. The FTIR absorption band, which was around 3,300 cm^{-1} – 3,500 cm^{-1} covered N-H stretching group bands in PNIPAAm and maleimide [31]. These results confirmed the polymerisation of PNIPAAm-CTA and the modification of its end-group to produce PNIPAAm-Maleimide.

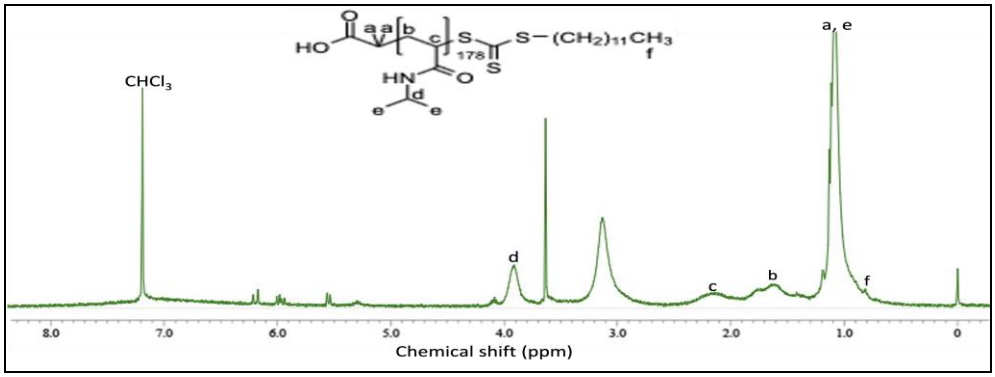

Figure 2. ^{1}H NMR spectrum of PNIPAAm-CTA

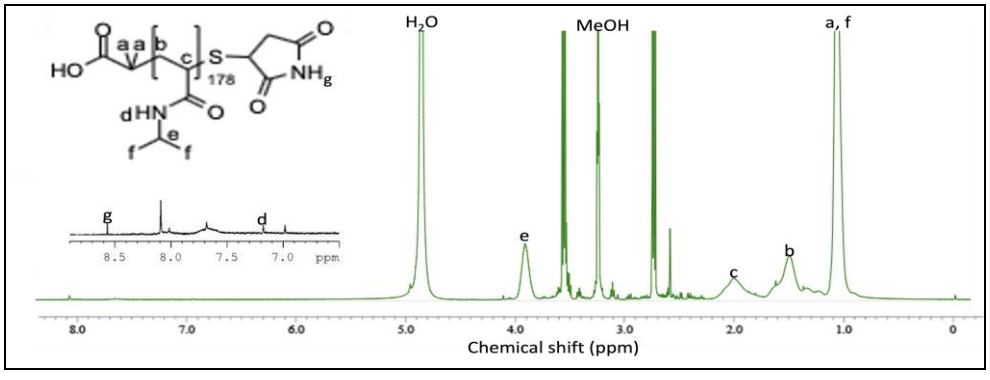

Figure 3. ^{1}H NMR spectrum of PNIPAAm-Maleimide

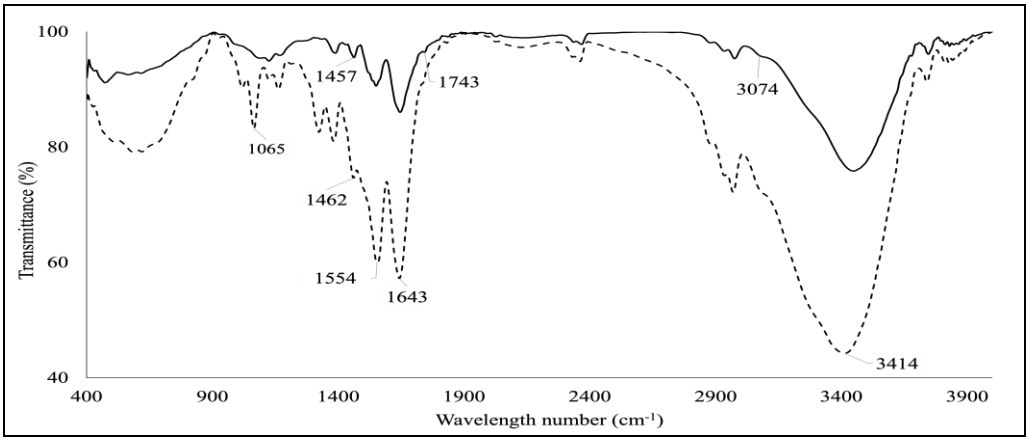

Figure 4. FTIR analysis for PNIPAAm-CTA (dash-line) and PNIPAAm-Maleimide (straight-line)

Characterisations of PNIPAAm-Ternatin conjugate

The esterification method was used to synthesise the PNIPAAm-Ternatin. The chemical structure of PNIPAAm-Ternatin was confirmed by the FTIR. In Figure 5 (a) showed the FTIR analysis for PNIPAAm-Ternatin, whereby the band at 1,635 cm^{-1} and 1,185 cm^{-1} were attributed to the C=O and C-O stretching frequencies of ester linkage, respectively [32]. Therefore, it was suggested that the PNIPAAm-Ternatin was successfully synthesised through esterification method. A broad stretch at 3,286 cm^{-1} was indexed to the NH group in ternatin [33]. The NH stretching group in PNIPAAm and maleimide at 3,300 cm^{-1} – 3,500 cm^{-1} were overlapped by the broad stretch of OH group in the ternatin [34].

The HPLC chart for PNIPAAm-Ternatin is shown in Figure 5 (b). The purpose of this analysis was to identify the retention time of ternatin, PNIPAAm-Maleimide and PNIPAAm-Ternatin and also to calculate the concentration and conjugation percentages of ternatin biomolecule to PNIPAAm chain. As a result, it was confirmed that the peak at the retention time of 2.57 minutes and 3.06 minutes for ternatin and PNIPAAm-Ternatin, respectively, clearly appeared in the HPLC chart. The concentration and conjugation percentages of PNIPAAm-Ternatin were obtained at 8.75 ppm and 87.5%, respectively, which was calculated based on ternatin calibration. Consequently, the collected PNIPAAm-Ternatin through RP-HPLC was purified using centrifugation against 10 mM HEPES pH 7.4 buffer solution and conducted for further analysis.

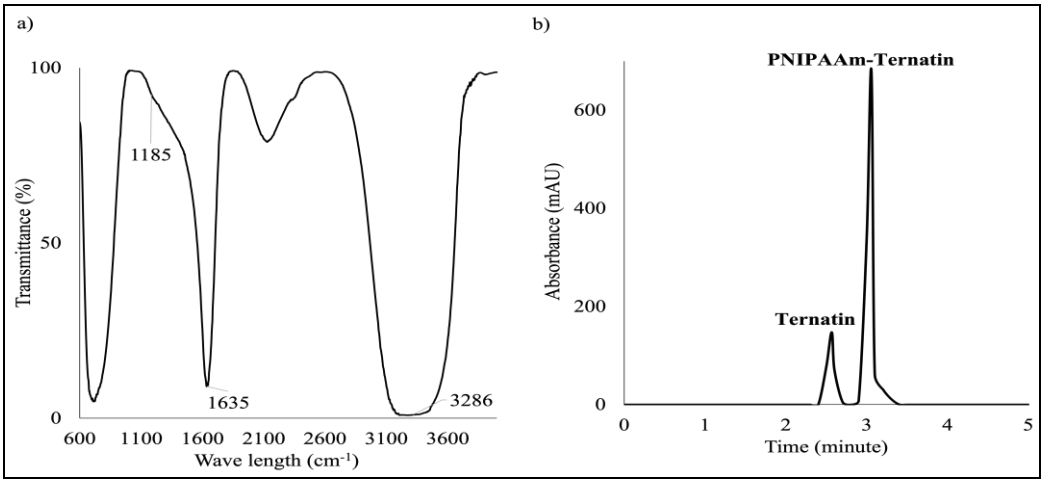

Figure 5. (a) FTIR analysis and (b) HPLC analysis for PNIPAAm-Ternatin

Thermoresponsive behaviour of PNIPAAm and its conjugate

The LCST of PNIPAAm and its conjugate were determined by light scattering intensity analysis. The resulting light scattering intensity of PNIPAAm and its conjugate are shown in Figure 6(a) for PNIPAAm-CTA, Figure 6(b) for PNIPAAm-Maleimide and Figure 6(c) for PNIPAAm-Ternatin. Upon heating solutions of PNIPAAm-CTA, PNIPAAm-Maleimide and PNIPAAm-Ternatin in 10 mM HEPES pH 7.4 from 25 °C to 40 °C, it could be seen that light scattering intensity of PNIPAAm-CTA started to increase at a temperature of 32 °C, whereas the change was shifted to the temperature at 34 °C in the case of PNIPAAm-Maleimide and at 35 °C for PNIPAAm-Ternatin. The increased light scattering intensity of PNIPAAm and its conjugate were due to the aggregation of globule form of PNIPAAm chain above the LCST [35]. The modification of chemical structure of PNIPAAm with hydrophilic or hydrophobic compound tuned the LCST of PNIPAAm [36]. Based on this study, the LCST for PNIPAAm-Maleimide and PNIPAAm-Ternatin were higher when compared to the LCST of PNIPAAm-CTA. This was due to the addition of hydrophilic maleimide compound and ternatin biomolecule at end-group of PNIPAAm chain that improved the LCST of the polymer. Therefore, the results indicated that the addition of hydrophilic compound increased the LCST of PNIPAAm. The small changes of LCST for PNIPAAm-Ternatin solution upon heating suggested that the conjugation of PNIPAAm with ternatin biomolecule did not contribute any effect on the thermoresponsive behaviour of PNIPAAm chain.

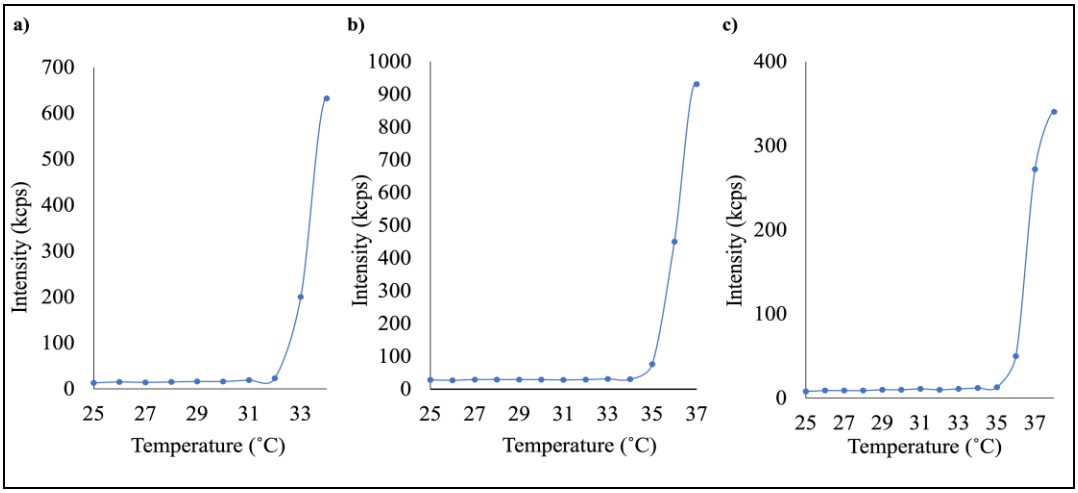

Figure 6. Light scattering intensities of (a) PNIPAAm-CTA, b) PNIPAAm-Maleimide and c) PNIPAAm-Ternatin solution at an indicated temperature in 10 mM HEPES pH 7.4 buffer solution

Conclusion

A thermoresponsive PNIPAAm conjugate was designed with ternatin biomolecule through controlled living radical polymerisation and esterification techniques. The synthesised PNIPAAm-CTA possessed molecular weight, Mw of 20140 g/mol and had quite a narrow molecular weight distribution (Mw/Mn) of 1.26, which revealed that the synthesised PNIPAAm through RAFT polymerisation was in a controlled structure. Moreover, PNIPAAm-Ternatin with conjugation percentage of 87.5% was successfully prepared through esterification technique. The synthesised PNIPAAm-CTA had a LCST at 32 °C. Meanwhile, the modification of PNIPAAm chain end-group by the addition of hydrophilic compound of maleimide (PNIPAAm-Maleimide) and the introduction of ternatin biomolecule (PNIPAAm-Ternatin) increased the LCST of PNIPAAm to 34 °C and 35 °C, respectively. Therefore, reported synthesised PNIPAAm and its chemical modifications are expected to provide a fundamental knowledge for further design and an excellent flexibility in tailoring for specific usage, particularly in the bioengineering and biomedical studies. Further studies on this topic are now in progress.

Acknowledgements

The authors thank the Ministry of Higher Education (MOHE) Malaysia for the financial support provided via the Fundamental Research Grant Scheme [ref no. FRGS/1/2018/STG05/UNIKL/02/5]. The authors also thank Universiti Kuala Lumpur Malaysian Institute of Chemical and Bioengineering Technology, Melaka, Malaysia for providing resources and necessary facilities for FTIR, HPLC and Light Scattering Intensity analyses. The authors also thank the Nuclear Magnetic Resonance Laboratory, University Industry Research Laboratory, Universiti Teknologi Malaysia, Johor, Malaysia for ^{1}H NMR analysis.

References

1. Hoffman, A. S. and Stayton, P. S. (2007). Conjugates of stimuli-responsive polymers and proteins. *Progress in Polymer Science,* 32(8-9): 922-932.
2. Martens, P. J., Bryant, S. J. and Anseth, K. S. (2003). Tailoring the degradation of hydrogels formed from multivinyl poly (ethylene glycol) and poly (vinyl alcohol) macromers for cartilage tissue engineering. *Biomacromolecules,* 4(2): 283-292.
3. Tan, L., Liu, J., Zhou, W., Wei, J. and Peng, Z. (2014). A novel thermal and pH responsive drug delivery system based on ZnO@PNIPAM hybrid nanoparticles. *Materials Science and Engineering: C,* 45(1): 524-529.
4. Tian, Y., Wei, X., Wang, Z. J., Pan, P., Li, F., Ling, D., Wu, Z. L. and Zheng, Q. (2017). A facile approach to prepare tough and responsive ultrathin

physical hydrogel films as artificial muscles. *ACS Applied Materials & Interfaces,* 9(39): 34349-34355.

5. Bajpai, A., Shukla, S. K., Bhanu, S. and Kankane, S. (2008). Responsive polymers in controlled drug delivery. *Progress in Polymer Science,* 33(11), 1088-1118.
6. Xiong, X., Del Campo, A. and Cui, J. (2019). Photoresponsive polymers. *Smart Polymers and Their Applications,* 1: 87-153.
7. Swift, T., Swanson, L., Geoghegan, M. and Rimmer, S. (2016). The pH-responsive behaviour of poly (acrylic acid) in aqueous solution is dependent on molar mass. *Soft Matter,* 12: 2542-2549.
8. Elbert, J., Mersini, J., Vilbrandt, N., Lederle, C., Kraska, M., Gallei, M., Stuhn, B., Plenio, H. and Rehahn, M. (2013). Reversible activity modulation of surface-attached grubbs second generation type catalysts using redox-responsive polymers. *Macromolecules,* 46(11): 4255-4267.
9. Lustig, S. R., Everlof, G. J. and Jaycox, G. D. (2001). Stimuli-responsive polymers. 5. Azobenzene modified polyaramides containing atropisomeric binaphthyl linkages: Tuning chiroptical behavior with light and heat. *Macromolecules,* 34(7): 2364-2372.
10. Schild, H. (1992). Poly(n-isopropylacrylamide): Experiment, theory and application. *Progress in Polymer Science,* 17(2): 163-249.
11. Abbott, L. J., Tucker, A. K. and Stevens, M. J. (2015). Single chain structure of a poly(n-isopropylacrylamide) surfactant in water. *The Journal of Physical Chemistry B,* 119 (9): 3837-3845.
12. Hirokawa, Y. and Tanaka, T. (1984). Volume phase transition in a nonionic gel. *The Journal of Chemical Physics,* 81 (12): 6379-6380.
13. Cook, M. T., Haddow, P., Kirton, S. B. and McAuley, W. J. (2020). Polymers exhibiting lower critical solution temperatures as a route to thermoreversible gelators for healthcare. *Advanced Functional Materials,* 31(8): 2008123.
14. Irani, C. A. and Cozewith, C. (1986). Lower critical solution temperature behavior of ethylene propylene copolymers in multicomponent solvents. *Journal of Applied Polymer Science,* 31(6): 1879-1899.
15. Maeda, Y., Higuchi, T. and Ikeda, I. (2000). Change in hydration state during the coil−globule transition of aqueous solutions of poly(n-isopropylacrylamide) as evidenced by FTIR spectroscopy. *Langmuir,* 16(19): 7503-7509.
16. García-Peñas, A., Biswas, C. S., Liang, W., Wang, Y., Yang, P. and Stadler, F. J. (2019). Effect of hydrophobic interactions on lower critical solution temperature for poly (n-isopropylacrylamide-co-dopamine methacrylamide) copolymers. *Polymers,* 11 (6): 991.
17. Ashbaugh, H. S. and Paulaitis, M. E. (2006). Monomer hydrophobicity as a mechanism for the LCST behavior of poly (ethylene oxide) in water. *Industrial & Engineering Chemistry Research,* 45(16): 5531-5537.
18. Che Harun, N., Takemoto, H., Nomoto, T., Tomoda, K., Matsui, M. and Nishiyama, N. (2016). Artificial control of gene silencing activity based on siRNA conjugation with polymeric molecule having coil-globule transition behavior. *Bioconjugate Chemistry,* 27(9): 1961-1964.
19. Nair, V., Bang, W. Y., Schreckinger, E., Andarwulan, N. and Cisneros-Zevallos, L. (2015). Protective role of ternatin anthocyanins and quercetin glycosides from butterfly pea (*Clitoria ternatea* Leguminosae) blue flower petals against lipopolysaccharide (LPS)-induced inflammation in macrophage cells. *Journal of Agricultural and Food Chemistry*, 63(28), 6355-6365.
20. Carelli, J. D., Sethofer, S. G., Smith, G. A., Miller, H. R., Simard, J. L., Merrick, W. C., Jain, R. K., Ross, N. T. and Taunton, J. (2015). Ternatin and improved synthetic variants kill cancer cells by targeting the elongation factor-1a ternary complex. *eLife*, 4: e10222.
21. Kobayashi, M., Kawashima, H., Takemori, K., Ito, H., Murai, A., Masuda, S., Yamada, K., Uemura, D. and Horio, F. (2012). Ternatin, a cyclic peptide isolated from mushroom, and its derivative suppress hyperglycemia and hepatic fatty acid synthesis in spontaneously diabetic KK-AY mice. *Biochemical and Biophysical Research Communications,* 427(2): 299-304.

22. Kuo, S.-W., Hong, J.-L., Huang, Y.-C., Chen, J.-K., Fan, S.-K., Ko, F.-H. and Chang, F.-C. (2012). Star poly(n-isopropylacrylamide) tethered to polyhedral oligomeric silsesquioxane (POSS) nanoparticles by a combination of ATRP and click chemistry. *Journal of Nanomaterials,* 2012: 1-10.
23. Coronado, R., Pekerar, S., Lorenzo, A. T. and Sabino, M. A. (2010). Characterization of thermo-sensitive hydrogels based on poly(n-isopropylacrylamide)/hyaluronic acid. *Polymer Bulletin*, 67(1): 101-124.
24. Ma, Y.-M., Wei, D.-X., Yao, H., Wu, L.-P. and Chen, G.-Q. (2016). Synthesis, characterization and application of thermoresponsive polyhydroxyalkanoate-graft-poly(n-isopropylacryl amide) *Biomacromolecules*, 17(8): 2680-2690.
25. Avila, A., Chinchilla, R. and Nájera, C. (2012). Enantioselective Michael addition of α,α-disubstituted aldehydes to maleimides organocatalyzed by chiral primary amine-guanidines. *Tetrahedron: Asymmetry*, 23(24): 1625-1627.
26. Ho, T. H., Levere, M., Soutif, J.-C., Montembault, V., Pascual, S. and Fontaine, L. (2011). Synthesis of thermoresponsive oxazolone end-functional polymers for reactions with amines using Thiol-Michael addition "click" chemistry. *Polymer Chemistry*, 2(6): 1258.
27. Lai, J. T., Filla, D. and Shea, R. (2002). Functional polymers from novel carboxyl-terminated trithiocarbonates as highly efficient RAFT agents. *Macromolecules,* 35(18): 6754-6756.
28. Roach, P., McGarvey, D., Lees, M. and Hoskins, C. (2013). Remotely triggered scaffolds for controlled release of pharmaceuticals. *International Journal of Molecular Sciences,* 14(4): 8585-8602.
29. Willcock, H. and O'Reilly, R. K. (2010). End group removal and modification of RAFT polymers. *Polymer Chemistry,* 1(2): 149-157.
30. Shen, G. (2004). X-ray photoelectron spectroscopy and infrared spectroscopy study of maleimide-activated supports for immobilization of oligodeoxyribonucleotides. *Nucleic Acids Research,* 32(20): 5973-5980.
31. Icriverzi, M., Rusen, L., Sima, L. E., Moldovan, A., Brajnicov, S., Bonciu, A., Mihailescu, N., Dinescu, M., Cimpean, A., Roseanu, A. and Dinca, V. (2018). *In vitro* behavior of human mesenchymal stem cells on poly (n-isopropylacrylamide) based biointerfaces obtained by matrix assisted pulsed laser evaporation. *Applied Surface Science,* 440: 712-724.
32. Smith, B. (2020). The C=O bond, Part VI: Esters and the rule of three. Access from https://www.spectroscopyonline.com/view/co-bon-part-vi-esters-and-rule-three. [Access online on 12 August 2021].
33. Ludin, N. (2018). Utilization of natural dyes from zingiber officinale leaves and *Clitoria ternatea* flowers to prepare new photosensitisers for dye-sensitised solar cells. *International Journal of Electrochemical Science,* (1): 7451-7465.
34. Ramesh, S., Sivasamy, A. and Kim, J. (2012). Synthesis and characterization of maleimide-functionalized polystyrene-SiO_2/TiO_2 hybrid nanocomposites by sol–gel process. *Nanoscale Research Letters,* 7(1): 350.
35. Chung, J., Yokoyama, M., Yamato, M., Aoyagi, T., Sakurai, Y. and Okano, T. (1999). Thermo-responsive drug delivery from polymeric micelles constructed using B lock copolymers of poly(n-isopropylacrylamide) and poly(butylmethacrylate). *Journal of Controlled Release,* 62(1-2), 115-127.
36. Yang, L., Fan, X., Zhang, J. and Ju, J. (2020). Preparation and characterization of thermoresponsive poly (n-isopropylacrylamide) for cell culture applications. *Polymers,* 12(2): 389.

Malaysian Journal of Analytical Sciences (MJAS)
Published by Malaysian Analytical Sciences Society

CATALYTIC CONVERSION OF CELLULOSE TO LEVULINIC ACID USING SUPPORTED NOBLE METAL PALLADIUM CATALYST

(Penukaran Bermangkin dari Selulosa ke Asid Levulinik Menggunakan Mangkin Disokong Logam Adi Paladium)

Puteri Nurain Syahirah Megat Muhammad Kamal, Norzahir Sapawe, Amin Safwan Alikasturi*

Universiti Kuala Lumpur Branch Campus Malaysian Institute of Chemical and Bioengineering Technology, Lot 1988 Vendor City, Taboh Naning, 78000 Alor Gajah, Melaka, Malaysia

**Corresponding author: aminsafwan@unikl.edu.my*

Received: 15 September 2021; Accepted: 30 December 2021; Published: 25 February 2022

Abstract

In resolving the current energy crisis, it is vital to effectively use the abundant biomass to produce platform chemicals, for instance levulinic acid (LA). LA is very flexible for the formation of high value-added chemicals as it belongs to the family of carboxyl and ketone. This valuable platform chemical can be produced from cellulose (the most abundant biomass in nature). Palladium (Pd) as a noble metal was incorporated with catalyst supports (silica-alumina; SiO_2-Al_2O_3 and gamma-alumina; γ-Al_2O_3) by using wet impregnation method, aiming for 4 wt.% of noble metal on supports followed by catalyst calcination at 500 ˚C. The catalyst was characterized using Fourier-transform infrared spectroscopy (FTIR) and Brunauer–Emmett–Teller (BET). The effects of reaction parameters such as agitation speed, reaction temperature, and cellulose loading were investigated using this catalyst in a semi-batch reactor for 8 hours. The highest conversion of cellulose (73.9%) and yield of LA (43.3%) was achieved under these conditions: agitation speed of 1100 rpm, reaction temperature of 200 ˚C, and cellulose loading of 1.5 g with pre-reduction of Pd/SiO_2-Al_2O_3 catalyst (surface area and pore volume up to 485.6 m^2/g and 0.2459 cm^3/g, respectively) at 150 ˚C and agitation speed of 1300 rpm (in 5 bars of hydrogen, H_2 for 1 hour).

Keywords: Pd/SiO_2-Al_2O_3, cellulose, hydrolysis, levulinic acid

Abstrak

Dalam menyelesaikan krisis tenaga semasa, adalah sangat penting untuk menggunakan biojisim yang berkesan dalam menghasilkan bahan kimia platform seperti asid levulinik (LA). LA sangat fleksibel untuk pembentukan bahan kimia bernilai tinggi, kerana ia tergolong dalam keluarga karboksil dan keton. Bahan kimia platform yang berharga ini boleh dihasilkan dari selulosa (biojisim yang paling banyak terdapat di alam semula jadi). Paladium (Pd) sebagai logam adi boleh digabungkan dengan penampung mangkin (silica-alumina; SiO_2-Al_2O_3 and gamma-alumina; γ-Al_2O_3) yang dihasilkan menggunakan kaedah impregnasi basah yang bertujuan untuk 4% logam adi pada penampung mangkin diikuti oleh kalsinasi mangkin pada suhu 500 ˚C. Mangkin dicirikan menggunakan spektroskopi inframerah transformasi Fourier (FTIR) dan *Brunauer–Emmett–Teller* (BET). Kajian mengenai pengaruh parameter reaksi seperti kelajuan pengadukan, suhu tindak balas, dan pemuatan selulosa disiasat menggunakan mangkin ini dalam reaktor semi-kelompok selama 8 jam. Penukaran selulosa tertinggi (73.9%) dan hasil LA (43.3%) dicapai dalam keadaan ini; kelajuan pengadukan 1100 rpm, suhu tindak balas 200 ˚C, dan pemuatan selulosa 1.5 g

dengan pra-pengurangan mangkin Pd/SiO_2-Al_2O_3 (luas permukaan dan isi pori 485.6 m^2/g dan 0.2459 cm^3/g, masing masing) pada suhu 150 ˚C dan kelajuan pengadukan 1300 rpm (dalam 5 bar hidrogen, H_2 selama 1 jam).

Kata kunci: Pd/SiO_2-Al_2O_3, selulosa, hidrolisis, asid levulinik

Introduction

Cellulose, a part of biomass, is a major component of lignocelluloses as it comprises 40-50% of lignocellulose composition. It is formed by dehydration and condensation of glucose produced from photosynthesis [1]. Starch, which is likewise created by photosynthesis but having a different characteristic than cellulose, can be classified as biomass. Starch, a polymer with α-1→4 glycosidic linkages, is soluble in hot water and is the main constituent of corn, potato, and rice. Even though considerable attention has been given to the production of fuels and chemicals, starch should be prioritized as a dietary source [2].

Furthermore, the amount of cellulose is so enormous that it is wasteful to simply let it decompose without exploring its potential benefits. The commercial feasibility of producing sugar alcohols such as sorbitol and mannitol, which are particularly valuable in the food sector as sweeteners and preservatives, by using hydrogenation method is one way to utilize this enormous resource [3]. When it comes to catalytic cellulose hydrolysis, LA is the main product produced after cellulose undergoes a few processes; 1) hydrolysis 2) dehydration and 3) rehydration [4]. Figure 1 shows the reaction pathway for the production of LA from cellulose.

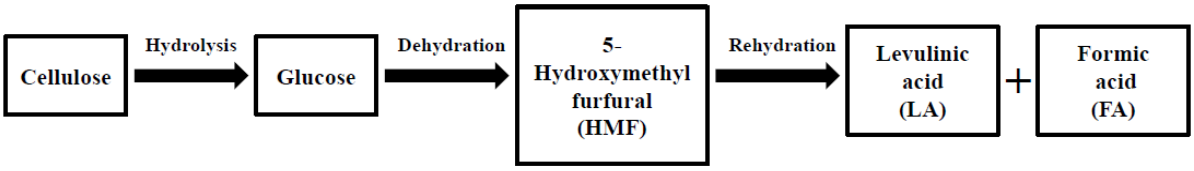

Figure 1. Reaction pathway for the production of LA from cellulose

LA is a water-soluble, organic compound that comes from the family of carboxylic acid and ketone, possessing a wide range of reactivity and functionality [5]. These two functional groups cause LA to be a very versatile building block for a vast chemical transformation of high-value organic chemicals, resin precursors, polymers precursors, and fuel additives with plenty of potential industrial applications [4]. Succinic acid and maleic anhydride are two high value-added chemicals that can be synthesized from LA and are useful in the food and textile industries, respectively. Aside from that, LA can be utilized as a starting material for the production of γ–valerolactone, as well as ethyl and methyl levulinate, making it a potential alternative to petroleum-based fuels or chemicals [6]. Aside from choosing LA as the final product, the reaction can be tuned up to produce various products with high yields, such as 5-hydroxymethylfurfural (HMF) and formic acid (FA).

Over the past decade, homogeneous catalysts have been used in many applications, including LA synthesis (using acids). Despite its efficiency, there are a few drawbacks to use this type of acid in the system, including the generation of additional wastes due to the difficulties of separation and recovery (environmental pollution). Besides that, this catalyst leads to equipment corrosion [7]. As a result, many researchers nowadays prefer to use heterogeneous catalysts in their systems, especially solid catalysts to overcome the issues that arise from the homogenous catalyst. Metal oxides, supported metals (nickel, Ni), H-form zeolites, carbonaceous acids, heteropoly acids, acid resins, magnetic acids, and functionalized silicas are the

examples of solid catalysts that have garnered attention as promising and appealing catalysts for the hydrolysis of cellulose [8].

Recently, there has been a noticeable growth towards employing cheap, non-noble metal-based catalysts such as Ni, yet the study on this catalyst's stability and recyclability needs to be emphasized as leaching and sintering can be mainly responsible for the decreasing catalytic activity [9]. Hence, in this research study, Palladium (Pd), a noble metal that can be regenerated and recycled up to 20 times without observing any significant loss of activity [10] was utilized as a catalyst. Even though Pd is relatively expensive when used individually, Pd can be incorporated into high dispersion and narrow sizes distribution of catalyst support such as silica (SiO_2) and alumina (Al_2O_3). Despite the high cost of Pd, it is widely acknowledged for its high chemical stability and catalytic abilities [11].

Therefore, this research was conducted to study the effects of various reaction conditions such as agitation speed, temperature, and substrate loading on the production of LA from cellulose using noble metal, Pd supported on different catalyst supports such as silica-alumina (SiO_2 -Al_2O_3) and gamma-alumina (γ-Al_2O_3). As a result, the most suitable catalyst that was effective in the conversion of cellulose to LA (under the conditions studied) could be determined throughout the experiments.

Materials and Methods

Materials

For the synthesis of catalyst, palladium (II) nitrate ($Pd(NO_3)_2$) with 40% w/w of Pd, SiO_2-Al_2O_3 grade 135 ($\leq$100%), and γ-Al_2O_3 (99.9%) were purchased from Sigma Aldrich and Alfa Aesar, respectively. As for the experimental work, microcrystalline cellulose (extra pure, 100%) from Acros Organics was used as substrates. In addition, glucose (>99.9%), HMF (>98%), LA (>98%), FA (>98%), and furfural (>99.9%) were used for standard reference calibration purposes. All the chemicals were analytical grade without further purification and distilled (DI) water was used for all the experiments.

Catalyst preparation

The solid noble catalyst was prepared using wet impregnation method. This method aimed to provide 5 g of 4 wt.% Pd on SiO_2-Al_2O_3 support. About 4.8 g of SiO_2-Al_2O_3 was weighed and spread on a petri dish. Then, 0.5 g of $Pd(NO_3)_4$ was dissolved in the minimum amount of DI water necessary to wet the SiO_2-Al_2O_3 support; this was found to be 3.3 ml of DI for 4.8 g of SiO_2-Al_2O_3. The diluted $Pd(NO_3)_4$ was dropped to the spread SiO_2-Al_2O_3 carefully using a syringe. The dropping was done in a circular motion where each $Pd(NO_3)_4$ droplet was at different point. After that, the $Pd(NO_3)_4$ was pressed using a spatula to achieve a homogenous mixture between $Pd(NO_3)_4$ and SiO_2-Al_2O_3. The prepared catalyst was dried using an oven at 110 ˚C for 12 hours to remove the excess moisture prior to calcination. The catalyst was then calcined at 500 ˚C for 5 hours. The catalyst was stored in a vial sealed with parafilm, and stored in desiccator prior to analysis and experimental work. The method was repeated to prepare 4 wt.% Pd on γ-Al_2O_3 support.

Catalyst characterization

The Fourier-transform infrared spectroscopy (FTIR) analysis was conducted with a Nicolet iS10 FTIR with a spectral resolution of 8 cm^{-1} at room temperature and accumulation of 5 scans in an open beam air background [12]. The spectrum ranged from 4000 cm^{-1} to 400 cm^{-1}. The Brunauer–Emmett–Teller (BET) method was used to determine the surface area and pore volume using Micromeritics 3Flex where the catalyst was degassed at 150 ˚C for 12 hours in N_2 prior to analysis.

Experimental procedure

The pre-reduction of catalyst and the experimental work for the catalytic conversion of cellulose to LA were carried out in a 100 ml stainless steel semi-batch reactor. The pre-reduction of catalyst was conducted with 5 bar of hydrogen gas (H_2). The desired temperature (130 ˚C and 150 ˚C) and agitation speed (600 rpm and 1300 rpm) were set according to the parameters studied for 1 hour. As for the reaction work, after the pre-reduction of catalyst, cellulose was loaded into the reactor containing catalyst and distilled water. The air inside the reactor was purged out using N_2

about three times. Once the desired temperature (170 ˚C and 200 ˚C) had been achieved, the stirring speed (1300 rpm) and timer were set accordingly. The reaction took place for 8 hrs. The samples were collected at the time interval of 0 min, 30 min, 60 min, 120 min, 180 min, and 480 min by opening the valve of the sample port. After releasing the gas inside the reactor, to stop the reaction, the reactor was quenched into a beaker with cold water.

The remaining solid product was collected and filtered using filter paper before drying in the oven at 100 ˚C overnight. The weight was recorded regularly until a constant weight of ±0.005 g was achieved. This data was essential for the calculation of cellulose conversion to products. The final weight of cellulose and cellulose conversion was calculated using Equations 1 and 2, respectively.

The weight of the cellulose could only be obtained at the end of the experiment because the reactor used was a semi-batch reactor. Thus, the remaining solid product could not be collected during the reaction process.

Product analysis

The liquid products were filtered to remove any impurities and analyzed using a High-Performance Liquid Chromatography (HPLC) system: Sugar SH1011 (SHODEX, Japan) with ion exclusion mode (column's physical size: 8.0 mm I.D X 300 mm) and UV as column and detector, respectively. An aqueous solution of sulphuric acid (0.05 M) at a flow rate of 1 ml/min was used as mobile phase and the column temperature was set at 40 ˚C [8].

$$\text{Weight}_{\text{final cellulose}}\,(a) = \text{Weight}_{\text{solid product after drying}} - \text{Weight}_{\text{filter paper}} - \text{Weight}_{\text{catalyst}} \quad (1)$$

$$\text{Cellulose conversion (\%)} = \frac{a - \text{Weight}_{\text{initial cellulose}}}{\text{Weight}_{\text{initial cellulose}}} \times 100\% \quad (2)$$

Results and Discussion

Catalyst characterization (FTIR)

The validation of the decomposition of precursor (nitrate) in the synthesized catalyst after calcination at 500˚C was verified by FTIR analysis. A FTIR spectrum comparison between catalysts before and after calcination was conducted, and the findings are presented in Figures 2 and 3. Table 1 shows the summary of the functional group present in this study.

Based on Figures 2 and 3, a similar trend of FTIR spectrum was obtained for each of the catalysts. The spectral range of 3600-3200 cm^{-1} and 1700-1600cm^{-1} were assigned to the stretching and bending modes of absorbed water molecules through hydrogen bonding, respectively [13,14]. The presence of C-O stretching band at the spectral range of 2400-2300 cm^{-1} represented atmospheric carbon dioxide (CO_2), an impurity and sign that contamination might have occurred [15,14].

The FTIR spectrum around 1450-1300 cm^{-1} proved the presence of nitrate precursor (NO_3^-) in the catalyst (before calcination) [16,17]. The diminishing intensity of the catalyst's peak after calcination implied that the decomposition of nitrate was successful at the calcination temperature of 500 ˚C [14]. As a result, it can be concluded that calcination temperature of 500 ˚C is effective in removing nitrate precursor. On the other hand, an extra peak was discovered from the FTIR spectra analysis for Pd/SiO_2-Al_2O_3 (Figure 2) at the range of 1200-1000 cm^{-1}, showing the presence of Si-O-Si [18,19].

Table 1. Summary of the functional group present in this study

Region	Wavelength (cm^{-1})	Peak Assignment
I	3600-3200	O-H stretching, strong, broad
II	2400-2300	C-O stretching
III	1700-1600	O-H bending
IV	1450-1300	NO_3^- (nitrate)
V	1200-1000 (for Pd/SiO_2-Al_2O_3)	Si-O-Si

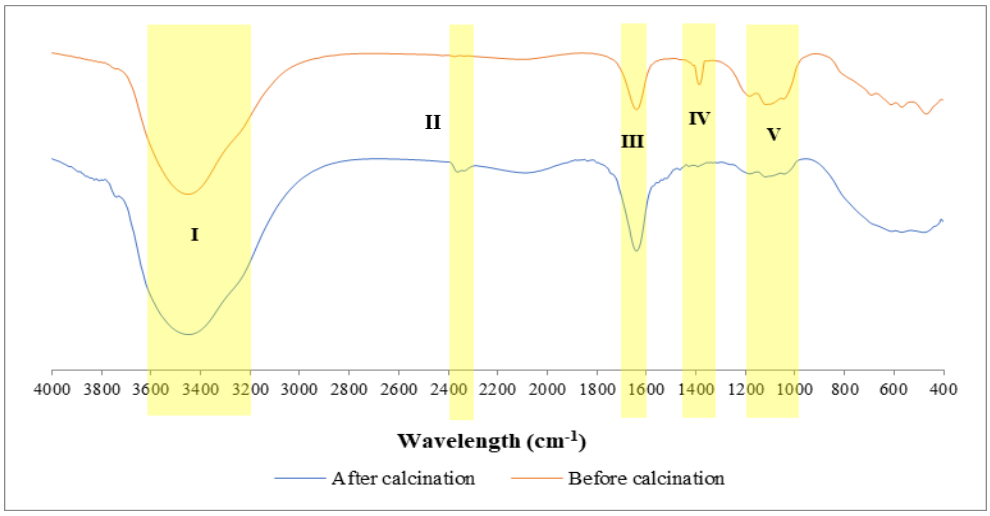

Figure 2. FTIR spectra before and after calcination for catalyst Pd/SiO_2-Al_2O_3

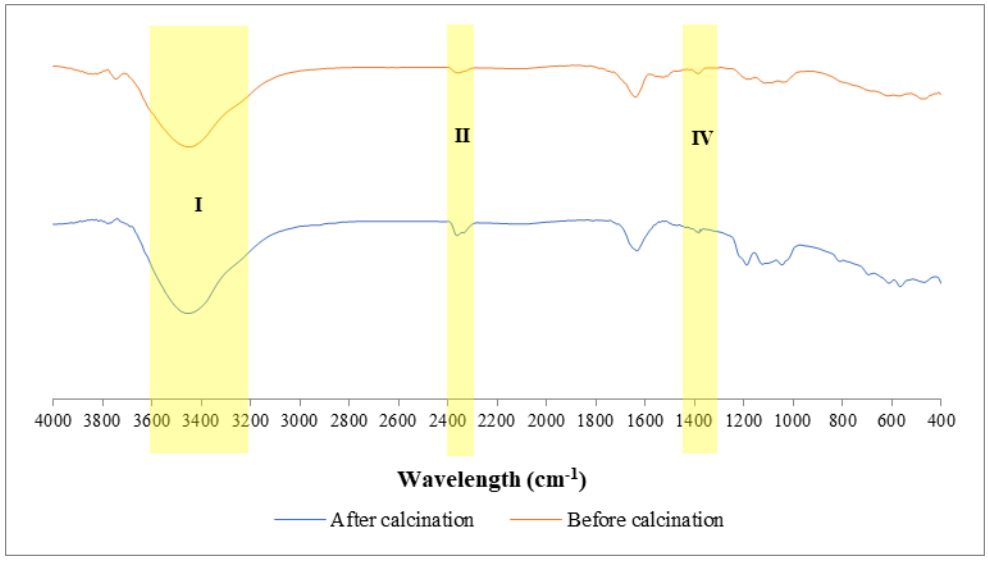

Figure 3. FTIR spectra before and after calcination for catalyst Pd/γ-Al_2O_3

Catalyst characterization (BET)

In heterogeneous catalysts, specific area and pore volume are significant factors to consider especially for the supported catalyst. The BET surface area and pore volume of raw supports and catalysts are listed in Table 2.

Based on Table 2, an increasing trend of surface area and pore volume was observed from raw SiO_2-Al_2O_3 to catalyst Pd/SiO_2-Al_2O_3 (after calcination). The surface area increased from 217.6 m^2/g to 485.6 m^2/g and the pore volume increased from 0.1068 cm^3/g to 0.2459 cm^3/g, which could be explained by the elimination of organic matters where many new pores were formed during the calcination [20]. However, for catalyst Pd/γ-Al_2O_3, the trend of the result was converse from that of the Pd/SiO_2-Al_2O_3 (after calcination) as the surface area and pore volume decreased from raw γ-Al_2O_3 to Pd/γ-Al_2O_3 possibly due to aggregation of catalyst, resulting in losing the surface area and decreasing the pore volume [21].

Catalyst Pd/SiO_2-Al_2O_3 possessed a high pore volume (0.2459 cm^3/g) and surface area (485.6 m^2/g) compared to catalyst Pd/γ-Al_2O_3 (pore volume and surface area of 0.0296 cm^3/g and 79.4 m^2/g, respectively) (Table 2). This could be due to the combination of materials such silica (SiO_2) and alumina (Al_2O_3) that significantly increased the porosity and surface area [22]. Moreover, this observation could be related to the findings according to Table 2 where the pore volume and surface area of the combined materials (SiO_2-Al_2O_3) were two times larger than raw γ-Al_2O_3.

Table 2. BET surface area, pore volume and particle size of raw supports and catalysts

Sample	Surface Area[a] (m^2/g)	Pore Volume[b] (cm^3/g)
SiO_2-Al_2O_3	217.6	0.1068
Pd/SiO_2-Al_2O_3 (After calcined)	485.6	0.2459
γ-Al_2O_3	101.3	0.0504
Pd/γ-Al_2O_3 (After calcined)	79.4	0.0296

[a]: Surface area is obtained from BET method,
[b]: Pore volume is obtained from BET method

Effects of agitation speed during pre-reduction of catalyst and reaction work

Based on Figure 4, at higher agitation speed, an increasing trend in the yield of LA was observed for both of the catalysts. This increasing trend of yield was also seen for HMF and FA, except for glucose possibly because glucose was converted to other products (HMF, LA, and FA). LA produced from cellulose was at the highest (33.5%) when the reaction agitation speed was at 1100 rpm with pre-reduction of Pd/SiO_2-Al_2O_3 catalyst at 1300 rpm. Up to 20.6% of cellulose was successfully converted to products. This high conversion of cellulose and production of LA might be due to the high agitation speed during the reaction; increasing the agitation speed increases the contact area and relative velocity between the two phases, and hence diminishes any external diffusion limitations [23]. Furthermore, the higher surface area and pore volume of Pd/SiO_2-Al_2O_3 catalyst (485.6 m^2/g and 0.2459 cm^3/g, respectively) caused the high conversion of cellulose and yield of LA as these properties led to the high availability of catalytic activity sites [24]. Thus, high catalytic activity could occur during the reaction compared to the usage of Pd/γ-Al_2O_3 catalyst, which possessed a smaller surface area and pore volume of 79.4 m^2/g and 0.0296 cm^3/g, respectively. Owing to these properties, an increment of only 6.4% of LA

yield was observed for catalyst Pd/γ-Al_2O_3 when an increase of reaction speed from 200 rpm to 1100 rpm was employed, with 12.2% of cellulose being converted to products.

Even though the usage of high agitation speed during the pre-reduction catalyst (activation) is not as crucial as high temperature [25], increasing agitation speed during the pre-reduction of catalyst might improve the performance of the catalyst by increasing the surface contact of the catalyst with H_2 which can activate the catalyst prior to the reaction [26]. The pre-reduction for both of the catalysts was aimed to reduce palladium oxide to metallic Pd. As a result, it can be concluded that the reaction agitation speed of 1100 rpm with the catalyst pre-reduction agitation speed at 1300 rpm was the most ideal condition in this study for further experimentation.

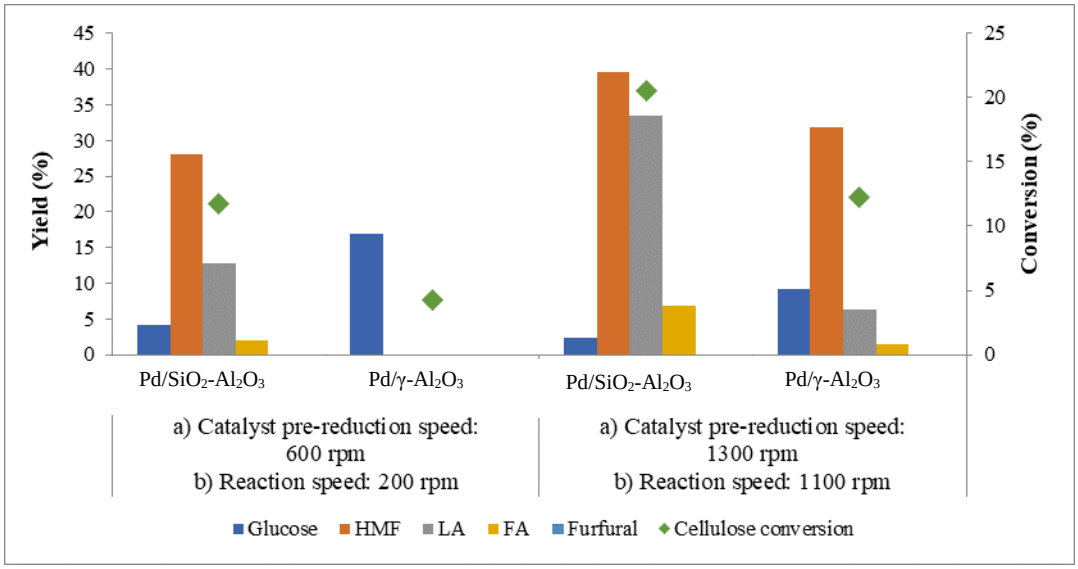

Figure 4. Effects of agitation speed on the conversion of cellulose to LA at 8 hours. Note: a) Catalyst pre-reduction condition: 0.5 g of catalyst, and 5 bar of H_2 at 130 ˚C for 1 hour; b) Reaction condition: 4 g of cellulose, 0.5 g of catalyst, reaction temperature of 170 ˚C, and reaction time of 8 hours.

Effects of temperature during pre-reduction of catalyst and reaction work

Temperature plays a significant role in the production of LA from cellulose, particularly at higher temperatures as demonstrated in a previous study [27]. The effects of temperature on the production of LA from cellulose at different cellulose loading is shown in Figure 5.

Based on Figure 5, a significant increment in the conversion of cellulose and production of LA was observed when the reaction temperature increased from 170 ˚C to 200 ˚C with catalyst pre-reduction at 150 ˚C. Except for glucose, the production of intermediate products and by-products such as HMF and FA, respectively also increased as the reaction temperature rose. According to this study, as the temperature increased (from 170 ˚C to 200 ˚C), the cellulose conversion increased gradually from 20.6% to 73.9% when Pd/SiO_2-Al_2O_3 catalyst (pre-reduction of catalyst at the temperature of 150 ˚C) was employed in the system where the highest LA was produced (up to 43.3%) possibly since the higher reaction temperature accelerated the rate of chemical reaction and provided a faster route for the cellulose to convert to products [8]. Furthermore, a higher reaction temperature promotes greater contact between cellulose and water molecules, resulting in a complete process of cellulose bond breaking to form LA [28]. A similar trend of results was observed with Pd/SiO_2-Al_2O_3 catalyst when

$Pd/\gamma\text{-}Al_2O_3$ catalyst was employed in the system; the conversion of cellulose and yield of LA increased as the reaction temperature increased. However, the conversion of cellulose and yield of LA were lower using $Pd/\gamma\text{-}Al_2O_3$ catalyst in the system compared to $Pd/SiO_2\text{-}Al_2O_3$ catalyst. The conversion of cellulose and yield of LA were only up to 37.1% and 9.5%, respectively.

Moreover, one of the parameters that improved the catalyst efficiency was increasing the temperature from 130 ˚C to 150 ˚C during the pre-reduction of the catalyst. It is advised to heat the catalyst at a high temperature during the catalyst pre-reduction for the metal to finely disperse on the support. Under these high temperatures during heating the catalyst, the mobility of the catalyst can be enhanced, increasing the active site of the catalyst, and thus greatly influencing the catalytic activity [25].

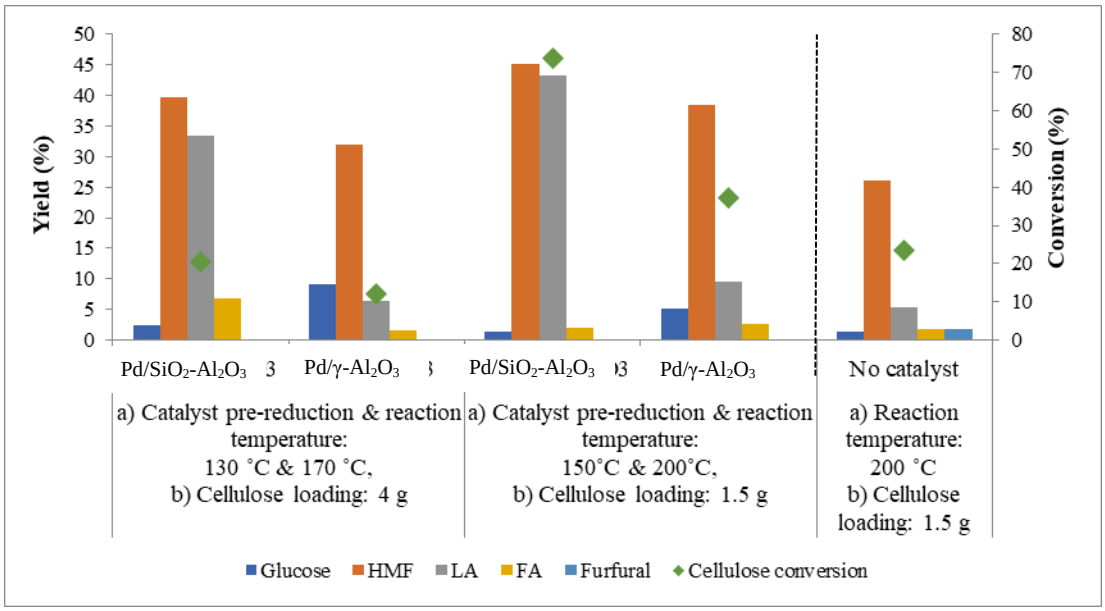

Figure 5. Effects of temperature on the conversion of cellulose towards LA at 8 hours. Note: a) Catalyst pre-reduction condition: 0.5 g of catalyst, agitation speed of 1300 rpm, and 5 bar of H_2 for 1 hour; b) Reaction condition: 0.5 g of catalyst, agitation speed of 1100 rpm, and reaction time of 8 hours

Effects of substrate loading

Based on Figure 5, the yield of LA increased gradually for all the catalysts ($Pd/SiO_2\text{-}Al_2O_3$ and $Pd/\gamma\text{-}Al_2O_3$) when 1.5 g of cellulose was used in the reaction (under high-temperature conditions). Increasing the substrates loading might lead to the increasing cellulose availability for the conversion, with a high concentration of LA being produced; however, the yield of LA was shown to eventually decrease as the cellulose loading increased. This might be due to the reactivity diminution or insufficient catalyst dosage for the additional cellulose [4].

Moreover, a blank experiment (without catalyst) was conducted for reference purposes. It was conducted under the ideal condition highlighted in this study. LA produced was at its lowest (5.3%) compared to the other reactions that used catalyst. This might be due to the side reaction that occurred during the reaction where it resulted in the production of furfural [29]. According to Figure 5, it can be highlighted that the production of HMF was more favorable if no catalyst was employed in the system.

Figure 6 shows the reaction profile of reaction using Pd/SiO_2-Al_2O_3 under the high condition in cellulose depolymerization, leading to the formation of LA. According to Figure 6, the yield of all products (HMF, LA, and FA) increased overtime except for glucose. An increasing yield of glucose was reported until 2 hours of reaction, then the yield subsequently decreased. This might be due to the glucose already being used up in converting to other products. Since the hydrolysis of cellulose to glucose was the rate-determining step, once glucose was formed, it was much easier to break down the glucose bond to other products. Hence, it resulted in the formation of HMF (5.73%), LA (17.4%), and FA (0.77%) at the 30 min of reaction time. As a result, 73.9% of cellulose was converted to products, and 43.4% of LA yield was produced at the end of the reaction.

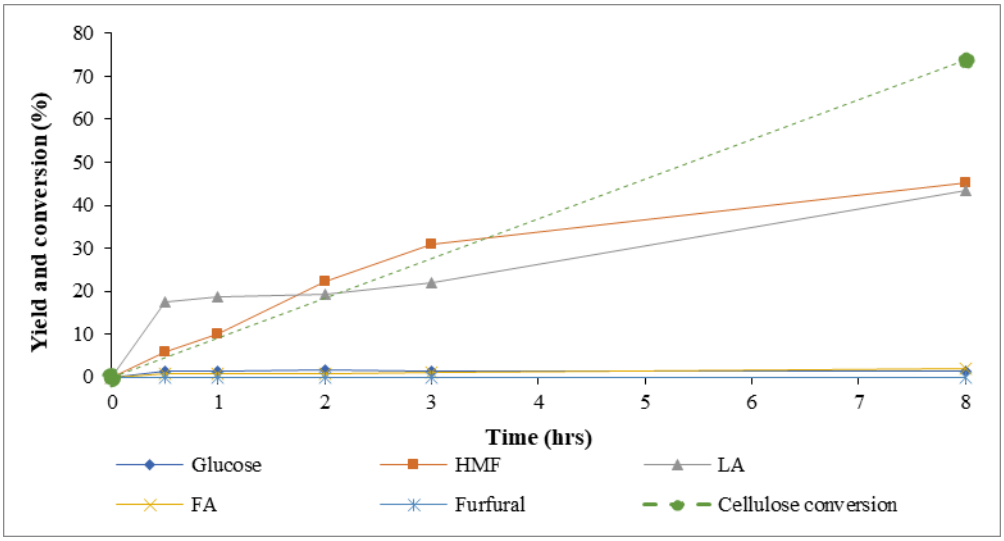

Figure 6. Reaction profile for catalyst Pd/SiO_2-Al_2O_3. Note: Reaction condition: 1.5 g of cellulose, 0.5 g of catalyst (pre-reduction at an agitation speed of 1300 rpm in H_2 at 150˚C for 1 hour), reaction temperature of 200 ˚C, agitation speed of 1100 rpm, and reaction time of 8 hours.

Conclusion

From this research, it can be concluded that the conversion of cellulose to LA is highly influenced by the reaction parameters: agitation speed (1100 rpm), temperature (200 ˚C), and substrate loading (1.5 g) with catalyst pre-reduction at the temperature of 150 ˚C and stirred at 1300 rpm for 1 hour. It was observed that under these conditions, the LA produced was at the highest which was 43.3% and the conversion of cellulose was up to 73.9%. Moreover, the higher surface area (485.6 m^2/g) and pore volume (0.2459 cm^3/g) of Pd/SiO_2-Al_2O_3 catalyst showed better performance to produce LA from cellulose compared to Pd/γ-Al_2O_3.

Acknowledgments

The authors would like to express their highest gratitude for the financial support from the Ministry of

Higher Education (MOHE) (under the Fundamental Research Grant Scheme, FRGS/1/2018/ TK02/UNIKL/02/3), Universiti Kuala Lumpur Malaysian Institute of Chemical and Bioengineering Technology (UniKL MICET), and Majlis Amanah Rakyat Malaysia (MARA).

References

1. Caretto, A. and Perosa, A. (2013). Upgrading of levulinic acid with dimethylcarbonate as solvent/ reagent. *Sustainable Chemistry & Engineering*, 1(8): 6-11.
2. Dhepe, P. L. and Fukuoka, A. (2007). Cracking of cellulose over supported metal catalysts. *Catalysis Surveys from Asia*, 11(4): 186-191.
3. Shrotri, A., Kobayashi, H. and Fukuoka, A. (2018). Cellulose depolymerization over heterogeneous catalysts. *Accounts of Chemical Research*, 51(3): 761-768.
4. Peng, L., Lin, L., Zhang, J., Zhuang, J., Zhang, B. and Gong, Y. (2010). Catalytic conversion of cellulose to levulinic acid by metal chlorides. *Molecules*, 15: 5258-5272.
5. Signoretto, M., Taghavi, S., Ghedini, E. and Menegazzo, F. (2019). Catalytic production of levulinic acid (LA) from actual biomass. *Molecules (Basel, Switzerland)*, 24(15): 1-20.
6. Jeong, H., Jang, S., Hong, C. and Kim, S. (2016). Levulinic acid production by two-step acid-catalyzed treatment of *Quercus mongolica* using dilute sulfuric acid. *Bioresource Technology*, 225: 1-28.
7. Thunyaratchatanon, C., Sinsakullert, W., Luengnaruemitchai, A. and Faungnawakij, K. (2019). 5-hydroxymethylfurfural production from hexose sugars using adjustable acid- and base-functionalized mesoporous SBA-15 catalysts in aqueous media. *Biomass Conversion and Biorefinery*, 2019: 1-15.
8. Li, G., Liu, W., Ye, C., Li, X. and Si, C. L. (2018). Chemocatalytic conversion of cellulose into key platform chemicals. *International Journal of Polymer Science*, 2018: 1-20.
9. Li, X., Zhang, L., Wang, S. and Wu, Y. (2020). Recent advances in aqueous-phase catalytic conversions of biomass platform chemicals over heterogeneous catalysts. *Frontiers in Chemistry*, 7(948): 1-21.
10. Xu, S., Yan, X., Bu, Q. and Xia, H. (2017). Catalytic conversion of cellulose into polyols using carbon-nanotube-supported monometallic Pd and bimetallic Pd–Fe catalysts. *Cellulose*, 24(6): 2403-2413.
11. Yoshimura, A., Tochigi, S. and Matsuno, Y. (2021). Fundamental study of palladium recycling using "dry aqua regia" considering the recovery from spent auto-catalyst. *Journal of Sustainable Metallurgy*, 7(1): 266-276.
12. Kamal, P. N. S. M. M., Mohamad, N. I., Serit, M. E. A., Rahim, N. S. A., Jimat, N. I. and Alikasturi, A. S. (2020). Study on the effect of reaction and calcination temperature towards glucose hydrolysis using solid acid catalyst. *Materials Today: Proceedings*, 31(8)*:* 282-286.
13. Benkhaled, M., Morin, S., Pichon, C., Thomazeau, C., Verdon, C. and Uzio, D. (2006). Synthesis of highly dispersed palladium alumina supported particles: Influence of the particle surface density on physico-chemical properties. *Applied Catalysis A: General*, 312(1–2): 1-11.
14. Yabushita, M., Kobayashi, H., Hara, K. and Fukuoka, A. (2014). Quantitative evaluation of ball-milling effects on the hydrolysis of cellulose catalysed by activated carbon. *Catalysis Science and Technology*, 4(8): 2312-2317.
15. Anderson, I. E., Shircliff, R. A., MacAuley, C., Smith, D. K., Lee, B. G., Agarwal, S., Stradins, P. and Collins, R. T. (2012). Silanization of low-temperature-plasma synthesized silicon quantum dots for production of a tunable, stable, colloidal solution. *Journal of Physical Chemistry C*, 116(6): 3979-3987.
16. Zhang, H., Huang, H., Ji, Y., Qiao, Z., Zhao, C. and He, J. (2010). Preparation, characterization, and application of magnetic Fe-SBA-15 mesoporous silica molecular sieves. *Journal of Automated Methods and Management in Chemistry*, 2010(1463–9246): 323509.

17. Amadine, O., Essamlali, Y., Fihri, A., Larzek, M. and Zahouily, M. (2017b). Effect of calcination temperature on the structure and catalytic performance of copper-ceria mixed oxide catalysts in phenol hydroxylation. *RSC Advances*, 7(21): 12586-12597.
18. Yadav, M. K., Kothari, A. V. and Naik, D. G. (2009). Morphological silica-supported acid catalyst for esterification of aliphatic fatty acid. *Green Chemistry Letters and Reviews*, 2(3):181-197.
19. Shah, K. A., Parikh, J. K., Dholakiya, B. Z. and Maheria, K. C. (2014). Fatty acid methyl ester production from acid oil using silica sulfuric acid: Process optimization and reaction kinetics. *Chemical Papers*, 68(4): 472-483.
20. Amadine, O., Essamlali, Y., Fihri, A., Larzek, M. and Zahouily, M. (2017a). Effect of calcination temperature on the structure and catalytic performance of copper-ceria mixed oxide catalyst in phenol hydroxylation. *RSC Advances*, 7:12586-12597.
21. Inmanee, T., Pinthong, P. and Jongsomjit, B. (2017). Effect of calcination temperatures and mo modification on nanocrystalline (γ-χ)-Al_2O_3 catalysts for catalytic ethanol dehydration. *Journal of Nanomaterials*, 2017(2011): 1-9.
22. Rahmati, M., Huang, B., Mortensen, M. K., Keyvanloo, K., Fletcher, T. H., Woodfield, B. F., Hecker, W. C. and Argyle, M. D. (2018). Effect of different alumina supports on performance of cobalt Fischer-Tropsch catalysts. *Journal of Catalysis*, 359: 92-100.
23. Ahlkvist, J. (2013). Formic and levulinic acid from cellulose via heterogeneous catalysis. Doctoral dissertation, Umeå Universitet.
24. Klinghoffer, N. B., Castaldi, M. J., Nzihou, A. (2012). Catalyst properties and catalytic performance of char from biomass gasification. *Industrial and Engineering Chemistry Research*, 51(40): 13113-13122.
25. Fadoni, M. and Lucarelli, L. (1999). Temperature programmed desorption, reduction, oxidation and flow chemisorption for the characterisation of heterogeneous catalysts. Theoretical aspects, instrumentation and applications. *Studies in Surface Science and Catalysis*, 120: 177-225.
26. Shim, W. G., Lee, J. W. and Kim, S. C. (2008). Analysis of catalytic oxidation of aromatic hydrocarbons over supported palladium catalyst with different pretreatments based on heterogeneous adsorption properties. *Applied Catalysis B: Environmental*, 84(1-2): 133-141.
27. Yuan, Z., Long, J., Xia, Y., Zhang, X. and Wang, T. (2016). Production of levulinic acid from *Pennisetum alopecuroides* in the presence of an acid catalyst. *Bioresources*, 11(2): 3511-3523.
28. Watanabe, M., Aizawa, Y., Iida, T., Aida, T. M., Levy, C., Sue, K. and Inomata, H. (2005). Glucose reactions with acid and base catalysts in hot compressed water at 473 K. *Carbohydrate Research*, 340: 1925-1930.
29. Liu, L., Li, Z., Hou, W. and Shen, H. (2018). Direct conversion of lignocellulose to levulinic acid catalyzed by ionic liquid. *Carbohydrate Polymers*, 181(7): 778-78.

Malaysian Journal of Analytical Sciences (MJAS)
Published by Malaysian Analytical Sciences Society

PHYSICAL AND CHEMICAL DISCRIMINATION OF METHAMPHETAMINE TABLETS FOR FORENSIC INTELLIGENCE

(Diskriminasi Fizikal dan Kimia bagi Pil Metamfetamin untuk Perisikan Forensik)

Noor Azlina Awang[1,2], Khai Lee[1], Way Koon Teoh[1], Vanitha Kunalan[3], Ahmad Fahmi Lim Abdullah[1], Kah Haw Chang[1]*

[1]Forensic Science Programme, School of Health Sciences,
Universiti Sains Malaysia, 16150 Kubang Kerian, Kelantan, Malaysia
[2]Department of Chemistry Malaysia (Kelantan Branch), 16100 Panji, Kota Bharu, Malaysia
[3]Narcotics Division, Forensic Science Analysis Centre,
Department of Chemistry, Jalan Sultan, 46661 Petaling Jaya, Selangor, Malaysia

**Corresponding author: changkh@usm.my*

Received: 16 September 2021; Accepted: 10 November 2021; Published: 25 February 2022

Abstract

Illicit methamphetamine seizures have risen significantly worldwide, and its widespread use threatens societal well-being. Thus, attention from various parties is required to stem methamphetamine trafficking; however, routine forensic analysis is generally limited to identifying and quantifying the controlled substances according to standard operating procedures. Although further analytical characterization and drug profiling via physical and chemical methods is not routinely conducted, it warrants further exploration for forensic comparison and intelligence. In this study, the physical and chemical profiles of seized illicit methamphetamine tablets were obtained employing various analytical techniques, including physical examination, attenuated total reflectance-Fourier transformed infrared (ATR-FTIR) spectroscopy, thin layer chromatography (TLC), and gas chromatography (GC). Physical characterization did not enable the identification of methamphetamine, but sample discrimination based on unique logos and dimensions was achieved. Based on ATR-FTIR and principal component analysis results, caffeine was found to be the most common adulterant, while the dyes used in the composition were identified via TLC analysis. GC analysis results confirmed the presence of methamphetamine and its quantity. Overall, a methamphetamine tablet profiling strategy was implemented to gather important information regarding the similarities and differences among illicit methamphetamine tablets, potentially beneficial for sample-to-sample, case-to-case, and seizure-to-seizure comparisons.

Keywords: forensic science, methamphetamine, drug profiling, physical examination, chemical analysis

Abstrak

Rampasan metamfetamin haram telah meningkat dengan ketara di seluruh dunia and penggunaannya secara meluas telah mengancam kesejahteraan masyarakat. Justeru, perhatian daripada pelbagai pihak adalah diperlukan untuk mengurangkan penjualan metamfetamin. Namun begitu, analisis forensik rutin secara umumnya dihadkan kepada pengenalpastian dan pengkuantitian bahan terkawal berdasarkan prosedur operasi standard. Sungguhpun pencirian analitikal dan pemprofilan dadah seterusnya melalui kaedah fizikal dan kaedah kimia tidak dilaksanakan secara rutin, hal ini membolehkan penerokaan selanjutnya untuk perbandingan dan perisikan forensik. Dalam kajian ini, profil fizikal and profil kimia pil metamfetamin haram

yang dirampas telah diperoleh dengan menggunakan pelbagai teknik analitikal, termasuk pemeriksaan fizikal, spektroskopi transformasi inframerah Fourier dengan pantulan keseluruhan dikecilkan (ATR-FTIR), kromatografi lapisan nipis (TLC) dan kromatografi gas (GC). Pencirian fizikal tidak membolehkan pengenalpastian metamfetamin tetapi diskriminasi sampel berdasarkan logo dan dimensi unik telah dicapai. Berdasarkan keputusan ATR-FTIR dan analisis komponen utama, kafien dinampakkan sebagai bahan adukan yang paling lazim, manakala pewarna yang digunakan dalam kandungan telah dikenal pasti melalui analisis TLC. Keputusan analisis GC telah memastikan kehadiran metamfetamin and kuantitinya. Secara keseluruhannya, satu strategi pemprofilan pil metamfetamin telah dilaksanakan untuk mengumpulkan maklumat penting berkenaan dengan kesamaan dan perbezaan antara pil metamfetamin haram. Hal ini berpotensi dalam memanfaatkan perbandingan sampel kepada sampel, kes kepada kes, dan rampasan kepada rampasan.

Kata kunci: sains forensik, metamfetamin, pemprofilan dadah, pemeriksaan fizikal, analisis kimia

Introduction

Methamphetamine acts on the central nervous system by stimulating excessive dopamine secretion [1]; thus, it has become one of the most abused stimulants worldwide, as evidenced by a sevenfold increase in global seizures thereof over the past two decades [2]. Although methamphetamine possession, trafficking, and manufacture is strictly enforced and punishable by law worldwide, cases of its abuse are increasing globally, especially in the United States, Europe, Australia, and New Zealand [2]. Users in East and South-East Asia account for more than 30% of the total estimated worldwide users of amphetamine-type stimulant (ATS) [2]. The severe societal well-being deterioration associated with illicit methamphetamine use necessitates collective strategic action, both domestically and internationally.

In recent years, methamphetamine manufacture in the United States, China, and the Islamic Republic of Iran has reportedly decreased, but a significant expansion of illicit methamphetamine drug trafficking has been encountered in Mexico, as well as in East and South-East Asia [3,4], suggesting a gradual shift in this illicit black market from North America to East and South-East Asia. Malaysia, the country where the present study was based, has reported a sharp increase in seized methamphetamine since 2015, wherein approximately 5.8 tons of crystalline methamphetamine and more than 1.6 million illicit methamphetamine tablets had been seized law enforcement authorities in 2019 alone [2]. Recent statistics and trend analyses have indicated that the expansion of the methamphetamine black market in East and South-East Asia has been driven by supply, as the organized crime groups have adapted their trafficking routes in response to law enforcement operations [5,6]. In fact, the growing methamphetamine manufacture in the region has also been supported by an increase in the diversion and trafficking of precursors and related chemicals [6].

Methamphetamine can appear in various forms: as an oily paste consisting of methamphetamine free-base, as a solid, which is the methamphetamine salt form, whereby high-purity methamphetamine salt can appear in crystalline form, commonly termed as “crystal” or “ice”. Methamphetamine is also commonly processed into tablet form known as “Yaba” tablets in Asia, especially in the golden triangle region bounded by Thailand, Laos, and Myanmar. Countries such as Malaysia, Australia, and China are inundated by transnational drug trafficking [7]. Transnational efforts to identify and disrupt the supply chain are therefore crucial. In routine forensic analysis, testing is frequently limited to identifying and quantifying the controlled substance in the illicit drug sample. However, limited information is retrieved regarding the source of origin, supply, trafficking, and distribution network thereof without further post-seizure profiling studies. Studies focused on the profiling of methamphetamine have been conducted, generally employing gas chromatographic techniques [8-10]. However, analytical characterization via physical and chemical methods is less likely to be conducted in forensic laboratories, and therefore gathering further information is required for subsequent forensic comparisons and intelligence. In non-ideal clandestine

laboratory production, the chemical composition of illicit drugs can vary significantly [11]. Illicit drug profiling involving the characterization of seized samples in a systematic manner should be conducted to elucidate the connection between suppliers, distributors, and users [11]. In this study, the physical and chemical profiles of illicit methamphetamine tablets were investigated employing various analytical techniques. Integrated approach for profiling illicit drugs could potentially support forensic intelligence [11-13] and be particularly useful for law enforcement authorities.

Materials and Methods

Standards and samples

Illicit methamphetamine tablets (164 samples) seized between January 2019 and December 2020 were used in this study. Methamphetamine, ephedrine, and caffeine standards were sourced from certified reference material suppliers, while various sugars, including glucose, lactose, dextrose, maltose, and mannitol were obtained from Merck (Whitehouse Station, NJ). For thin layer chromatography (TLC) analysis, various dye standards, including Amaranth, Rhodamine B, Erythrosine BS, Carmoisine, Red 2G, Ponceau 4R, Tartrazine, Sunset Yellow, Fast Green, Green S, and Brilliant Blue were sourced from Merck (Whitehouse Station, NJ). All solvents used, including glacial acetic acid, 25% w/w ammonia (S.G. 0.880), acetone, methanol, 2-propanol, n-butanol, and butanone, were of analytical grade. Nortriptyline HCl was used as the internal standard (IS) for gas chromatography (GC) analysis. Chloroform and methanol used to dissolve the standards and samples were of GC grade and were sourced from Merck (Whitehouse Station, NJ).

Physical examination

Physical examination was performed on the seized tablets by observation of the stamp or logo on each tablet, and that of their respective colors. The diameter and thickness of each sample (± 0.02 mm) were also measured using vernier calipers, while the weight (± 0.01 mg) was determined using an analytical balance. All physical characteristics were recorded and compared.

Attenuated total reflectance-fourier transform infrared spectroscopy

Various drug and adulterant standards, and the illicit methamphetamine samples in powdered form were analyzed directly using a Bruker Fourier transformed infrared (FTIR) Tensor 27 instrument (Bruker Corporation, Billerica, MA) equipped with a single-reflection zinc selenide attenuated total reflectance (ATR) sampling accessory, at a controlled ambient temperature (≈25˚C). Approximately 10 mg of the standard or sample was placed onto the ATR crystal to obtain their ATR-FTIR profiles. A background spectrum was recorded before each analysis run and absorbances were measured in the wavelength range between 4000 and 600 cm^{-1}. The resolution was set at 4 cm^{-1} and 16 scans were performed. The built-in software, OPUS 7.0.122 (Bruker Corporation, Billerica, MA) was utilized for spectrum acquisition. All spectra were recorded in duplicate, compared, and the differences evaluated. A repeatability test was performed by analyzing a representative sample thrice. A reproducibility test was also performed by analyzing a representative sample on three consecutive days. All spectral data were reported as absorbance values at each data point for subsequent interpretation and comparison.

It is often the case that the illicit drugs seized in forensic cases are normally in the form of mixture, which not only contain the drug alone but also adulterants and/or diluents. The influence of mixture composition on the respective ATR-FTIR profiles was investigated. Mixture samples consisting of methamphetamine and different adulterants in varying quantities were prepared. Based on the literature search, caffeine, ephedrine, and various sugars are more common [14,15]. Caffeine is a legal substance, inexpensive and readily available. The stimulant properties of caffeine could also create milder but very similar effect of methamphetamine. Ephedrine is the precursor during manufacturing, usually through Nagai pathway. On the other hand, sugars do not contribute to any additional effects on the methamphetamine but used to dilute or add the bulk of the illicit drugs. Being legal and readily available, sugars give greater margin to the illicit drug manufacturers [14,15]. In this study,

four commonly reported adulterants were used, namely caffeine, ephedrine, lactose, and mannitol. The mixtures (w/w) of methamphetamine and the respective adulterant were prepared at 100%, 90%, 75%, 50%, 25%, 10%, and 0%. All the prepared mixtures then underwent ATR-FTIR analysis.

For statistical analysis, data points of regions with noticeable variations, in the ranges of 3200-2550 cm^{-1} and 1800-600 cm^{-1}, were used. Data points of all ATR-FTIR spectra were transferred into Microsoft Excel® (Redmond, WA) and normalized to remove any possible variation resulting from inconsistent sample quantity. This was done by dividing the absorbance value at each data point to the total absorbance under the spectrum of the standards and samples. The normalized data were then analyzed using Minitab 18 software (Minitab Inc., State College, PA). Principal component analysis (PCA) was implemented for the characterization of illicit methamphetamine samples, and any potential differences among the samples were evaluated.

Thin layer chromatography

Prior to TLC analysis, the dye was extracted from the tablets to remove any sugars, fats, or other substances contained in a tablet [16,17]. The presence of any sugar might cause blurring of the spots upon TLC analysis [18]. Therefore, acidification coupled with alkaline treatment on the samples was suggested for the extraction of dye from tablet-coating formulations [17-19].

Dyes present in the samples were extracted for TLC analysis according to the following procedure. Approximately 10 mg of powdered sample was transferred into a vial. Acetic acid (5% v/v) was added to the vial, followed by the introduction of a knotted piece of white knitting wool, 5 cm in length. Knitting wool was knotted to avoid disassembling of the thread. Note that the wool was firstly washed with dilute ammonium hydroxide and water to minimize the effect of possible interference and to enhance the absorption of dye onto the treated wool. Warming of the mixture in a temperature range of 70-80ºC allowed the transfer of dye onto the knitting wool, and the entire procedure was complete within approximately 15 min. Then, the wool was carefully removed using tweezers and washed thoroughly with distilled water. The treated wool, now visibly colored, was dried and then placed into another vial. Dye extraction was performed by adding 1 mL of a solution consisting of equal volumes of acetone and 3N ammonia and warming for 15 min between 70-80ºC, after which time the wool was removed from the vial. Finally, the resultant dye solution was gently warmed in a water bath to evaporate the solvent and concentrate the solution. All the targeted dye standards were prepared following the above-described procedure for comparison.

TLC separation was performed using silica gel 60 F254 (Merck, Darmstadt, Germany). Four solvent systems were evaluated to select the optimal system for the separation of dyes possibly contained in illicit methamphetamine tablets. The four solvent systems were as follows:

(1) Solvent system A- isopropanol: ammonia (4:1)
(2) Solvent system B- n-butanol: glacial acetic acid: water (10:5:6)
(3) Solvent system C- acetone: butanone: ammonia: water (60:140:1:60)
(4) Solvent system D- isopropanol: ammonia: water (7:2:1)

The various dye solutions obtained from the samples were analyzed using the optimal solvent system. All the visible bands were compared to those of the reference dye standards. The TLC plates were also visualized under UV light to detect the presence of fluorescent spots. Any potential differences among the illicit drugs samples were evaluated based on their TLC profile and the respective dyes contained in the tablets were identified.

Gas chromatography

A methamphetamine standard containing a precisely known concentration thereof was used in both qualitative and quantitative analyses using gas chromatography-mass spectrometry (GC-MS) and a gas chromatography-flame ionization detector (GC-

FID), respectively. Prior to sample analysis, a calibration curve was constructed using the data obtained from the GC-FID analysis of methamphetamine calibration standards in a concentration range of 0.10 – 1.40 mg/mL. Such calibration range had allowed the determination of concentration of the target substance within an illicit tablet. Note that the GC method was adapted from United Nations Office on Drugs and Crime [20] and is utilized in the country of study for routine forensic analysis.

A Perkin Elmer Clarus 600 Gas Chromatographic system coupled with Mass Spectroscopy (MS) (Perkin Elmer, Waltham, MA) was used to confirm the presence of methamphetamine using a HP-5 capillary column (30 m × 0.25 mm i.d., 0.25 µm film thickness) (Agilent Technologies, Santa Clara, CA). Purified helium gas (99.99%) was used as the carrier gas at a constant flow rate of 1.5 mL/min. The front injection temperature was set to 270°C. The initial temperature was 80°C, and it was held for 1 min. The temperature was then increased to 200°C at 30°C/min, followed by a further increase to 270°C at 50°C/min. The final temperature was held for 1.0 mins. The temperature of the transfer line of the MS detector was set to 280°C. The data acquisition rate was 1.0 sec/scan and mass fragments were collected in the 50–500 m/z range. Turbomass Ver 5.4.2 Properties (Perkin Elmer, Waltham, MA) was used for data analysis. The spectra of the target compounds were interpreted, evaluated, and the resultant peaks were identified using the mass spectral library (NIST MS 2014 version 2.2) (National Institute of Standards and Technology, Gaithersbury, MD).

An Agilent 7890B Gas Chromatography system equipped with a split/splitless injector, and an FID (Agilent Technologies, Santa Clara, CA) was used for methamphetamine quantification upon positive identification based on GC-MS results. Liquid injection was performed at a constant inlet temperature of 270°C. Chromatographic separation was achieved using a HP-5 capillary column (30 m × 0.32 µm i.d., 0.25 µm film thickness). Purified helium gas (99.99%) was used as the carrier gas at a constant flow rate of 0.6 mL/min. The initial oven temperature was set at 150°C and held for 1 min. A temperature ramp of 30°C/min was selected to reach the maximum of 270°C and held for 2.5 min. Hydrogen flow, air flow, and the make-up flow were supplied to the detector at 30, 400, and 29.4 mL/min, respectively. Standard solution (1 µL) was introduced into the injector port. Chemstation software (Rev. B.04.02, Agilent, Santa Clara, CA) was used for GC automation and data analysis. All standards and IS were identified by comparison of the retention times.

The drug samples were prepared by weighing an accurately weighed amount of the powdered sample into a 10 mL volumetric flask. The sample was then dissolved using the IS solution to the levelling of mark and ultrasonicated for five minutes to allow for complete dissolution. An IS solution with a concentration of 0.60 mg/mL nortriptyline HCl was used. The solution formed upon the sonication was transferred into GC vial and properly labelled. All prepared samples were then introduced into the GC systems.

Upon analysis by GC-FID, the area under the chromatogram of each peak was integrated and the peak area ratio of the target substance was determined. The percentage of methamphetamine was calculated using Equation 1.

$$\% \text{ methamphetamine} = [(\text{Concentration} \times 10)/\text{weight of sample taken}] \times 100\% \quad (1)$$

where concentration is in mg/mL; 10 is the volume of dissolved sample in a 10 mL volumetric flask, and weight of sample taken is measured in mg. The purity among all the samples tested in this study was then compared.

Drug profiling strategy

A drug profiling scheme involving the physical characterization and chemical analyses of illicit methamphetamine tablets was conducted in that order. A comparative study was performed on the samples

and possible differences were determined on a case-by-case basis.

Results and Discussion

A total of 164 seized illicit methamphetamine tablets were analyzed in this study. Among them, six were green in color (3.7%), differing from the commonly encountered red tablets (96.3%). Therefore, the six green samples were labelled as G01-G06, while the remaining 158 samples were labelled as S001–S158.

Physical examination

Color

The samples analyzed in this study were predominantly red. However, the red color of each tablet differed slightly in terms of the hue, likely due to the use of different dyes. Some tablets appeared cherry-red, while some were maroon in color. Such variation in color could be due to the presence of different dyes or combinations of dyes that had been used in the manufacturing process, which can be determined by chemical analysis of the dye composition. In addition to the red tablets, six tablets were green in color. Generally, only one or two such green tablets are encountered in larger packages of seized samples containing 100 or 200 tablets.

Logo variant

All the methamphetamine tablets were round in shape with a deep convex center. A specific logo was observed on one of the sides, consisting of the letter's "w" and "y", as shown in Figure 1. However, different variations of the logo were noted, whereby "wY", "WY," or "wy" were present. In our case, the "wY" logo was dominant with 155 out of 164 samples (94.5%) being stamped with it [Figure 1(a)-(d)]. A slight variation in the size and positioning of the markings was also noted among the "wY"-labelled tablets, likely due to the use of different tableting machines. Some of the tablets exhibited deeply stamped logos, whereby the two letters could be seen clearly (Figure 1(a)-(b)), while most of the logos appeared very faint (Figure 1(c)-(d)).

Previous studies have indicated that such variations are a result of manufacture by different drug syndicates [21]. Tablets with the "wY" insignia were the most common in the sample set, and it is believed that they are produced by the United Wa State Army [21]. The other two variants, that is tablets bearing the "WY" and "wy" logos, were not common, being noted on only two (1.2%) [Figure 1(e)] and one sample (0.6%), respectively, [Figure 1(f)]. Reportedly, the former variant likely originated from the Myanmar National Defense Alliance Army, while the latter was produced by the Shah United Army 15. The "Wy" insignia was not observed among our seized samples; neither were other less common variants, such as "R", "OK", "888", and "Ã/99" [21,22]. None of the tablets bore an imprint on the reverse side.

The presence of a logo indicated the unique physical characteristics of the methamphetamine tablets, as it appeared on most of our tested samples. However, drug syndicates and trafficking groups other than those mentioned above reportedly stamp the same logos on their tablets, essentially counterfeiting illicit methamphetamine tablets [21,23]. As the samples tested in this study had all been seized, they could have been exposed to unknown physical and environmental conditions; thus, the faintness of the markings and/ or the rough texture of some tablets possibly resulted from exposure to moisture or due to transport and handling practices. Tablets whereby the logo on the surface could not be clearly determined through visual observation accounted for 3.7% of the total samples, or six out of 164 samples.

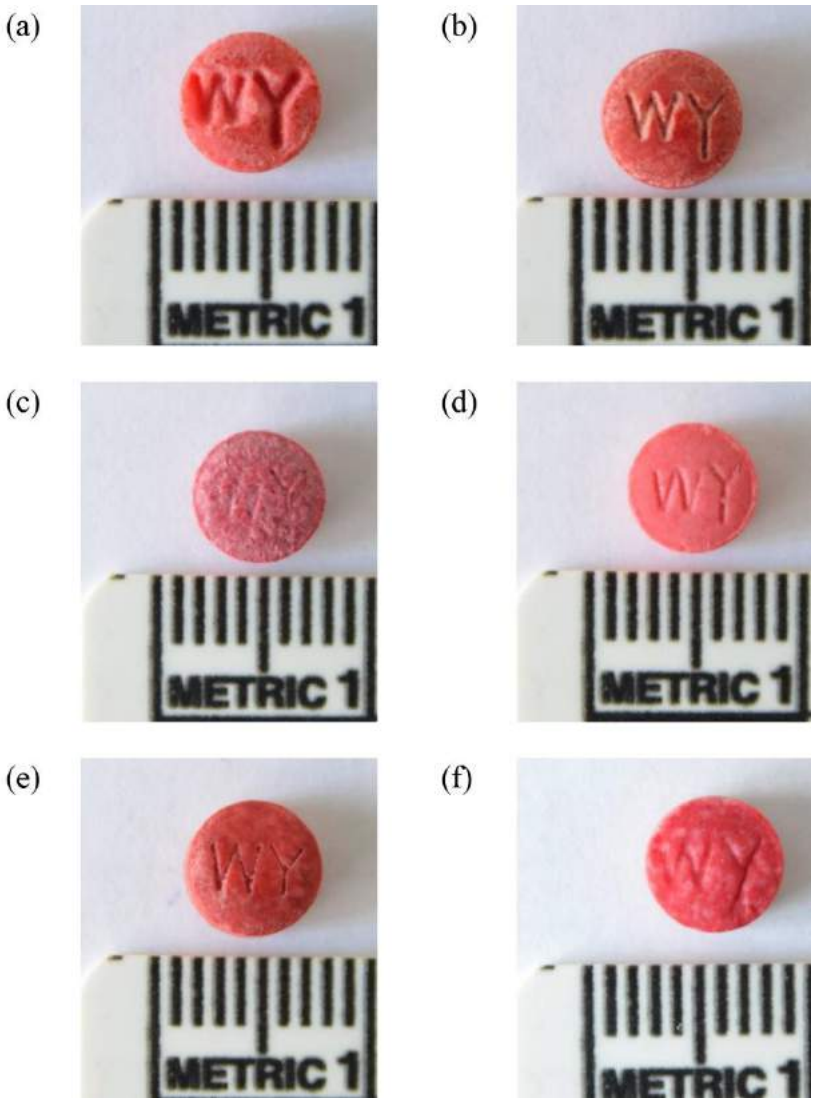

Figure 1. Physical observation of illicit drug tablets encountered in this study.

Dimensions

In terms of size, all of the tablets appeared very similar to each other, and the average diameter and thickness were 6.21 ± 0.21 mm and 3.06 ± 0.14 mm, respectively. Four of the samples were slightly larger in diameter, especially S077, measuring 8.16 mm in diameter. On the other hand, the diameter of S001 was relatively smaller at only 5.60 mm. The weight of each tablet was directly related to its dimensions. In this study, the average weight of the tablets was 97.63 ± 32.52 mg, but the range was from 26.50 mg to 474.95 mg, showing significant variation. The heaviest sample was S017, although its diameter and thickness were within the dimension range of the dominant group. Figure 2 illustrates the number and percentage of samples with a certain diameter, thickness, and weight.

In most instances, drug tablets produced using the same tableting machine present uniform dimensions and thickness [24]. A tableting machine compresses pharmaceutical powder with a specific formulation into tablet form, resulting in the production of tablets with uniform size, shape, and weight [24,25]. Thus, the variation in the physical characteristics could be as a

result of the use of different tableting machines in the production step [21,23]. Any differences in terms of the punches and dies of a tableting machine could potentially produce tablets that differ in diameter [21]. Tablet thickness could be affected by the compressive force, even when a consistent ingredient fills of the die is practiced [21,26]. Tablet weight is governed by the volume of the ingredient filling the die cavity in a tableting machine, and the size of the granule and void space would influence the weight [21].

For forensic intelligence, our findings suggested that the majority of illicit drug samples were likely to have similar physical characteristics, but several samples that showed significant variation from the dominant group were identified. Taking note of such variation could be beneficial for differentiating between batches and manufacturers, at least for sample-to-sample, case-to-case, and seizure-to-seizure direct comparisons [27]. The physical examination would additionally be supported by the information obtained from the chemical analyses for forensic characterization.

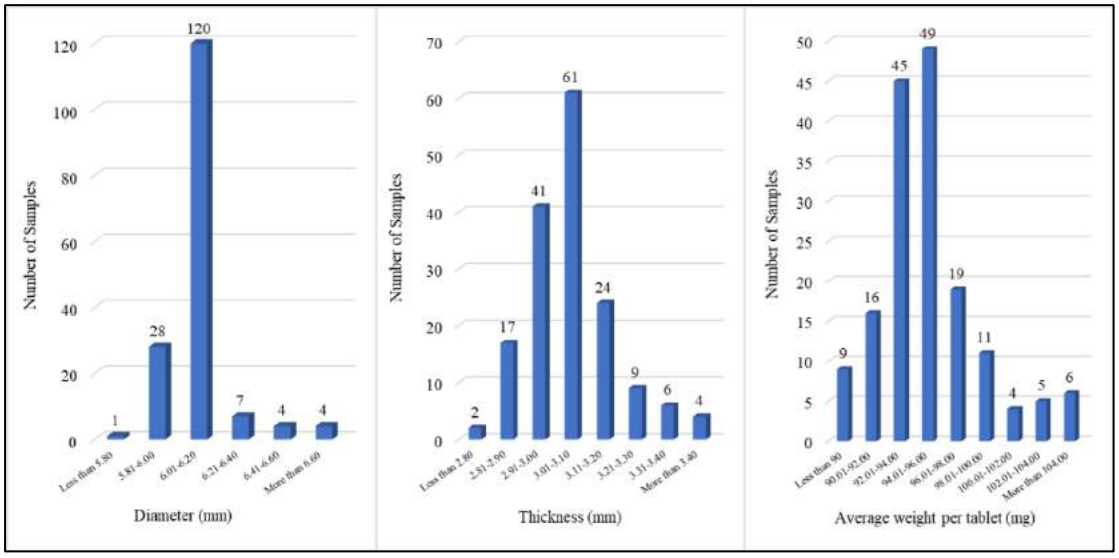

Figure 2. The number and percentages of samples in term of their (a) diameters, (b) thicknesses and (c) weights

ATR-FTIR analysis

ATR-FTIR spectral comparison of illicit drug samples and standards

ATR-FTIR spectroscopy is a useful technique for analyzing and identifying samples, as well as for comparing various samples in numerous forensic applications [28,29]. All 164 illicit drug samples (158 red-colored and 6 green-colored samples) were analyzed using ATR-FTIR spectroscopy to determine their structure, compare their spectra with that of the methamphetamine standard, and to differentiate the seized samples. Prior to determination and comparative studies, repeatability and reproducibility tests were performed. A representative sample (S001) from the same seizure was used in the repeatability study, showing close agreement between three successive measurements under the same conditions [Figure 3(a)]. In the reproducibility study, no differences were observed in ATR-FTIR spectra when S100 was analyzed thrice on three consecutive days [Figure 3(b)], indicating that ATR-FTIR spectroscopy is capable of generating comparable results from multiple analyses and preparations of the same sample. For both repeatability and reproducibility tests, the intensity of three major peaks appearing at 1691, 1653 and 743 cm^{-1} were respectively measured, and their relative standard deviations were determined to be less than 5%.

Complex interacting vibrations were evident in the ATR-FTIR spectra of both the standards and samples. Figure 4 depicts the ATR-FTIR spectra of the methamphetamine standard and common adulterants, including caffeine, ephedrine, and various sugars [14,15], added during the manufacture of illicit methamphetamine tablets.

With reference to (Figure 4(a)), the absorbance pattern of methamphetamine contained major peaks in regions ranging from 3200 to 2550 cm^{-1} and 1800 to 650 cm^{-1} [29-31]. Broad absorbance bands were observed at 2972, 2726, and 2457 cm^{-1}, and were attributed to C-H ($C-CH_3$), NH_2, and C-N-C stretching vibrations, respectively. Meanwhile, two sharp absorbance peaks were also observed at 699 cm^{-1} and 747 cm^{-1}, likely arising from the aromatic C-H out-of-lane bending vibration. The existence of an aromatic ring stretching vibration (C=C-C) at 1602 cm^{-1} could be unique to aromatic ring bonding, while the absorbances at 1454, 1386, and 1046 cm^{-1} likely arose due to C-H bond deformation in the chemical structure. Absorbance peaks in the region of 1192 cm^{-1} possibly represented C-N stretching in a secondary amine structure of methamphetamine.

The ATR-FTIR profile of ephedrine (Figure 4(c)) appeared very similar to that of methamphetamine due to their similar structure. However, the distinguishing feature of the ephedrine spectrum was the presence of additional absorbance bands at 3400 and 3200 cm^{-1} ascribed to hydroxyl stretching. Additionally, the absorbance peaks of ephedrine appeared weaker than those of methamphetamine in the region of 2400-3100 cm^{-1}.

In the spectrum of caffeine (Figure 4(b)), prominent absorbance peaks were evident in the region of 1655-1705 cm^{-1}, attributed to C=O bond vibration, C=C bonds of cyclic hydrocarbons, and/or C=N bond stretching. The ketone group present in caffeine gave rise to peaks at 1025 and 1237 cm^{-1}. Additionally, C-N stretching gave rise to an absorbance peak at 1359 cm^{-1}, while C=C vibration contributed to the peak at 1486 cm^{-1}.

From the ATR-FTIR spectra of the five types of sugars tested in this study, glucose [Figure 4(d)] and dextrose (Figure 4(h)) had very similar profiles. As disaccharides, the spectra of lactose [Figure 4(e)] and maltose [Figure 4(f)] also appeared very similar to each other. Lastly, the spectrum of mannitol [Figure 4(g)], a type of sugar alcohol used as sweetener, was distinct, containing two intense absorbances at 1074 and 1015 cm^{-1}. Absorbance peaks in the ATR-FTIR profiles of sugars arise predominantly from skeletal C-C vibrations (1300-700 cm^{-1}), methyne C-H bending (1350-1330 cm^{-1}), and H-bonded OH stretching (3570-3200 cm^{-1}).

Visually, two unique ATR-FTIR spectral patterns were observed for the illicit drug samples tested in this study, as depicted in Figures 4(i) and 4(j). Careful analysis suggested that pattern A (Figure 4(i)) contained peaks similar to those of caffeine, while pattern B (Figure 4(j)) resembled the spectrum of mannitol. In this study, only one sample, namely S077, showed ATR-FTIR profile of pattern B. Experimental results can be used to determine the major adulterant added to the composition of illicit drug tablets during the manufacturing process. It was noted that the choice of adulterants can differ among the drug distributors and manufacturers, due to factors such as user preference, drug syndicate "trade-marks," the availability of these substances, and differing strategies for increasing the profit margin [32,33]. The ATR-FTIR profiles of the six green tablets did not differ from those of the red tablets, suggesting that the tablets had a similar composition, with the exception of the dye.

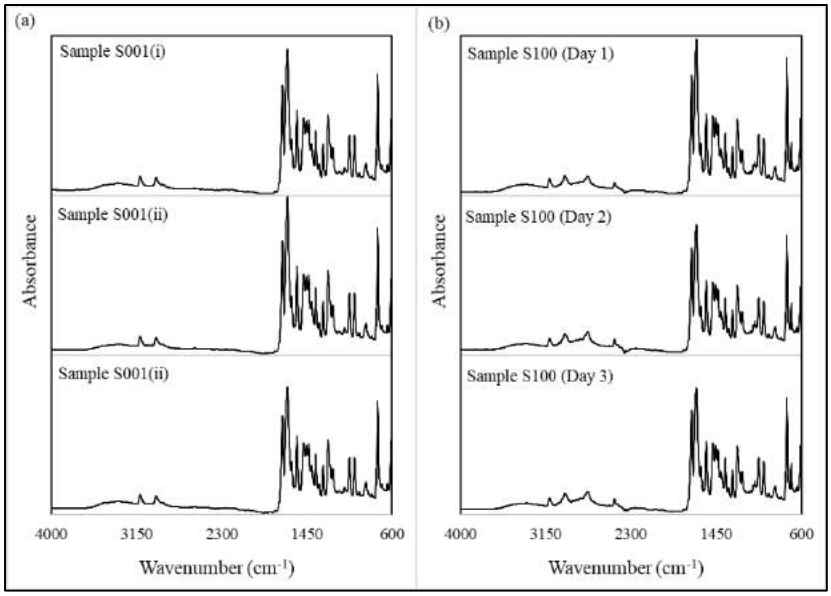

Figure 3. (a) Repeatability test using sample S001 as representative sample, and (b) reproducibility test using sample S100 as representative sample

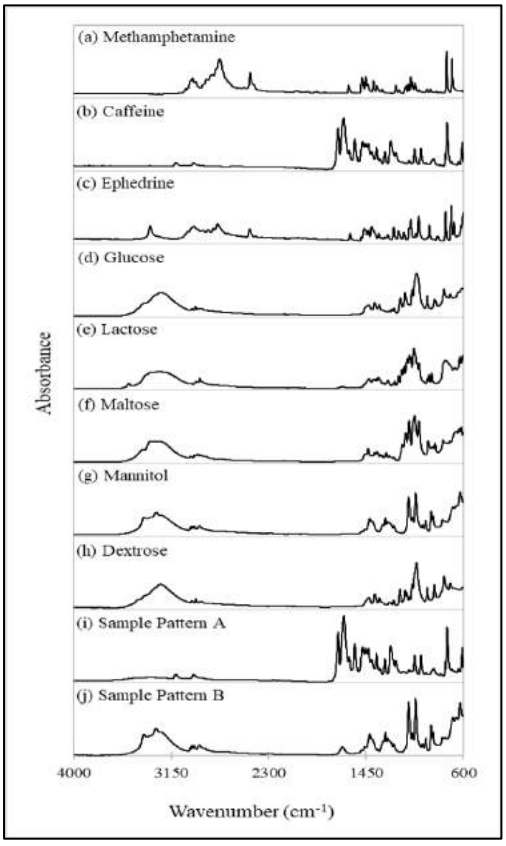

Figure 4. ATR-FTIR spectra of drug standards and seized illicit drug samples in the region of 4000 to 600 cm^{-1}

ATR-FTIR spectral comparison of adulterated methamphetamine at varying percentages

To further evaluate the inclusion of adulterants and their influence on the resultant ATR-FTIR profiles, varying ratios of methamphetamine and adulterants were prepared, and the spectra of the mixtures were examined. Figure 5 illustrates the comparison of the ATR-FTIR profiles of the methamphetamine standard containing varying adulterant amounts.

As evident in Figure 5, the ATR-FTIR profile of methamphetamine changed upon the addition of adulterants, regardless of the choice of adulterant. With increasing adulterant content, the prominent methamphetamine absorbance peaks gradually reduced in intensity or became concealed by the intense peaks originating from the adulterant. For instance, an increase in caffeine content in a mixture led to a gradual decrease in the intensity of the main absorbance peak at 699 cm^{-1}. When methamphetamine content reached 25% in the mixture, the peak was no longer detectable. Additionally, the broad absorbances within the wavenumber region of 3100-2400 cm^{-1} also underwent significant changes. On the other hand, absorbance peaks arising from caffeine were evident in the range of 1655-1705 cm^{-1} for a mixture containing 25% caffeine. Absorbance peaks in this region became more intense with increasing caffeine content. From Figure 5(a), the absorbance peaks attributed to methamphetamine were virtually absent for a mixture containing > 75% caffeine, and the spectrum resembled that of the pure caffeine standard. Based on the ATR-FTIR spectra of the methamphetamine and ephedrine standards, the spectrum of their mixture contained an additional peak at 3340 cm^{-1} due to the presence of a hydroxyl group in ephedrine (Figures 5(b)). When sugars were added to the composition, the dominant peaks from methamphetamine also decreased in intensity, gradually being replaced by the peaks arising from the sugars. In other words, the ATR-FTIR profile of the mixture started to resemble that of the sugars with increasing sugar concentration (Figures 5(c) and (d)).

Regardless of the adulterant added, the peaks ascribed to methamphetamine remained prominent in the ATR-FTIR spectrum when methamphetamine content was 75% and above. However, with the addition of 50% or more of any adulterant, the presence of methamphetamine was challenging to confirm using the ATR-FTIR profile of the mixture. A previous study has suggested the potential of using ATR-FTIR spectra to identify methamphetamine when the concentration thereof is >30% [34]; however, the presence of adulterants impeded the determination of methamphetamine in our study. In our case, at least 75% methamphetamine content was required for confident determination of its presence in a mixture. Thus, the ATR-FTIR technique has several limitations, particularly when the screening for the presence of methamphetamine as a controlled substance. However, the ATR-FTIR technique could be applied in clandestine laboratory settings where illicit drugs of very high purity have been synthesized prior to the packaging stage. In such cases, ATR-FTIR spectroscopic analysis would allow for rapid determination and portable on-site detection.

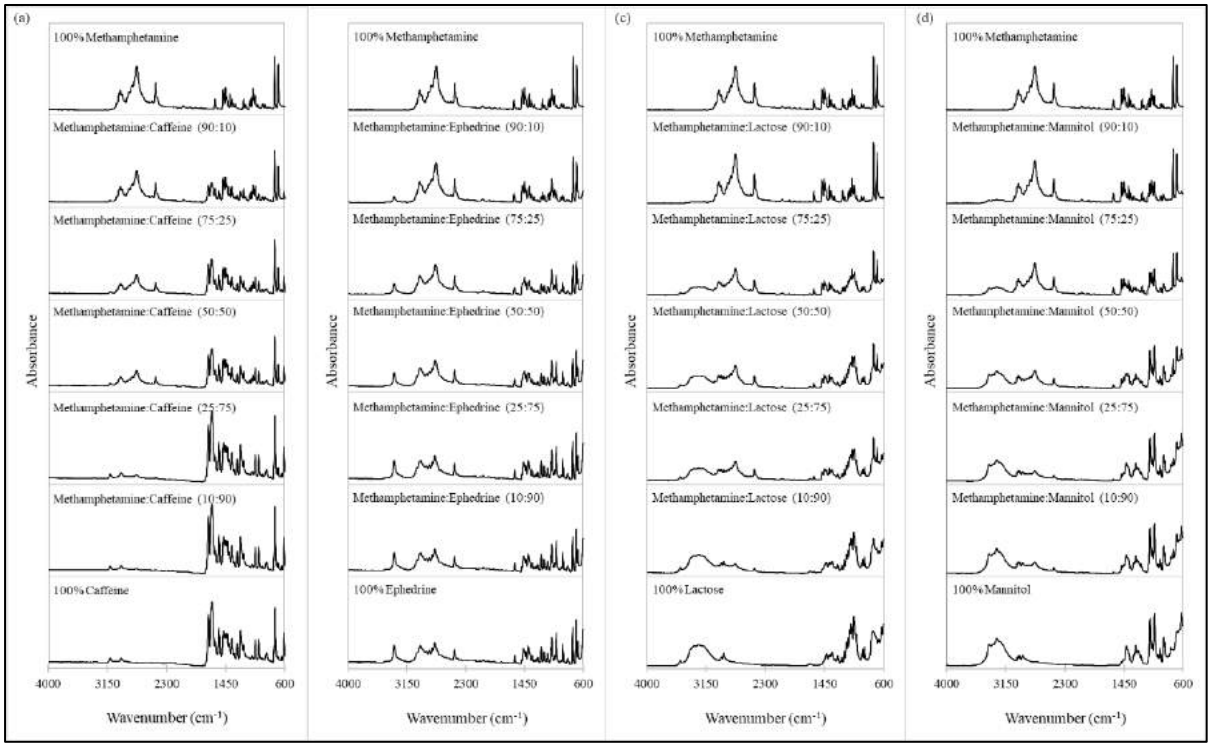

Figure 5. ATR-FTIR profiles of methamphetamine with varying percentage of adulterants

PCA decomposition of ATR-FTIR profiles

Our findings indicated that the determination of methamphetamine presence in illicit drug tablets using ATR-FTIR spectroscopy could be challenging. However, the identity of the adulterant in an illicit drug pill could be determined via this technique based on the obtained spectrum, and consequently, samples of differing composition can be differentiated. PCA was performed to decompose the large dataset into a smaller set that represented the variability of all the 164 samples tested in this study. Prior to the PCA, the ATR-FTIR spectra were pre-treated and normalized. From the ATR-FTIR spectra in Figure 4, the regions with noticeable variations among the standards and samples, namely those ranging from 3200 to 2550 cm^{-1} and 1800 to 650 cm^{-1}, were subjected to PCA. Figure 6 illustrates the two-dimensional score plot upon PCA decomposition of data for the 164 illicit drug samples and related standards.

The majority of the illicit drug samples tended to locate closely, as seen for cluster P in the score plot (Figure 6). These samples were clustered together with the caffeine standard, suggesting the similarity in their ATR-FTIR profiles. This observation was supported by the visual comparison of their ATR-FTIR spectra, wherein they appeared very similar, as demonstrated in Figures 4(b) and 4(i). On the other hand, the S077 sample was located away from the cluster P, while being close to the sugar standards, denoted as cluster Q. S077 could have been adulterated with any sugar, most likely mannitol, based on the similarities of its ATR-FTIR profile with that of mannitol (Figure 4(g)). The PCA grouped the green samples into cluster P, as the color did not contribute to significant changes in the ATR-FTIR profile.

The PCA score plot indicated that all the illicit drug samples were located very far away from the methamphetamine standard data point, found in the right bottom corner. This observation implied that the absorbance peaks comprising the ATR-FTIR profile of the methamphetamine standard were not useful for determining its presence in the illicit drug tablets, as

they were concealed by the peaks originating from the adulterants. It was noted that the ephedrine standard was located close to methamphetamine (cluster R), indicating significant similarities between their ATR-FTIR profiles. Generally, PC1 (52.8%) discriminated the majority of the samples from the standards and adulterants, including methamphetamine, ephedrine, and various sugars. PC2 (26.9%) further separated the methamphetamine and ephedrine standards from the data points consisting of various sugars. The presence of adulterant had modified the ATR-FTIR profiles of methamphetamine. As evident in Figure 7 demonstrating the score plot decomposing drug samples and the standard-adulterant mixtures, data points of the mixture carrying greater percentage of adulterant, in this case caffeine, had been dispersed away from cluster R to cluster P. Majority of the drug sample tested in this study could have contained less than 25% active compound and adulterated with caffeine. The sample S077 might have also contained a percentage of methamphetamine at a level of less than 10% and adulterated with sugar, probably mannitol based on the ATR-FTIR spectrum.

In this study, the discrimination of illicit drug samples was possible through the use of ATR-FTIR spectroscopy by recognizing the corresponding pattern and comparing it to that of the standards and adulterants. PCA allowed for more objective clustering and discrimination. The majority of the illicit drug samples tested in this study were adulterated with caffeine, except for one sample, namely S077, that likely contained mannitol. The literature has suggested the preference for utilizing caffeine as the adulterant during illicit drug production probably due to the similar stimulant effect of caffeine as in methamphetamine [15,23]. Perhaps more samples from different regions of the country should be included in future profiling activities to evaluate if the choice of caffeine was restricted to the east coast of the country, or generally, across the country and in nearby countries.

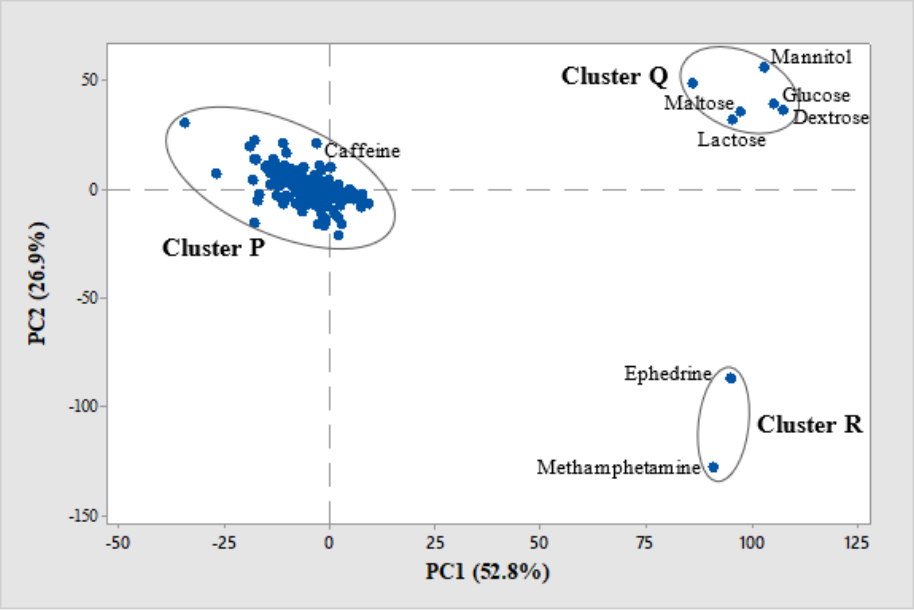

Figure 6. Decomposition of 164 samples and standards into two-dimensional score plot

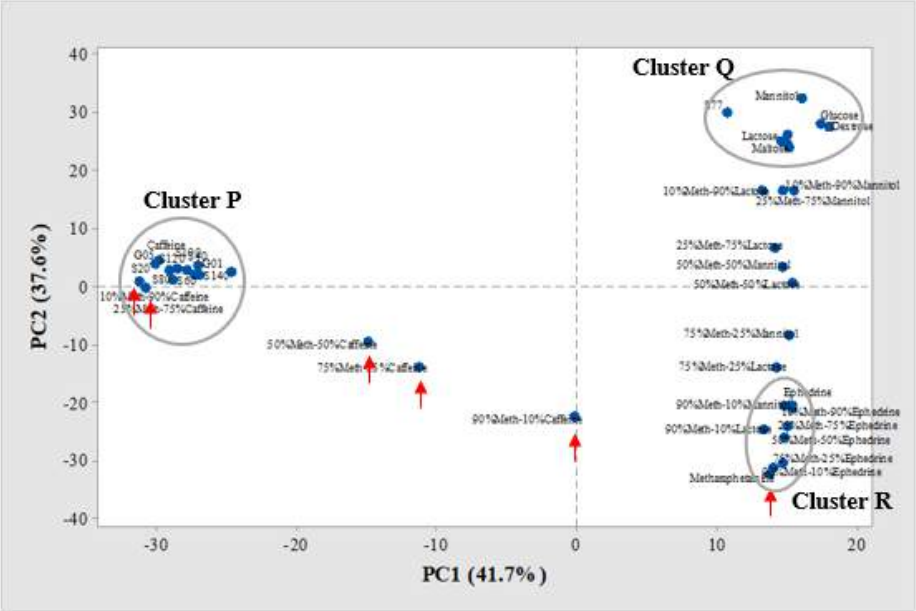

Figure 7. Decomposition of drug samples and standard-adulterant mixture into two-dimensional score plot

TLC analysis

Choice of Solvent System

Prior to TLC analysis, the dye was extracted from the tablets to remove any sugars, fats, or other substances contained therein [16,17] that could potentially cause blurring of the spots upon analysis [18]. Thus, the dye was transferred to a piece of wool via acidification and subsequently stripped from the wool by alkaline treatment [17-19,35]. All the dye standards used in this study underwent the same procedure as did the negative control. Upon TLC analysis, all the standards developed colored spot(s) on the plate when various solvent systems were applied, and their respective retention factor (R_f) values are given in Table 1.

Among the dye standards, the Rhodamine B dye standard exhibited strong fluorescence under long-wave UV light illumination; Erythrosine BS fluoresced weakly. Adequate separation of the dye standards could not be achieved using solvent systems B or C for TLC analysis. These solvent systems were excessively polar, and the dye components moved high up the plate due to insufficient interaction with the stationary phase. Solvent system A consisting of isopropanol and ammonia (4:1 v/v) reportedly achieves effective separation of synthetic food colorants with minimum tailing effects [17]. However, it was found that certain dye standards were not adequately separated using solvent system A, as evident from the very close R_f values of the color spots formed by Tartrazine and Brilliant Blue. The color spot generated from Brilliant blue dye was also very close to those formed by the two green-colored dye standards used in this study, namely Fast Green and Green S. These occurrences hamper interpretation, especially in the analysis of green tablets. In fact, the green color may be the result of a blue and yellow dye mixture.

Favorable separation among the dye standards was achieved with silica gel plates eluted with solvent system D consisting of isopropanol, ammonia, and water in a volume composition of 7:2:1, especially in the case of the red dyes. Furthermore, the greater separating distance between the spots formed by Tartrazine and Sunset Yellow dye standards resulting from the use of solvent system D would allow for more confident discrimination between these two dyes potentially found in the green tablets. Thus, solvent system D was used for the subsequent determination of dye components in the illicit drug samples.

Table 1. R_f values of the color dye standards upon TLC analysis

Standard	Solvent system A	Solvent system B	Solvent system C	Solvent system D
Amaranth	0.81	0.81	1.00	0.64
Carmoisine	0.88	0.91	1.00	0.70
Erythrosine BS	(0.93)	(0.94)	(1.00)	(0.82)
Ponceau 4R	0.81	0.87	1.00	0.65
Rhodamine B	(0.90)	(0.90)	(1.00)	(0.82)
	(0.74)	(0.87)	(0.88)	(0.76)
	(0.71)		(0.80)	(0.65)
Red 2G	0.84	0.90	1.00	0.73
Tartrazine	0.78	0.87	1.00	0.64
Sunset Yellow	0.83	0.88	1.00	0.73
Fast Green	0.83	0.88	1.00	0.68
	0.80	0.86		0.65
Green S	0.78	0.81	1.00	0.64
	0.72			
	0.64			
Brilliant Blue	0.77	0.87	0.95	0.73

( ) indicates fluoresced colored spot under UV illumination

Determination of dye components in illicit drug samples

In pharmaceutical products, the addition of color aids in enhancing drug acceptability, discrimination among different drugs, and prevents counterfeiting 18. In illicit drugs, dyes are used to improve their external appearance, and to render them readily identifiable on the drug scene [36]. Figure 8 illustrates the percentages of drug samples that contained specific dye components. Upon examination, a total of 151 samples (95.6%) contained Ponceau 4R as the only dye. In addition to Ponceau 4R, Erythrosine BS (0.6%), Sunset Yellow (1.9%), and Tartrazine (0.6%) were also concurrently detected in certain drug samples, suggesting that the dye used during the manufacturing of certain drug samples was not restricted to a single type. Only two samples were found to be unique and not to contain Ponceau 4R (1.3%), namely S001 and S002, which contained Rhodamine B and Erythrosine BS. The six green-colored illicit drug samples were classified into two separate groups, according to whether they contained Tartrazine and Brilliant Blue (66.7%), or Ponceau 4R as well (33.3%). However, the presence of Ponceau 4R in the two green-colored samples possibly originated from contamination by red-colored tablets as they were all placed in the same packaging.

TLC analysis contributed significantly to the identification of the various dyes contained in the illicit drug samples. Importantly, the dye must be carefully extracted from the samples to ensure satisfactory TLC separation. Ponceau 4R was the most commonly used dye in red-colored samples, but a mixture of dyes was also encountered. Based on TLC analysis results, at least seven different groups of illicit drug samples were determined.

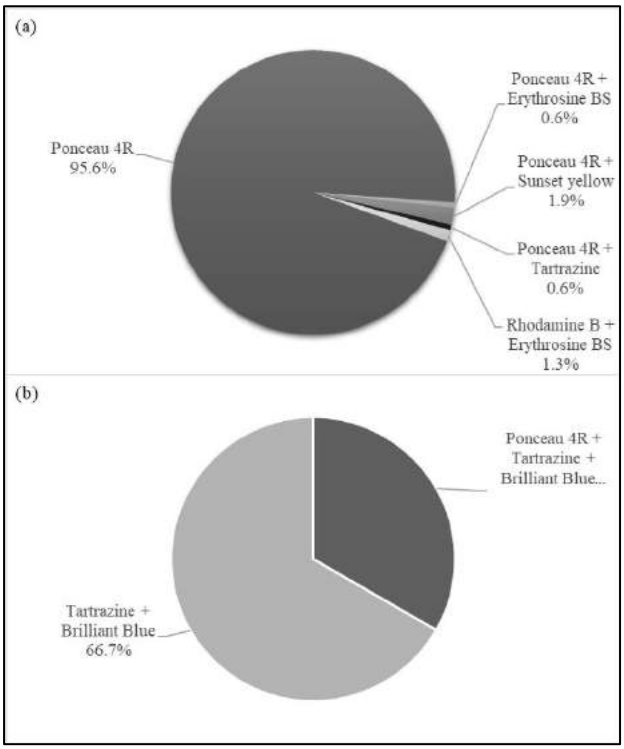

Figure 8. Percentages of samples of varying dye composition in (a) red-colored and (b) green colored illicit drug samples tested in this study

Gas chromatographic analysis

Confirmation of methamphetamine presence

Due to the excellent sensitivity of GC-MS, it was chosen to confirm the presence of methamphetamine [8,11]. Figure 9 shows a representative chromatogram showing methamphetamine and IS peaks upon sample analysis. The methamphetamine and IS peaks appeared at 3.72 and 7.27 min, respectively. The presence of caffeine was also evident in the majority of samples, supporting the findings of ATR-FTIR analysis. The caffeine peak dominated the chromatogram, appearing at a retention time of 6.33 min. The mass spectrum of methamphetamine displayed an M-1 peak with an m/z ratio of 148. The base peak was found at m/z 58, followed by m/z 91 and 134.

Of the 164 samples tested in this study, 162 of them were found to contain methamphetamine; samples S077 and G02 did not. A probability index of greater than 80% was considered for a positive determination of methamphetamine. It was noted that physical examination alone could not confidently indicate the presence of methamphetamine. As evident in these two samples, the target substance was not detected using our analytical method, either because it was absent, or its content was too low for detection.

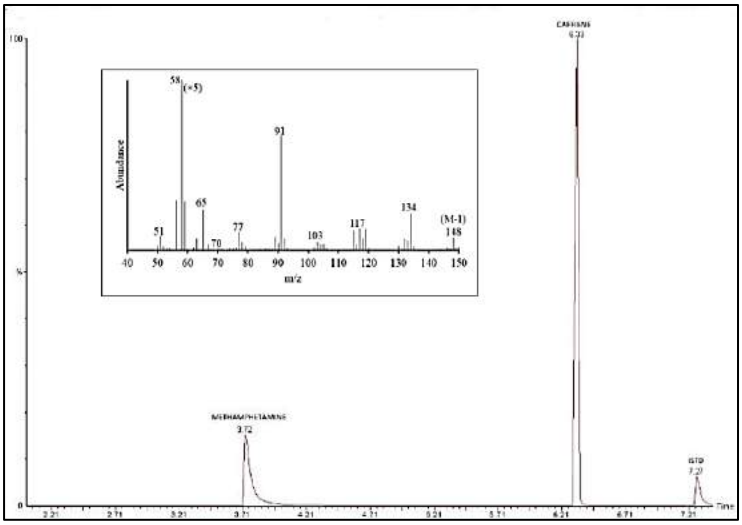

Figure 9. Representative chromatogram showing the peaks of methamphetamine, caffeine, and IS upon GC-MS analysis of sample S001 (Inset: mass spectrum of methamphetamine)

Quantification of methamphetamine in illicit drug tablets

A calibration curve was constructed using the GC-FID analysis results obtained for methamphetamine solutions of varying concentrations and linear least regression analysis, and the percentage of methamphetamine (w/w) in each illicit drug tablet was determined, as shown in Figure 10.

The mass of methamphetamine in individual samples was found to vary. Most of the samples contained 15.01% – 17.50% w/w of methamphetamine, accounting for 64.8% of the total samples. In fact, > 98% of the samples (159 samples) were found to contain < 20% methamphetamine. Our experimental data indicated that most of the tablets had been adulterated with caffeine to add bulk during the manufacturing and tableting processes; however, caffeine quantification was not pursued in this study. Considering the w/w ratios and the tablet weight, approximately 16 mg of methamphetamine was generally present in a single tablet.

Several samples were distinct in terms of their methamphetamine content, which was either significantly higher or lower than the average, allowing for their discrimination from the majority groups. The two samples with a relative higher percentage of methamphetamine were S082 (35.04% methamphetamine) and S094 (56.60% methamphetamine). In other words, they contained significantly lower amounts of adulterant. The empty space between the granules may have been larger, reducing their measured weights [21]. On the other hand, five samples (3.08%) were found to contain <10% methamphetamine. The lowest methamphetamine content was found in sample S002, wherein only 10 mg methamphetamine was detected for all 300 tablets encountered in a single packaging. The remaining w/w percentage of each tablet was principally made up of the adulterant. Samples with such low methamphetamine content are not commonly encountered as their effects upon consumption would be diminished. The other four samples within the same group contained approximately 7% methamphetamine.

Thus, the presence methamphetamine in seized drug samples was confirmed based on GC-MS analysis results and its quantity was determined through the GC-FID analysis. In this study, 98.7% of the samples contained methamphetamine, and only several tablets contained either very high or very low levels of methamphetamine.

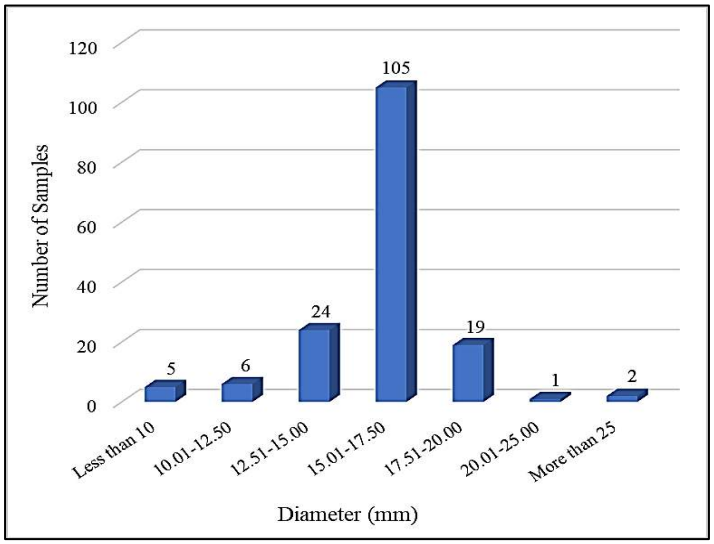

Figure 10. Percentages of methamphetamine (w/w) of 162 illicit drug tablets positively confirmed by GC-MS

General discussion

Based on physical characterization and chemical analyses results, valid information was retrieved regarding the composition of illicit drug samples [37]. In routine forensic analysis, the ultimate objective is to detect the presence of a controlled substance and quantify it. However, more in-depth analysis of illicit drug samples could contribute to a greater comparative study to gather information regarding sample-to-sample, case-to-case, seizure-to-seizure connections, especially when a large number of samples are encountered by the enforcement authorities [38-41]. To a certain extent, this approach could contribute to establishing the origins of illicit drug samples, the possible manufacturing pathway, as well as the potential trafficking and distribution network [42-43], enabling the tracking of drug syndicates or manufacturers.

In this study, illicit drug samples from various seizures were profiled for possible clustering or discrimination among them. Although physical characterization did not provide information on the identity of the substance in the illicit drugs, it allowed for the discrimination of a few samples from the major groups due to their unique physical appearance, especially in relation to their respective logos, diameter, thickness, and weight. ATR-FTIR analysis coupled with PCA indicated that the majority of the illicit drug samples were adulterated with caffeine. TLC analysis enabled the identification of the dyes that had been added to the tablets, whereby Ponceau 4R was found to be the most commonly used dye. Lastly, GC-MS analysis enabled the determination of the presence of methamphetamine as well as that of its content in each tablet through GC-FID. All the analytical results are summarized in Figure 11; the classification of samples into several groups was based on the drug profiling results. The proposed strategy can be used by law enforcement agencies and forensic laboratories to profile illicit drugs, in this case, methamphetamine tablets. Illicit methamphetamine samples tested in this study had demonstrated certain degree of physical and chemical differences. Differentiation among drug samples would be advantageous for sample-to-sample and seizure-to-seizure comparison. It was noted that this profiling study could have been restricted by the availability of methamphetamine samples, limited to the east coast region of Malaysia. A greater number of samples, perhaps from different regions of the country, would

provide information of the current situation of illicit methamphetamine in the country. Nonetheless, data from such analytical endeavors should be further collated as it is necessary for wider forensic intelligence to provide information on the possible connection among seized samples to law enforcement authorities.

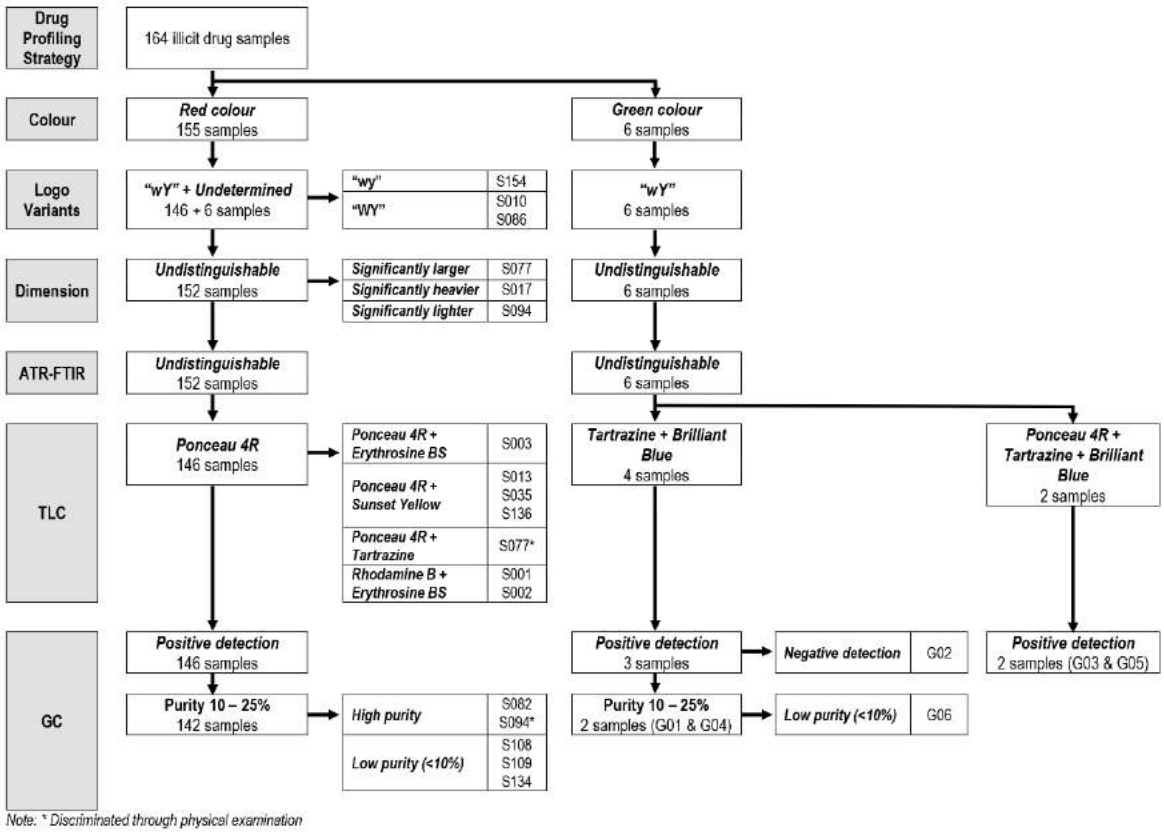

Figure 11. Drug profiling strategy and grouping of illicit drug samples

Conclusion

Forensic drug profiling was conducted with the aim of benefiting forensic investigation and intelligence. In this study, samples were differentiated based on several physical and chemical characteristics, allowing sample-to-sample comparison. With a greater number of illicit drug samples being processed, the linkages between seizures could be revealed, beneficial for tracking down the sources of these illicit drugs on the black market and their related distribution chain. Drug profiling strategies on a global level in accordance with comparative analyses of illicit drug samples would be advantageous for uncovering complex trafficking networks. This information could advance the body of knowledge useful to drug-related investigations and intelligence.

Acknowledgement

The authors thank the financial support via the USM RUI grant (1001/PPSK/8012236).

References

1. National Institute on Drug Abuse (2021). Methamphetamine. Access from https://www.drugabuse.gov/publications/drugfacts/methamphetamine. [Access online 29 May 2021].

2. United Nations Office on Drugs and Crime (2020). Drug use and health consequences. Vienna: United Nations Office on Drugs and Crime.
3. United Nations Office on Drugs and Crime (2020). Synthetic drugs in east and southeast Asia: Trends and patterns of amphetamine-type stimulants and new psychoactive substances. Vienna: United Nations Office on Drugs and Crime.
4. United Nations Office on Drugs and Crime (2020). Drug supply. Vienna: United Nations Office on Drugs and Crime.
5. Hamdan, R., Nik Hassan, N. F., Mat Desa, W. N. S., Kunalan, V., Sulaiman, M. and Abdullah, A. F. L. (2015). Characterisation of seized clandestine methamphetamine in Malaysia. *Malaysian Journal of Forensic Sciences*, 6(1): 20-29.
6. United Nations Office on Drugs and Crime (2020). Synthetic drugs in east and southeast Asia: Latest developments and challenges. Vienna: United Nations Office on Drugs and Crime.
7. Libby H. (2018). Myanmar's meth crisis reaches as far as Australia. ABC News. Access https://www.abc.net.au/news/2018-07-29/myanmars-meth-crisis-reaches-australia/10044502 [Access online 29 May 2021].
8. Puthaviriyakorn, V., Siriviriyasomboon, N., Phorachata, J., Pan-ox, W., Sasaki, T. and Tanaka, K. (2002). Identification of impurities and statistical classification of methamphetamine tablets (Ya-Ba) seized in Thailand. *Forensic Science International*, 126(2): 105-113.
9. Sennello, L. T. (1971). GLC determination of methamphetamine hydrochloride in methyl acrylate-methyl methacrylate sustained-release tablets. *Journal of Pharmaceutical Sciences*, 60 (4): 595-596.
10. Mitrevski, B. and Zdravkovski, Z. (2005). Rapid and simple method for direct determination of several amphetamines in seized tablets by GC–FID. *Forensic Science International*, 152 (2-3): 199-203.
11. United Nations Office on Drugs and Crime (2001). Drug characterization/impurity profiling – Background and concept. Vienna: United Nations Office on Drugs and Crime.
12. Dufey, V., Dujourdy, L., Besacier, F. and Chaudron, H. (2007). A quick and automated method for profiling heroin samples for tactical intelligence purposes. *Forensic Science International*, 169:108-117.
13. Esseiva, P., Dujourdy, L., Anglada, F., Taroni, F. and Margot, P. (2003). A methodology for illicit heroin seizures comparison in a drug intelligence perspective using large databases. *Forensic Science International*, 132(2): 139-152.
14. European Monitoring Centre for Drugs and Drug Addiction (2009). Methamphetamine: A european union perspective in the global context. Portugal: European monitoring centre for drugs and drug addiction.
15. Cole, C., Jones, L., Mcveigh, J., Kicman, A., Syed, Q. and Mark, A. B. (2010). A guide to adulterants, bulking agents and other contaminants found in illicit drugs. Faculty of Health and Applied Social Sciences, Liverpool John Moores University, Liverpool.
16. De Andrade, F. I., Florindo Guedes, M. I., Pinto Vieira, Í. G., Pereira Mendes, F. N., Salmito Rodrigues, P. A., Costa Maia, C. S., Marques Ávila, M. M. and de Matos Ribeiro, L. (2014). Determination of Synthetic Food Dyes in Commercial Soft Drinks by TLC and Ion-pair HPLC. *Food Chemistry*, 157: 193-198.
17. Dixon, E. A. and Renyk, G. (1982). Isolation, separation, and identification of synthetic food colors. *Journal of Chemical Education*, 59(1): 67-69.
18. Kucharska, M. and Grabka, J. (2010). A review of chromatographic methods for determination of synthetic food dyes. *Talanta*, 80(3): 1045-1051.
19. Fadil, F. A. and McSharry, W. O. (1979). Extraction and TLC separation of food, drug, and cosmetic dyes from tablet-coating formulations. *Journal of Pharmaceutical Sciences*, 68(1): 97-98.
20. United Nations on Office Drugs and Crime (2006). Recommended methods for the identification and analysis of amphetamine, methamphetamine and their ring-substituted analogues in seized materials. Vienna: United Nations Office on Drugs and Crime.

21. Adam, P., Natakankitkul, S., Sirithunyalug, J. and Aramrattana, A. (2005). Physio-chemical profiles of methamphetamine tablets. *CMU Journal*, 4(1): 65-70.
22. Adam, P., Natakankitkul, S., Sirithunyalug, J. and Aramrattana, A. (2004). Drug characterization of methamphetamine tablets – a scientific tool to help identify drug production and trafficking networks. In: The third Australasian drug strategy conference – preventing and reducing substance abuse, 4-6 May 2004, Alice Springs, Australia.
23. Li, T., Hua, Z., Meng, X. and Liu, C. (2018). A Simple and effective physical characteristic profiling method for methamphetamine tablet seized in China. *Journal of Forensic Sciences*, 63(2): 541-547.
24. Haywood, A. and Glass, B. D. (2011). Pharmaceutical excipients - where do we begin? *Australian Prescriber*, 34(4): 112-114.
25. Armstrong, N. (2006). Tablet manufacturer. In: Encyclopedia of pharmaceutical technology (3rd edition). Marcel Dekker, New York.
26. Gordon, R. E., Rosanske, T. W. and Fonner, D. E. (1990). Granulation technology and tablet characterization. In: Pharmaceutical dosage forms. Marcel Dekker, New York.
27. Cole, M. D. (2003). The analysis of controlled substances. John Wiley and Sons Ltd Wiley, New Jersey.
28. Bunaciu, A. A. and Aboul-Enein, H. Y. (2021). Adulterated drug analysis using FTIR spectroscopy. *Applied Spectroscopy Reviews*, 56 (5): 423-437.
29. Mail, R., Teoh, W. K., Kunalan, V., Chang, K. H. and Abdullah, A. F. L. (2021). Quick discrimination of seized erimin-5 tablets by attenuated total reflectance-Fourier transform infra-red spectroscopy. *Australian Journal of Forensic Sciences*, In Press.
30. Liu, C-M., Han, Y., Min, S-G., Jia, W., Meng, X. and Liu, P-P. (2018). Rapid qualitative analysis of methamphetamine, ketamine, heroin, and cocaine by Fourier transform infrared spectroscopy (FTIR). *Forensic Science International*, 290: 162-168.
31. He, X., Wang, J., You, X., Niu, F., Fan, L. and Lv, Y. (2020). Classification of heroin, methamphetamine, ketamine and their additives by attenuated total reflection-Fourier transform infrared spectroscopy and chemometrics. *Spectrochimica Acta Part A: Molecular and Biomolecular*, 241: 118665.
32. Chan, K. W., Tan, G. H. and Wong, R. C. S. (2012). Gas chromatographic method validation for the analysis of major components in illicit heroin seized in Malaysia. *Science and Justice*, 52(1): 9-16.
33. Broséus, J., Gentile, N. and Esseiva, P. (2016). The cutting of cocaine and heroin: A critical review. *Forensic Science International*, 262: 73-83.
34. Hughes, J., Ayoko, G., Collett, S. and Golding, G. (2013). Rapid quantification of methamphetamine: Using attenuated total reflectance Fourier transform infrared spectroscopy (ATR-FTIR) and chemometrics. *PLoS One* 8(7): e69609.
35. Abdullah, A. F. L., Abraham, A. A., Sulaiman, M. and Kunalan, V. (2012). Forensic drug profiling of erimin-5 using TLC and GC-MS. *Malaysian Journal of Forensic Sciences*, 3 (1): 11-15.
36. Joyce, J. R. (1980). The identification of dyes in illicit tablets. *Journal of Forensic Science Society*, 20(4): 247-252.
37. Chiarotti, M., Fucci, N. and Furnari, C. (1991). Comparative analysis of illicit heroin samples. *Forensic Science International*, 50(1): 47-56.
38. Barnfield, C., Burns, S., Byrom, D. L. and Kemmenoe, A. V. (1988). The routine profiling of forensic heroin samples. *Forensic Science International*, 39(2): 107-117.
39. Johnston, A. and King, L. A. (1988). Heroin profiling: Predicting the country of origin of seized heroin. *Forensic Science International*, 95(1): 47-55.
40. Yusoff, M. Z., Chang, K. H. and Abdullah, A. F. L. (2017). Attenuated total reflectance – Fourier transform infra-red spectral profiling of illicit heroin for forensic intelligence. *Australian Journal of Forensic Sciences*, 50(5): 543-551.

41. Collins, M., Huttunen, J., Evans, I. and Robertson, J. (2007). Illicit drug profiling: The Australian experience. *Australian Journal of Forensic Sciences*, 39(1): 25-32.
42. Dams, R., Benijts, T., Lambert, W. E., Massart, D. L. and De Leenheer, A. P. (2001). Heroin impurity profiling: Trends throughout a decade of experimenting. *Forensic Science International*, 123(2-3): 81-88.
43. United Nations on Office Drugs and Crime (2005). Methods for impurity profiling of heroin and cocaine - manual for use by national drug testing laboratories. Vienna: United Nations Office on Drugs and Crime.

Malaysian Journal of Analytical Sciences (MJAS)
Published by Malaysian Analytical Sciences Society

CATALYTIC NEUTRALIZATION OF ACIDIC PETROLEUM CRUDE OIL UTILIZING 2-METHYLIMIDAZOLE WITH ADDITION OF Cu/Ce(10:90)/Al_2O_3 CATALYST

(Peneutralan Pemangkin Minyak Mentah Petroleum Berasid Menggunakan 2-Metilimidazol dengan Tambahan Mangkin Cu/Ce(10:90)/Al_2O_3)

Norshahidatul Akmar Mohd Shohaimi[1]*, Noraini Safar Che Harun[1], Hisyam Saufi Tajudin[1], Wan Azelee Wan Abu Bakar[2], Nurasmat Mohd Shukri[3], Nor Hakimin Abdullah[4], Ahmad Zamani Ab Halim[5]

[1]*Faculty of Applied Sciences,*
Universiti Teknologi MARA Pahang, Bandar Tun Abdul Razak Jengka, Pahang, Malaysia
[2]*Faculty of Sciences,*
Universiti Teknologi Malaysia, Johor Bahru, Johor, Malaysia
[3]*School of Health Sciences,*
Universiti Sains Malaysia, Health Campus, 16150 Kubang Kerian, Kelantan
[4]*Advanced Materials Research Centre (AMRC), Faculty of Bioengineering and Technology,*
Universiti Malaysia Kelantan, Locked Bag 100, 17600 Jeli, Kelantan
[5]*Faculty of Industrial Sciences & Technology,*
Universiti Malaysia Pahang, 26300 Gambang, Kuantan, Pahang, Malaysia

**Corresponding author: akmarshohaimi@uitm.edu.my*

Received: 22 December 2021; Accepted: 3 February 2022; Published: 25 February 2022

Abstract

The presence of naphthenic acid (NA) in crude oil leads to corrosion problems within oil refineries which may increase the maintenance cost and produce lower quality of crude oil. The objective of this study is to reduce the total acid number (TAN) of Petronas Penapisan Melaka (PPM)'s crude oil (TAN = 2.43 mgKOH/g) using 2-methylimidazole with the aid of Cu/Ce (10:90)/Al_2O_3 catalyst through the catalytic neutralization technique. A 10% of 2-methylimidazole in ethanol solution was used as the acid removal agent. Cerium oxide based catalysts with copper as a dopant were supported onto alumina and calcined at different calcination temperatures of 800 ℃, 900 ℃ and 1000 ℃. The potential catalyst was characterized by using TGA-DTG, FTIR and XRD for its physicochemical properties. The results showed TAN was reduced to 0.53 mg KOH/g with 78.2% reduction at catalyst calcination temperature of 900 ℃, 0.5% catalyst loading, reaction temperature of 27 ℃ and 10 minutes reaction time. The small particle size of catalyst calcined at 900 ℃ which was 18.02 nm led to bigger surface areas that enhanced the neutralization process. These structural properties contributed to the excellent catalytic performance which removed the NAs in the PPM's crude oil and concurrently reduced the TAN value below than one.

Keywords: catalyst, catalytic neutralization, crude oil, naphthenic acid

Abstrak

Kehadiran asid naftenik (NA) dalam minyak mentah membawa kepada masalah kakisan dalam kilang penapisan minyak yang boleh meningkatkan kos penyelenggaraan dan menghasilkan minyak mentah yang berkualiti rendah. Objektif kajian ini adalah untuk mengurangkan jumlah asid (TAN) minyak mentah Petronas Penapisan Melaka (PPM) (TAN = 2.43 mgKOH/g) menggunakan 2-metilimidazol dengan bantuan mangkin Cu/Ce (10:90)/ Al_2O_3 melalui teknik peneutralan pemangkin. 10% daripada 2-metilimidazol dalam larutan etanol digunakan sebagai agen penyingkiran asid. Pemangkin berasaskan serium oksida dengan kuprum sebagai dopan disokong pada alumina dan dikalsinkan pada suhu pengkalsinan berbeza 800 ℃, 900 ℃ dan 1000 ℃. Mangkin berpotensi dicirikan dengan menggunakan TGA-DTG, FTIR dan XRD untuk sifat fizikokimianya. Keputusan menunjukkan TAN dikurangkan kepada 0.53 mg KOH/g dengan pengurangan 78.2% pada suhu pengkalsinan mangkin 900 ℃, 0.5% pemuatan mangkin, suhu tindak balas 27 ℃ dan 10 minit masa tindak balas. Saiz zarah kecil pemangkin yang dikalsinkan pada 900 ℃ iaitu 18.02 nm membawa kepada kawasan permukaan yang lebih besar yang meningkatkan proses peneutralan. Ciri-ciri struktur ini menyumbang kepada prestasi pemangkin yang sangat baik yang mengeluarkan NA dalam minyak mentah PPM dan secara serentak mengurangkan nilai TAN di bawah satu.

Kata kunci: mangkin, peneutralan pemangkin, minyak mentah, asid naftenik

Introduction

Nowadays, crude oil had become one of the most important source of energy in the world. Since raw petroleum is an important source of energy, it is imperative to overcome the issue of acidic crude oil to have better oil production [1]. In recent years, acidic crude oil production has raised by 0.3% per year worldwide. The naphthenic acid (NA) compound present in crude oil leads to the high acidity of oil. The term “naphthenic acids” is used to account for all carboxylic acids present in crude oil including acyclic and aromatic acids, which is also referred to as complicated mixtures [2].

The acidity of petroleum crude oil is measured by its total acid number (TAN), which refers the number of milligrams of KOH required to reduce the corrosiveness in one gram of oil [3]. Currently, the treatment for acidic oil either relies upon weakening or caustic washing techniques to decrease the TAN number of overwhelming rough oils. Moreover, neither of these method is altogether attractive. For example, even though mixing high TAN unrefined petroleum with a low TAN unrefined petroleum might decrease the NAs content to a worthy level, the acidic mixes still remain [1]. Burning treatment can also considerably evacuate NAs, but the procedure creates critical measures of wastewater and emulsion that are problematic to treat. Specifically, once an emulsion is formed, it is exceptionally hard to evacuate [4, 5]. A series of homogeneous basic catalysts are widely used in the petroleum industry such as KOH and NaOH but these types of catalysts would induce an emulsion problem and no catalyst recovery. Solid acid catalysts have attracted a lot of attention in recent years in various industrial organic transformations, owing to their non-toxicity, non-corrosiveness, low cost, easy handling, recovery, and reusability. Among the several mesoporous materials, such as MCM-41 and SBA-16, the most important amphoteric substance is ɣ-alumina (ɣ-Al_2O_3), which is commercially accessible. It has been employed directly as a catalyst and as a catalyst support material in the automotive and petroleum industries due to its combination of textural features such as surface area, pore volume, and pore size dispersion.

Due to the fact that crude oil upgrading is important to ensure the crude oil produced is in a high quality with a good price, an extensive treatment will be carried out for the high acidic crude oil. In this study, the catalytic neutralization technique was introduced utilizing a 2-methylimidazole in ethanol solution with the aids of copper doped cerium based catalyst with alumina as a support.

Materials and Methods

Catalyst preparation and characterization

In this study, cerium oxides were used as catalysts of interest and supported onto alumina with copper as a dopant. Cerium nitrate and copper nitrate were chosen as the metal precursor as it is easily soluble in water.

The ratio of based-dopant used was 10 (dopant) to 90 (base) according to the metal precursor molar ratio and then calcined at a temperatures of 800 ℃, 900 ℃, and 1000 ℃ [6]. An aqueous Incipient Wetness Impregnation (IWI) method was used to prepare the catalyst. According to the desired ratio, each of the metal salts was weighted in a beaker and it was dissolved in small amount of distilled water. To homogenize the mixture, the solutions were mixed together and the mixture solution was stirred continuously by magnetic bar for 30 minutes at 27 ℃. The alumina (Al_2O_3) beads as a support material were immersed into the catalysts solution for 1 hour and the supported catalysts were transferred onto an evaporating dish covered with glass wool [7, 8].

To remove water and allow good coating of catalyst solution on the surface of alumina, it was then aged inside an oven at 80-90 ℃ for 24 hour. To eliminate all the metals precursor, excess water and impurities, this steps were followed by calcination in the furnace at 800 ℃ for 5 hours using a ramp rate of 5℃/min [9]. The preparation of the best catalyst was further optimized at temperatures of 900 ℃ and 1000 ℃ [4]. To study its physicochemical properties, the potential catalyst was characterized by a several methods. The data obtained were exceedingly valuable to comprehend the relationship between catalyst properties and its catalytic performance towards the neutralization activity. The characterization techniques that were used are X-ray Diffraction Spectroscopy (XRD), Fourier Transform Infrared Spectroscopy (FTIR), and Thermal Gravimetry Analysis (TGA-DTG) [10].

Feedstock and basic chemical

The materials were purchased from QReCTM and used as supplied. Feedstock used in this study was obtained from Petronas Penapisan Melaka (PPM), Malaysia with TAN of 2.43 mg KOH/g. In this study, the 2-propanol and toluene was used as titration solvents. The indicator used in the neutralization reaction is a phenolphthalein solution, 1% (w/v) in ethanol. Potassium hydroxide pellets and barium hydroxide were utilized as titrants [11, 12].

Catalytic neutralization reaction

Crude oil and 2-methylimidazole solution in ethanol by a certain mass ratio was stirred. A total of 10% (w/w) of imidazole derivative solutions in ethanol and cerium oxide as catalyst were added to Petronas Penapisan Melaka (PPM)'s crude oil. Then the mixture solution was put into 2 neck round bottom flask equip with a magnetic stirrer and thermometer to control the constant temperature. Parafin oil was used to ease the maintaining of the constant temperature that was 27 ℃, 40 ℃, 50 ℃ and 60 ℃ [13]. The mixture then was stirred at the various temperatures for 5, 10 and 15 minutes to study the effect of reaction time [2]. After the extraction process, the mixture was put into a centrifuge container and was centrifuge with a speed of 50×106 rpm for 30 minutes. The mixture was centrifuged to achieve the gravity separation of the reagent with the acidic compounds extracted from the crude oil sample. The reagent with ionic liquid was on top of the centrifuge tube, while the neutralized crude oil was collected at the bottom of the tube [9].

Total acid number (TAN) determination

A 0.2 g Melaka crude oil sample after neutralization treatment was measured and placed in a titration beaker. The titration solvent, 40 mL with a mixture of 2-propanol: toluene: distilled water (50:49.5:0.5) was poured into the crude oil sample in the titration beaker. Then, the petroleum crude oil sample was titrated with potassium hydroxide and barium hydroxide solution (0.01 mol/L).

TAN value for Melaka's crude oil (TAN = 2.43 mg KOH/g) was determined by semi-micro colour indicator titration method. The indicator used was phenolphthalein solution, 0.1 mL where the stable red colour was observed and indicated the end-point for the titration method. The titration method was performed on Melaka's crude oil before and after the catalytic neutralization reaction. In order to express the results, the TAN of the sample was calculated in milligrams of potassium hydroxide per gram of sample (mg KOH/g) by using Equation 1.

$$\text{TAN} = 56.1 \times c \times \frac{(V_{KOH} - V_B)}{m} \quad (1)$$

where 56.1 is the molecular mass of KOH (g/mol), c is the concentration of the standard volumetric potassium hydroxide solution (mol/L), V_{KOH} is the volume of titrant used to reach the equilibrium point (mL), V_B is the volume of titrant required for the blank titration (mL), and m is the sample mass (g).

Results and Discussion

Thermogravimetry analysis-differential thermal gravimetry (TGA-DTG)

TGA-DTG analysis was studied to obtain thermal stability of potential catalyst after being aged overnight in an oven at 80-90 ℃ [1]. TGA profile exhibited some well-defined sections of weight loss accompanied by different slopes of thermogravimetric trace (weight loss rate). The thermogram of the Cu/Ce(10:90)/Al_2O_3 catalyst showed three phases of weight loss as depicted in Figure 1 while the Table 1 tabulated the type of species deduction corresponding to the heating temperature.

The weight loss in the range of 100-200 ℃ was due to the loss of physisorbed water molecules and was assigned to the evaporation of chemically adsorbed water molecules[14]. Between the temperature of 200–380℃, the weight loss was attributed to the loss of hydroxyl molecules and lastly the weight loss at the range of 380–650℃ was due to the decomposition of nitrate precursors as shown in equation

$$2Ce(NO_3)_3 \rightarrow 2CeO_2 + 6NO_2 + O_2 \quad (2)$$

The theoretical mass loss when the nitrates were decomposed can be calculated in terms of the final mixture form (CeO_2/Al_2O_3) from 650 ℃ to 1000 ℃ for being a stable form [15]. From the overall of TGA–DTG analysis, it can be concluded that thermal treatment had eliminated the impurities and water from the materials with 14.50% of total weight loss in 8.15 mg of catalyst and the pure metal oxide was obtained after heating at 650 ℃ [16].

This observation is in agreement with the result shown in Figure 5 where by using Cu/Ce (10:90)/Al_2O_3 catalyst calcined at 900 ℃, the TAN value of PPM's crude oil can be reduced from the original TAN value as the catalyst calcined at this temperature show complete formation of metal oxide. The detailed weight loss and the deduction for each stages of weight loss is presented in Table 1.

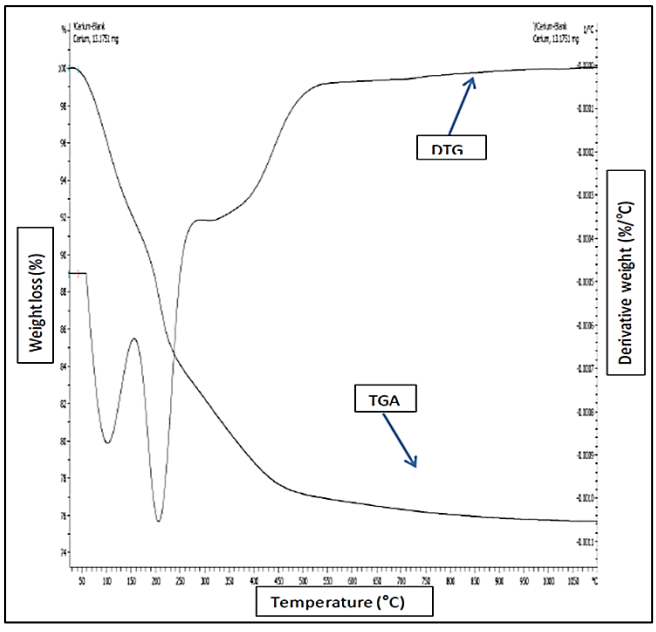

Figure 1. TGA-DTG thermogram of Cu/Ce (10:90)/Al_2O_3 catalyst after aging in an oven for 24 hours at 80-90 ℃

Table 1. TGA analysis results for Cu/Ce (10:90)/Al_2O_3 catalyst

Heating Temperature, ºC	Weight Loss, %	Deduction
100-200	14.50	Loss of crystal water and surface water molecule
200-380	8.20	Complete removal of water and formation of pure metal oxide
380-650	1.30	Loss of nitrate compound and surface hydroxyl molecule

X-ray diffraction

The XRD diffractogram for the bimetallic catalyst of Cu/Ce (10:90)/Al_2O_3 calcined at different temperatures of 800 ℃, 900 ℃, and 1000 ℃ were compiled in Figure 2. From the XRD diffractogram pattern, it can be seen that Cu/Ce(10:90)/Al_2O_3 catalyst calcined at 800 ℃ and 900 ℃ were less crystalline compared to the catalyst calcined at 1000 ℃. Typically, the calcination process of a catalyst involves the loss of chemically bound water or precursors, modification of the texture through sintering, modification of the structure, generation of an active phase and stabilization of mechanical properties which result in the development of an increased surface area of these catalysts [17].

The polycrystallinity phase of the catalyst calcined at 800 ºC and 900 ºC was dominated by the CeO_2 face-centered cubic (fcc) species and some of the alumina orthorhombic (o) phase. The broadening of CeO_2 peak calcined at 800 ℃ and polycrystalline of CeO_2 calcined 900 ℃ were attributed to the presence of a mixture of metal oxides and also due to loose arrangement of atom in the compound [18]. The high crystallinity of CeO_2 peak observed at 1000 ºC calcination temperature is in agreement with the finding from [19] who stated that the size of catalyst will increase as it was calcined at high temperature. Increasing in particle size of catalyst will lead to the smaller surface area. Therefore, 900 ℃ was an ideal calcination temperature for Cu/Ce (10:90)/Al_2O_3 catalyst in order to reduce the NAs content of PPM's crude oils.

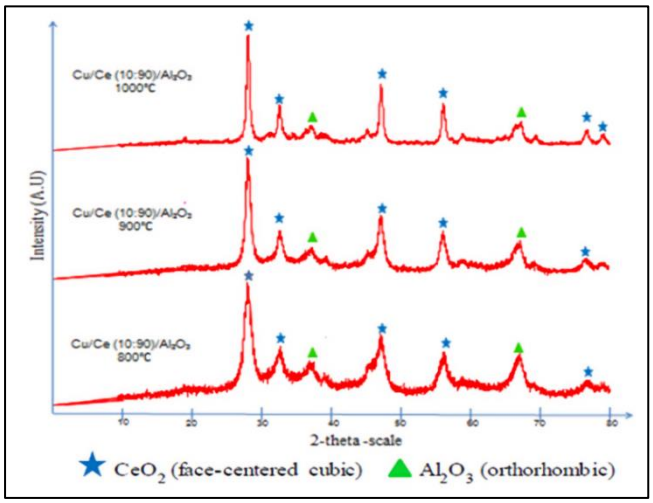

Figure 2. The XRD diffractograms of Cu/Ce(10:90)/Al_2O_3 catalyst calcined at temperatures of 800, 900 and 1000 ℃ for 5 hours

Fourier transform infrared spectroscopy

The FTIR spectra of Cu/Ce (10:90)/Al_2O_3 is shown in Figure 3. The peaks assignments for the catalyst is tabulated in Table 2. The results showed a group assignment for peak at 567.46 – 541.32 cm^{-1} at calcination temperature of 900 ℃ before and after neutralization process was due to the stretching mode of metal oxide group which resulted from the complete formation of pure metal oxide catalyst as also reported by Roy and Bhattacharya [20]. Based on the figure, it can be observed that after deacidification process (b), the new peak appeared at stretching frequency of 1310.65, 1478.24, 2810.87, and 2987.87 due to the attachment of impurities on the surface of the catalyst. It could be suggested that the catalyst should be pre-treated before use in the next cycle of reaction.

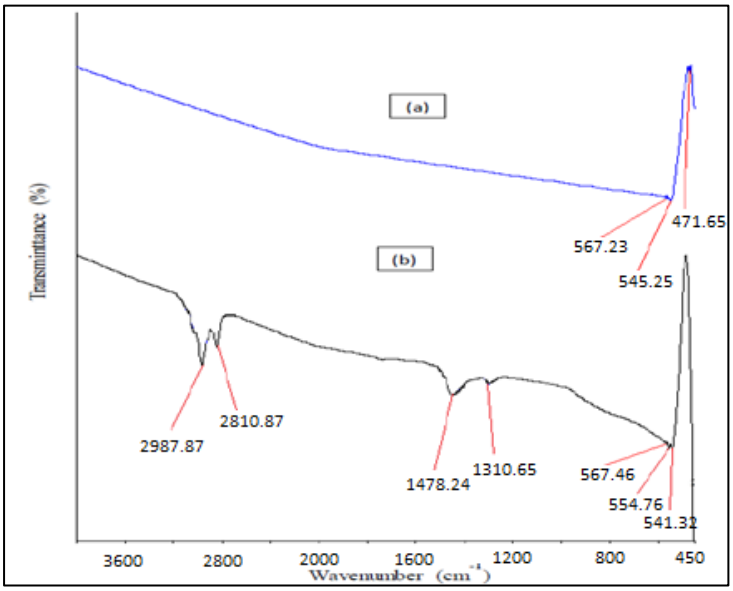

Figure 3. FTIR spectra of Cu/Ce (10:90)/Al_2O_3 catalyst at calcination temperatures of 900 ℃, (a) before neutralization reaction (b) after neutralization reaction

Wavenumber, cm^{-1}	**Peak Assignment**
2987.87 and 2810.87	sp^3 C-H stretching
1478.24	sp^2 C-H stretching
1310.65	Stretching mode of free nitrate (NO_3^-) group from metal precursors
567.46 – 541.32	Stretching mode of Metal=Oxygen (M=O)

Table 2. FTIR peak assignment of Cu/Ce (10:90)/Al_2O_3 catalyst

Effect of reagent concentration towards crude oil TAN without catalyst

Shi et al. [13] had reported the effect of different imidazole derivatives on the reduction of TAN value of PPM's crude oil. It could be seen that when ethanol was used to extract NA from crude oil, the acid removal rate reached up to 17.6%. The polar NAs could be partially dissolved in alcohol especially the smaller molecular weight ones with larger polarity were more easily dissolved in ethanol according to the

similar dissolve mutually theory. Due to this theory, when imidazole derivatives were added into ethanol solution, the acid removal rate was significantly improved. The stronger the alkalinity of imidazole derivatives, the easier the reaction to occur because NA is a weak acid.

Figure 4 shows various amount of 2-methylimidazole concentration from 5% to 15% that were tested in order to reduce the TAN of untreated PPM's crude oil sample. When higher percentages of 2-methylimidazole were used, the TAN value of PPM's crude oils was further decreased. The best result showing the highest concentration of 2-methylimidazole (15%) reduced TAN value from 2.43 mg KOH/g to 1.10 mg KOH/g is when the percentage removal of NA was 55%.

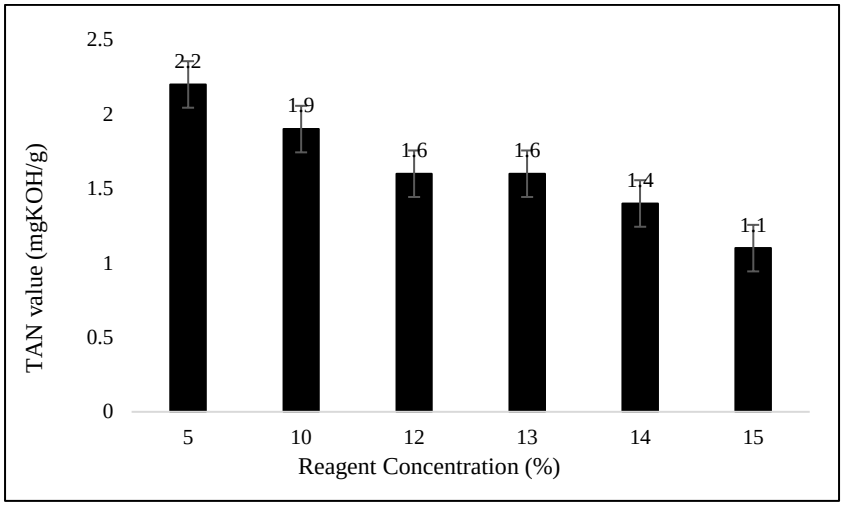

Figure 4. Effect of different reagent concentration towards TAN value without presence of catalyst

Effect of catalyst calcination temperature

An investigation on this parameter was conducted to determine the effect of calcination temperature on the alumina supported catalyst by using 10% of 2-methylimidazole. Figure 5 showed the trends of TAN value based on different catalyst calcination temperature. The trend of TAN value of PPM's crude oils decreased from calcination temperature of 800 ℃ to 900 ℃ and increased when the catalyst calcined at 1000 ℃. The catalysts which calcined at lower calcination temperatures (800 ℃) showed poor performance in this study while the catalyst functioned well in the removal of NAs process when calcined at a medium calcination temperature of 900 ℃. At 900 ℃ calcination temperature, it showed an improvement in reducing acidic content of crude oil due to the larger surface area of the catalyst from smaller particle size as supported from the BET results obtained by [4]. Thus, it provided sufficient surface sites for an excellent NAs removal process [21].

Lower performance was shown by this catalyst calcined at 1000 ℃, which gave TAN value of 1.87 mg KOH/g which is above than one. This is probably due to the fact that increasing calcination temperature will increase particle size of the catalyst which leads to a smaller surface area because of high crystallinity of the catalyst observed by the narrow peak as shown by diffractogram in XRD analysis. Therefore, 900℃ was selected as the ideal calcination temperature for removal of NA for PPM's crude oil samples [6].

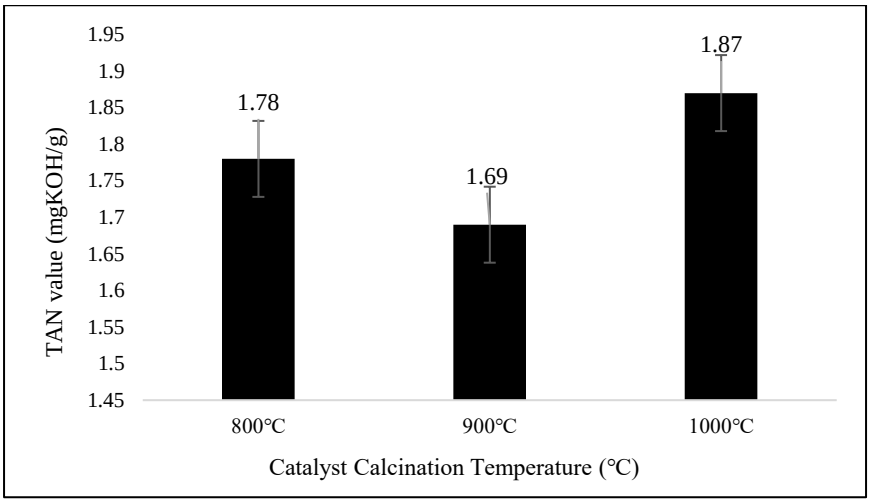

Figure 5. Effect of different calcination temperature towards TAN value

Effect of catalyst loading

Catalyst loading is the percentage of the catalyst used by calculating the weight of catalyst used over mass of crude oil. In this study, this parameter was observed to study the effectiveness and efficiency of various catalyst loading towards TAN value. Figure 6 showed the trend of TAN value for PPM's crude oil based on different catalyst loading. The trend of TAN value for PPM's crude oils was decreasing with an increase in the percentage of the catalyst loading. It could be seen that the highest catalyst loading of 0.5% successfully reduced TAN value to 0.53 mg KOH/g while the lowest loading percentages that was 0.1% only reduced the TAN value to 1.69 mg KOH/g. An increased in the catalyst loading made the catalytic reaction became faster and more efficient.

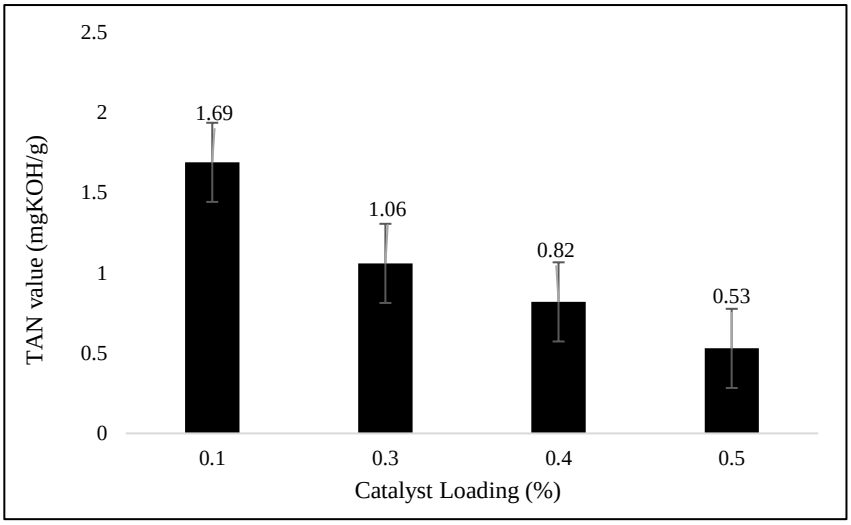

Figure 6. Effect of different percentage of catalyst loading towards TAN value (Catalyst calcination temperature: 900 ºC)

Effect of reaction temperature

In this study, different reaction temperatures were studied for catalytic neutralization process on PPM's crude oils. The temperature can be used to determine the speed of the neutralization reaction and can also decrease the viscosity of the crude oil, making the crude oil more accessible to the 2-methylimidazole. The trend of TAN for PPM's crude oils was increased when the reaction temperature increased as shown in Figure 7.

The percentage of catalytic neutralization activity decreased from 27 ℃ until 40 ℃ for PPM's crude oil samples as the TAN value for 27 ℃ reduced from 2.43 to 0.53 mg KOH/g while at 40 ℃, TAN reduced from 2.43 to 0.74 mg KOH/g and at 50 ℃ it decreased to 1.24 mg KOH/g and lastly, for 60 ℃ the TAN decreased from 2.43 to 1.44 mg KOH/g. This was because the reaction occured at higher temperature was not profitable for the reaction between 2-methylimizadole and NAs in crude oil as the higher temperature can increase the viscosity of the crude oil. This occurrence probably stabilized the NA in crude oil and inhibited the reagent to react with NA effectively. In addition, this study offered an environmental friendly process because lower reaction temperature can lead to lower energy consumption and at the same time can reduce air pollution [3].

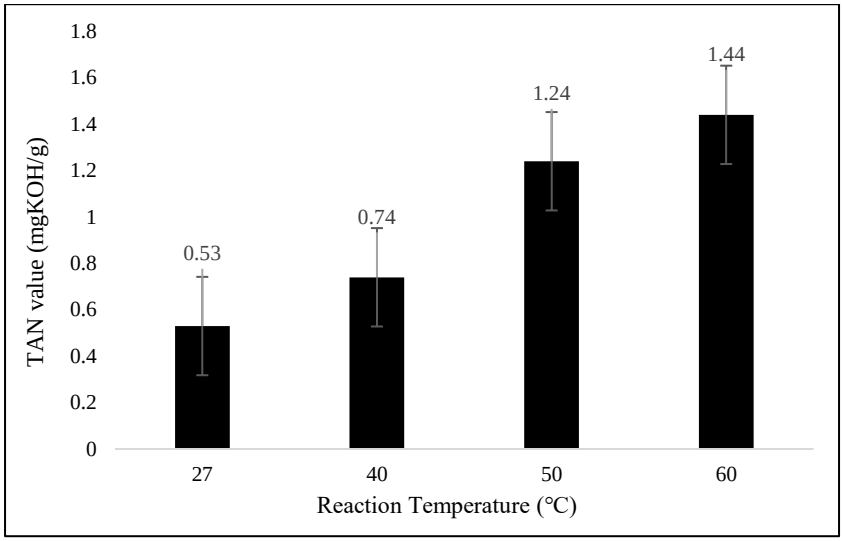

Figure 7. Effect of different reaction temperature towards TAN value (Catalyst calcination temperature: 900 ℃, catalyst loading: 0.5%)

Effect of reaction time

The effect of different reaction times on the neutralization process with Cu/Ce (10:90)/Al_2O_3 catalyst calcined at 900 ℃ with addition of 0.5% catalyst loading, 10% of 2-methyl imidazole concentration, and reaction temperature of 27 ℃ was performed on PPM's crude oils shown in Figure 8. The results illustrated that the TAN values decreased when the reaction time was increased from 5 to 15 minutes. This substantial reduction of the TAN value was attributed to the elevated opportunity for a reaction between 2-methylimidazole aided by a catalyst and NA in the crude oil. The longer the reaction time, the longer the duration for which the solution was stirred, which consequently meant the more markedly the 2-methylimidazole aided by Cu/Ce (10:90)/Al_2O_3 catalyst in the solution reacted to remove NA in PPM's crude oils.

According to Shi et al. [13] when the reaction time was increased above 15 minutes, the TAN values became constant for PPM's crude oil samples. This is because after 15 minutes, reagent successfully reduced and removed all NAs in crude oils. As a longer reaction time will only consume more energy, the optimum reaction time recommended is 10 minutes for the basic chemical to remove NA effectively and the best TAN value reduced is to 0.53 mg KOH/g for PPM's crude oils. It was observed that the acid-removal rate was increased by increasing the reaction time from 5 minutes to 10 minutes at 27 ℃, but showed very small improvement of TAN value when the reaction time is between 10 minutes and 15 minutes. TGA–DTG analysis concluded that thermal treatment had eliminated the impurities and water from the materials with 14.50% of total weight loss in 8.15 mg of catalyst and the pure metal oxide was obtained after heating at 650 ℃.

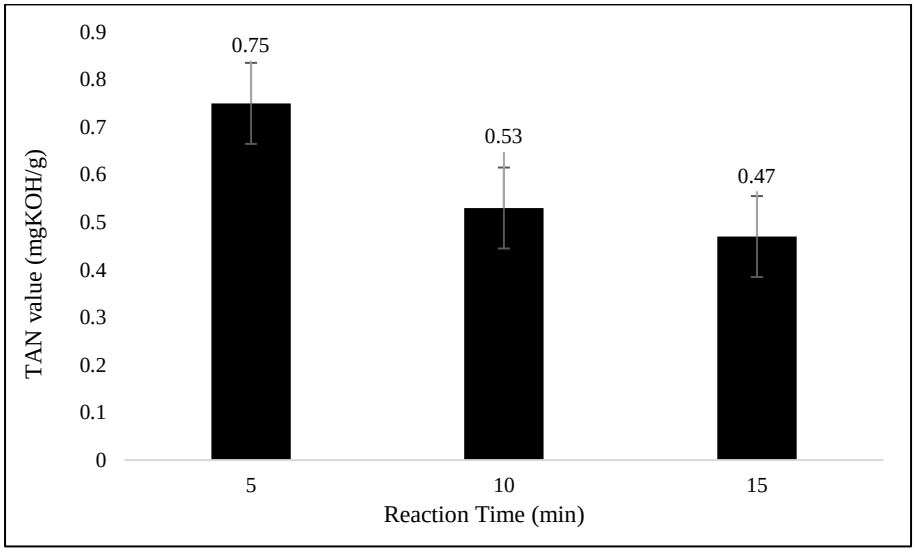

Figure 8. Effect of the different reaction times on the TAN values of PPM crude oils

Conclusion

The catalytic neutralization technique had successfully been applied in this study for the removal of NA and simultaneously solved the corrosion and emulsion problem by meeting the PETRONAS benchmark for TAN value less than 1 mg KOH/g. PPM's crude oil which possessed an initial TAN value of 2.43 mg KOH/g was reduced to 0.53 mg KOH/g with addition of 10% of 2-methylimidazole, catalyst calcination temperature of 900 ℃, 0.5% of Cu/Ce (10:90)/Al_2O_3 catalyst loading (4 beads), reaction temperature of 27 ℃ and reaction time of 10 minutes. XRD results revealed the polycrystallinity phase of the catalyst which was dominated by the CeO_2 face-centered cubic (fcc) species and some of the alumina orthorhombic (o) phase. As a recommendation for further study, other instruments to characterize the physicochemical properties of catalyst such as Brunauer–Emmett–Teller (BET), and Transmission Electron Microscopy (TEM) could be implemented.

Acknowledgement

The authors acknowledged the funding from Research Grant, FRGS with Grant No.: 011000190001 (File no.: 600 IRMI/FRGS 5/3 (108/2019)).

References

1. Shohaimi, N. A., Mohd Halim, N. S., Ab Halim, A. Z., Mohd Shukri, N. and Abdullah, N. H. (2020). Catalytic study of Ni/Ce/Al_2O_3 and Ni/Ca/Al_2O_3 on the removal of naphthenic acid from petroleum crude oil utilizing sodium thiocyanate in ethanol. *Petroleum Science and Technology,* 38(6): 602-608.
2. Sun, Y. and Shi, L. (2012). Basic ionic liquids with imidazole anion: New reagents to remove naphthenic acids from crude oil with high total acid number. *Fuel*, 99: 83-87.
3. Cho, K., Rana, B. S., Cho, D. W., Beum, H. T., Kim, C. H. and Kim, J. N. (2020). Catalytic removal of naphthenic acids over Co-Mo/γ-Al_2O_3 catalyst to reduce total acid number (TAN) of highly acidic crude oil. *Applied Catalysis A: General,* 606: 117835.
4. Shukri, N. M., Bakar, W. A., Jaafar, J. and Majid, Z. A. (2015). Removal of naphthenic acids from high acidity Korean crude oil utilizing catalytic deacidification method. *Journal of Industrial and Engineering Chemistry*. 28: 110-116.
5. Wu, C., De Visscher, A. and Gates, I. D. (2019). On naphthenic acids removal from crude oil and oil sands process-affected water. *Fuel*, 253: 1229-1246.
6. Shukri, N. M., Bakar, W. A., Jaafar, J. and Majid, Z. A. (2015b) Optimization of basic catalyst with ammoniated polyethylene glycol for the removal of naphthenic acid from petroleum crude oil by Box–Behnken design. *Clean Techn Environ Policy Clean Technologies and Environmental Policy*, 17(8), 2387-2400.
7. Zamani, A. H., Shohaimi, N. A. M., Rosid, S. J. M., Abdullah, N. H. and Shukri, N. M. (2019). Enhanced low temperature reaction for the CO_2 methanation over Ru promoted Cu/Mn on alumina support catalyst using double reactor system. *Journal of the Taiwan Institute of Chemical Engineers*, 96: 400-408.
8. Shohaimi, N. A. M., and Marodzi, N. F. S. (2018). Transesterification of waste cooking oil in biodiesel production utilizing CaO/Al_2O_3 Heterogeneous Catalyst. *Malaysian Journal of Analytical Sciences*, 22(1): 157-165.
9. Aziz, N. H., Shohaimi, N. A. M. and Che Harun, N. S. (2021). The effectiveness of Ni/Ce/Al_2O_3 catalyst in the extraction of naphthenic acids from acidic crude oil. *Materials Science Forum*, 1025: pp. 284-289.
10. Shohaimi, N. A. M, Jelani, N., Ab Halim, A. Z., Abdullah, N. H. and Shukri, N. M. (2021). Catalytic neutralization of naphthenic acid from petroleum crude oil by using cerium oxide catalyst and 2-methylimidazole in polyethylene glycol. *Recent Innovations in Chemical Engineering*, 14(3): 219-227.
11. Shohaimi, N. A. M., Jaafar, J. and Bakar, W. A. W. A. (2015). Catalytic deacidification optimization of Korean crude oil based on response surface methodology. *Clean Technologies and Environmental Policy*, 17(6), 1513-1522.
12. Shohaimi N.A.M, Bakar, W. A. W. A. and Jaafar, J. (2014). Catalytic neutralization of acidic crude oil utilizing ammonia in ethylene glycol basic solution. *Journal of Industrial and Engineering Chemistry*, 20(4): 2086-2094 .
13. Shi, L. J., Shen, B. X., Wang, G. Q. (2008). Removal of naphthenic acids from beijiang crude oil by forming ionic liquids. *Energy & Fuels Energy Fuels.* 22(6): 4177-4181.
14. Shohaimi, N. A. M., Bakar, W. A. W. A. and Jaafar, J. (2014). Catalytic neutralization method for naphthenic acid removal in crude oil by alumina supported Ca and Ba catalysts. *Petroleum Science and Technology*, 32(19): 2365-2375.
15. Dias, A. P. S., Bernardo, J., Felizardo, P. and Neiva Correi, M. J. (2012). Biodiesel production over thermal activated cerium modified Mg-Al hydrotalcites. *Energy.* 41: 344-353.
16. Alouche, A. (2008). Preparation and characterization of copper and/or cerium catalysts supported on alumina or ceria. *Jordan Journal of Mechanical and Industrial Engineering*, 2: 111-116.
17. Bakar, W. A. W. A., Ali, R., Sulaiman, N. and Rahim, H. A. (2010). Manganese oxide doped noble metals supported catalyst for carbon dioxide methanation reaction. *Iranian Journal of Science and Technology Transactions*. 17: 115-123.

18. Lamonier, C., Bennani, A., D'Huysser, A., Aboukais, A. and Wrobel, G. (1996). Evidence for different copper species in precursors of copper-cerium oxide catalysts for hydrogenation reactions: An X-ray diffraction, EPR and X-ray photoelectron spectroscopy study. *Journal of Chemical Society Faraday Transaction*, 92(l): 131-136.
19. Bueno-Ferrer, C., Parres-Esclapez, S., Lozano-Castello, D. and Bueno-Lopez, A., (2010). Relationship between surface area and crystal size of pure and doped cerium oxides. *Journal of Rare Earths*, 28: 647-656.
20. Roy, A. and Bhattacharya, J., (2011). Microwave-assisted synthesis and characterization of CaO nanoparticles. *International Journal Nanoscience,* 10(41): 3-8.
21. Li, X., Zhu, J., Liu, Q. and Wu, B., (2013). The removal of naphthenic acids from dewaxed VGO via esterification catalyzed by Mg–Al hydrotalcite. *Fuel Processing Technology*, 111: 68-77.

Malaysian Journal of Analytical Sciences (MJAS)
Published by Malaysian Analytical Sciences Society

TEMPERATURE EFFECT ON THE ENCAPSULATION OF THE DRUG TETRACAINE HYDROCHLORIDE IN DIFFERENT CYCLODEXTRINS

(Kesan Suhu Terhadap Pengkapsulan Dadah Tetrakain Hidroklorida dalam Siklodekstrin yang Berbeza)

Houria Boudjoras, Teffaha Fergoug, Mansour Azayez*, Youcef Bouhadda, Noureddine Meddah-araibi, Cherifa Zelmat

Laboratory of Physical Chemistry of Macromolecular and Biological Interfaces,
Faculty of Exact Sciences,
University of Mustapha Stambouli, Mascara, Algeria

**Corresponding author: m.azayez@univ-mascara.dz*

Received: 25 September 2021; Accepted: 30 December 2021; Published: 25 February 2022

Abstract

The encapsulation of tetrakain hydrochloride (TC-HCl) in α-cyclodextrin (α-CD), β -cyclodextrin (β-CD) and hydroxypropyl-β-cyclodextrin (HPβ-CD) has been studied by UV-Visible at different temsperatures. The appearance of isosbestic points as well as hyperchromic and bathochromic shifts on the different UV-Visible spectra confirm the complexes formation. From the complexation constants values the stability of the 1:1 type complexes is in the order of α-CD < HPβ-CD < β-CD and decreases with increasing temperature for each complex. All complexation processes are spontaneous, with a favorable enthalpic contribution and an unfavorable entropic term as deduced from Van't Hoff plot analysis. The negative values obtained for ΔCp ° indicate that the apolar part of TC-HCl is encapsulated in the cavities of the CDs.

Keywords: UV-Vis spectrophotometry, cyclodextrins, tetracaine drug, temperature effect, Van't Hoff analysis

Abstrak

Pengkapsulan tetrakain hidroklorida (TC, HCl) dalam α-siklodekstrin (α-CD), β-sikloododekstrin (β-CD) dan hidroksipropil-β-siklodekstrin (HPβ-CD) telah dikaji mengunakan spektrofotometri UV-cahaya nampak pada suhu yang berbeza. Kemunculan titik isosbestik serta pergeseran hipokromik dan bathokromik pada spektrum UV-cahaya nampak yang berbeza mengesahkan pembentukan kompleks. Daripada nilai pemalar kompleks, kestabilan kompleks jenis 1: 1 berada dalam urutan α-CD <HPβ-CD <β-CD dan menurun dengan kenaikan suhu bagi setiap kompleks. Semua proses pengkompleksan adalah spontan, dengan sumbangan entalpik yang menggalakkan dan istilah entropik yang tidak menguntungkan seperti hasil analisis plot Van't Hoff. Nilai negatif yang diperoleh untuk ΔCp ° menunjukkan bahawa bahagian tidak berkutub TC-HCl dikemas dalam rongga CD.

Kata kunci: spektrofotometri UV-cahaya nampak, siklodekstrin, dadah tetrakain, kesan suhu, analisis Van't Hoff

Introduction

The administration of local anesthetics such as tetracaine or procaine during ophthalmologic or dentistry surgeries often shows adverse side effects such as irritations and sometimes cardiac arrhythmias and neurological after effects [1-3]. To reduce these discomforting effects an alternative approach consisting in reformulating these anesthetics as

molecular complexes with adapted complexing agents, has emerged. In this option, the complexing agent is generally a molecule with a peculiar structural conformation shaping a hydrophobic pocket-like site suited to fully encompass the anesthetic molecule or a part of it. Molecules such as cyclodextrin, crown-ether and calixarene are examples of these complexing agents and they operate based on the molecular recognition principle better known as host-guest interaction [4-6].

Cyclodextrins (CDs) represent the most used molecules in host-guest processes because of their biodegradability, non-toxicity and aqueous solubility. They are cyclic oligomers comprising many α(1,4) bound glucopyranose units. They are often schematized in the form of a torus-shaped molecule having a dual nature with hydrophilic external faces and a hydrophobic cavity making them able to form non-covalently bonded inclusion complexes with a variety of hydrophobic molecules in an aqueous solution. The size of each cyclodextrin (CD) varies according to the number of glucose units forming the structure (α-, β- and γ-CD contain respectively 6, 7 and 8 units of D-glucopyranosyl) [7-9] (Figure 1a). The stability of the formed complex is therefore depending partly on the size compatibility between the host and the guest molecule and in the other part on the nature of interacting forces. According to the chemical nature of the guest molecule different interactions may take place as Van der Waals interactions, hydrophobic effect, solvent reorganization, hydrogen bonding, charge transfer, etc. [10, 11]. So, structural information such as complex stoichiometry and geometry are important to know as well as thermodynamic parameters as the association constant, the variation of the free enthalpy (ΔG^0) and the entropy (ΔS^0) of binding. All these are necessary to achieve the best formulation of these complexes [12, 13].

In this present study, the formation of complexes made of tetracaine-hydrochloride (TC-HCl) and different CDs in an aqueous solution are investigated by UV-Visible spectrophotometry from a thermodynamic point of view. The guest molecule (Figure 1b) is a potent local anesthetic, primarily used for topical anesthesia and spinal block, but has a fairly toxic effect resulting in cauda equina syndrome among other compelling side effects [14]. Chemically, TC-HCl is an amino ester where the ester group links a hydrophilic ammonium group to an aromatic lipophilic ring. These peculiarities allow TC-HCl to behave both as a surfactant molecule and as a weak acid with a PKa of 8.5 [15].

(a)

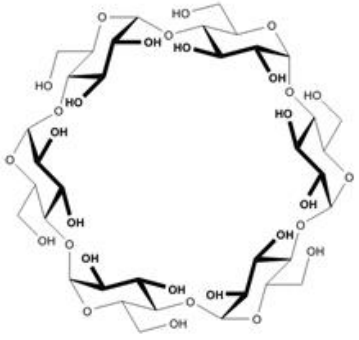

α-CD

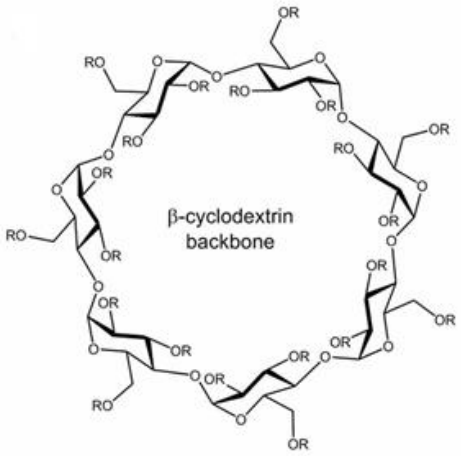

R=$CH_2CHOHCH_3$ for HPβ-CD

(b)

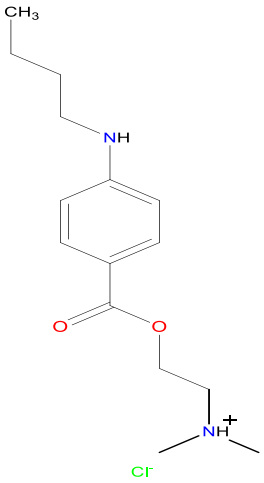

Figure 1. Chemical structures of: (a) CDs, (b) tetracaine hydrochloride

Materials and Methods

Materials

4-(Butylamino)benzoic acid 2-(dimethylamino)ethyl ester monohydrochloride, called tetracaine hydrochloride (TC-HCl) was obtained from Sigma in the crystalline form and was used without further purification. The β-cyclodextrin (β-CD), *α*-cyclodextrin (α-CD), and hydroxypropyl-*β*-cyclodextrin (HPβ-CD) were purchased from Sigma. 6-Hydroxypropyl-β-cyclodextrin (HPβ-CD), containing an average of 0.64 hydroxypropyl groups per glucopyranose unit. All of them, with 99% purity or greater, were used without further purification. All the solutions were freshly prepared with a distilled/deionized water of a conductivity value lower than 2 µS/cm. The homogeneity of the initial solutions was assured by sonicating them in an ultrasonic bath.

UV-Vis measurements

The UV-Vis spectra were recorded with a Specord 200plus double-beam UV-Vis spectrophotometer (Germany), from 190 to 400 nm with 1 nm intervals at 15, 20, 25 and 37 °C, which temperature was kept constant with thermostated cell. Data acquisition of UV-Vis spectra was performed with software (Winspec) supported by the manufacturer and converted to ASCII format for their analysis. On the experiments with the Drug/water binary systems, the (TC-HCl) concentration was varied from 0 to 0.1mM, while for the CD/Drug/water ternary systems, the drug concentration was kept constant at 10^{-5} mol.l^{-1} and CD concentration was varied from 0 to 10 mmol.l^{-1}.

Modeling stoichiometry and association constants

Assuming that a 1:1 complex between any CD and the drug is formed, the following chemical equilibrium takes place.

$$CD + G \leftrightarrows CD\text{-}G \quad (1)$$

If one takes that the activity coefficients of all species are equal to unity, the equilibrium constant K can be written as:

$$K = \frac{[CD-G]}{[CD][G]} \quad (2)$$

The laws of mass conservation for all species require that

$$[CD]_0 = [CD] + [CD-G] \quad (3)$$

$$[G]_0 = [G] + [CD-G] \quad (4)$$

with $[CD]_0$: initial (total) concentration of host molecule, $[G]_0$: initial (total) concentration of the guest molecule. [CD], [G], [CD-G]: equilibrium concentrations of host, guest and complex respectively. The combination of these equations gives the expression of K the equilibrium constant as a function of initial concentrations of the host and the guest molecules as well as one of the formed complexes:

$$K = \frac{[CD-G]}{([CD]_0 - [CD-G])([G]_0 - [CD-G])} \quad (5)$$

So, to compute the equilibrium constant one has to determine the concentration of the formed complex since all other quantities are available. This quantity can be extracted from any technique for which intensity variation is proportional to the concentration of the complex. Amongst all available techniques, UV-Vis spectrophotometry represents the most used technique because of its simplicity and repeatability. For this technique, it is well known that the absorbance or optical density is proportional to the concentration of the absorbing chromophore so the observed absorbance for a system constituted of CD, guest and complex species is expressed as:

$$A_{abs} = A_{CD} + A_G + A_{CD-G} \quad (6)$$

A_{CD}, A_G and $A_{CD\text{-}G}$ represent respectively the absorbance of the host, the guest and the complex. Taking that the length of the optical path is fixed to 1 cm, the different absorbances can be expressed as a function of the molar extinction coefficients ε of each absorbing species in solution.

$$A_0 = \varepsilon_G [G]_0 \quad (7)$$

$$A_{CD} = \varepsilon_{CD} ([CD]_0 - [CD-G]) \quad (8)$$

$$A_G = \varepsilon_G ([G]_0 - [CD-G]) \quad (9)$$

$$A_{CD-G} = \varepsilon_{CD-G} [CD-G] \quad (10)$$

where A_0 represents the absorbance of the drug in absence of cyclodextrin and A_{CD}, A_G and $A_{CD\text{-}G}$ are absorbances of CD, Guest and the complex in the solution. Assuming that CD doesn't absorb light in the near-UV-Visible domain and combining equations 5 to 10 gives after a rearrangement the following equation (11) [16].

$$\Delta A = [\varepsilon_G - \varepsilon_{CD-G}] \left[\left([G]_0 + [CD]_0 + \frac{1}{K} \right) - \sqrt{\left(\left([G]_0 + [CD]_0 + \frac{1}{K} \right)^2 - 4[G]_0[G]_0 \right)_0} \right] \quad (11)$$

which relates the difference in absorbance $\Delta A = A_{abs} - A_0$ to the equilibrium constant K. The use of a nonlinear regression permits to extract simultaneously the values of Δε and K from the experimental curve of the variation of ΔA versus [CD].

Results and Discussion

The UV-Visible spectra of the drug TC-HCl in an aqueous solution at different concentrations at 25 °C are reported on Figure 2(a).

It can be observed that the spectra show three peaks centered at wavelength 190, 227 and 312 nm, corresponding to π-π* and n-π* electronic transitions of the unsaturated C = C bonds of the aromatic ring and the non-binding doublets of the nitrogen and the oxygen atoms [17]. With increasing drug concentration no significant wavelength shift occurs but the absorbance (A) increases obeying to a typical Lambert-Beer law (2*b*). This means that in this concentration range the solutions are dilute and no important intermolecular interactions exist as well as any solvent effect. From the linear fitting of the absorbance data as a function of drug concentration, the molar absorption coefficient, ε=20604 is determined for λ_{max}=312nm. The extracted value is comparable to one published by Merino *et al* for procaine hydrochloride anesthetic which possesses an identical chromophore as tetracaine, they reported a value of ε=19825 for λ_{max}=311nm [18].

Figure 3 shows the UV spectra of aqueous solutions of TC-HCl at a constant concentration of 10^{-5}M in the absence and the presence of β-CD, at three different temperatures. The analysis of the obtained three spectra shows the presence of isosbestic points which indicates the occurrence of chemical equilibrium between the free and the complexed TC-HCl. For the spectrum at 15°C both absorbance and wavelength variations (ΔA and Δλ) are obvious but for the spectra at 25 and 37°C the wavelength shift Δλ diminishes considerably with temperature increase. When the same sets of experiments are

conducted with α-CD and HPβ-CD instead of β-CD different behaviors are noted as shown in Figure 4.
Figure 4 shows, as an example, the experiments performed at 25 °C. For α-CD only one isosbestic point is visible at λ=329 nm and only absorbance variation ΔA is observed. For HPβ-CD both ΔA and Δλ variation are noticeable and many isosbestic points close to ones observed for β-CD appear. All these observations underline that an inclusion complexation has occurred between these CDs and the drug [19]. These results agree with ones reported by García et al. using the fluorimetry method [20].

The analysis of the obtained three spectra shows the presence of isosbestic points which indicates the occurrence of chemical equilibrium between the free and the complexed TC-HCl. For the spectrum at 15°C both absorbance and wavelength variations (ΔA and Δλ) are obvious but for the spectra at 25 and 37°C the wavelength shift Δλ diminishes considerably with temperature increase. When the same sets of experiments are conducted with α-CD and HPβ-CD instead of β-CD different behaviors are noted as shown in Figure 4.

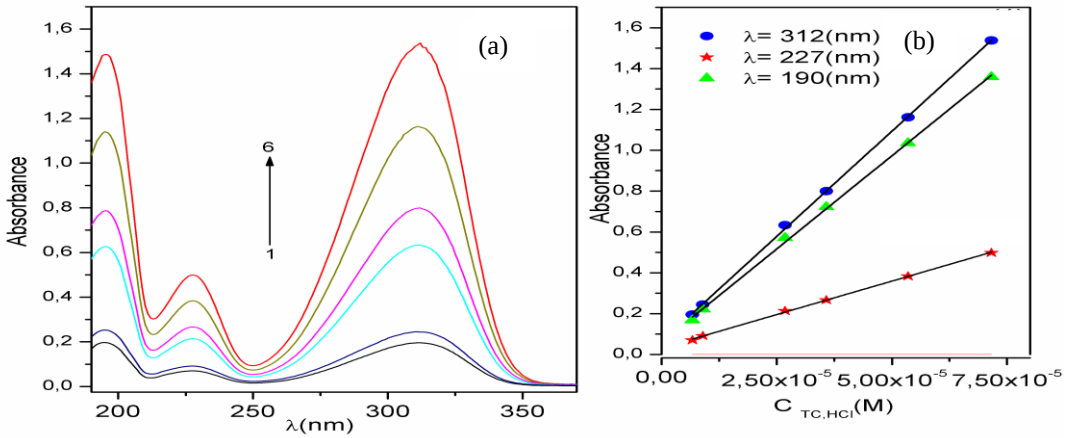

Figure 2. (a) UV-Visible spectra of aqueous solution of TC-HCl for different concentrations at 25°C. 1) 3.43x10^{-6}M, 2) 5.52 x 10^{-6} M, 3) 9.2 x 10^{-6} M, 4) 1.48 x 10^{-5}M, 5) 3.1 x 10^{-5} M, 6) 5 x 10^{-5}M. (b) Absorbance as function of concentration for different wavelengths.

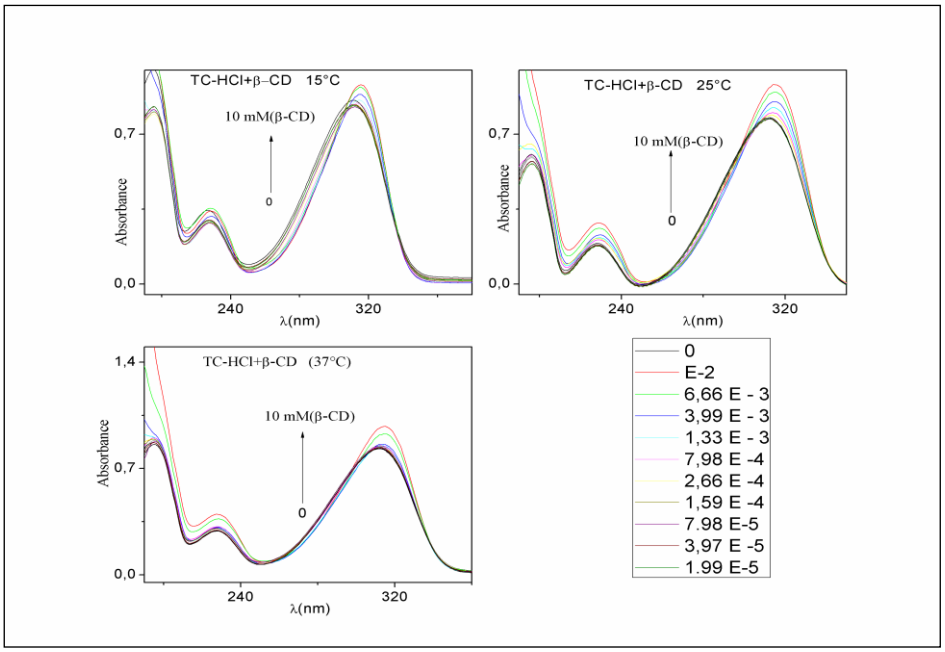

Figure 3. UV-Visible spectra of aqueous solutions of tetracaine hydrochloride (TC-HCl) 10^{-5}M with different amounts of β-CD (0-10mM) at different temperatures

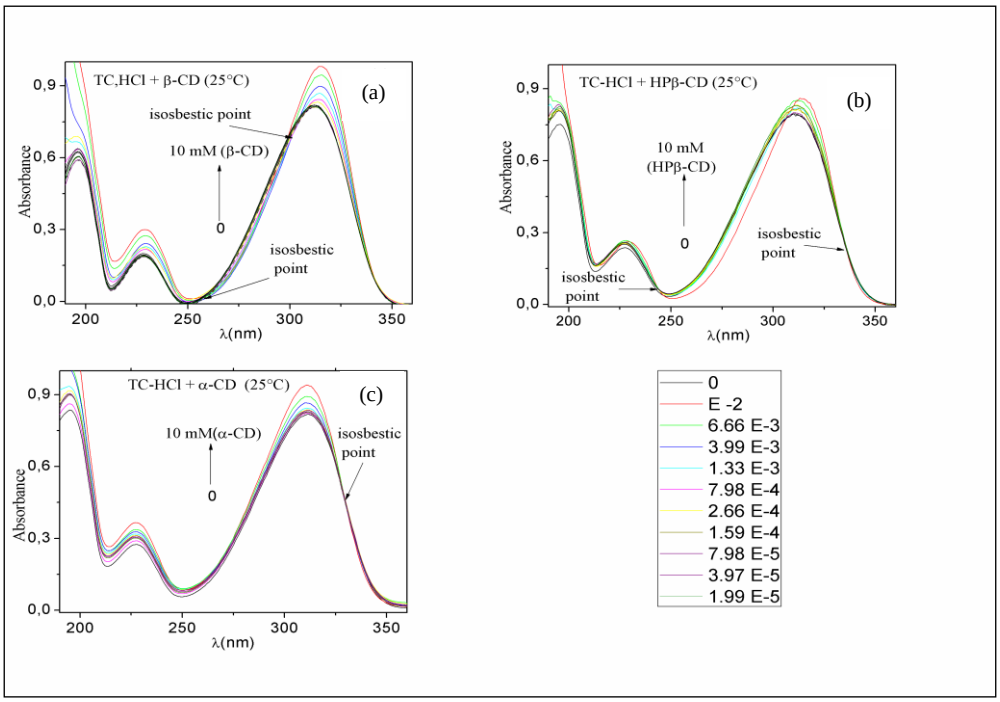

Figure 4. UV-Visible spectra of aqueous solutions (TC-HCl) 10^{-5}M in the presence of different host molecules. (a) β-CD, (b) HPβ-CD and (c) α-CD at 25 °C

In order to confirm the formation of complexes the same set of experiments were carried out in the presence of d-(+)-glucose at amounts analogous to ones used for CD's experiments at 25 °C. Because CDs are oligomers of glucose molecule units, they have mainly the same elemental composition but different spatial conformational characteristics. With this choice one tries to preserve the solvent-molecule interaction (water-CD interaction are supposed close to water-glucose one) and letting the geometry differences be the only influencing parameter. From Figure 5 it is easy to note that for d-(+)-glucose no isosbestic points exist, only a slight red shift of the order of 1 nm is obtained with a very weak effect on absorbance values.

From the variation of the curve of ΔA against CD concentration it is possible to extract the K values by a nonlinear regression method [19]. As an example, Figure 6 shows the variation of ΔA against CD's concentration at T=25°C. The same method was applied for all the studied systems at different temperatures and the corresponding association constants are reported in Table 1.

The dependence of equilibrium constants with the temperature can be noticed in Table 1, where the affinity of all cyclodextrins for the drug decreases as long as the temperature increases. Our results at T=25 °C agree with the findings of Takisawa and al. [21] who studied the inclusion of TC-HCl into α-CD and β-CD using the potentiometric method using drug-sensitive electrodes. They reported that the (β-CD/TC-HCl) formed complex is more stable than (α-CD/TC-HCl) one. From the preceding results, it is possible to determine some thermodynamic parameters of complexation from the variation of R$\ln K$ against $1/T$. Figure 7 shows the Van't Hoff plots of all association processes using both linear ($\Delta C_p° = 0$) and non-linear ($\Delta C_p° \neq 0$) fitting functions.

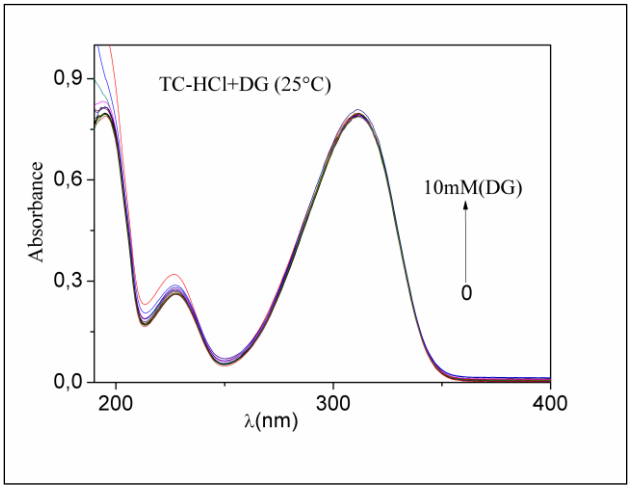

Figure 5. UV-Vis spectra of aqueous solutions of TC-HCl (10^{-5}M) for different amounts of d-(+)-glucose

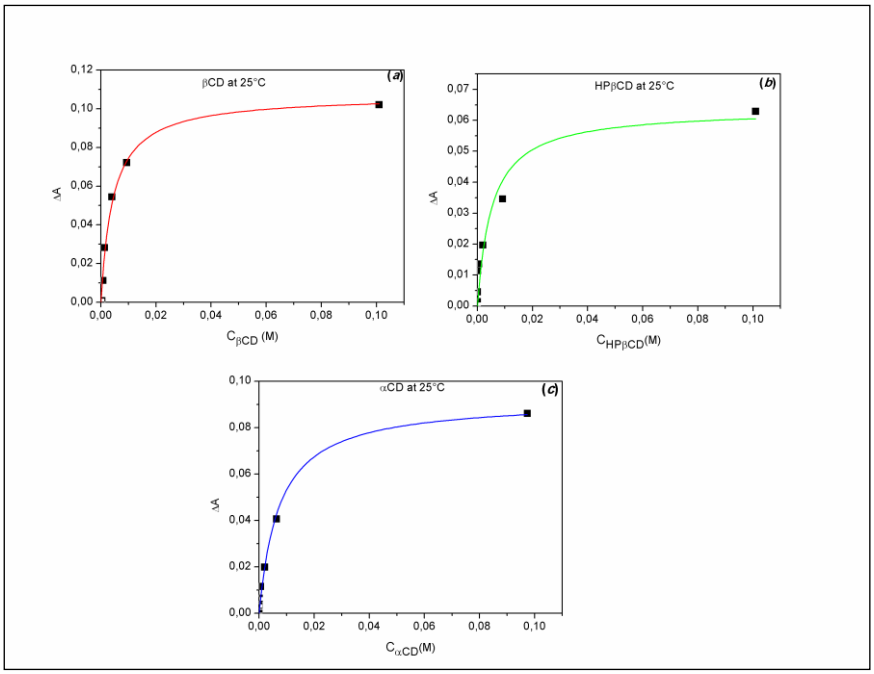

Figure 6. Non-Linear fitting of the variation of ΔA as a function of CD's concentration at 25°C for λ=310 nm

Table 1. Values of the association constant (K_{CD}) at different temperatures, obtained from UV-Vis measurements for the complex β-CD/TC-HCl, HPβ-CD/TC-HCl and α-CD/TC-HCl

T (°C)	***K*** **$_{\alpha\text{-CD}}$ (l.mol^{-1})**	***K*** **$_{\beta\text{-CD}}$ (l.mol^{-1})**	***K*** **$_{HP\beta\text{-CD}}$ (l.mol^{-1})**
15	155 ± 2	293 ± 26	285 ± 22
20	152 ± 14	263 ± 20	234 ± 12
25	137 ± 24 252 ± 14$^{(**)}$	229 ± 36 1090 ± 40$^{(**)}$	193 ± 81
37	76 ± 5.58	121 ± 9.6	91 ± 20

(**): reference [21]

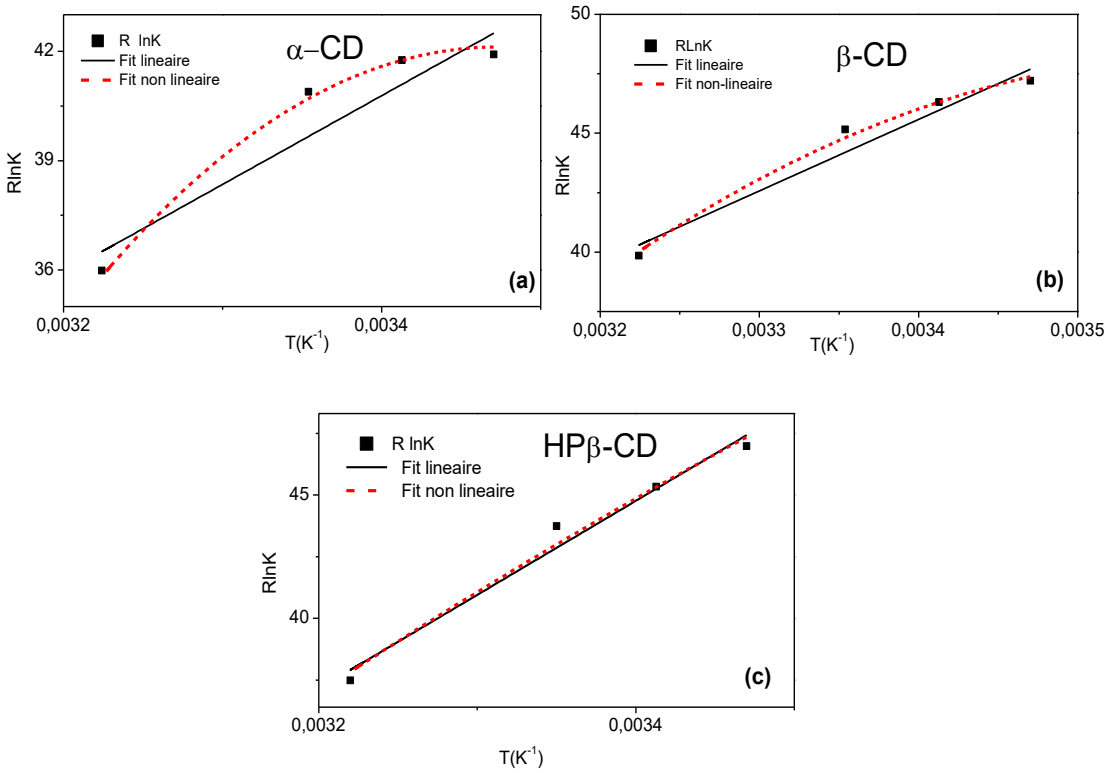

Figure 7. Van't Hoff plot for the association of TC-HCl with a) *α*-CD, *b)* β-CD and c) HPβ-CD

From the slopes of the linear fits of the data to the classical Van't Hoff equation *(R*ln*K= −ΔH°/T + ΔS°),* values of *ΔH°* equal to -24.3, -30.06 and -38.08 Kj.mol^{-1} are obtained respectively for α-CD, β-CD and HPβ-CD complexes (Table 2). Negative values of the binding enthalpy are the sign that the drug establishes favorable interactions with cyclodextrins. In such association, the enthalpy change is the result of two main conflicting contributions: the favorable enthalpy associated with van der Waals forces coupled to the host/guest hydrogen bonds formation and the unfavorable enthalpy associated with the desolvation of the guest polar groups [11-13]. Van der Waals interactions become maximal when a perfect size fitting between cyclodextrin and the drug takes place while the hydrogen bonds formation optimization is reached when drug polar groups prefer forming hydrogen bond with the cyclodextrin prior to the surrounding water molecules. Thus, an unfavorable binding enthalpy usually indicates that the desolvation is not enough to permit the inclusion of the guest molecule. However, the enthalpic contribution is not the sole provider of the stabilization of the complex and one has to consider the entropic contribution *ΔS°*. Two major terms contribute to the entropy of binding; the first one is the favorable desolvation entropy change which originates from the release of water molecules as the drug molecule and the binding cavity undergo desolvation upon binding [11-13].

The second term is related to the conformational entropy change which is almost always unfavorable since during the binding process both the drug and the cyclodextrin molecules induce the loss of conformational degrees of freedom. Thus, for our studied system, from the intercepts of Van't Hoff plot, *ΔS°* values equal to −41.8, -56.63 and -84.73 J.K^{-1}.mol^{-1} are extracted for α-CD, β-CD and HPβ-CD complexes respectively (Table 2). For all cases it can be observed that the drug bind to CDs with a favorable enthalpic term *(ΔH° < 0)* and an unfavorable entropic term *(ΔS° < 0)*. All processes are exothermic and enthalpy driven (*|ΔH°| > T|ΔS°|*), as usually found for such associations [10, 22]. With its negative entropy *ΔS° < 0* the complexation seems

to be mainly driven by Van der Waals attractive forces ($\Delta H° < 0$; $\Delta S° < 0$) and solvent reorganization effects. The contribution coming from the hydrophobic effect seems to be negligible especially for HPβ-CD ($\Delta S°$ =-84 J.mol^{-1}.K^{-1}).

For HPβ-CD a linear relationship has been found in the Van Hoff plot, revealing independence of both the $\Delta H°$ and the $\Delta S°$ of the association processes with *T*. For β-CD and α-CD, Van Hoff plots are better described by nonlinear curves as usually reported for this kind of processes by different authors [10, 22]. With its hydroxypropyl hydrocarbon chains the HPβ-CD second rim is a relatively flexible structure compared to one belonging to native βCD which is more rigid since hydrogen bonds belt is thought to exist all around the rim. These hydrocarbon chains can hinder the complete inclusion of the guest molecule and decrease the desolvation process and thus diminish the strength of the desolvation positive entropy contribution. So, the contribution of solvent reorganization and hydrophobic effects couldn't be similar in both inclusion processes which make the binding of β-CD and TC-HCl energetically more favorable than that of HPβ-CD with TC-HCl. The proposed architecture of the complexes formed can then be illustrated in Figure 8.

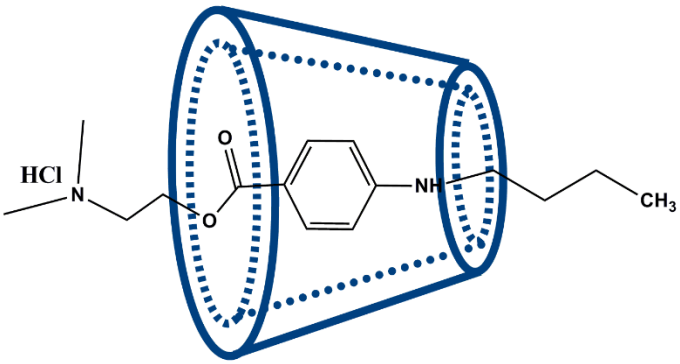

Figure 8. Architecture of inclusion complexes TC-HCl/CD

The negative value of all the ΔC_p° in table 2 obtained from the fitting of the experimental data with the non-linear Van Hoff equation ($R.\ln K = [-(\Delta H° + (T-T_o)\ \Delta C_p^\circ)/T + \Delta S° + (\Delta C_p^\circ \ln(T/T_o))]$) are close to values generally found when apolar solutes are encapsulated in CD's [23]. The difference found in the values of ΔC_p° for β-CD and HPβ-CD confirm the fact that the β-CD complex is more stable than the HPβ-CD one probably due to the diminution of the OH groups on the HPβ-CD molecule, which limit the formation of hydrogen bonds with the surrounding water.

The β-CD secondary face diameter is larger than the α-CD one and could better accommodate the inclusion of a guest molecule bearing a benzene structure. This hypothesis is confirmed by the appearance of shifts of the absorbance and wavelength λ and consequently the attractive Van der Walls interactions must be optimal for the TC-HCl/β-CD complex compared to the TC-HCl/α-CD one. The hyperchromic effect is usually attributed to the dissociation of the hydrogen bonds and the bathocromic is related to change of drug surrounding environment which become more apolar. According to Bernardi's theoretical DFT calculation in water the terminal nitrogen end of tetracaine possesses appreciable hydrophilicity which can reach the ester function close to the benzene cycle whereas the hydrocarbon butyl chain is completely hydrophobic [23, 24]. So, it can be proposed that the drug penetrates deeply in the β-CD cavity to an extent where both hydrophobic butyl chain and the benzene aromatic structure are influenced by the cavity walls which explain the simultaneous variation of ΔA and Δλ. For α-CD because of its narrower rim diameter only hydrophobic chain is penetrated and hyperchromic signature is revealed by UV-Visible spectrophotometry.

Table 2. Values of ΔH°; ΔS°, and ΔC_P^0 for the association of TC-HCl with different CDs obtained from the linear and nonlinear fitting of Van't Hoff equation

CD	**Fitting**	**ΔH° (KJ.mol^{-1})** linear	**ΔS° (J.mol^{-1}.K^{-1})**	**ΔC_P^0 (J.mol^{-1}.K^{-1})**
α-CD	Linear	-24.3 ± 7.74	-41.8 ± 25.9	-
	Nonlinear	-23.0 ± 0.077	-39.29	-2311 ± 464.4
β-CD	Linear	-30.06 ± 6.68	-56.63 ± 22.4	-
	Nonlinear	-29.23 ± 0.00	-53.40 ± 4.81	-1000 ± 4.85
HPβ-CD	Linear	-38.08 ± 6.06	-84.73 ± 20	-
	Nonlinear	-37.78 ± 5.10	-83.57 ± 17.08	-300

Conclusion

Employing the spectrophotometry technique for the inclusion complexation of tetracaine hydrochloride in different type of CDs (α-CD, β-CD and HPβ-CD) was demonstrated. The occurrence of the complexation is confirmed by the appearance of isosbestic points, hyperchromic and bathochromic shift effects on the UV-Visible spectra. From the values of complexation constants, the strength of the complexation increases from α-CD to β-CD in accord with the majority of the studies earlier reported by different authors with other techniques. From the Van't Hoff analysis, the studied complexation processes are spontaneous, with a favorable enthalpic contribution and an unfavorable entropic term. This means that the complexation seems to be driven by Van der Waals attractive forces (ΔH° < 0; ΔS° < 0) and to the solvent reorganization effects. Van't Hoff plots well show that for the drug/HPβ-CD association process linear fitting function is sufficient to describe the phenomena. However, for the α-CD and β-CD a non-linear fitting is necessary (ΔCp°≠0) to characterize their association with the drug.

Acknowledgement

The authors would like to thank the general directorate of scientific research and technological development, Algeria for the financial support.

References

1. Mary Ann Vann, M. D., Babatunde O. Ogunnaike, M. D. and Girish P. Joshi, M.B. (2007). Sedation and anesthesia care for ophthalmologic surgery during local/regional anesthesia. *Anesthesiology,* 107(3): 502-508.
2. Glantz, L., Drenger, B. and Gozal, Y. (2007). Perioperative myocardial ischemia in cataract surgery patients: general versus local anesthesia. *Anesthesia & Analgesia,* 91(6): 1415-1419.
3. Cherobin, A. C. F. P. and Tavares, G. T. (2020). Safety of local anesthetics. *Anais Brasileiros de Dermatologia,* 95 (1):82-90.
4. Ariga**,** K. and Kunitake, T. (2006). Supramolecular chemistry-fundamentals and applications. Springer-Verlag Berlin, Heidelberg: pp. 207-238.
5. Torchilin, V. P. (2006). Multifunctional nanocarriers. *Advanced Drug Delivery Reviews*, 58(14): 1532-1555.
6. Loftsson, T. and Masson, M. (2001). Cyclodextrin in topical drug formulation: Theory and practice. *International Journal of Pharmaceutics*, 225(1-2): 15-30.
7. Frömming, K. H. and Szejtli, J. (1994). Cyclodextrin in pharmacy. Klumer Academies Publishers, Dordrecht: pp. 1-18.
8. Martin Del Valle, E. M. (2004). Cyclodextrins and their uses: A review. *Process Biochemistry*, 39: 1033-1046.
9. Maheriya, P. M. (2017). Cyclodextrin: A promising candidate in enhancing oral bioavailability of poorly water soluble drugs. *Bioequivalence &Bioavailability*, 3(3): 60-63.

10. Junquera, E. and Aicart, E. (1997). Potentiometric study of the encapsulation of ketoprophen by hydroxypropyl-β-cyclodextrin. Temperature, solvent, and salt effects. *Journal Physical Chemistry. B*, 101(36), 7163–7171.
11. Astray, G., Mejuto, J. C., Morales, J., Rial-Otero, R. and Simal-Gándara, J. (2010). Factors controlling flavors binding constants to cyclodextrins and their applications in foods. *Food Research International*, 43 (4): 1212-1218.
12. Rekharsky, M. V. and Inoue, Y. (1998). Complexation thermodynamics of cyclodextrins. *Chemical Reviews*, 98(5): 1875-1918.
13. Santos, C. I. A. V., Ribeiro, A. C. F. and Esteso, M. A. (2019). Drug delivery systems: Study of inclusion complex formation between methylxanthines and cyclodextrins and their thermodynamic and transport properties. *Biomolecules*, 9(5): 196-216.
14. Hugh, C., Hemmings, Jr. and Talmage D. E. (2019). Pharmacology and physiology for anesthesia: Foundations and clinical application, Elsevier, Philadelphia. pp: 20-43.
15. Shibata, A., Ikawa, K. and Terada, H. (1995). Site of action of the local anesthetic tetracaine in a phosphatidylcholine bilayer with incorporated cardiolipin. *Biophysical Journal*, 69(2): 470-477.
16. Schalley, C. (2007). Analytical methods in supramolecular chemistry. Wiley-VCH Verlag GmbH & Co. KGaA, Weinheim. pp: 419-471.
17. Nouiri, M. A., Fergoug, T., Azayez, M., Boujores, H., Zelmat, C. and Bouhadda, Y. (2017). Experimental and theoretical study of tetracaine-hydrochloride β-cyclodextrin complexation. *Journal of Materials Environmental Sciences*, 8(5): 1589-1598.
18. Merino, C., Junquera, E., Jiménez-Barbero, J. and Aicart, E. (2000). Effect of the presence of β-cyclodextrin on the solution behavior of procaine hydrochloride. spectroscopic and thermodynamic studies. *Langmuir*, 16(4): 1557-1565.
19. Mura, P. (2014). Analytical techniques for characterization of cyclodextrin complexes in aqueous solution: A review. *Journal of Pharmaceutical and Biomedical Analysis*, 101: 238-250.
20. García, I., Brandariz, I. and Iglesias, E. (2010). Fluorescence study of tetracaine-cyclodextrin inclusion complexes. *Journal of Supramolecular Chemistry*, 22(4): 228-236.
21. Takisawa, N., Shirahama, K. and Tanaka, I. (1993). Interactions of amphiphilic drugs with α-, β-, and γ- cyclodextrins. C*olloid and Polymer Science*, 271: 499-506.
22. Cano, J. Rodriguez, A. Aicart, E. and Junquera, E. (2007). Temperature effect on the complex formation between tricyclic antidepressant drugs (amitriptyline or imipramine) and hydroxypropyl-β-cyclodextrin in water. *Journal of Inclusion Phenomena and Macrocyclic Chemistry*, 59: 279-285.
23. Bernardi, R. C., Gomes, D. E. B., Pascutti, P., Ito, A. S. and Ota, A. T. (2006). Theoretical studies on water–tetracaine interaction. *International Journal Quantum Chemistry*, 106: 1277-1282.
24. Bernardi, R. C. Gomes, D. E. B. Ito, A. S. Ota, A. T. Pascutti, P. G. and Taft, C. (2007). Density functional and molecular dynamics simulations of local anesthetics in 0.9% NaCl solution. *Molecular Simulation*, 33(14): 1135-1141.